Technical University of Denmark

DTU

On-Chip Magnetorelaxometry Using Planar Hall Effect Magnetic Field Sensors

Østerberg, Frederik Westergaard; Hansen, Mikkel Fougt

Publication date:
2013

Document Version
Publisher's PDF, also known as Version of record

Link back to DTU Orbit

Citation (APA):
Østerberg, F. W., & Hansen, M. F. (2013). On-Chip Magnetorelaxometry Using Planar Hall Effect Magnetic Field Sensors. DTU Nanotech.

DTU Library
Technical Information Center of Denmark

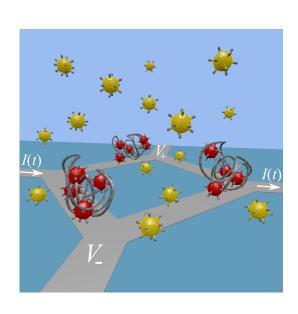# On-Chip Magnetorelaxometry Using Planar Hall Effect Magnetic Field Sensors

Frederik Westergaard Østerberg

Department of Micro- and Nanotechnology
Technical University of Denmark

Ph.D. Thesis, February 14th 2013

Frontpage picture: (Left) Shows a mixture of magnetic beads in suspensions over a planar Hall effect bridge sensor. The red beads are bound to DNA coils, while the yellow beads are free. The sensor is operated by sending a current $I(t)$ through the sensor, while measuring the signal V across the sensor. (Right) Shows a sketch of the dynamic signals obtained for beads bound to DNA coils and free beads. Beads bound to DNA coils will have a lower Brownian relaxation peak f_{B} than free beads.

Abstract

In recent years there has been an increasing interest in developing lab-on-a-chip devices that potentially can be used as point-of-care biosensors. The advantage of point-of-care biosensors is that they can analyze samples obtained from patients immediately, cutting away the time needed for sending the sample to a laboratory for analysis. Many different read out techniques can be used for point-of-care biosensors, among these are magnetic readouts, which are especially interesting because most biological samples are non-magnetic.

The goal of this thesis is to explore the possibilities and limitations of using planar Hall effect magnetic field sensors to measure magnetorelaxomety of magnetic beads. This can be used as the readout principle for volume-based biosensing, by detecting changes in the hydrodynamic diameter of magnetic beads due to binding of analytes. Traditionally magnetorelaxomety is measured by AC susceptibility measurements performed with large expensive instruments, which cannot easily be integrated with a lab-on-a-chip system. The advantages of planar Hall effect sensors are that they are small and can easily be integrated as the readout method for a lab-on-a-chip device.

In this thesis, the theoretical background for how magnetorelaxometry is measured using planar Hall effect sensors is derived. This includes a description of the relaxation mechanism of magnetic beads in both the time and frequency domains, how the planar Hall effect sensors are utilized for measuring the relaxation of magnetic beads without the need of any external fields and estimates of the forces that influence magnetic beads near a planar Hall effect sensor.

The temperature dependence of measurements using planar Hall effect sensors is investigated. This is done both with respect to how the sensor signals depend on temperature and how temperature influences the Brownian relaxation of magnetic beads. It is shown that the hydrodynamic diameter of the magnetic beads can be extracted from AC susceptibility measurements with planar Hall effect sensors when the temperature and dynamic viscosity of the liquid in which the beads are suspended are known.

AC susceptibility measurements of beads are shown to be possible using two different sensor geometries, planar Hall effect cross sensors and planar Hall effect bridge sensors. For the geometries used, the bridge sensor yields an amplification of the bead signals by a factor of six compared to the cross sensor without significant noise being added to the measurements.

A study varying the concentration of magnetic beads with a nominal diameter of 40 nm shows that the hydrodynamic diameters can be extracted reliably for concentrations down to 64 µg/mL, and the presence of beads can be detected down to 16 µg/mL. However, higher bead concentration leads to higher signal and thereby hydrodynamic diameters can be extracted more reliably.

Furthermore, it is shown that the planar Hall effect can be operated at frequencies ranging from DC to 1 MHz. This wide range of frequencies allows for measuring Brownian relaxation of magnetic beads with nominal diameters ranging from 10 nm to 250 nm. However, it is not appropriate to use beads as large as 250 nm with the planar Hall effect sensors as they are captured by magnetostatic forces from the sensor stack.

Experiments with streptavidin coated beads and biotin-conjugated bovine serum albumin show that planar Hall effect sensors can detect the presence of biotin-conjugated bovine serum albumin in the nanomolar range. Finally, measurements are performed to detect DNA-coils formed by rolling amplification using planar Hall effect bridge sensors. These results show that DNA-coils can be detected in concentrations down to 4 pM, which is comparable to what has been obtained for similar samples using commercially available measurement equipment. However, the planar Hall effect sensor have the advantage of being considerably smaller, much more simple and potentially cheaper.

Resumé

I de senere år er der opstået en interesse for at udvikle lab-on-a-chip systemer, der potentielt kan benyttes som point-of-care biosensorer. Fordelen ved point-of-care biosensorer er at de straks kan analysere prøver udtaget fra patienter og der derved undgås spildtid ved at sende prøven til et laboratorium for at blive analyseret. Mange forskellige udlæsningsmetoder kan benyttes til point-of-care biosensorer, heriblandt magnetiske udlæsningsmetoder, hvilke er specielt interessante da de fleste biologiske prøver er umagnetiske.

Målet med denne afhandling er at udforske mulighederne og begrænsningerne ved at bruge planar Hall effekt magnetisk felt sensorer til at måle magnetorelaksometry af magnetiske kugler. Dette kan benyttes som udlæsningsmetode for volumen-baseret biodetektion, ved at måle ændringer af magnetiske kuglers hydrodynamiske diameter forsaget af binding til analytter. Traditionelt måles magnetorelaksometry ved at måle AC susceptibilitet med store dyre instrumenter, der ikke let kan integreres med lab-on-a-chip systemer. Fordelene ved planar Hall effekt sensorer er at de er små og derfor let integreres som udlæsningsmetode i lab-on-a-chip systemer.

I denne afhandling er den teoretiske baggrund udledt for hvordan magnetorelaksometry måles med planar Hall effect sensorer. Dette inkluderer en beskrivelse af relaksationsmekanismer for magnetiske kugler i både tids og frekvens domænerne, hvordan planar Hall effekt sensorer kan måle relaksation af magnetiske kugler uden brug af eksterne magnetfelter samt estimater for de kræfter, der påvirker magnetiske kugler i nærheden af planar Hall effekt sensorer.

Temperatur afhængigheden af målinger med planar Hall effekt sensorer er undersøgt. Herunder hvordan sensor signalerne afhænger af temperaturen og hvordan den Brownske relaksation af magnetiske kugler påvirkes. Det vises at magnetiske kuglers hydrodynamiske diametre kan bestemmes udfra AC susceptibilitetsmålinger med planar Hall effect sensorer, når temperaturen og væskens viskositet er kendte.

AC susceptibilitetsmålinger på magnetiske kugler er påvist mulige for to forskellige sensor geometrier, planar Hall effekt kryds sensorer og planar Hall effekt bro sensorer. Med de benyttede geometrier, viste bro sensorerne at give seks gange signalet målt med kryds sensorerne uden at tilføje signifikant mere støj til målingerne.

Et studie hvor koncentrationen af magnetiske kugler med diametre på 40 nm blev varieret viste, at hydrodynamiske diametre kan bestemmes for koncentrationer over 64 µg/mL, og tilstedeværelsen af magnetiske kugler kan spores ned til 16 µg/mL. Når det er sagt, så giver højere koncentrationer større signaler og hermed kan de hydrodynamiske diametre bestemmes mere nøjagtigt.

Herudover er det påvist at planar Hall effekt sensorer kan benyttes i frekvens området fra DC til 1 MHz. Dette brede frekvensområde tillader at måle den Brownske relaksation of magnetiske

kugler med diametre fra 10 nm til 250 nm. Det viste sig dog at 250 nm ikke er egnede til målinger med planar Hall effect sensorer, da de bliver indfanget af magnetostatiske kræfter fra sensor stacken.

Eksperimenter udført med magnetiske kugler med streptavidin blandet med biotin-konjugeret bovine serum albumin viser at planar Hall effekt sensorer kan måle tilstedeværelsen af biotin-konjugeret bovine serum albumin i nanomolar området. Til slut er målinger med planar Hall effect sensorer foretaget for at detektere DNA coils fremstillet ved rolling circle amplificering. Disse resultater viser at DNA coils kan detekteres ned til koncentrationer på 4 pM, hvilket er sammenligneligt med hvad der er opnået på lignende prøver målt med kommercielt tilgængeligt måleudstyr. Planar Hall effect sensorer har dog den fordel at de er betydelig mindre, simplere og potentielt billigere.

Preface

This dissertation is written in order to partial fulfill the requirements for obtaining the PhD degree at the Technical University of Denmark (DTU). The work, on which this thesis is based, has primarily been performed at the Department of Micro– and Nanotechnology (DTU Nanotech) in the period from January 2010 to February 2013. The work has been been supervised by associate professor Mikkel F. Hansen.

Frederik Westergaard Østerberg
Department of Micro– and Nanotechnology
Technical University of Denmark
February 14th, 2013

Contents

List of Papers

Paper I
G. Rizzi, N. C. Lundtoft, F. W. Østerberg and M. F. Hansen
Reversible and Irreversible Temperature-induced Changes in Exchange-biased Planar Hall Effect
Bridge (PHEB) Magnetic Field Sensors
Sensors & Transducers Journal **15**, 22 (2012)

Paper II
F. W. Østerberg, B. T. Dalslet, D. Snakenborg, C. Johansson and M. F. Hansen
Chip-Based Measurements of Brownian Relaxation of Magnetic Beads Using a Planar Hall Effect Magnetic Field Sensor
AIP Conf. Proc. **1311**, 176 (2010)

Paper III
F. W. Østerberg, G. Rizzi, T. Zardán Gómez de la Torre, M. Strömberg, M. Strømme, P. Svedlindh and M. F. Hansen
Measurements of Brownian relaxation of magnetic nanobeads using planar Hall effect bridge sensors
Biosens.Bioelectron. **40**, 147 (2013)

Paper IV
F. W. Østerberg, G. Rizzi and M. F. Hansen
On-chip measurements of Brownian relaxation vs. concentration of 40 nm magnetic beads
J. Appl. Phys. **112**, 124512 (2012)

Paper V
F. W. Østerberg, G. Rizzi and M. F. Hansen
On-chip measurements of Brownian relaxation of magnetic beads with diameters from 10 nm to 250 nm
Submitted to J. Appl. Phys. (January 2013)

Paper VI
F. W. Østerberg, G. Rizzi and M. F. Hansen
On-chip measurements of Brownian relaxation in both frequency- and time domain
Draft (January 2013)

Papers not included in the thesis
Paper A
A. Persson, R. S. Bejhed, H. Nguyen, K. Gunnarsson, B. T. Dalslet, <u>F. W. Østerberg</u>, M. F. Hansen,
P. Svedlindh
Low-frequency noise in planar Hall effect bridge sensors
Sensor. Actuat. A-Phys. **171**, 212 (2011)

Paper B
A. Persson, R. S. Bejhed, <u>F. W. Østerberg</u>, K. Gunnarsson, H. Nguyen, G. Rizzi, M. F. Hansen,
P. Svedlindh
Modelling and design of planar Hall effect bridge sensors for low-frequency applications
Sensor. Actuat. A-Phys. **189**, 459 (2013)

List of Symbols

Symbol	Description	Unit
$\mathbf{B}$	Magnetic inductance	T
c	Molar concentration	M
D_h	Hydrodynamic diameter	m
D_nom	Nominal diameter	m
$\tilde{D}_\mathrm{h}$	Median hydrodynamic diameter	m
D_dif	Diffusivity	$\mathrm{m^2/s}$
$\mathbf{E}$	Electric field	V/m
$\mathbf{F}_\mathrm{buoy}$	Buoyancy force	N
$\mathbf{F}_\mathrm{Brown}$	Brownian force	N
$\mathbf{F}_\mathrm{drag}$	Drag force	N
$\mathbf{F}_\mathrm{mag}$	Magnetic force	N
f	Frequency	Hz
f_B	Brownian relaxation frequency	Hz
f_LN	Log-normal distribution	
g	Gravitational acceleration constant	$\mathrm{m/s^2}$
$\mathbf{H}$	Magnetic field strength	A/m
H_beads	Magnetic field of beads	A/m
H_c	Coercivity field	A/m
H_De	Demagnetization field	A/m
H_ex	Exchange field	A/m
H_ext	External applied magnetic field	A/m
H_K	Anisotropy field	A/m
H_ms	Magnetostatic field	A/m
H_sf	Magnetic self-field	A/m
h	Height	m
I	Bias current	A
I_c	Conductor current	A
I_0	Current amplitude DC	A
I_AC	Current amplitude AC	A
i	Imaginary unit	
$\mathbf{J}$	Current density	A

Symbol	Description	Unit
$\hat{\mathbf{J}}$	Current density unit vector	
K	Magnetic anisotropy constant	J/m^3
K_b	Surface current	A/m
k_B	Boltzman constant	J/K
l	Length	m
$\mathbf{m}$	Magnetic moment	Am^2
M	Magnetization	A/m
$\mathbf{M}$	Magnetization vector	A/m
$\hat{\mathbf{M}}$	Magnetization unit vector	
M_0	Magnetization at equilibrium	A/m
M_r	Remanent Magnetization	A/m
M_s	Saturation Magnetization	A/m
$\hat{\mathbf{n}}$	Unit vector normal to the surface	
R	Resistance	Ω
R_offset	Resistance offset	Ω
S_0	Low-field sensitivity	V/(AT)
T	Absolute temperature	K
T_0	Period	s
t	Time	s
t_dif	Diffusion time	s
t_sedi	Sedimentation time	s
t_FM	Thickness of ferromagnetic layer	m
U_De	Demagnetization energy	J
U_ex	Exchange energy	J
U_K	Anisotropic energy	J
U_Z	Zeeman energy	J
$\tilde{u}$	Energy volume density	A/m
V	Volume	m^3
V_h	Hydrodynamic volume	m^3
V	Voltage	V
V_C	Cross-shaped sensor signal	V
V_B	Bridge sensor signal	V
V_1'	In-phase first harmonic signal	V
V_1''	Out-of-phase first harmonic signal	V
V_2'	In-phase second harmonic signal	V
V_2''	Out-of -phase second harmonic signal	V
V_0t	Signal amplitude	V
V_0	Fitting parameter modified Cole-Cole	V
V_∞	Fitting parameter modified Cole-Cole	V
v_b	Bead velocity	m/s

Symbol	Description	Unit
v_f	Fluid velocity	m/s
w	Width	m
α	Polydispersity	
α_J	Current density angle	rad
χ	Complex magnetic susceptibility	
χ'	In-phase component of complex magnetic susceptibility	
χ''	Out-of-phase component of complex magnetic susceptibility	
χ_0	DC magnetic susceptibility	
χ_∞	High frequency magnetic susceptibility	
$\Delta\rho$	$\rho_\parallel - \rho_\perp$	Ωm
η	Dynamic viscosity	kg/(ms)
γ_0	Effect of self-field due to assymmetry of sensor stack	
γ_1	Effect of self-field due to magnetic beads	
μ_0	Permeability of free space	Vs/(Am)
ρ	Resistivity	Ωm
$\underline{\underline{\rho}}$	Resistivity tensor	Ωm
$\rho_\parallel$	Resistivity at parallel current density and magnetization	Ωm
$\rho_\perp$	Resistivity at orthogonal current density and magnetization	Ωm
ρ_ave	Average resistivity	Ωm
ρ_bead	Bead mass density	kg/m^3
ρ_fluid	Fluid mass density	kg/m^3
σ_ex	Interface energy per area	J/m^2
σ_s	Specific saturation magnetization	Am^2/kg
τ_N	Néel relaxation time	s
τ_B	Brownian relaxation time	s
τ_eff	Effective relaxation time	s
θ	Magnetization angle	rad

List of Abbreviations

Abbreviation	Description
AMR	Anisotropic magnetoresistance
ANOVA	Analysis of variance
BSA	Bovine serum albumin albumin
bBSA	Biotin-conjugated bovine serum albumin
CEA	Carcinoembryonic antigen
DAQ	Data acquisition box
GMR	Giant magneto resistance
GPIB	General Purpose Interface Bus
MM	Micromod
ON	Ocean Nanotech
PBS	Phosphate buffer saline
PCB	Printed circuit board
PDMS	Polydimethylsiloxane
PID	Proportional-integral-derivative
PMMA	Polymethylmethacrylate
RCA	Rolling circle amplification
SQUID	Superconducting quantum interference device
VSM	Vibrating sample magnetometer

Chapter 1

Introduction

For any patient suffering from a given condition, a quick recovery depends on a fast and accurate diagnosis. Physicians have throughout history based diagnoses on the information the patient was able to provide combined with a physical examination of the patient. Given advancement in technology and medical engineering, the diagnosis of a patient is nowadays also supported by information obtained from human samples, i.e., blood, urine, saliva, tissue samples depending on the condition suspected by the physician based on a previous examination. To obtain information from the human samples, they need to be analyzed. The analysis of samples can be performed in many ways, but most often samples collected by physicians at the point-of-care are sent to and analyzed at distant laboratories. This is most often a time consuming process, which slows the diagnosis. A less time consuming procedure would be to be able to analyze the sample at the point-of-care, i.e., by utilization of biosensors, in order to quickly combine and assess all information and provide the patient with a diagnosis, hopefully, immediately.

1.1   Point-of-care biosensors

In order for point-of-care biosensors to become successful, the benefit that a sensor provides must out-weigh the cost of the sensor. That is, the price per analyzed sample must be sufficiently low and not exceed the benefit of a quick response. For instance, if no treatment exists for a disease, a fast diagnosis might not be of much benefit unless the disease is contagious and requires isolation of the patient.

The most widely used biosensor is the glucose sensor, which in 2005 represented 85 % of the world market of biosensing [1]. The glucose sensor is a great aid for people suffering from diabetes, as it can tell them how much insulin they need to stabilize their blood sugar [2, 3]. The glucose sensors are typically based on electrochemistry, where the oxidation of glucose is measured by electrodes. Other common biosensors are lateral flow assays, which can be used for qualitative detection of bacteria and viruses, but is best known in their use as pregnancy tests [4]. In addition to these two types of biosensors, a lot of other techniques are being utilized and developed. Amongst these are magnetic biosensors, which are the focus of this PhD thesis.

1.2   Magnetic biosensors

Magnetic biosensors cover a very broad category of sensors and the sensing principles vary a lot. Many magnetic biosensors use magnetic beads in some way, either as a magnetic label or for actuation. Since most biological samples are non-magnetic, a common approach is to detect a change in the magnetic field from the beads when a specific analyte is present. Due to the non-magnetic properties of a sample it will not add a background signal, which is a possible drawback of non-magnetic techniques. Other techniques use the magnetic properties of the beads to actuate the beads by an external magnetic field and measure changes in the optical properties of the sample [5, 6, 7].

1.2.1   Magnetic beads

Magnetic beads are fairly easy and inexpensive to produce and are commercially available in sizes ranging from a few nanometers [8] to hundreds of micrometers [9]. This wide range of possible sizes allows for optimizing the binding of beads to proteins, viruses and even cells [10, 11].

Typically, magnetic beads are spherical particles composed of a magnetic core surrounded by a non-magnetic shell. The core can be composed of different magnetic materials, such as iron oxides (e.g. Fe_3O_4, γ-Fe_2O_3), ferrites (e.g. $CoFe_2O_4$, $MnFe_2O_4$), metals (e.g. Fe, Ni, Co) and alloys (e.g. FePt, $CoPt_3$); magnetite Fe_3O_4 and maghemite γ-Fe_2O_3 are the most commonly used materials [12]. The magnetic beads can be fabricated such that the core contains either a single magnetic core particle or multiple magnetic core particles. Beads with single core particles are typically smaller than 50 nm in diameter. Beads with multiple magnetic core particles are typically larger and the individual core particles are distributed in a matrix. For beads with diameters ranging from 50 nm to 500 nm the individual core particles are often packed in a cluster to maximize the magnetic material in each bead. For particles above 500 nm the individual core particles are often distributed over the matrix to decrease the density of the particles.

The magnetic cores are usually covered by a non-magnetic shell, which can be surfactants (oleic acid and stearic acid), polymers (starch, dextran and polyethylene glycol), or inorganic (e.g. Gold and Silica) [13]. The shell serves several different purposes: It makes the magnetic beads biocompatible [14], it decreases hydrophobic interactions to prevent beads from agglomerating [13], it protects the core from oxidation thus making the beads stable over time [11], and it prevents the metal ions in the core from contaminating the solution they are diluted in, which is a potential problem if the polymerase chain reaction (PCR) is to be performed on the sample. Furthermore, the shell allows for easy functionalization of the beads such that they can specifically bind to many different types of analytes.

Besides being used for indirect detection of analytes, magnetic beads have also proven useful within other aspects of biomedicine including, sample separation [15], sample manipulation [14], hyperthermia [11] and targeted drug delivery [10, 16].

1.2.2   Types of sensors

Many different types of sensors that can measure the magnetic field from magnetic beads exist. Among magnetic field sensors commonly used for biosensing are: superconducting quantum interference devices (SQUID) [17, 18], inductive methods [19], fluxgates [20] and magnetoresistive

sensors [21, 22, 23]. The SQUIDs are known for their very high sensitivities but they are generally large in size and require cryogenics, which make them expensive and therefore not suited for point-of-care biosensors, a picture of a SQUID is shown in Fig. 1.1. Instruments based on the inductive method and fluxgates are also fairly large in size and therefore not easily integrated with sample preparation on a lab-on-a-chip device. A picture of a DynoMag (Imego AB, Sweden), which is an instrument based on the inductive method, is shown in Fig. 1.2. Magnetoresistive sensors are very flexible in their designs and the sizes are typically in the micrometer range. Due to their small size they require small sample volumes and can potentially be integrated with a lab-on-chip sample preparation device.

Fig. 1.1: Magnetic Property Measurement System XL (Quantum Design, Inc., USA) based on a SQUID. Source: http://www.qdusa.com.

Fig. 1.2: DynoMag (Imego AB, Sweden) based on inductive method. Source: http://www.imego.com.

Thomson [24] discovered that the resistance of certain materials depends on the magnetization. He observed changes in the resistivities of iron and nickel of less than 1 % when applying magnetic fields. Since the discovery of the giant magneto resistance (GMR) [25, 26] in thin-film, where the resistivity at 4.2 K could be almost halved by applying a magnetic field, there has been a lot of research within the field of magnetoresistive sensors, mainly due to their usage in read heads in hard disk drives [27]. The increased interest in magnetoresistive sensors led to their usage for detection of magnetic beads. Magnetoresistive sensors used for detecting magnetic beads include GMR sensors [21, 28, 29], magnetic tunnel junction (MTJ) sensors [30] and anisotropic magnetoresistive (AMR) sensors [31].

Two approaches exist for combining magnetic field sensors with magnetic beads to form a biosensor [11]. One is to functionalize both the magnetic bead and the sensor surface, such that the presence of an analyte will act as glue between the bead and surface. This approach is known as surface-based biosensing or a sandwich assay, due to the analyte being sandwiched between the surface and the bead. The other approach, known as volume-based biosensing, is to functionalize only the beads and then measure changes in the hydrodynamic size of the beads due to the binding of analytes.

1.2.3 Surface-based biosensing

The aim of surface-based biosensors is to measure beads bound to the surface when a specific analyte is present. The simplest way to achieve this is by using magnetic field sensors that are more sensitive to beads near the surface than beads in suspension. This is sketched in Fig. 1.3, where it is shown that when no analytes are present (a) the beads are floating freely and only give rise to a small effective field at the sensor. When the specific analytes are present (b), the beads will attach to the surface, resulting in a smaller effective field acting on the sensor. From Fig. 1.3 it is seen that the beads are magnetized by an external applied field (H_{ext}). In order for this to work, the beads should be stable in the solution and not sediment to the bottom as this would make it difficult to distinguish between beads bound to the surface and sedimented beads. If the beads are sedimenting, a washing step could be employed to remove all the beads not bound to the surface.
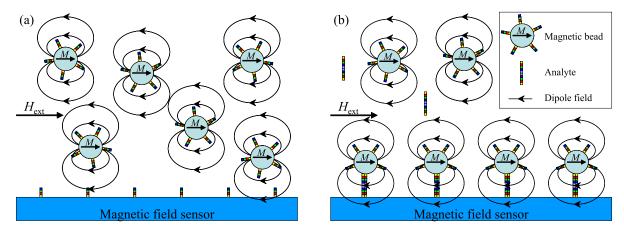
Fig. 1.3: Schematic of surface-based biosensing. (a) Shows functionalized surface and magnetic beads without any analytes present. Beads are floating freely. (b) When analytes are added to the solution the magnetic beads will attach near the sensor surface. Thus, increasing the magnetic field from the beads acting on the sensor.

The surface-based magnetic biosensor is very similar to detection using fluorescent labels. The differences are that the fluorescence tags have been replaced by magnetic beads, the exciting laser is replaced by the external field, and the detection optics is replaced by the magnetic field sensors. However, due to larger background signal when using fluorescence tags, Schotter *et al.* [32] showed that magnetic tags detected using GMR sensors were more sensitive for detection of DNA. Martins *et al.* [33] have demonstrated that GMR sensors can be used to detect DNA concentrations down to a few femtomolar and with a dynamic range of 5 orders of magnitude.

Some of the most promising results of surface-based magnetic biosensing have been achieved by the group of S. X. Wang at Stanford University using GMR sensors to detect proteins. They have shown that they are able to detect the tumor marker carcinoembryonic antigen (CEA) down to concentrations of 5 fM with a linear dynamic range over 6 orders of magnitude without amplification [34]. Also, their results are independent of pH and whether the CEA is spiked in 0.1% bovine serum albumin (BSA) in phosphate buffered saline (PBS) or mouse serum. Temperature variations, which are often a problem for magnetoresistive sensors, are accurately corrected for [35]. They have also demonstrated the possibility of multiplexing 64 sensors on

one chip and being able to measure in real time, getting a data point from each sensor with 5 s interval [36, 37, 38] and they have even made a portable version of the setup [39]. Furthermore, chips with 1008 sensors have been fabricated with a sensor density allowing for up to 100,000 per cm^2 [40], which allows for detecting the same number of different analytes on a single chip.

1.2.4 Volume-based biosensing

As mentioned, volume-based detection requires only functionalization of the magnetic beads and not the sensor surface. When the magnetic beads bind to analytes, the effective hydrodynamic size of the magnetic beads changes due to the size of the analyte. One way of detecting the hydrodynamic size change of the magnetic beads is by measuring a change in the Brownian relaxation of the beads. This method was first proposed by Connolly and St Pierre [41]. Depending on the nature of the analyte, the change in the hydrodynamic size can be small or large. For instance, if the analyte is only able to bind to one magnetic bead and the bead is much larger than the analyte, the hydrodynamic diameter will not change much [19, 42]. If the analyte has multiple binding sites, the analytes can bind two or more beads together, which significantly increases the hydrodynamic diameter [43]. A third possibility is if the analytes themselves are large compared to the beads, then the hydrodynamic size will also increase significantly [44]. Examples of these different types of analytes are sketched in Fig. 1.4.
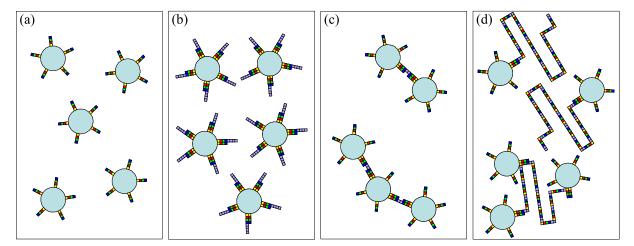
Fig. 1.4: Schematic of volume-based biosensing. (a) The sample contains no analytes; thus the beads are free to rotate. (b) The sample contains small analytes with only one binding site, the hydrodynamic diameter is slightly increased. (c) The sample contains small analytes with more than one binding site, which allow for formation of beads clusters, the hydrodynamic diameter is increased more than (b). (d) The sample contains large analytes with multiple binding sites, the hydrodynamic diameter is significantly increased.

Measurements of Brownian relaxation of magnetic beads for biosensing are performed by magnetorelaxometry, typically in the frequency domain by AC susceptibility measurements, where the magnetic beads are placed in an alternating magnetic field and the dynamic magnetic response is measured as function of the field frequency. AC susceptibility measurements have been demonstrated using SQUID magnetometers [45], inductive methods [19, 46], fluxgates [47] and magnetoresistive sensors [48, 49]. However, it is also possible to measure the relaxation in

the time domain [50, 51, 52, 53, 54], where a magnetic field is applied such that all the beads are magnetized in the same direction. When the field is turned off the magnetic beads will relax, which can be measured by a decrease in the effective field from the beads. The advantage of the time domain measurements is that they are much faster to perform than the measurements in the frequency domain. However, time domain measurements are measured in DC and noise may therefore affect the measurements more.

So far, the lowest limit of detection for the volume-based detection schemes based on Brownian relaxing measurements have been reported by Strömberg *et al.* [44] using a SQUID magnetometer and Zardán Gómez de la Torre *et al.* [55] using a DynoMag based on inductive method. Both readout techniques are used to detect DNA coils produced by padlock probe target recognition [56] and rolling circle amplification (RCA) [57, 58]. The DNA coils are long single stranded DNA consisting of multiple repetitions of the same DNA sequence entangled into a coil with a diameter on the order of 1 µm. By functionalizing magnetic beads with the complementary DNA sequence the presence of the DNA coils is able to significantly increase the hydrodynamic diameter of the magnetic beads. For both readout techniques, the limit of detection obtained is on the order of 3-4 pM with a dynamic range of 3 orders of magnitude. The drawback of detecting DNA coils formed by padlock probe target recognition and RCA is that sample preparation is necessary. Currently, the sample preparation is performed manually, and this would need to be replaced by a lab-on-a-chip device before the technique potentially can be turned into a point-of-care device. Also, the SQUID and the inductive detection methods would need to be replaced by a smaller and less expensive technology.

In the literature there are several reports of miniaturized AC susceptometers: Enpuku *et al.* [48, 59] have used a commercial available AMR barber pole sensor positioned below and adjacent to the sample; such when the exciting magnetic field is applied perpendicular to the sensitive direction of the AMR sensor, the sensor will only detect the magnetic field from the sample orthogonal to the exciting field. With this setup they have demonstrated AC susceptibility measurements in the frequency range 1 Hz–10 kHz. Haraszczuk *et al.* [60] have shown that it is possible to use spin valve GMR sensors placed on a needle probe. Four GMR sensors are arranged in a Wheatstone bridge configuration, where one of the sensors is near the sample and the three remaining are still in the exciting field. If the Wheatstone bridge is balanced only the signal due to the magnetic field from the sample is picked up. With this setup they have demonstrated AC susceptibility measurements in the frequency range 5 Hz–1 kHz. Oisjoen *et al.* [61] have built a high-temperature SQUID, where the exciting field is applied in the insensitive direction of the SQUID and the sample is placed such that it gives rise to a magnetic field along the sensitive direction of the SQUID. With this setup they have demonstrated that relaxation measurements can be performed in both the time domain and the frequency domain in the range 1 Hz–10 kHz. However, the high-temperature SQUID operates at 77 K and therefore still requires cryogenics. These three techniques all use miniaturized sensors but still require electromagnets to generate the magnetic excitation field. Dalslet *et al.* [49] have shown that it is possible to use a planar Hall effect cross sensor without the need for external electromagnets to measure AC susceptibility in the frequency range 1 Hz–1 kHz. Instead the magnetic field arising from the bias current through the sensor can be used to excite the beads.

1.3 Motivation and outline

The work presented in this thesis continues the work by Dalslet *et al.* [49] of using planar Hall effect sensors for measuring magnetorelaxometry on-chip without the need of external electromagnets. Recently, Henriksen *et al.* [62] showed that the low-field sensitivity of the planar Hall effect cross sensors like those used by Dalslet *et al.* [49] could be increased more than 100 times by changing the shape from a cross to a Wheatstone bridge.

The aim of this PhD project is to investigate the possibilities and limitation of using planar Hall effect bridge sensors for measuring AC susceptibility of magnetic beads. In this thesis, AC susceptibility measurements are performed on magnetic beads using both planar Hall effect cross sensors and planar Hall effect bridge sensors. Furthermore, the effects of varying parameters, such as temperature, bias current, bead concentration and bead size are investigated. The possibility of measuring Brownian relaxation of magnetic beads in the time domain is also explored. Finally, in collaboration with Uppsala University, Brownian relaxation measurements are performed using planar Hall effect bridge sensors to detect DNA coils formed by RCA similar to those detected by Strömberg *et al.* [44] using a SQUID magnetometer and by Zardán Gómez de la Torre *et al.* [55]using a DynoMag, such that the performance of planar Hall effect bridge sensors as volume-based biosensors can be determined and compared to the measurements already performed with the SQUID and the DynoMag.

Here is a short overview of the structure of the thesis:

- In Chapter 2 the theoretical background for the thesis is described. This includes the governing equations of how magnetic beads relax in the time and frequency domains, followed by the principles of how the planar Hall effect bridge and cross sensors can be used to measure bead relaxation. In the end of the chapter, the forces influencing magnetic beads near planar Hall effect sensors are estimated.

- In Chapter 3 it is explained how the planar Hall effect sensors are fabricated and characterized, followed by a description of how the experimental setup is constructed to be able to perform measurements with the planar Hall effect sensors. Furthermore, it is described how measurements are recorded and analyzed.

- Chapter 4 contains a study on how planar Hall effect bridge sensors depend on temperature. It is also investigated how low-temperature annealing in an applied magnetic field affects the temperature dependence of the sensors. In the study, the temperature dependence is separated into reversible and irreversible changes. These results are published in Paper I.

- Chapter 5 contains AC susceptibility measurements performed with planar Hall effect bridge sensors. The effects that are investigated include: varying the temperature, changing sensor geometry from a cross to a Wheatstone bridge type, varying the bias current through the sensor, varying the bead concentration and varying the nominal bead size. In the last part of the chapter, AC susceptibility measurements performed with planar Hall effect sensors are compared to measurements performed with a commercial AC susceptometer. The results in this chapter are from Papers II, III, IV and V.

- Chapter 6 contains relaxation measurements of magnetic beads performed in the time domain. Measurements are performed for varying bias current and nominal bead sizes. These results have been written into a draft, which can be seen in Paper VI.

- In Chapter 7, initial experiments of detecting biotin-conjugated bovine serum albumin (bBSA) are presented for measurements in both the time and frequency domains. The chapter also contains results from experiments detecting DNA coils formed by RCA with planar Hall effect bridge sensors, which was the primary aim of the project. Finally, different methods for analyzing the measurement of detecting DNA coils are discussed to find the optimal detection scheme for volume-based biosensing with planar Hall effect sensors.

- Chapter 8 contains an outlook, which include the ideas that due to time limitations were not carried out within this thesis.

- In Chapter 9 the conclusions of the thesis are presented.

Chapter 2

Theory

In this chapter the theory necessary for understanding how relaxation of magnetic beads can be measured with planar Hall effect sensors is presented. The first section describes the magnetic properties of magnetic beads relevant to this thesis. In the following section it is described how a magnetic bead will relax when placed in a magnetic field in both the time and frequency domains and how the relaxation mechanisms depend on the size of the bead. In the following sections, the sensor signals are derived for planar Hall effect bridge and cross sensors, both with respect to detecting externally applied magnetic fields and magnetic fields from magnetic beads magnetized by the magnetic field arising from the bias current through the sensors. Finally, the forces acting on magnetic beads placed near a planar Hall effect sensor are estimated.

2.1   Magnetic beads

In this section the magnetic properties of magnetic beads that are important in relation to this thesis are described. When a magnetic field strength $\mathbf{H}$ is applied to a magnetic material, the magnetic inductance $\mathbf{B}$ is given as

$$\mathbf{B} = \mu_0(\mathbf{H} + \mathbf{M}), \tag{2.1}$$

where μ_0 is the permeability of free space and $\mathbf{M}$ is the magnetization of the material, which is given as the magnetic moment per unit volume

$$\mathbf{M} = \frac{\mathbf{m}}{V}. \tag{2.2}$$

Here $\mathbf{m}$ is the magnetic moment and V is the volume of the material. The magnetization of a linear magnetic material is related to the applied field by

$$\mathbf{M} = \chi\mathbf{H}, \tag{2.3}$$

where χ is the magnetic susceptibility. In reality, the magnetization cannot be described as simple as this, but depends on the magnetic properties of the material. In Fig. 2.1 the magnetization is sketched as a function of applied magnetic field for (A) a ferromagnetic material

and (B) a superparamagnetic material. It is seen that Eq. (2.3) is only valid for a superparamagnetic material near $\mathbf{H} = 0$ and that the magnetization of both the ferromagnetic and the superparamagnetic material saturates at $M = M_s$ for large applied fields. It is also seen that the ferromagnetic material has a remanent magnetization M_r, when the applied field is zero, while the superparamagnetic material is defined as having an average magnetization of zero in zero applied field. For the ferromagnetic material, the coercivity field H_c is defined as the magnetic field that must be applied for making the magnetization zero.
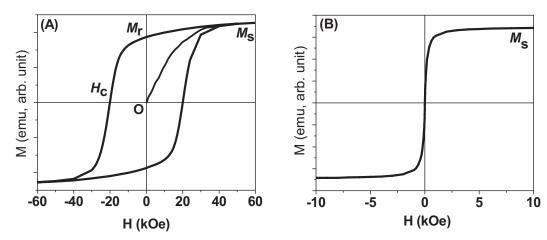
Fig. 2.1: Magnetization curves for (A) ferromagnetic and (B) superparamagnetic materials. The magnetic properties are also denoted on the figure: Saturation magnetization M_S, remanent magnetization M_r and coercivity field H_c. Source: Sun [63]

As mentioned in the introduction, magnetic beads can be composed of a variety of different materials and the core can contain either a single or multiple magnetic core particles. Depending on the individual core particle size and the time scale of the experiment, the magnetic beads will exhibit ferromagnetic or superparamagnetic behavior. If the individual core particles are made of Fe_3O_4 and are smaller than ~ 10 nm they will exhibit superparamagnetic behavior at room temperature, while larger particles will exhibit ferromagnetic behavior.

In this thesis both beads consisting of a single core particle and multi-core particles are used. The single core beads from the company Ocean Nanotech (ON) (USA) have nominal diameters D_{nom} of 10 nm, 25 nm and 40 nm. The cores of the 10 nm beads are maghemite (γ-Fe_2O_3) and the cores of 25 nm and 40 nm beads are magnetite (Fe_3O_4). The multi-core beads are from the company Micromod (MM) (Germany) and consist of a cluster of magnetite particles. For the beads with nominal diameters of 50 nm and 80 nm the core particles are distributed in a starch matrix, while the core particles for the beads with nominal diameters of 130 nm and 250 nm are distributed in a dextran matrix. The beads used in this thesis are listed in Table 2.1.

In the following section, where relaxation mechanisms are described, the magnetic beads are assumed to behave ferromagnetically, i.e., the beads are treated as having a permanent magnetization. This is believed to be a valid assumption since Micromod, the producer of the multi-core beads with nominal diameters from 50 nm to 250 nm, claims that these beads are thermally blocked. The single core beads with nominal diameters 25 nm and 40 nm from Ocean Nanotech have core sizes that are also expected to have a remnant magnetization in zero applied

field. Only for the beads with a diameter of 10 nm the assumption may not be entirely valid. By assuming that the beads have a permanent magnetization, the only way for the beads to align their magnetization with the applied magnetic field is by a physical rotation of the beads. However, even superparamagnetic beads may rotate physically as described by Janssen *et al.* [64] as long as there is a phase-lag between the magnetization of the bead and the applied magnetic field, which gives rise to a torque.

In Section 2.9, where the forces acting on magnetic beads are considered, the beads will be assumed to be superparamagnetic and behave like a linear magnetic material ($\mathbf{M} = \chi \mathbf{H}$), i.e., the bead magnetization is induced by an applied magnetic field. This is assumed in order to be able to simply estimate the magnetic forces acting on a magnetic bead.

Table 2.1: Magnetic beads used throughout the thesis. Information supplied by the two producers: Ocean Nanotech (ON) and Micromod (MM). The saturation magnetization is reported in specific saturation magnetization, which is related to the saturation magnetization by $M_\mathrm{s} = \rho \sigma_\mathrm{s}$.

D_nom [nm]	Producer	Type	ρ [kg/m^3]	Core type	Surface group	σ_s Am^2/kg Fe	H_c kA/m
10	ON	SHP	-	Single (γ-Fe$_2$O$_3$)	COOH		
25	ON	SHP	-	Single (Fe$_3$O$_4$)	COOH		
40	ON	SHP	-	Single (Fe$_3$O$_4$)	COOH		
50	MM	BNF-Starch	3200	Multi (Fe$_3$O$_4$)	NH$_2$	>76	0.449
80	MM	BNF-Starch	3200	Multi (Fe$_3$O$_4$)	Streptavidin	>76	0.449
80	MM	BNF-Starch	3200	Multi (Fe$_3$O$_4$)	Plain	>76	0.449
130	MM	Nanomag-D	3000	Multi (Fe$_3$O$_4$)	Plain	>75	0.444
250	MM	Nanomag-D	2500	Multi (Fe$_3$O$_4$)	Plain	>75	0.704

Throughout the thesis, the beads will be referred to by their nominal diameter, i.e., when the "50 nm beads" is mentioned it refers to the BNF-Starch bead with a nominal diameter of 50 nm from Micromod listed in Table 2.1. However, two types of 80 nm beads are used. The plain beads will be referred to as simply "the 80 nm beads," while the streptavidin coated beads will be referred to as the 80 nm beads with streptavidin.

2.2 Relaxation of magnetic beads

A magnetic bead placed in an external applied magnetic field will align its magnetic moment to the field. The magnetic moment of the bead can align to the applied field by either an internal flipping of the magnetic moment or by a physical rotation of the entire bead. The internal flipping of the magnetic moment is called Néel relaxation [65], while the physical rotation is called Brownian relaxation [66]. The relaxation of a magnetic bead can be measured in both the time and frequency domains. Below, the governing equations for both domains are briefly described.

2.2.1 Time domain

For time domain measurements, both the Néel and Brownian relaxations are characterized by relaxation times that depend on the physical properties of the magnetic bead and the liquid in

which the bead is suspended. The Néel relaxation time is given by [65]

$$\tau_{\mathrm{N}} = \tau_0 \exp\left(\frac{KV}{k_{\mathrm{B}}T}\right), \tag{2.4}$$

where τ_0 is a material dependent constant of typically 0.1–1 ns, K is the magnetic anisotropy constant, V is the volume of the magnetic domain, k_{B} is the Boltzmann constant and T is the absolute temperature.

The Brownian relaxation time is given by [66]

$$\tau_{\mathrm{B}} = \frac{3\eta V_{\mathrm{h}}}{k_{\mathrm{B}}T}, \tag{2.5}$$

where η is the dynamic viscosity of the liquid in which the bead is suspended, V_{h} is the hydrodynamic volume of the bead, which for a spherical bead is given by

$$V_{\mathrm{h}} = \tfrac{1}{6}\pi D_{\mathrm{h}}^3, \tag{2.6}$$

where D_{h} is the hydrodynamic diameter of the bead.

The effective relaxation time τ_{eff} is given by

$$\frac{1}{\tau_{\mathrm{eff}}} = \frac{1}{\tau_{\mathrm{N}}} + \frac{1}{\tau_{\mathrm{B}}}. \tag{2.7}$$

From this it is seen that the relaxation mechanism with the shortest relaxation time dominates. As mentioned in the previous section only beads with diameters ranging from 10 nm to 250 nm are used in this thesis. The multi-core beads are claimed to be thermally blocked by the producer and it is assumed that this is also the case for the single core beads. That the beads are thermally blocked means that the Néel relaxation times are on the order of seconds, while the Brownian relaxation times for these sizes are in fractions of a second. Thus, Brownian relaxation is the dominating relaxation mechanism and Néel relaxation is neglected for the remaining part of the thesis. This means that hydrodynamic diameter can be determined from the relaxation time, if the temperature and dynamic viscosity are known.

2.2.1.1   Relaxation in a flipping magnetic field

Consider a thermally blocked magnetic bead placed in an external magnetic field with the magnetization of the bead parallel to the field. At $t = 0$, the direction of the magnetic field is flipped and the magnetization of the bead is then initially antiparallel to the direction of the applied field. As the magnetic energy of the bead is minimized when the magnetization and the applied field are parallel, the magnetic bead will rotate such that the magnetization again becomes parallel to the applied field. This situation is sketched in Fig. 2.2 for the case where the applied field is flipped from $B = -B_0$ to $B = +B_0$ at $t = 0$.

The rotation of the magnetization of the magnetic bead is described by Brownian relaxation. For the situation sketched in Fig. 2.2, the magnetization will relax from being $-M_0$ immediately after flipping the field to being $+M_0$ at equilibrium. Thus, the time dependent magnetization
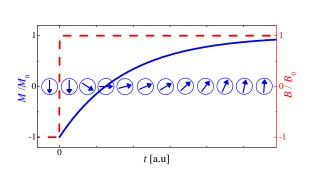
Fig. 2.2: Schematic of a magnetic bead relaxing in a flipping magnetic field. Before $t = 0$ the magnetization of the bead is parallel to the applied field. Immediately after $t = 0$ the magnetization of the bead is antiparallel to the applied field and the bead will rotate to align the magnetization to the applied field.
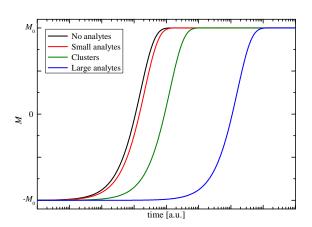
Fig. 2.3: Theoretical magnetization in the time domain for hydrodynamic diameter changing due to the presence of various analytes. No analytes ($D_h = D_{h,free}$), small analytes ($D_h = 1.1 D_{h,free}$), bead clusters ($D_h = 2 D_{h,free}$) and large cluster ($D_h = 10 D_{h,free}$), where $D_{h,free}$ is the hydrodynamic diameter of free beads.

due to Brownian relaxation in the time domain is assumed to be described by an exponential recovery

$$M(t) = M_0(1 - 2\exp(-t/\tau_B)), \tag{2.8}$$

where t is the time after flipping the direction of the field.

In Fig. 2.3, the theoretical relaxation of the magnetization of a bead in the time domain is calculated for estimates of the four different cases shown in Fig. 1.4: Plain beads, beads bound to small analytes (where the hydrodynamic diameter is increased by 10 %); beads forming clusters (where the hydrodynamic diameter is increased by 100 %); and beads bound to large analytes (where the hydrodynamic diameter is increased 900 %). It is seen that as the hydrodynamic diameter increases the flipping of the magnetization takes longer time. However, measurements on real samples will not behave like this. Instead, the samples will contain a combination of free beads and beads bound to analytes.

2.2.2 Frequency domain

Relaxation of a magnetic bead can also be measured in the frequency domain by placing the bead in a magnetic field alternating at a frequency f and measure the complex magnetic susceptibility $\chi = \chi' - i\chi''$ as function of frequency, where χ' and χ'' are the in-phase and out-of-phase components of the complex magnetic susceptibility, respectively. The complex magnetic susceptibility as function of frequency is described by the Debye model [67]

$$\chi(f) = \chi' - i\chi'' = \frac{\chi_0 - \chi_\infty}{1 + (if/f_B)} + \chi_\infty, \tag{2.9}$$

where i is the imaginary unit defined as $i \equiv \sqrt{-1}$; χ_0 and χ_∞ are the DC and high frequency magnetic susceptibilities, respectively; and f_B is the Brownian relaxation frequency, which is given by

$$f_B = \frac{1}{2\pi\tau_B} = \frac{k_B T}{6\pi\eta V_h}. \tag{2.10}$$

In fig. 2.4 the in-phase (top) and out-of-phase (bottom) complex magnetic susceptibility are plotted vs. frequency calculated for the same four changes in hydrodynamic diameter as shown in Fig. 2.3 for the time domain. It is seen that for small changes in the hydrodynamic diameter, both the in-phase and out-phase susceptibility overlap a lot. Thus, small changes in hydrodynamic diameters can prove difficult to resolve.

From Fig. 2.4 it is also seen that at frequencies well below the Brownian relaxation frequency, the entire susceptibility is in the in-phase component, which means that the magnetization of the magnetic bead is in-phase with the alternating applied field. As the frequency is increased the magnetization will begin to lag-behind the alternating field and the phase-lag will become maximal when $f = f_B$. Above the Brownian relaxation frequency the magnetization is not able to keep up with the alternating field and both the in-phase and out-phase component of the susceptibility decrease as the frequency is increased.


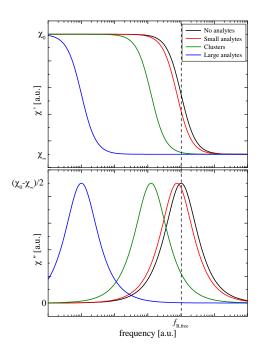**Fig. 2.4:** Theoretical signals in the frequency domain for hydrodynamic diameter changing due to the presence of various analytes. No analytes ($D_h = D_{h,\text{free}}$), small analytes ($D_h = 1.1D_{h,\text{free}}$), bead clusters ($D_h = 2D_{h,\text{free}}$) and large cluster ($D_h = 10D_{h,\text{free}}$), where $D_{h,\text{free}}$ is the hydrodynamic diameter of free beads.

2.2.3 Bead ensembles

In the sections above only a single bead was considered. However, real measurements are performed on an ensemble of beads, which, due to the fabrication process will not all have the same physical properties. To account for this, the distribution of the hydrodynamic bead diameter is assumed to be log-normal distributed. This is described by the probability density function of the log-normal distribution

$$f_{\mathrm{LN}}(D_{\mathrm{h}};\mu,\sigma)\mathrm{d}D_{\mathrm{h}} = \frac{1}{D_{\mathrm{h}}\sigma\sqrt{2\pi}}\exp\left(-\frac{(\ln D_{\mathrm{h}} - \mu)^2}{2\sigma^2}\right)\mathrm{d}D_{\mathrm{h}}, \tag{2.11}$$

where μ and σ are the mean and standard deviation on the logarithmic scale. Since the beads signals obtained are proportional to the bead volume the probability density function is also assumed to be volume weighted, i.e., the volume fraction of the particles with hydrodynamic diameters between D_{h} and $D_{\mathrm{h}} + \mathrm{d}D_{\mathrm{h}}$ is $f_{\mathrm{LN}}(D_{\mathrm{h}};\mu,\sigma)\mathrm{d}D_{\mathrm{h}}$. The median hydrodynamic diameter $\tilde{D}_{\mathrm{h}}$ of the log-normal distribution is found by

$$\tilde{D}_{\mathrm{h}} = \exp(\mu). \tag{2.12}$$

Throughout this thesis the median hydrodynamic diameter and the standard deviation on the logarithmic scale are used as the parameters governing the log-normal distribution.

Further, the equations for $M(t)$ and $\chi(f)$ are averaged over the log-normal distribution to account for the polydispersity of samples. However, Cole and Cole [68] showed that for very polydisperse samples, averaging over a log-normal distribution is not sufficient. Instead they proposed the empirical Cole–Cole model

$$\chi(f) = \chi' - \mathrm{i}\chi'' = \frac{\chi_0 - \chi_\infty}{1 + (\mathrm{i}f/f_{\mathrm{B}}(D_{\mathrm{h}}))^{(1-\alpha)}} + \chi_\infty. \tag{2.13}$$

where α is a measure of the polydispersity of the samples that assumes values between 0 and 1. When $\alpha = 0$ the sample is monodisperse and the Cole–Cole model reduces to the Debye model. The Cole–Cole model is the preferred model for analyzing relaxation measurements performed in the frequency domain. However, the Cole–Cole model cannot be applied to measurements in the time domain. Thus, $M(t)$ have to be averaged over the log-normal distribution to account for the polydispersity of the samples. When measurements in the time and frequency domains are compared, both $M(t)$ and $\chi(f)$ are averaged over the log-normal distribution.

2.3 Anisotropic magnetoresistance

The magnetic field sensors used in this thesis are based on the anisotropic magnetoresistance (AMR) effect, which means that the resistivity ρ depends on the angle between the current density $\mathbf{J}$ and an in-plane magnetization $\mathbf{M}$. The resistivities when the current density and magnetization are parallel and orthogonal are denoted $\rho_\parallel$ and $\rho_\perp$, respectively.

Traditionally, the AMR effect is quantified by the AMR ratio

$$\mathrm{AMR} = \frac{\Delta\rho}{\rho_{\mathrm{ave}}}, \tag{2.14}$$

where $\Delta\rho = \rho_\parallel - \rho_\perp$ is the difference in resistivity between when the current density and the magnetization are parallel and orthogonal; and ρ_{ave} is the average resistivity, which is given by $\rho_{\mathrm{ave}} = \frac{1}{3}\rho_\parallel + \frac{2}{3}\rho_\perp$. The AMR ratio depends on the material, but is for permalloy ($\mathrm{Ni_{80}Fe_{20}}$) around 2–3 % [69]. Furthermore, $\rho_\parallel$ is larger than $\rho_\perp$ for permalloy.

To illustrate the AMR effect, consider a ferromagnetic conductor slab exhibiting the AMR effect with width×length $= w \times l$; with the magnetization along the unit vector $\hat{\mathbf{M}} = (\cos(\theta), \sin(\theta))$, where θ is the angle of the magnetization measured from the positive x-direction; and the current density along the unit vector $\hat{\mathbf{J}} = (\cos(\alpha_J), \sin(\alpha_J))$, where α_J is the angle of the current density measured from the positive x-direction as shown in Fig. 2.5. The direction of the magnetization is determined by minimizing the magnetic energy (see Section 2.6). The direction of the current is determined by the shape of the conductor, i.e., for a long thin conductor the current will run parallel to the edges.
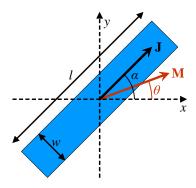
Fig. 2.5: Sketch of a conductor slab exhibiting the AMR effect. l and w of the slab are defined on the sketch, as well as the direction of the magnetization and current density.

The resistivity tensor $\underline{\underline{\rho}}(\theta)$ that relates the current density to the electric field by $\mathbf{E} = \underline{\underline{\rho}}(\theta)\mathbf{J}$ is given by [62]

$$\underline{\underline{\rho}}(\theta) = \left[\begin{array}{cc} \rho_\parallel - (\Delta\rho)\sin^2\theta & \frac{1}{2}(\Delta\rho)\sin(2\theta) \\ \frac{1}{2}(\Delta\rho)\sin(2\theta) & \rho_\parallel - (\Delta\rho)\cos^2\theta \end{array} \right], \tag{2.15}$$

The diagonal terms are the traditional AMR effects, where the resistivity is measured along the current direction. The off-diagonal terms give rise to the so-called planar Hall effect, where the electric field (or the potential difference) is measured perpendicular to the current direction. This effect has been named planar Hall effect because it is traditionally measured using the same cross geometry as the ordinary Hall effect. However, while the ordinary Hall effect is sensitive to magnetic fields applied perpendicular to the plane, the planar Hall effect is sensitive to the magnetic fields applied in the plane.

The resistance R of a single ferromagnetic conductor slab with thickness t_{FM} as shown in Fig. 2.5 is given by [62]

$$R(\alpha_J, \theta) = \frac{l}{t_{\mathrm{FM}}w} \left(\cos^2(\alpha_J)(\rho_\parallel - \Delta\rho\sin^2(\theta)) + \frac{1}{2}\Delta\rho\sin(2\alpha_J)\sin(2\theta) + \sin^2(\alpha_J)(\rho_\parallel - \Delta\rho\cos^2(\theta)) \right),$$
$$\tag{2.16}$$

which can be simplified to

$$R(\alpha_J, \theta) = \frac{l}{t_{\mathrm{FM}} w} \left(\frac{\rho_\parallel + \rho_\perp}{2} + \tfrac{1}{2} \Delta\rho \cos(2(\alpha_J - \theta)) \right). \tag{2.17}$$

This expression will be used below to calculate the signal for planar Hall effect bridge sensors.

2.4 Signal of planar Hall effect cross sensors

As mentioned, the planar Hall effect is traditionally measured with a cross geometry as the one shown in Fig. 2.6. This kind of sensor is called a planar Hall effect cross sensor. The sensors work by forcing a bias current I through the sensor in the x-direction. If the magnetization of the sensor is pointing in a different direction than the x-direction, the off-diagonal elements of Eq. (2.15) will give rise to a potential drop across the sensor, which is measured across the arms in the y-direction. This is also depicted in Fig. 2.6, which also shows the width of the sensor arms, denoted w.
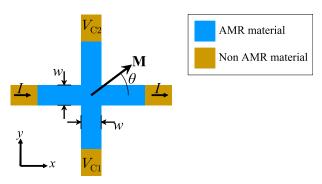
Fig. 2.6: Cross sensor for measuring the planar Hall effect. A current is passed through the sensor in the x-direction, while a voltage drop is measured across the arms in the y-direction.

The sensor signal as function of the magnetization angle θ is for a planar Hall cross sensor consisting of a single magnetic domain given by [31]

$$V_{\mathrm{C}} = \frac{\Delta\rho}{2t_{\mathrm{FM}}} I \sin(2\theta), \tag{2.18}$$

from where it is seen that the maximum and minimum signals are achieved when the angles of the magnetization are $\theta = \pi/4$ and $\theta = -\pi/4$, respectively. It is also seen than the signal returns to zero, when the magnetization is saturated along the y-direction ($\theta = \pm\pi/2$).

2.5 Signals of planar Hall effect bridge sensors

Henriksen *et al.* [62] have recently shown that arranging a material exhibiting the AMR effect in a particular Wheatstone bridge configuration leads to a geometrical amplification of the signal measured with the planar Hall effect cross sensor. Since the geometry is changed from a cross to a Wheatstone bridge, these sensors are termed planar Hall effect bridge sensors. In the following, it will be described how the planar Hall effect bridge sensors work.

Wheatstone bridge signal

As mentioned, the sensors are a arranged in a Wheatstone bridge as shown in Fig. 2.7. For such Wheatstone bridge, where the bias current is applied through the arms in the x-direction, the voltage drop measured in the y-direction is given by

$$V = \frac{R_1 R_4 - R_2 R_3}{R_1 + R_2 + R_3 + R_4} I, \tag{2.19}$$

where R_i is the resistance of the ith resistor in Fig. 2.7.
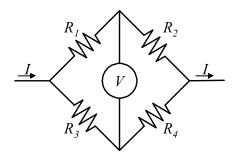
Fig. 2.7: Schematic of Wheatstone bridge. Current is passing through in horizontal direction and voltage measured across the vertical direction.

In order to keep the current in both the upper and lower half of the bridge constant at $I/2$, $R_1 + R_3$ must equal $R_2 + R_4$. This can be achieved by setting $R_1 = R_4$ and $R_2 = R_3$, which reduces the Wheatstone voltage to

$$V = \tfrac{1}{2}(R_1 - R_2)I. \tag{2.20}$$

Sensor signal

By inserting the resistance of an conductor slab exhibiting the AMR effect from Eq. (2.17) such that $R_1 = R_4 = R(\alpha_J, \theta)$ and $R_2 = R_3 = R(-\alpha_J, \theta)$ the following signal is obtained when assuming that the magnetization angels are identical in all four resistors and that each resistor consists of a single magnetic domain:

$$V_{\text{B}} = \frac{l}{w} \frac{\Delta \rho}{2 t_{\text{FM}}} I \sin(2\alpha_J) \sin(2\theta). \tag{2.21}$$

From this equation it seen that the signal of the bridge sensor is maximum when $\alpha_J = \pi/4$, assuming that θ does not depend on α_J, which is not entirely true. All the bridge sensors used for this thesis have $\alpha_J = \pi/4$ and in the following this angle is used as the standard. Thus, the signals for bridge and cross sensors are related by

$$V_{\text{B}} = \frac{l}{w} V_{\text{C}}, \tag{2.22}$$

which means the ratio between the signals for the bridge and cross sensors is a geometrical amplifications.

In Fig. 2.8, a planar Hall effect bridge sensor is sketched for different directions of the magnetization. In Fig. 2.8 (a) $\theta = 0$ and it is seen that the angle between the current and the magnetization is $\pi/4$ in all four resistors, which means that the bridge is balanced and the bridge voltage is zero. In (b), the magnetization is rotated such $\theta = -\pi/4$, which leads to the resistivity in the top left and bottom right resistors to be $\rho_\perp$ and the resistivity in the two remaining resistors to be $\rho_\parallel$. Recalling that $\rho_\parallel > \rho_\perp$, this results in the bridge voltage being minimized. In (c), $\theta = \pi/4$ leads to an interchange of the resistivities compared to the situation in (b) and the bridge voltage is maximized. In (d), the magnetization is pointing along the y-direction and it is again seen that the angle between the current and the magnetization is identical for all four resistors, which leads to the bridge voltage being zero. In the following section, the magnetization angle is calculated as function of magnetic fields acting on the sensor, such that the sensor signals can be written as function of magnetic field instead of angle of magnetization.
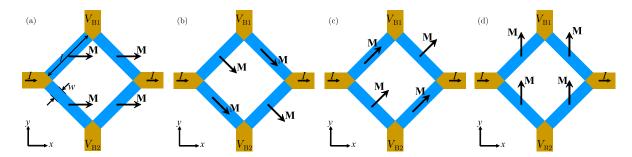
Fig. 2.8: Sketches of planar Hall effect bridge sensor for different directions of the magnetization. Current is forced through the arms in the x-direction, while a voltage drop is measured across the arms in the y-direction. (a) $\theta = 0$, angle between the current and the magnetization is identical for all four resistors, which leads to equal resistivities and a balanced bridge. (b) $\theta = -\pi/4$, the signal is minimum due the resistivity being $\rho_\parallel$ in the top left and bottom right resistor and $\rho_\perp$ in the remaining two. (c) $\theta = \pi/4$, the signal is maximum due the resistivity being $\rho_\perp$ in the top left and bottom right resistor and $\rho_\parallel$ in the remaining two. (d) $\theta = \pi/2$, the signal is zero due to the angle between the current and the magnetization being identical in all four resistors.

2.6 Magnetic energy

The magnetization angle for a single magnetic domain is found by minimizing the magnetic energy. In order to be able to account for all the magnetic energies, it should be mentioned that the sensors stack consists of a ferromagnetic layer and an antiferromagnetic layer. The ferromagnetic layer is the layer exhibiting the AMR effect and is therefore the actual sensing layer. The antiferromagnetic layer gives rise to an exchange biasing [70] of the ferromagnetic layer, which means that the magnetization of the ferromagnetic layer has a unique preferred direction when no magnetic fields are applied. The direction of the exchange coupling is defined by applying a magnetic field along the positive x-direction during deposition of the sensor stack.

The magnetic energy of the ferromagnetic layer is the sum of the following magnetic energies. It should be noted that it is assumed that the ferromagnetic layer consists of a single domain.

Zeeman energy

When a magnetic field $\mathbf{H}$ is applied to the ferromagnetic layer, the Zeeman energy is given by

$$U_Z = -\mu_0 V \mathbf{M} \cdot \mathbf{H}, \tag{2.23}$$

where V is the volume of the ferromagnetic layer. It is seen that the Zeeman energy is minimized when the direction of the magnetization is parallel to the direction of the applied field and maximized when they are antiparallel.

Exchange energy

Due to the exchange coupling between the antiferromagnetic layer and the ferromagnetic layer, the exchange energy is [70]

$$U_{\text{ex}} = -\sigma_{\text{ex}} V t_{\text{FM}}^{-1} (\hat{\mathbf{M}} \cdot \hat{\mathbf{e}}_{\text{ex}}), \tag{2.24}$$

where σ_{ex} is the interface energy per area, $V t_{\text{FM}}^{-1}$ is the area of the interface, $\hat{\mathbf{M}}$ is the unit vector of the magnetization of the ferromagnetic layer and $\hat{\mathbf{e}}_{\text{ex}}$ is the unit vector of the exchange bias direction. The exchange energy is minimized when the direction of the magnetization is parallel to the exchange bias direction and maximized when they are antiparallel.

Uniaxial anisotropy energy

Due to the applied field during deposition, the crystal structure of the ferromagnetic layer will have a preferred magnetization axis along the direction of the field applied during deposition, this axis is a called the easy axis. The uniaxial anisotropy energy is given by

$$U_K = -KV(\hat{\mathbf{M}} \cdot \hat{\mathbf{e}}_K)^2, \tag{2.25}$$

where K is the anisotropy constant and $\hat{\mathbf{e}}_K$ is the unit vector along the easy axis. It is seen that the uniaxial anisotropy energy is minimized when the direction of the magnetization is either parallel or antiparallel to the easy axis.

Total energy

By adding the above three energy contributions and normalizing with $\mu_0 M_s V$, the normalized energy volume density $\tilde{u}$ is obtained

$$\tilde{u} = \frac{U}{\mu_0 M_s V} = -\hat{\mathbf{M}} \cdot \mathbf{H} - \frac{K}{\mu_0 M_s}(\hat{\mathbf{M}} \cdot \hat{\mathbf{e}}_K)^2 - \frac{\sigma}{t_{\text{FM}} \mu_0 M_s}(\hat{\mathbf{M}} \cdot \hat{\mathbf{e}}_{\text{ex}}) + \text{constant}. \tag{2.26}$$

By assuming that $\hat{\mathbf{e}}_K$ and $\hat{\mathbf{e}}_{\text{ex}}$ are both along the x-direction, and defining the anisotropy field H_K and exchange field H_{ex} as

$$H_K = \frac{2K}{\mu_0 M_s} \tag{2.27}$$

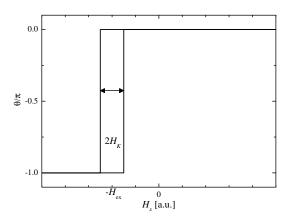$$H_{\text{ex}} = \frac{\sigma}{t_{\text{FM}} \mu_0 M_s}, \tag{2.28}$$

the normalized energy volume density can be written as

$$\tilde{u} = -H_x \cos(\theta) - H_y \sin(\theta) - \frac{H_K}{2} \cos^2(\theta) - H_{ex} \cos(\theta) + \text{constant},\tag{2.29}$$

where $\mathbf{H} = (H_x, H_y)$ has also been inserted.

Magnetization angle as function of H_x and H_y

The magnetization angle can be calculated numerically as function of H_x and H_y by minimizing the normalized energy volume density in Eq. (2.29). First H_y is set to zero and $\tilde{u}$ is minimized as function of H_x, which results in the magnetization in the x-direction as function of H_x plotted in Fig. 2.10. It is seen that only two possible energy minima exist; either the magnetization is parallel or antiparallel to the x-direction. It is also seen that the magnetization curve have hysteresis and that the center of the hysteresis is $-H_{ex}$, while the width of the hysteresis is $2H_K$. Likewise, by setting H_x to zero the magnetic energy can be minimized as function of H_y to yield the magnetization in the y-direction as shown in Fig. 2.10. It is seen that the curve is almost linear around $H_y = 0$. Since the application of a field along the x-axis only had two possible values of θ, applying the field in the y-direction is the direction of interest for using this magnetic stack for sensing. In Section 3.2.2 it is described how magnetization curves are measured to obtain the magnetic properties of the fabricated magnetic stacks.
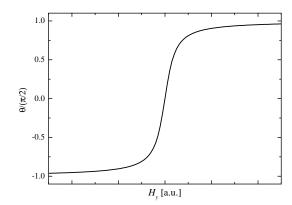
Fig. 2.9: Magnetization in the x-direction normalized with the saturation magnetization as function of applied field in the x-direction. Hysteresis depends on H_{ex} and H_K.

Fig. 2.10: Magnetization in the y-direction normalized with the saturation magnetization as function of applied field in the y-direction. The slope at $H_y = 0$ is given by Eq. (2.31).

By minimizing Eq. (2.29), assuming only small angles of θ and Taylor expanding to the first order around $\theta = 0$ results in

$$\theta = \frac{H_y}{H_K + H_{ex} + H_x}.\tag{2.30}$$

For $H_x \ll H_K + H_{ex}$, H_x can be neglected. $\mu_0 H_K$, $\mu_0 H_{ex}$ are on the order of mT, which means that unless an external field is applied along the x-direction, the assumption $H_x \ll H_K + H_{ex}$ is

true. Thus, the angle of the magnetization can be simplified to

$$\theta = \frac{H_y}{H_K + H_{ex}}. \tag{2.31}$$

This is now inserted into Eq. (2.18) and Eq. (2.21), still assuming small angles of θ, and results in

$$V_C = S_{C,0}IH_y, \tag{2.32}$$
$$V_B = S_{B,0}IH_y, \tag{2.33}$$

where $S_{C,0}$ and $S_{B,0}$ are the low-field sensitivities for the cross and bridge sensors, respectively. The two low-field sensitivities are given by

$$S_{C,0} = \frac{\Delta\rho}{t_{FM}} \frac{1}{H_K + H_{ex}} \tag{2.34}$$
$$S_{B,0} = \frac{l}{w} \frac{\Delta\rho}{t_{FM}} \frac{1}{H_K + H_{ex}} \tag{2.35}$$

In several of the appended papers, the low-field sensitivities are reported in units of V/(TA), which means that the reported values are in fact S_0/μ_0. Generally the electrical connections to the sensors are made such that the sensor response is negative when a positive field is applied, thus the low-field sensitivities become negative.

2.7 Self-field generated by bias current

As already mentioned the beads are magnetized by the magnetic field arising from the bias current through the sensor. In this section the field acting back on the sensor will be described.

Magnetic fields generated due to the bias current through the sensor are named self-fields. This means that when no current is running through the sensor, all self-fields are zero. The primary self-fields are the fields that are generated directly from the current through the sensor. Most of the current runs through the ferromagnetic layer, which generates a magnetic field that is symmetrical around the ferromagnetic layer. Thus, the self-field from the ferromagnetic layer does not result in an effective field acting on the ferromagnetic layer. On the other hand, the fraction of the current running in the antiferromagnetic layer gives rise to a non-zero effective field in the ferromagnetic layer as sketched in Fig. 2.11. When a bead is present near the sensor, a secondary self-field is generated because the two primary self-fields magnetize the bead. The dipole-field from the bead acts back on the ferromagnetic layer, which is also sketched in Fig. 2.11. From the figure it is seen that the two self-fields affecting the ferromagnetic layer have the same direction, both orthogonal to the current direction.

The effective self-field acting on the ferromagnetic layer H_{sf} can be written as [71]

$$H_{sf} = \gamma_0 I_c + H_{beads}, \tag{2.36}$$

where γ_0 is a constant that describes the effect of the self-field due to the asymmetry of the sensor stack. γ_0 is positive when the antiferromagnetic layer is on top of the ferromagnet and
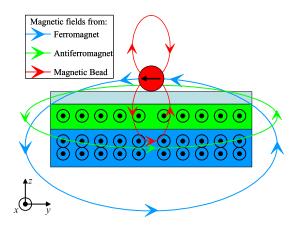
Fig. 2.11: Schematic of the two self-fields affecting the ferromagnetic layer. The first component of the self-field arises from the current through the antiferromagnetic layer. The second component of the self-field arises from the dipole field from the bead magnetized by the field generated from the current through the entire stack. The ⊙ symbolize that the current is applied in the positive x-direction.

depends on the geometry of the sensor. I_c is the current running in the conductor and H_beads is the magnetic field acting on the ferromagnetic layer from the beads. H_beads will be defined slightly differently for measurements in the time and frequency domains. In the time domain

$$H_\mathrm{beads}^\mathrm{time} = \gamma_{1t} M(t) I_\mathrm{c} \tag{2.37}$$

and in the frequency domain

$$H_\mathrm{beads}^\mathrm{freq} = \gamma_{1f} \chi(f) I_\mathrm{c}, \tag{2.38}$$

where γ_{1t} and γ_{1f} are constants that depend on the sensor geometry and bead distribution and relates $M(t)$ and $\chi(f)$ to the effective field acting on the ferromagnetic layer. Since the magnetization of the beads is due to the primary self-fields, the effective field from the beads is also proportional to the current through the conductor.

The magnetic field from the beads decreases with distance, such that the beads closes to the sensor surface will give rise to the most signal. Hansen *et al.* [71] have made a theoretical study about the magnetic field from beads magnetized by the self-field and found that 85 % of the effective magnetic field acting on the sensor comes from beads that are within $1.3w$ of the sensor. This is also shown in Fig. 2.12, where contours of the cumulative bead signal are plotted for a homogeneous distribution of beads. It is seen that the closer the beads are to the sensor, the more they will contribute to the signal.

Figure 2.13 shows a top-view of a bridge and a cross sensor connected in series. On the picture the directions of the self-fields acting on the ferromagnetic layer are shown for the different sensor segments. It is seen that for the cross sensor, the current is along the x-direction and the self-fields act on the ferromagnetic layer in the positive y-direction. For the bridge sensor, the current direction changes with the segments and therefore the direction of the self-fields also changes. However, for the bridge shown, the y-components of the self-fields are the same in all four segments and only the x-component changes sign. Since the x-components of
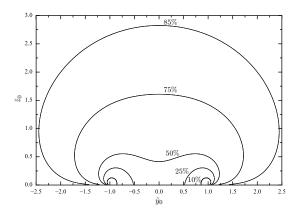
Fig. 2.12: Contour plot of the cumulative bead signal for bead magnetized by the self-field homogeneously distributed for $\tilde{z}_0 > 0.01$. $\tilde{z}_0 = 2z/w$ and $\tilde{y}_0 = 2y/w$. Source: [71].

the self-fields are much smaller than $H_{\mathrm{K}} + H_{\mathrm{ex}}$, the x-components of the self-fields can safely be neglected.
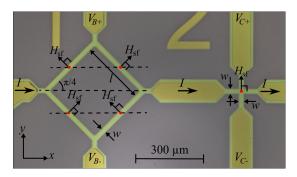
Fig. 2.13: Top view of bridge and cross sensors, with directions of self-field acting on the ferromagnetic layer. The figure is from Paper III.

The effective self-field acting on the ferromagnetic layer in the y direction is therefore written as

$$H_{y,\mathrm{sf}} = \cos(\alpha_J)H_{\mathrm{sf}}. \tag{2.39}$$

If the same current I is passed through the bridge and cross sensor as shown in Fig. 2.13, the average magnetic self-field acting on the bridge sensor is only $2^{-3/2}$ of that acting on the cross sensor. This is because the current in each branch of the bridge sensor is $I_{\mathrm{c}} = I/2$ and only the y-component of the self-field affects the sensor ($H_{y,\mathrm{sf}} = H_{\mathrm{sf}}/\sqrt{2}$), whereas $I_{\mathrm{c}} = I$ and $H_{y,\mathrm{sf}} = H_{\mathrm{sf}}$ for the cross sensor.

2.8 Sensor signals

Here, the results from the past three sections are joined to yield the sensor response due to magnetic beads magnetized by the self-field. Additional to the self-fields an external field can be

applied in the y-direction $H_{y,\text{ext}}$, which means that the total field acting on the ferromagnetic layer in the y-direction is written as

$$H_y = \cos(\alpha_J)(\gamma_0 I_c + H_{\text{beads}}) + H_{y,\text{ext}}. \tag{2.40}$$

In the above, only ideal sensors were considered. In reality, the sensor signals have an offset due to an imperfect fabrication process. Hence, the sensor signals for the cross and bridge sensors become

$$V_C = S_{C,0} I(\gamma_0 I + H_{\text{beads}} + H_{y,\text{ext}}) + R_{\text{offset}} I, \tag{2.41}$$

$$V_B = S_{B,0} I(2^{-1/2}(\tfrac{1}{2}\gamma_0 I + H_{\text{beads}}) + H_{y,\text{ext}}) + R_{\text{offset}} I, \tag{2.42}$$

Since H_{beads} has been defined differently depending on whether the signal is measured in the time or frequency domain, the signal will have to be evaluated individually for each domain.

2.8.1 Time domain

In Section 2.2.1.1 relaxation of a magnetic bead was only considered when the applied field was flipped from negative to positive. When measuring the relaxation with a planar Hall effect sensor, the direction of the self-field is flipped, which make the bead relax. The direction of the self-field is flipped by changing the direction of the bias current between $I = +I_0$ and $I = -I_0$.
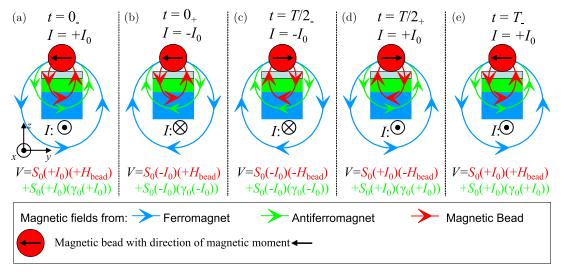
Fig. 2.14: Field directions and their contribution to the sensor signal for the following five situations: (a) Immediately before and (b) immediately after changing the current direction from $I = +I_0$ and $I = -I_0$, (c) Immediately before and (d) immediately after changing the current direction from $I = -I_0$ and $I = +I_0$. (e) Immediately before changing the current direction from $I = +I_0$ (same as (a)). It is seen that the signal contribution from the antiferromagnet is constant due to the signal being proportional to both the field and current, while the signal contribution from the bead is positive right before the current direction is changed and negative immediately after.

How changing the current direction affects the sensor signal is sketched in Fig. 2.14 and Fig. 2.15. Immediately before the current is flipped ((a) $t = 0_-$) the magnetic moment of
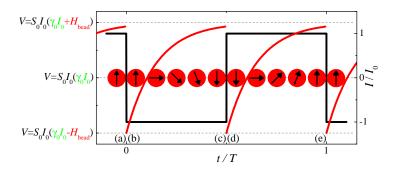
Fig. 2.15: How the signal change over time in between the situations described in Fig. 2.14.

the bead is parallel to the self-field and the field from the bead adds to the field from the antiferromagnet acting on the ferromagnet. Right after the current changes direction from $I = +I_0$ to $I = -I_0$ ((b) $t = 0_+$) the direction of the field from the antiferromagnet also changes, while the magnetic moment of the bead still has not had time to change and is therefore antiparallel to the self-field. Due to the signal being proportional to the both the current and applied field changing the current direction changes the sign of the signal due to the bead, while the signal due to the antiferromagnet remains constant. As time goes the bead will rotate by Brownian relaxation to align the magnetic moment to the self-field, which gives rise to the exponential recovery of the signal seen in Fig. 2.15 from $t = 0$ to $t = T/2$. Once the magnetic moment of the bead is again parallel to the self-field ((c) $t = T/2_-$) the signal contribution from the bead has become positive. Then at $t = T/2_+$ (d) the current direction has changed from $I = -I_0$ to $I = +I_0$, again the field from the antiferromagnet changes immediately, while the bead has not had time to rotate. Again the signal contribution from the antiferromagnet remains positive, while the contribution from the bead becomes negative, which is exactly the same situation as when the current direction changed from $I = +I_0$ and $I = -I_0$. The bead will rotate by Brownian relaxation and the signal will increase by the exponential recovery as shown in Fig. 2.15 from $t = T/2$ to $t = T$. From this it is seen that the exponential recovery of the signal is independent of whether the current is changed from $I = +I_0$ to $I = -I_0$ or vice versa. The magnetic field from the bead acting on the ferromagnetic layer in the positive signal direction can therefore be described by

$$H_{\text{beads}}^{\text{time}} = \gamma_{1t} M(t) I_{\text{c}}. \tag{2.43}$$

This allows for writing the signal in the time domain for a bridge sensor, when including the possible external field and resistance offset as

$$V_{\text{B}} = 2^{-3/2} I S_{\text{B},0}(\gamma_0 I + \gamma_{1t} M(t) I) + I({}_{\text{B},0} H_{y,\text{ext}} + R_{\text{offset}}), \tag{2.44}$$

and the two possible signals for $I = +I_0$ and $I = -I_0$ becomes

$$V_{\text{B}}|_{I=+I_0} = 2^{-3} S_{\text{B},0} I_0^2 (\gamma_0 + \gamma_{1t} M(t)) + I_0(S_{\text{B},0} H_{y,\text{ext}} + R_{\text{offset}}) \tag{2.45}$$

$$V_{\text{B}}|_{I=-I_0} = 2^{-3} S_{\text{B},0} I_0^2 (\gamma_0 + \gamma_{1t} M(t)) - I_0(S_{\text{B},0} H_{y,\text{ext}} + R_{\text{offset}}) \tag{2.46}$$

From these expressions, it is seen that the signals can be separated into a part due to the self-fields and another part due to external fields and the potential sensor offset. This is done by calculating the average and difference of the two possible signals

$$V_{\text{ave}} = \frac{V_{\text{B}}|_{I=+I_0} + V_{\text{B}}|_{I=-I_0}}{2} = 2^{-3/2} S_{\text{B},0} I_0^2 (\gamma_0 + \gamma_{1t} M(t)) \tag{2.47}$$

$$V_{\text{diff}} = \frac{V_{\text{B}}|_{I=+I_0} - V_{\text{B}}|_{I=-I_0}}{2} = I_0 (S_{\text{B},0} H_{y,\text{ext}} + R_{\text{offset}}). \tag{2.48}$$

Since the term due to the asymmetric stack, γ_0, is not of any interest for detecting beads, V_{ave} can be corrected for γ_0 by subtracting V_{ave} from a measurement without beads. This leads to

$$V_{\text{ave,cor}} = S_0 I_0^2 \gamma_{1t} M(t). \tag{2.49}$$

However, the expression is only valid for a monodisperse bead ensemble. In order to be able to fit the model to experimental data, the signal should be integrated over the log-normal distribution (cf. Section 2.2.3), which results in

$$V_{\text{ave,fit}} = V_{0t} \int_0^\infty \left(1 - 2\exp\left(\frac{-t}{\tau_{\text{B}}(D_{\text{h}})}\right)\right) f_{\text{LN}}(D_{\text{h}}; \tilde{D}_{\text{h}}, \sigma)\mathrm{d}D_{\text{h}} + V_{\text{offset}}. \tag{2.50}$$

This model has four free fitting parameters: the median hydrodynamic diameter $\tilde{D}_{\text{h}}$, the log-normal standard deviation σ, the signal amplitude V_{0t} and finally a potential offset V_{offset}.

2.8.2 Frequency domain

In the frequency domain the sensor signal for the cross sensor is given by

$$V_{\text{C}} = S_{\text{C},0} I^2 (\gamma_0 + \gamma_{1f} \chi(f)) + I(S_{\text{C},0} H_{y,\text{ext}} + R_{\text{offset}}). \tag{2.51}$$

For measurements in the frequency domain an alternating bias current of $I = I_{\text{AC}} \sin(2\pi f t)$ is passed through the sensor, where I_{AC} is the current amplitude. It is seen that the signal due to the external field and the offset is proportional to the current, and that the signal due to the self-fields are proportional to the current squared. This means that the signal from the external field can be detected with lock-in technique in the first harmonic lock-in signal $V_1 = V_1' + iV_1''$ and the signal due to the self-fields can be detected in the second harmonic lock-in signal $V_2 = V_2' + iV_2''$. The first harmonic in-phase V_1' and out-of-phase V_1'' signals are for the cross sensor given by [71]

$$V_{\text{C},1}' = 2^{-1/2} I_{\text{AC}} (S_{\text{C},0} H_{y,\text{ext}} + R_{\text{offset}}), \tag{2.52}$$

$$V_{\text{C},1}'' = 0. \tag{2.53}$$

The similar expressions for the bridge sensor are obtained by replacing the sensitivity

$$V_{\text{B},1}' = 2^{-1/2} I_{\text{AC}} (S_{\text{B},0} H_{y,\text{ext}} + R_{\text{offset}}), \tag{2.54}$$

$$V_{\text{B},1}'' = 0. \tag{2.55}$$

The second harmonic in-phase (V_2') and out-of-phase (V_2'') signals for a cross sensor are given by [49]

$$V_{C,2}' = -2^{-3/2}S_{C,0}I_{AC}^2\gamma_{1f}\chi''(f) \tag{2.56}$$

$$V_{C,2}'' = -2^{-3/2}S_{C,0}I_{AC}^2(\gamma_0 + \gamma_{1f}\chi'(f)). \tag{2.57}$$

To obtain similar expressions for the bridge sensor, the sensitivity should be replaced and multiplied with the factor $2^{-3/2}$ due to only half the current is running in each resistor and the projection of the field on to the y-axis as discussed in Section 2.7

$$V_{B,2}' = -2^{-3}S_{B,0}I_{AC}^2\gamma_{1f}\chi''(f) \tag{2.58}$$

$$V_{B,2}'' = -2^{-3}S_{B,0}I_{AC}^2(\gamma_0 + \gamma_{1f}\chi'(f)). \tag{2.59}$$

From Eq. (2.56) – Eq. (2.59) it is seen that the in-phase second harmonic signal is proportional to the out-of-phase complex magnetic susceptibility and the out-of-phase second harmonic signal is linearly dependent on the in-phase complex magnetic susceptibility. Also, in the frequency domain the term γ_0 can be found from a measurement without beads and subtracted from the out-of-phase sensor signal. The resulting corrected out-phase signal $V_{2,\text{cor}}''$ is now proportional to the in-phase complex magnetic susceptibility. This means that $V_{2,\text{cor}} = V_2' + iV_{2,\text{cor}}''$ is proportional to $i\chi = \chi'' + i\chi'$. In order to fit the Cole–Cole model to the measured data it needs to be modified to

$$V_{2,\text{fit,Cole}} = V_2' + iV_{2,\text{cor}}'' = i\frac{V_0 - V_\infty}{1 + (if/f_B(D_h))^{(1-\alpha_J)}} + iV_\infty, \tag{2.60}$$

where V_0 and V_∞ are defined for the cross sensor as

$$V_0 = -2^{-3/2}I_{AC}^2S_{0,C}\gamma_1\chi_0 \tag{2.61}$$

$$V_\infty = -2^{-3/2}I_{AC}^2S_{0,C}\gamma_1\chi_\infty. \tag{2.62}$$

To fit the second harmonic signal using the log-normal distribution instead of the Cole–Cole model, the following expression is used

$$V_{2,\text{fit,LN}} = V_2' + iV_{2,\text{cor}}'' = \int_0^\infty i\frac{V_0 - V_\infty}{1 + (if/f_B(D_h))}f_{LN}(D_h; \tilde{D}_h, \sigma)dD_h + iV_\infty. \tag{2.63}$$

2.9   Forces acting on a bead near a planar Hall effect bridge sensor

The theory of Brownian relaxation is valid under the assumption that the beads are freely suspended and not affected by any other forces. It is therefore important to discuss the forces that affect magnetic beads when placed near a planar Hall effect sensors. This is done to get an idea of how beads with different diameters will behave near planar Hall effect sensor and estimate if any of the forces could cause a potential problem for measuring relaxation of magnetic beads.

2.9.1 Stokes drag force

Whenever a fluid and a bead is moving at different velocities, the bead will experience a drag force $\mathbf{F}_{\mathrm{drag}}$, which for laminar flows in an infinite container is given by the Stokes drag [72]

$$\mathbf{F}_{\mathrm{drag}} = 3\pi\eta D(\mathbf{v}_{\mathrm{fluid}} - \mathbf{v}_{\mathrm{bead}}), \tag{2.64}$$

where $\mathbf{v}_{\mathrm{fluid}}$ and $\mathbf{v}_{\mathrm{bead}}$ are the velocity of the fluid and bead, respectively. To keep the calculations as simple as possible the hydrodynamic diameter of the beads is assumed to be identical to the nominal diameter. The fluidic channel around a planar Hall effect sensor is not an infinite container, but this expression will be used as an approximation.

2.9.2 Buoyancy

The buoyancy force $\mathbf{F}_{\mathrm{buoy}}$ acting on a bead suspended in a fluid is given by

$$\mathbf{F}_{\mathrm{buoy}} = \frac{-(\rho_{\mathrm{bead}} - \rho_{\mathrm{fluid}})g\pi D^3}{6}\hat{\mathbf{z}}, \tag{2.65}$$

where ρ_{bead} and ρ_{fluid} are the mass densities of the bead and the fluid, respectively, g is the gravitational acceleration constant and $\hat{\mathbf{z}}$ is a unit vector along the z-direction.

Sedimentation due to buoyancy

In the typical measurement situation there will be no fluid flow. Thus, when only buoyancy and the drag force are considered there will be no forces acting on the bead in the x and y directions and the bead sedimentation velocity in the z-direction $v_{\mathrm{bead},z}$ can be calculated from

$$F_{\mathrm{drag+buoy},z} = m\frac{\mathrm{d}v_{\mathrm{bead},z}}{\mathrm{d}t} = -3\pi\eta D v_{\mathrm{bead},z} - \frac{(\rho_{\mathrm{bead}} - \rho_{\mathrm{fluid}})g\pi D^3}{6}. \tag{2.66}$$

The solution to this ordinary differential equation is found to be

$$v_{\mathrm{bead},z}(t) = A_0 \exp\left(\frac{-3\pi\eta D t}{m}\right) - \frac{(\rho_{\mathrm{bead}} - \rho_{\mathrm{fluid}})g D^2}{18\eta}, \tag{2.67}$$

where A_0 is a constant that can be determined from the initial velocity of the bead. It is now seen that the sedimentation velocity consists of two terms; an exponential decay with respect to time and a constant. The exponential decaying term is the acceleration term. The term $\frac{-3\pi\eta D}{m}$ for a bead with a diameter of 80 nm suspended in water at 25°C is found to -8.79×10^8 s^{-1} (see Table 2.1 for physical properties of beads used), which means this term is decaying to zero so fast that it can be neglected when considering time scales on the order of milliseconds and above. Thus, the velocity in the z-direction is given by

$$v_{\mathrm{bead},z} = -\frac{(\rho_{\mathrm{bead}} - \rho_{\mathrm{fluid}})g D^2}{18\eta}. \tag{2.68}$$

From the velocity in the z-direction, the deterministic sedimentation time t_{sedi} for a bead placed at the height h can be calculated by $t_{\mathrm{sedi}} = -h/v_{\mathrm{bead},z}$. In Table 2.2 the sedimentation times when considering only buoyancy and the drag force of six different bead sizes are calculated for $h = 1$ mm and $h = 0.1$ mm.

Table 2.2: Estimates of sedimentation times when considering only buoyancy and the drag force for six different bead sizes falling 1 mm and 0.1 mm and estimates of diffusion times for beads moving 1 mm or 1 mm. The physical properties of the beads can be found in Table 2.1. No information about the density of the beads with diameters of 10, 25 and 40 nm was available, so the density of the 80 nm bead has been used.

D [nm]	t_{sedi} [hr]		$t_{\text{dif}}[hr]$	
	$h = 1$ mm	$h = 0.1$ mm	$h = 1$ mm	$h = 0.1$ mm
10	2069	206.9	5.7	0.057
25	331	33.1	14	0.14
40	129	12.9	22	0.22
80	33.3	3.33	45	0.45
130	13.5	1.35	74	0.74
250	4.9	0.49	142	1.42

2.9.3 "Brownian force"

The "Brownian force" (F_{Brown}) is not a real force but an estimate for when Brownian motion will influence the bead motion to such a degree that calculating deterministic trajectories does no longer make sense. The "Brownian force" is estimated by dividing the thermal energy ($k_{\text{B}}T$) by a characteristic length, in this case the diameter of the bead [73]

$$F_{\text{Brown}} = \frac{k_{\text{B}}T}{D}, \tag{2.69}$$

Brownian motion can also be described by diffusion. The diffusivity of particles is given by the Stokes–Einstein equation

$$D_{\text{dif}} = \frac{k_{\text{B}}T}{3\pi\eta D}. \tag{2.70}$$

Similar to the sedimentation times it is also possible to estimate diffusion times by $t_{\text{dif}} = h^2 D_{\text{dif}}^{-1}$. Again the times are estimated for the two channel heights $h = 1$ mm and $h = 0.1$ mm and are listed in Table 2.2. By comparing the diffusion times with the sedimentation times, it can be seen whether sedimentation or diffusion will dominate for varying channel heights and bead sizes. This can also be done by comparing the sedimentation time to the diffusion time. For diffusion to dominate, the sedimentation time must be much longer than the diffusion time

$$t_{\text{dif}} \ll t_{\text{sedi}} \quad \Leftrightarrow \tag{2.71}$$

$$\frac{3\pi\eta D h^2}{k_{\text{B}}T} \ll \frac{18h\eta}{(\rho_{\text{bead}} - \rho_{\text{fluid}})gD^2} \quad \Leftrightarrow \tag{2.72}$$

$$D^3 \ll \frac{18k_{\text{B}}T}{3\pi(\rho_{\text{bead}} - \rho_{\text{fluid}})gh} \tag{2.73}$$

By setting $\rho_{\text{bead}} = 3200$ kg/m^3 and $\rho_{\text{fluid}} = 1000$ kg/m^3 the following criteria for when diffusion dominates over sedimentation are obtained for 25°C: $D < 71$ nm and $D < 154$ nm for the channel heights of 1 mm and 0.1 mm, respectively.

2.9.4   Magnetic forces

In addition to the non-magnetic forces discussed above, also magnetic forces act on a magnetic bead. In general, the magnetic force acting on a magnetic bead is written as [74]

$$\mathbf{F}_{\text{mag}} = \int_V d^3r[\mu_0(\mathbf{M} \cdot \nabla)\mathbf{H}_0], \tag{2.74}$$

where V is the particle volume, $\mathbf{M}$ is the magnetization of the bead, and $\mathbf{H}_0$ is the applied field in the absence of the bead. Assuming that a bead is a linear magnetic material ($\mathbf{M} = \chi\mathbf{H}_0$) and that the integrand in Eq. (2.74) is approximately constant over the volume of the bead, the force can be simplified to [10]

$$\mathbf{F}_{\text{mag}} = \frac{1}{12}\pi D^3\mu_0\chi\nabla(\mathbf{H}^2), \tag{2.75}$$

In the following, two sources of $\mathbf{H}$ will be discussed: the self-field from the bias current and the magnetostatic field from the ferromagnetic sensor material.

2.9.4.1   Self-field

The $\mathbf{H}$-field generated from the bias current running in the sensor cannot be derived analytically for the planar Hall effect bridge sensors. Instead, the problem is simplified by considering one of the four branches as an infinitely long bar with the width w and the thickness t. Since $t \ll w$ the bar is also treated as infinitely thin. The infinitely long bar is sketched in Fig. 2.16 from where it is seen that a new coordinate system has been defined such that $x' = x\cos(\alpha_J) - y\sin(\alpha_J)$ and $y' = y\cos(\alpha_J) + x\sin(\alpha_J)$ is parallel and orthogonal to the infinite direction of the bar, respectively. The $\mathbf{H}$-field from such an infinitely long bar centered at $(x', y', z) = (x', 0, z_0)$ is
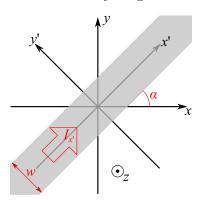
Fig. 2.16: Infinitely long and infinitely thin conductor with width w. x' and y' are defined to be parallel and orthogonal to the infinite direction of the bar, respectively.

from Biot and Savart's law given as [75]

$$\mathbf{H}_{\text{sf}}(x', y', z) = \frac{K_{\text{B}}}{2\pi}\left[\left(\arctan\left(\frac{y' + w/2}{z - z_0}\right) - \arctan\left(\frac{y' - w/2}{z - z_0}\right)\right)\hat{\mathbf{y}}'\right.$$
$$\left. - \frac{1}{2}\log\left(\frac{(y' + w/2)^2 + (z - z_0)^2}{(y' - w/2)^2 + (z - z_0)^2}\right)\hat{\mathbf{z}}\right], \tag{2.76}$$

where K_B is a bound surface current, which in this case is given by $I_{x'}/w$. By inserting Eq. (2.76) into Eq. (2.75), the magnetic force from the self-field $\mathbf{F}_{\mathrm{mag,sf}}$ is calculated. In Fig. 2.17 (a) and (b) the y' and z components of the magnetic force normalized with F_{Brown} are plotted as function of y', respectively. Values used to compute the graphs can be found in the figure caption.
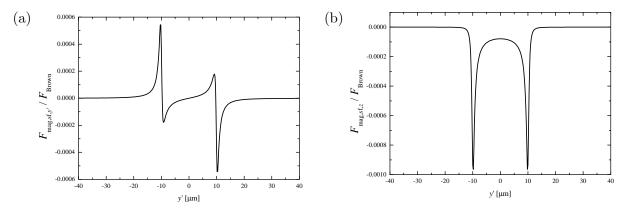
Fig. 2.17: (a) y'-component and (b) z-component of the magnetic force from the self-field acting on a 80 nm bead. The plots are computed for a bead with a diameter of 80 nm and a susceptibility of 1.4, which has been found experimentally (see Appendix A). The bead is placed in a height of 1 µm above the sensor, with a bias current of 15 mA. The width of the sensor has been set to 20 µm, which means that the edges of the sensor are at $y' = \pm 10$µm. α_J has been set to $\pi/4$ which is the standard from the previous sections.

From Fig. 2.17 it is seen that the magnetic force action on a 80 nm bead is very small compared to the "Brownian force". Thus, the attraction force due to the self-field is neglected.

Since the shape of the curves are determined by $\nabla(\mathbf{H}^2)$, changing the bead type will only change the amplitude of the curves. From Eq. (2.75) it is seen that the magnetic force scales with $D^3\chi$. Since F_{Brown} scales with D^{-1}, the normalized forces scales with $D^4\chi$. Hence, the normalized force for the 250 nm beads will be 95 times larger when assuming χ is identical for the 80 and 250 nm beads and the magnetic force will therefore not affect the 250 nm beads significantly either.

2.9.4.2 Magnetostatic force from sensor stack

Due to the exchange biasing of the sensor, the sensor stack has a static magnetization along the x-direction in zero applied field. The field from this permanent magnetization is again calculated for an infinitely long bar. This is sketched in Fig. 2.18 and Fig. 2.19. From these figures it is seen that the same reference coordinate system as for the self-field calculations has been defined.

To calculate the magnetic field, the magnetization can be described as bound surface currents ($\mathbf{K}_\mathrm{b}$) [76]

$$\mathbf{K}_\mathrm{b} = \mathbf{M} \times \hat{\mathbf{n}}, \tag{2.77}$$

where $\hat{\mathbf{n}}$ is the unit vector normal to the surface. $\mathbf{M}$ can be expressed in (x', y', z) coordinates as $(|M|\cos(\alpha_J), |M|\sin(\alpha_J), 0)$. Thus, the surface currents at the top and bottom are found by

$$\mathbf{K}_{\mathrm{top}} = (|M|\cos(\alpha_J), -|M|\sin(\alpha_J), 0) \times (0, 0, 1) = (-|M|\sin(\alpha_J), -|M|\cos(\alpha_J), 0), \tag{2.78}$$

$$\mathbf{K}_{\mathrm{bot}} = (|M|\cos(\alpha_J), -|M|\sin(\alpha_J), 0) \times (0, 0, -1) = (|M|\sin(\alpha_J), |M|\cos(\alpha_J), 0). \tag{2.79}$$
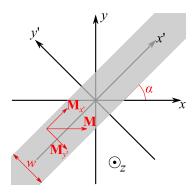
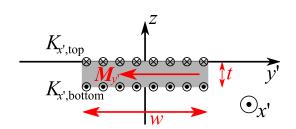**Fig. 2.18:** Infinitely long bar magnetized along the x-direction.

Fig. 2.19: Cross section of the infinitely long bar. Shows how the magnetization are described by bound surface currents.

Only the surface currents running along the conductor give rise to magnetic fields. Thus, only $K_{\text{top},x'} = -|M|\sin(\alpha_J)$ and $K_{\text{bot},x'} = |M|\sin(\alpha_J)$ are considered. The magnetic field $\mathbf{H}_{\text{ms}}$ is now calculated as the sum of the fields from two infinitely thin conductors (Eq. (2.76)); the top one placed at $z = 0$ and the bottom one at $z = -t$

$$\mathbf{H}_{\text{ms}}(x', y', z) = \frac{M_y'}{2\pi} \left[\left(\arctan\left(\frac{y' + w/2}{z+t} \right) - \arctan\left(\frac{y' - w/2}{z+t} \right) \right) \hat{\mathbf{y}}' \right.$$
$$-\frac{1}{2} \log\left(\frac{(y' + w/2)^2 + (z+t)^2}{(y' - w/2)^2 + (z+t)^2} \right) \hat{\mathbf{z}}$$
$$-\left(\arctan\left(\frac{y' + w/2}{z} \right) - \arctan\left(\frac{y' - w/2}{z} \right) \right) \hat{\mathbf{y}}'$$
$$\left. +\frac{1}{2} \log\left(\frac{(y' + w/2)^2 + (z)^2}{(y' - w/2)^2 + (z)^2} \right) \hat{\mathbf{z}} \right]. \tag{2.80}$$

As for the self-field in the previous section, the force acting on a bead is found by inserting the expression for $\mathbf{H}_{\text{ms}}$ into Eq. (2.75). The magnetization used to calculate the force is the saturation magnetization of permalloy (Ni$_{80}$Fe$_{20}$) [77] $M_s = 1.1$ T$/\mu_0$. The thickness of the permalloy layer is set to 30 nm, the width of the sensor is still 20 μm, $\alpha_J = 45°$ and the properties for a 80 nm bead is used. The forces in the y' and z-direction are normalized by F_{Brown} and plotted in Fig. 2.20.

From Fig. 2.20 (a) it is seen that the force in the y'-direction from the magnetostatic field is positive to the left of an edge and negative to the right of an edge, which means that the beads will be attracted to the edges of the sensor. It is also seen that the magnetostatic force in the y'-direction is less than 20% of the "Brownian force". Thus, the magnetostatic forces will not be dominating for 80 nm beads. The normalized force in the z-direction plotted in Fig. 2.20 (b) has a minimum of -0.6, which still means that the "Brownian force" dominates, but the magnetostatic force cannot be entirely neglected. It is also seen that the peaks are very narrow, meaning that the magnetostatic force is localized above the edges. Thus, the magnetostatic force will not attract beads to the edges but if they get close they will be captured.

As for the self-field, the shape of the force curves does not change with the bead size, but the amplitudes scale with $D^4\chi$. Thus, for the 130 nm and 250 nm beads the normalized forces
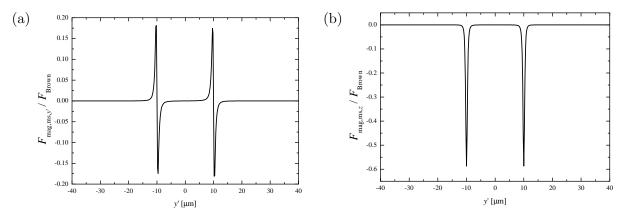
Fig. 2.20: y'-component(a) and z-component (b) of the magnetic force from the magnetostatic field acting on a 80 nm bead. The plots are computed for a bead with a diameter of 80 nm and a susceptibility of 1.4, which has been found experimentally (see Appendix A). The bead is placed in a height of 1 μm above the sensor. The width of the sensor has been set to 20 μm, which means that the edges of the sensor are at $y' = \pm 10$μm. α_J has been set to $\pi/4$ which is the standard from the previous sections.

are 7 and 91 times the force on a 80 nm bead, respectively. Hence, the magnetostatic force is slightly larger than the Brownian force for 130 nm beads and it will dominate the Brownian force near the edge of the sensor stack for the 250 nm beads. This implies that bead capturing on the sensor edges can be a problem for the larger beads.

2.9.5   Summary

Based on the above estimation of forces acting on magnetic beads it was found that sedimentation could be a problem for larger beads. It was estimated that for a channel height of 0.1 mm, the diameter of the bead should be smaller than 154 nm in order for the sedimentation time to be smaller than the diffusion time. It was also found that the magnetic force acting on the bead from the self-field can be neglected due to the effect of thermal motion being much larger. The magnetostatic forces in the sensor stack cannot be entirely neglected for beads with diameters of 80 nm and larger. For 250 nm beads the magnetostatic force is many times larger than the Brownian force near the edges of the sensor. However, it was also found that the magnetostatic forces are localized around the sensor edge and the force will therefore only affect beads that get close to the edges by sedimentation or Brownian motion.

Chapter 3

Fabrication and experimental setup

In this chapter the general information necessary to perform the experimental work of this thesis is described, the specific experimental setting will be described for each experiment as the results are presented in the following chapters. First, a description of the fabrication process is given. Secondly, it is described how the planar Hall effect sensors are characterized. Then the setup built for measurements with planar Hall effect sensors is described. Finally, the measurement equipment is explained and the settings used described along with the data treatment performed.

3.1 Fabrication of planar Hall effect sensors

All planar Hall effect sensors used for this PhD thesis were fabricated in the Danchip cleanroom facilities at DTU. The sensors were fabricated on 4-inch silicon p-type wafers, on which a 800–1000 nm oxide layer was grown by wet thermal oxidation. On all wafers the magnetic stack was first deposited, followed by deposition of the contact layer. After these two layers the wafers were treated slightly differently. Some of the wafers were not processed any further, while the wafers used for bead detection had a protective coating added.

3.1.1 Deposition of magnetic stack

The magnetic stacks (Ta (3 nm) / $Ni_{80}Fe_{20}$(30 nm)/ $Mn_{80}Ir_{20}$(20 nm) / Ta (3 nm)) were sputter-deposited in a Kurt J. Lesker CMS-18 magnetron sputter system. During deposition, a magnetic field of 20 mT was applied along the x-direction to define an easy axis of the magnetization and the exchange coupling between the ferromagnetic layer ($Ni_{80}Fe_{20}$) and the antiferromagnetic layer ($Mn_{80}Ir_{20}$). The tantalum layer below and above the magnetic materials are for better adhesion. The pattern of the magnetic stack layer was defined by a negative photolithography step prior to the stack deposition and followed by lift-off after deposition.

3.1.2 Deposition of contact stack

The contact stack (Ti (t_{Ti-1}) / Pt (t_{Pt}) / Au (t_{Au}) / Ti (t_{Ti-2})) were deposited by e-beam evaporation and also defined by lift-off, again using a photolithography step. The thickness of the different layers are listed in Table 3.1 for each wafer used during this project.

Table 3.1: Contact layer composition for the wafers used throughout the project.

Wafer	$t_{\text{Ti}-1}$	t_{Pt}	t_{Au}	$t_{\text{Ti}-2}$
86	10 nm	0	200 nm	0
208, 224, 225, 226 and 227	10 nm	100 nm	100 nm	10 nm

3.1.3 Low-temperature annealing

The wafers 225–227 were low-temperature annealed after the above described stacks had been deposited. This was done in the deposition system used to deposit the magnetic stack by applying a magnetic field of 20 mT along the x axis in vacuum and heating wafers 225–227 for 1 hour at 240°C, 280°C and 320°C , respectively.

3.1.4 Protective coating

The wafers used for bead measurements had to have a non-conducting protective coating deposited on top of the sensor and contact stack. The purpose of the protective coating was to ensure that the bias current through the sensor did not pass into the liquid. When a current was passed through the sensor and contact stack directly exposed to water, an electrochemical process occurred that oxidized the sensors and thereby changed the sensor signals.

Two different protective coatings were used. For wafer 86, a 580 nm layer of Ta_2O_5 was reactively sputter deposited through a shadow-mask, such that only the contact pads were left uncovered by the coating. Due to pin-holes, the Ta_2O_5 layer did not last long, especially if salts were present in the water. Instead, a 900 nm thick layer of Ormocomp (micro resist technology GmbH, Germany) was spun onto wafer 208 and patterned by photolithography. The Ormocomp layer turned out to be a better solution than the Ta_2O_5 both in terms of the voltage it could withstand and for how long. In order to cure Ormocomp, the wafer was left on a hot plate at 150°C for 3 hrs.

The remaining wafers did not have any protective coating as they were not used in wet conditions.

3.1.5 Masks

Two different mask sets have been used to fabricate the sensors used to fabricate sensors with different designs. Each mask set consisted of a mask for the magnetic stack and a mask for the contact stack. In addition, a third mask layout was used for the wafers on which protective coating was applied. Besides changing the chip designs on different masks, the chip size was increased from width×length = 3.6×5.5 mm^2 to 4.5×7.5 mm^2. This size increase allowed for increasing the number of contact pads from 8 to 20, which resulted in increased flexibility of designs. Since two pads were needed for the current connections, the design with 8 contact pads could hold 3 sensors and the 20-pad design could hold 9 sensors. However, 9 sensors were not placed on a single chip as the resistance through 9 sensors would be too high. Wafer 86 was fabricated with the 8-pad design while wafers 208 and 224–227 were fabricated with the 20-pad design. In Fig. 3.1 examples of chips for both the 8 and 20-pad designs are shown. It is seen that only 5 sensors were in fact placed on the 20-pad chip. It is also seen that an extra current

connector has been placed between sensor 2 and 3 to be able to only pass current through 2 or 3 of the sensors at once, to avoid large voltage drops along the current direction.
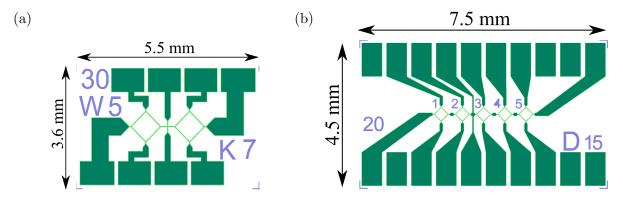

Fig. 3.1: Examples of planar Hall effect sensor chips. The light green represents the magnetic stack, the violet is the contact stack and the dark green is contact stack on top of magnetic stack. for (a) 8-pad chip design. The chip shown consists of one cross sensor surrounded by two bridge sensors, all three sensors are in series. (b) 20-pad chip design. The chip shown consists of 5 identical bridge sensors. The vertical line between sensor 2 and 3 is an extra current connector allowing for bypassing some of the sensors.

3.2 Characterization

The wafers were characterized to find the difference in resistivities, the anisotropy field and the exchange field, which are the three parameters needed for calculating the theoretical low-field sensitivity. Furthermore, each sensor was also characterized by measuring the signal vs. applied field in the y-direction from which the low-field sensitivities were determined.

3.2.1 Anisotropic magnetoresistance

In order to characterize the electrical properties of the fabricated wafers, a special AMR-test structure was included on each set of masks. Two different designs of test structures were used depending on the chip size of the mask. The two different designs are shown in Fig. 3.2 for both the 8 and 20-pad design, respectively. It is seen that the 20-pad design had several different conductor lengths more than the 8-pad design.

Four point measurements of the resistance were performed for a series of the possible conductor lengths, with both a saturation field applied perpendicular and parallel to the current direction. An example of such a set of resistances is shown in Fig. 3.3 for wafer 208. From the slopes of the fits the parameter $\Delta\rho/t_{\mathrm{FM}}$ was calculated by

$$\Delta\rho/t_{\mathrm{FM}} = w \left(\frac{\partial R_{\parallel}}{\partial l} - \frac{\partial R_{\perp}}{\partial l} \right), \tag{3.1}$$

where w is the width of the conductor and $\frac{\partial R_{\parallel}}{\partial l}$ and $\frac{\partial R_{\perp}}{\partial l}$ denote the slope of the curves in Fig. 3.3.
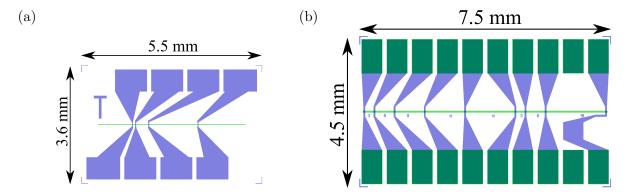
Fig. 3.2: AMR test structures. (a) 8-pad chip design, the width of the conductor is 20 µm. The lengths of the three segments are 100 µm, 400 µm 1500 µm. (b) 20-pad chip design, the width of the conductor is 50 µm and the number correspond to the number of hundred micrometers of the segment.
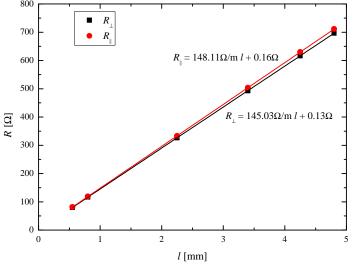
Table 3.2: Summary of the resistivities and contact resistances for the wafers used throughout the project.

Wafer	$\Delta\rho/t_{\mathrm{FM}}$
86	unknown
208	0.154 Ω
224	0.130 Ω
225	0.132 Ω
226	0.132 Ω
227	0.132 Ω

Fig. 3.3: Resistance measured on an AMR test structure (Fig. 3.2 (b)) from wafer 208, with a saturating magnetic field applied first parallel and then perpendicular to the length of the conductor.
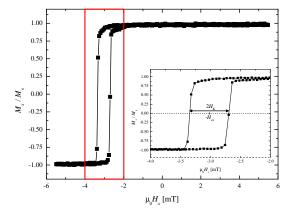
The values of $\Delta\rho/t_{\mathrm{FM}}$ for the wafers used in this project are listed in Table 3.2. It is seen that the values of $\Delta\rho/t_{\mathrm{FM}}$ change slightly for the different wafers. The exact reason for this is unknown, but it is most likely due to differences in the batch to batch film quality.

3.2.2   Magnetic properties

The magnetic properties H_{K} and H_{ex} of the fabricated wafers were characterized by measuring the magnetization as function of applied field for 3×3 mm^2 pads consisting of continuous stacks. These measurements were performed in a LakeShore model 7407 vibrating sample magnetometer (VSM) by applying the field both parallel and perpendicular to the x-axis. A set of magnetization

curves are shown in Fig. 3.4 and Fig. 3.5 for measurements parallel and orthogonal to the x-axis of wafer 86, respectively. The anisotropy and exchange fields were found from the hysteresis curve measured along the x-axis, where H_K is half the width of the hysteresis and $-H_{ex}$ is the center of the hysteresis loop (see inset Fig. 3.4).
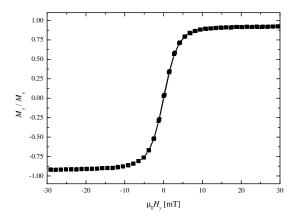
Fig. 3.4: Magnetization in the x-direction as function of applied field in the x-direction. The inset shows how H_{ex} and H_K are determined.

Fig. 3.5: Magnetization in the y-direction as function of applied field in the y-direction.

The values of H_K and H_{ex} found from the easy axis hysteresis loops are listed in Table 3.3 for the wafers used for this project. From the table it is seen that H_K and H_{ex} are similar for wafers 86 and 224, which nominally have the same thicknesses and have experienced approximately the same process sequence. Wafer 208 have the same nominal thicknesses as wafers 86 and 224. The difference is that wafer 208 has Ormocomp on it and therefore it has been exposed to 150°C for 3 hours. The wafers 225–227 had been low-temperature annealed in a magnetic field and it is seen that this results in a similar change as heating the wafer 208 without applying a magnetic field.

Table 3.3: Summary of the anisotropy and exchange fields obtained from VSM measurements for the wafers used throughout the project.

Wafer	$\mu_0 H_K$ [mT]	$\mu_0 H_{ex}$ [mT]
86	0.33	3.02
208	0.23	1.70
224	0.39	2.89
225	0.41	2.02
226	0.50	1.90
227	0.46	1.39

3.2.3 Low-field sensitivity

The last parameter to characterize was the low-field sensitivity. This was measured for each sensor and not on a wafer level as for the parameters described above. The low-field sensitivity

was measured by sweeping an applied field in the y-direction from $\mu_0 H_y = -45$ mT to $\mu_0 H_y = 45$ mT and back to $\mu_0 H_y = -45$ mT and simultaneously measuring the first harmonic in-phase signal. This type of measurement is referred to as a "field sweep". When measuring field sweeps, an alternating current with an amplitude of 1 mA was forced through the sensor. An example of such measurements are shown for bridge sensors with different aspect ratios in Fig. 3.6. The low-field sensitivity was found from a linear fit to the points within ± 1 mT (see Fig. 3.6 (b)). The low-field sensitivity obtained for each sensor used will be stated for the individual studies.
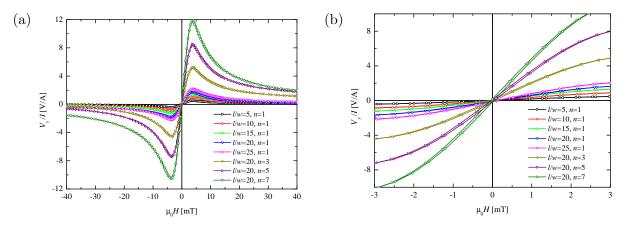
Fig. 3.6: Field sweeps for bridge sensors with varying ratios of l/w. Solid lines are not fits, but to guide the eye. (a) Shows the full range of the applied field. This Figure is from Paper A not appended. (b) Shows zoom-in of (a).

3.3 Experimental setup

To perform measurements with the planar Hall effect sensors, the experimental setup shown in Fig. 3.7 was constructed. A CPU cooler was fixed in a polycarbonate plate and on top of the CPU cooler a Peltier element was placed. On top of the Peltier element a copper plate welded to a T-shaped copper block was placed and in the T-shaped block a thermometer was placed. On top of the T-shaped copper block a piece of aluminum was placed, in which a small groove was milled such that the chip would be aligned with the fluidic system. The aluminum well was changed depending on which chip size was used. From Fig. 3.7 it is also seen that a microscope was placed above the setup for visual inspection of the sensors.

3.3.1 Temperature control

The temperature control system was composed of the liquid CPU cooler, the Peltier element and the thermometer. The CPU cooler was running at a constant flow rate, keeping the bottom side of the Peltier at a room temperature. The Peltier element and the thermometer were connected to a proportional-integral-derivative (PID) controller. At the beginning of the thesis, the PID controller was a LabVIEW (National Instruments Corp., TC, USA) program, but since small delays in the program would result in unstable temperatures, the PID controller was replaced by a LFI-3751 temperature controller (Wavelength Electronics, Inc., MT, USA). When

Fig. 3.7: Photos of experimental setup. (a) Side view along the y-direction. (b) angled top view. The tubing at the bottom of image (a) are the inlet and outlet of the CPU cooler. The red and black wires are for the Peltier element. 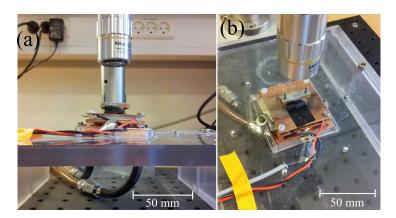On top the Peltier element the T-shaped copper piece can be seen with the aluminum well placed on top. Above the setup the lens of the microscope is seen.

the LabVIEW program was used, a Pt1000 resistance temperature was used as thermometer, whereas when using the LFI-3751 a thermistor was used.

3.3.2 Fluidic system

The fluidic system served two purposes: first, to define the fluidic chamber, where a bead suspension could be injected into; second, to facilitate electrical contacts to the chip to allow for a current to be passed through the sensor and a voltage to be measured. The fluidic system consisted of layers of polymethylmethacrylate (PMMA), which had been micromilled to define channels, holes for spring-loaded contact pins (POGO-PIN-5.94-1, Emulation Technology, Inc., Camarillo, CA, USA) and holes for assembling the system. After milling, the layers were bonded together by first cleaning the surfaces to be bonded with isopropanol, followed by exposure to UV light for 60–90 s. Finally, the layers were aligned and placed in a bonding press at 88°C with an applied force of 1 kN for 1 hour. To define the fluidic channel over the sensors, a polydimethylsiloxane (PDMS) gasket was fabricated from Sylgard 184 silicone elastomer kit (Dow Corning Corp., MI, USA). The PDMS gasket was fabricated such that it would fit into a groove milled in the bottom PMMA layer. The height of the PDMS gasket was 50 μm taller than the groove, such that when the fluidic system was tightened onto a chip, the PDMS gasket would seal off the fluidic channel over the chip. The spring-loaded contact pins were longer than the fluidic system was high to connect the contact pads on the sensor chip to a printed circuit board (PCB) on top of the fluidic system. The PCB had connectors to the power supply and the measurement equipment.

Due to the two different chip designs also two different fluidic systems were needed. The fluidic systems of the 8- and 20-pad chips are shown in Fig. 3.8 and Fig. 3.9, respectively. Besides the obvious changes, i.e., the position and number of Pogo Pins, the inlet and outlet connectors, the PDMS gasket, and the printed circuit board (PCB) were also changed.

The inlet and outlet were connected to the 8-pad version of the fluidic system by first making a thread and then fitting in the inlet and outlet connectors. The durability of these connections
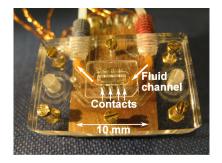
Fig. 3.8: Fluidic system used for measurements on 8-pad chips. This figure is from Paper II.
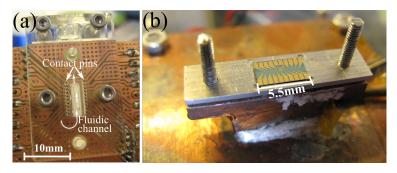

Fig. 3.9: (a) Fluidic system used for measurements on 20-pad chips. (b) 20-pad chip mounted in aluminum well. This figure is from Paper IV

were limited as they would fall out over time or the PMMA layers would crack. Instead, the connectors were replaced by tube connectors as described by Sabourin, Snakenborg, and Dufva [78] and Sabourin *et al.* [79]. Another important difference between the 8- and 20-pad designs was that the PDMS gasket was modified from having the Pogo Pins going through the gasket to the gasket being so narrow that it would fit between the Pogo Pins. This greatly reduced problems with liquids leaking from the fluidic channel to the Pogo Pins. If the Pogo Pins got in contact with the liquid, the electrical measurements were no longer reliable and the experiment would have to be aborted, the fluidic system demounted and the Pogo Pins dried. The last change from the 8-pad fluidic system to the 20-pad version was the PCB. The design had to be changed because of the new positions and increased number of Pogo Pins, but also the connector types was changed from a 8 DIN plug to 20 pin connectors, which made connections to the chip much more flexible.

Pumps

In order to pump liquid into the fluidic channel two different pumps were used; a standard commercial syringe pump (Harvard Apparatus, CA, USA) as shown in Fig. 3.10 and an in-house custom built peristaltic pump [79] as shown in Fig. 3.11. The advantages of the peristaltic pump were that it could be controlled from the PC with Lego Mindstorm and it could hold up to 6 different solutions, which allowed for injection of and washing off beads without having to change syringes manually. The drawback of the peristaltic pump was that the PDMS ribbons broke every now and then and were time consuming to fabricate. No experimental differences were observed between the two pumps. The dead volumes were also close to 10 μL for both pumps. The reported sample volumes were the volumes prepared, which means the dead volume should be subtracted in order to get the volumes flushed over the sensors.

3.3.3 Electromagnet

When the sensors were characterized by measuring field sweeps, an electromagnet was placed in the setup as shown in Fig. 3.12. The magnet was powered by a Kepco bipolar power supply (Kepco, Inc., NY, USA) and controlled from LabVIEW through a USB data acquisition (DAQ)
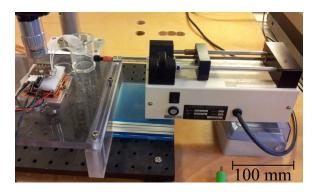
Fig. 3.10: Photo showing the Harvard pump connected to the fluidic system.
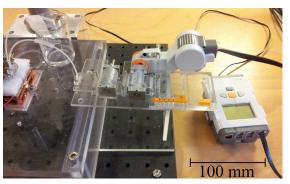
Fig. 3.11: Photo showing the Lego pump connected to the fluidic system.

unit. Commercial Hall probes were placed at the poles of the magnet to measure the generated field at the poles, which after a calibration could be converted to the applied field on the chip.
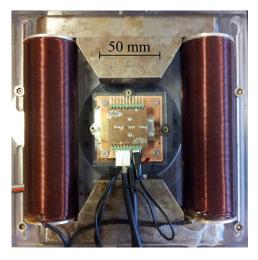
Fig. 3.12: Magnet frame used for measuring field sweeps as described in Section 3.2.3.

3.4   Measurements

In this section the measurement of bead relaxation using planar Hall effect sensors is described. First, the technique used for the measurements in the frequency domain is described, followed by a description of how measurements in the time domain are performed.

3.4.1   AC susceptibility measurements

In order to measure AC susceptibility of beads with a planar Hall effect sensor, a bias current was forced through the sensor through the arms in the x-direction, while the second harmonic signals were measured across the arms in the y-direction using a lock-in amplifier. The bias

current was delivered either by a Keithley Model 6221 AC and DC Current Source (Keithley Instruments Inc., OH, USA) or the internal power supply of the lock-in amplifier. For recording the second harmonic voltage, two different lock-in amplifiers were available. For alternating current at frequencies below 50 kHz a SR830 lock-in amplifier (Stanford Research Systems, Inc., CA, USA) was used and for frequencies above 50 kHz an HF2LI lock-in amplifier (Zurich Instruments AG, Switzerland) was used. All of the measurement equipment was controlled from a PC running LabVIEW (National Instruments Corp., TX, USA). Communication with the Keithley 6221 and SR830 lock-in amplifier was through General Purpose Interface Bus (GPIB), whereas communication with the HF2LI lock-in amplifier was through USB.

All AC susceptibility measurements were performed by varying the bias current frequency from high to low frequencies in logarithmically equidistant steps. After setting each frequency, the lock-in amplifiers were given time to let the signal become stable before recording the second harmonic sensor signal. For some of the experiments, additional measurements were performed between each frequency at a reference frequency, typically close to the expected Brownian relaxation frequency. These reference points made it possible to monitor the time evolution of the signal at that specific frequency, which was useful to determine whether or not the bead suspension was in equilibrium. The drawback of the reference points was that the total measurement time increased. A series of measurements at different frequencies including possible reference points will throughout this thesis be referred to as a "frequency sweep".

3.4.1.1   Measurements below 50 kHz

Below, the settings specific to measurements with the SR830 lock-in amplifier are described and discussed. The goal was to obtain as accurate measurement results in the shortest possible time.

Sampling method   The simplest and fastest way to obtain data from the SR830 was to record one sample at each frequency. However, this approach was not very appropriate as the lock-in signal was slightly fluctuating. In order to obtain more reliable recordings, several samples were recorded over a specific time period and the average value calculated. The SR830 had two ways of doing this; either by recording samples when requested from the PC or by using the internal buffer of the lock-in. The advantage of recording samples at requests was that they were transferred to the PC immediately, whereas when using the buffer, all points were first stored in the lock-in and then transferred to the PC resulting in slightly longer measuring times. On the other hand, when using the buffer all points were evenly distributed over the measurement time, whereas when sampling at request the time between points would vary due to the PC not being able to request points accurately. Knowing the exact time between the samples allowed for recording a whole number of periods exactly. This was especially useful at low frequencies where the signal was oscillating due to the averaging over the time constant. With the exception of the results in Section 5.1 all frequency sweeps measured with the SR830 shown in this thesis have been recorded using the internal buffer.

Frequency dependent settings for SR830   Some of the settings depended on the current frequency. These settings included the time constant, the waiting time and the measuring time. In order to measure true values of the signal, the waiting time had to be at least 20 times the

time constant to allow the signal to stabilize. For this reason, the time constant was set as low as possible to reduce the waiting time. However, a low time constant resulted in an oscillating output signal. It was decided that the oscillation of the lock-in signal should not exceed $\pm 1\%$ of its mean value. This resulted in the time constants shown in Table 3.4 for different frequency ranges.

Table 3.4: Time constants and waiting times as function of frequency for SR830.

Frequency range	Time constant	Waiting times
0.3 Hz − 1.5 Hz	1000 ms	20 s
1.5 Hz − 11 Hz	300 ms	6 s
11 Hz − 40 Hz	100 ms	2 s
40 Hz − 50 kHz	30 ms	0.6 s

Table 3.5: Measurement time as function of frequency for SR830.

Frequency range	Measurement time
0.3 Hz − 1 Hz	25.5 s
1 Hz − 2 Hz	12.8 s
2 Hz − 5 Hz	6.4 s
5 Hz − 10 Hz	3.2 s
10 Hz − 20 Hz	1.6 s
20 Hz − 50 kHz	0.8 s

The measurement time for each frequency was chosen such that the standard deviation of repeated measurements at each frequency did not exceed 20 nV and resulted in the measurement times listed in Table 3.5. The measurement time for each individual frequency was set such that the measurements were performed over a whole number of periods exactly. If the measurement times were chosen randomly, the data from the extra fraction of a period would result in additional noise.

Lock-in settings kept constant throughout a sweep The factors that potentially influence the measurement results with the SR830 lock-in are listed in Table 3.6 along with the possible settings for each factor and the setting found to be the best. The details on how the optimal settings were determined are described in Appendix B.1. Only a short discussion of the SR552 preamplifier (Stanford Research Systems, Inc., CA, USA) is given here.

Table 3.6: Factors believed to influence measurements with SR830. The second column shows the available choices. The third column shows the settings found to the best. The horizontal line separated the physical factors from lock-in setting.

Factor	Possible settings	Optimal settings
Power supply	Keihtley 6221 or SR830 Internal	Keihtley 6221
Preamplifier	Not Connected or SR552	Not Connected
Coupling	AC or DC	DC
Shield	Ground or Float	Ground
Reserve	High, Normal or Low Noise	Low Noise
Slope	6, 12, 18 or 24 dB/Oct	24 dB/Oct
Synchronous filter	On or Off	Off
Line filters	Out, 50 Hz, 60 Hz or Both In	Out

The SR552 preamplifier resulted in higher reproducibility of the measurements, but due to a low-pass filter in the amplifier, the measurements below 10 Hz were attenuated. In addition, the out-of-phase signals had an offset that could not be explained. Thus, it was decided not

to use the SR552 preamplifier. However, the measurements for Paper II and Section 5.1 were performed with the SR552 preamplifier because they were made before this test.

Reproducibility   To check the reproducibility of the SR830 setup with the settings described above, 41 frequency sweeps were performed with a bridge sensor connected and the standard deviations were calculated for both the in-phase and out-of-phase second harmonic raw signals at each frequency, which is plotted in Fig. 3.13.
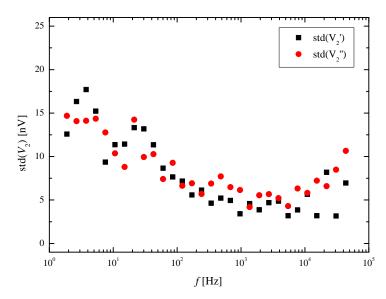
Fig. 3.13:   Standard deviation as function of frequency calculated based on 41 repeated frequency sweeps measured on a bridge sensor in dry condition with the SR830 lock-in amplifier and using the Keithley 6221 to supply a current amplitude of 20 mA.

From Fig. 3.13 it is seen that the standard deviation for both the in-phase and out-of-phase signals decrease as the frequency is increased, until 10 kHz where the standard deviation increases slightly again. This means that longer measurements time should be used at the lower frequencies to enhance the reproducibility. However, as seen from Table 3.5 the measurement time at low frequency is already many times longer than for the measurements above 20 Hz and also longer waiting times are used. The total measurement time was 2 min and 21 s for a frequency sweep from 1.88 Hz to 43.7 kHz with 30 measurements points and no reference points. Half of this time was spent on measuring the 6 points from 1.88 Hz to 10.7 Hz and the other half of the time on the remaining 24 points.

3.4.1.2   Measurements above 50 kHz

The HF2LI Zurich instrument lock-in amplifier had fewer user options. The only available power supply that could operate at up to 5 MHz was the internal voltage generator of the HF2LI lock-in amplifier. No appropriate preamplifier was available either and most of the lock-in settings had only one meaningful option for measurements on planar Hall effect sensors. The input should be DC coupled since the AC coupling added a high pass filter at 1 kHz, which was not useful when

measurements below this value were of interest. The input impedance could also be changed from 1 MΩ to 50 Ω, which means the resistance of the voltage input to ground was decreased to 50 Ω. However, reducing the input impedance resulted in a current running in the voltage arms of the sensor, which is not appropriate.

The remaining settings are the time constant, slope and sample rate. To test if any of these settings would affect the measurements, results of a full factorial design was made and analysis of variance (ANOVA) performed. The results of these measurements are shown in Appendix B.2. From the ANOVA it was found that neither of the settings affected the mean value or the standard deviation. For this reason the settings shown in Table 3.7 was chosen.

Table 3.7: Standard settings of HF2LI for frequency sweeps

Setting	Value
Sensitivity	As low as possible
AC coupling	Off
Differential	On
50 Ohm Input-Ground	Off
Synchronous filter	Off
Time constant	71 ms
Slope	48 dB/Oct
Sample rate	28.1 Sa/s

Table 3.8: Measurement times as function of frequency for HF2LI.
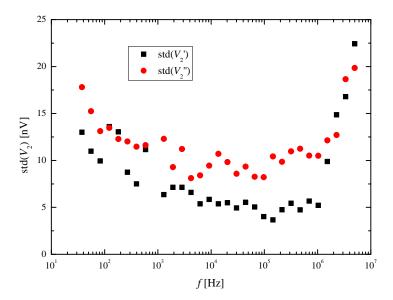
Frequency range	Measurement time
10 Hz – 50 Hz	15 s
50 Hz – 100 Hz	10 s
100 Hz – 500 Hz	5 s
500 Hz – 5 MHz	2.5 s

The measurement times used for measurements with the HF2LI lock-in amplifier are listed in Table 3.8 as function of the bias frequency. It is seen that these measurement times were longer than those used for the SR830 lock-in amplifier. The reason for this is believed to be that the HF2LI lock-in amplifier only has a 14-bit analog to digital converter, whereas the SR830 lock-in amplifier has 18-bits of resolution. In addition, the range of the HF2LI lock-in amplifier could not be set lower than 1 mV, while the input range of the SR830 lock-in amplifier could be set to 0.2 mV. Thus, the SR830 had a much higher resolution than the HF2LI lock-in amplifier.

Reproducibility To check the reproducibility of the HF2LI setup with the settings described above, 41 frequency sweeps were performed with a bridge sensor connected and the standard deviations were calculated for both the in-phase and out-of-phase second harmonic raw signals at each frequency, which is plotted in Fig. 3.14.

Figure 3.14 shows that the standard deviation decreases with increasing frequency until 1 MHz. Above 1 MHz the standard deviation increases again. The standard deviations for the out-of-phase signal were larger than for the in-phase signal. This is believed to be because the HF2LI lock-in amplifier controlled the voltage over the sensor instead of the current. Thus, small changes in temperature will change the current slightly and thereby also the offset in the second harmonic out-of-phase signal. The total measurement time was 3 min and 21 s for a frequency sweep consisting of 31 point from 37.7 Hz to 5 MHz. With the HF2LI lock-in amplifier the time was spent more equally through the frequency range due to the time constant being held constant and no long waiting times were required at lower frequencies.

For both lock-in amplifiers it was possible to decrease the standard deviation by increasing the measurement time. In theory, the standard deviation should be halved if the measurement

Fig. 3.14: Standard deviation as function of frequency calculated based on 41 repeated frequency sweeps measured on a bridge sensor in dry condition with the HF2LI lock-in amplifier with a bias voltage amplitude of 7 V, which corresponded a current amplitude of 20 mA.

time is multiplied by four. However, increasing the total measurement time would require that the setup remains in a constant state for a longer time such that the first and last frequencies of each sweeps were measured under almost identical conditions.

3.4.1.3 Data treatment

In this section the data treatment is described. No matter which lock-in amplifier was used for measuring frequency sweeps, the data needed to be corrected for an instrumental phase-shift $\Delta\varphi(f)$ and the offset in the out-of-phase data due to γ_0, as described in Section 2.8.2. Both the phase-shift and the offset were corrected for by measuring one or more frequency sweeps prior to the injection of beads, containing the same liquid as the beads were suspended in. These measurements are denoted $V_{2,\mathrm{ref}}$.

It was assumed that the phase-shifts were constant over time such that once the phase-shifts were determined from the reference sweeps, these could be used to correct the data measured with beads. The raw in-phase and out-of-phase signals measured are given by

$$V'_{2,\mathrm{Raw}} = V'_{2,\mathrm{True}} \cos(\Delta\varphi(f)) - V''_{2,\mathrm{True}} \sin(\Delta\varphi(f)) \tag{3.2}$$
$$V''_{2,\mathrm{Raw}} = V'_{2,\mathrm{True}} \sin(\Delta\varphi(f)) + V''_{2,\mathrm{True}} \cos(\Delta\varphi(f)) \tag{3.3}$$

in terms of the true in-phase $V'_{2,\mathrm{True}}$ and out-of-phase ($V''_{2,\mathrm{True}}$) signals. And likewise the true signals are found from

$$V'_{2,\mathrm{True}} = V'_{2,\mathrm{Raw}} \cos(\Delta\varphi(f)) + V''_{2,\mathrm{Raw}} \sin(\Delta\varphi(f)) \tag{3.4}$$
$$V''_{2,\mathrm{True}} = -V'_{2,\mathrm{Raw}} \sin(\Delta\varphi(f)) + V''_{2,\mathrm{Raw}} \cos(\Delta\varphi(f)) \tag{3.5}$$

The phase-shifts were found by assuming that the true in-phase signal should be 0 for all f when no beads were present in the sensor. Thus, $\Delta\varphi(f)$ are determined by solving

$$V'_{2,\text{True,ref}} = V'_{2,\text{Raw,ref}} \cos(\Delta\varphi(f)) + V''_{2,\text{Raw,ref}} \sin(\Delta\varphi(f)) = 0 \tag{3.6}$$

for each frequency. The corrected values for measurements both with and without beads were calculated by inserting $\Delta\varphi(f)$ in Eq. (3.4) and Eq. (3.5). This correction is shown in Fig. 3.15 (a), where raw data measured with and without beads are plotted vs. frequency. It is seen that $\Delta\varphi(f)$ has been determined such that $V'_{2,\text{True,ref}} = 0$ for all frequencies. It is also noticed that the data is positive, which is because the low-field sensitivity has been defined to be negative.

Finally, the offset due to γ_0 was corrected for by

$$V'_2 = V'_{2,\text{True,bead}} \tag{3.7}$$

$$V''_2 = V''_{2,\text{True,bead}} - V''_{2,\text{True,ref}}. \tag{3.8}$$

Since $V'_{2,\text{ref}}$ is defined to be zero when determining $\Delta\varphi(f)$ it is not subtracted from $V'_{2,\text{True,bead}}$. In Fig. 3.15 (b) the data from Fig. 3.15 (a) has been corrected for the offset due to γ_0. From this, it is seen that the signal due to the magnetic beads were less that 3% of the raw signal, which means that even a relatively small change in the offset between measurements with and without beads could, potentially, influence the bead signal significantly.

3.4.2   Time domain measurements

In order to measure the Brownian relaxation in the time domain with planar Hall effect sensors, the bias current was supplied by the Keithley 6221 and a NI-6281 DAQ (National Instruments Corp., TX, USA) was used for recording the voltages. The Keithley 6221 was configured to deliver a square wave at a frequency of 8 Hz. The advantage of using a square wave instead of a simple DC output with changing sign, was that the Keithley 6221 sends out a trigger signal (phase marker), which was used to accurately start the sampling with the NI-6281. Without accurate sampling recordings the steps of the bias current would have to be determined later, which proved more tedious and less accurate. The NI-6281 was set to sample 600.000 samples per second, and the range fixed at 100 mV, which was the lowest possible. The bit resolution was 18 bits, which resulted in a resolution of 0.76 µV. Also for these measurements the voltage was measured such the low-field sensitivity was negative. Thus, the sign from the theory chapter is reversed.

3.4.2.1   Data treatment

In this section it will be described how V_{ave} and V_{diff} were obtained from measurements. The sample data presented here were all performed on a bridge sensor ($w = 20$ µm and $l = 280$ µm from wafer 208) without beads present. The sensor was biased with a square wave current with an amplitude of 20 mA, which means that the current was changing between $+20$ mA and -20 mA every 62.5 ms.

In Fig. 3.16 two sets of raw data is shown where the phase markers were set at 0° and 180°, respectively. The phase marker informed the NI-6281 DAQ when to start sampling. With the
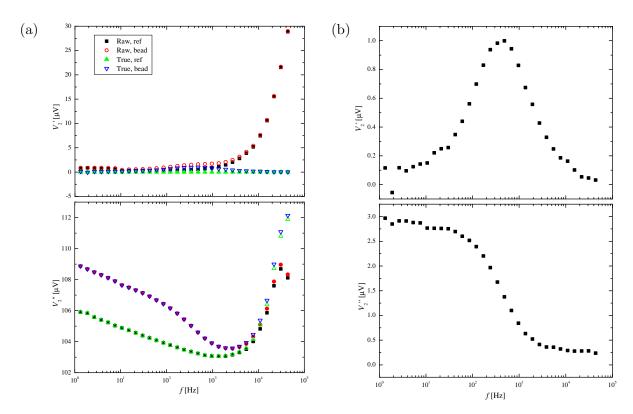
Fig. 3.15: Example of phase shift correction. (a) Raw signals plotted vs. frequency for measurements with and without beads. True signals calculated by finding $\Delta\varphi(f)$ from Eq. (3.6) and inserting into Eq. (3.4) and Eq. (3.4). (b) Bead signal calculated by $V_2'' = V_{2,\text{True}}''$ and $V_2'' = V_{2,\text{True}}'' - V_{2,\text{True,ref}}''$.

phase marker set to $0°$ the measurement started when the current changed from $-I_0$ to $+I_0$ and vice versa for a phase marker of $180°$. Phase markers received during sampling were ignored by the NI-6281 DAQ. This approach was chosen as it resulted in the best synchronization between measurements at $I = +I_0$ and $I = -I_0$. Changing the phase marker between each sampling also decreased the total measuring time, since the time from ending one recording to the start of the next was reduced from a whole to half a period.

The average of and difference between the signals recorded with the phase marker set at $0°$ and $180°$ were calculated and shown in Fig. 3.17. Each of these plots contain four repetitions of V_{ave} and V_{diff}. Each data set was then split into four and averaged, which is shown in Fig. 3.18, where the 10 first points are skipped because the current was changing while these were recorded.

From Fig. 3.18 it is seen that both V_{ave} and V_{diff} are quite noisy. It is also noted that V_{ave} decays with time and almost reach a constant value near the end. On the other hand, V_{diff} looks constant vs. time when disregarding the noise. By repeating the measurements and averaging the repetitions it was possible to reduce the noise level. For the measurements shown in Chapter 6, the signals were in total averaged over 192 periods, which means the current was flipped 384 times.
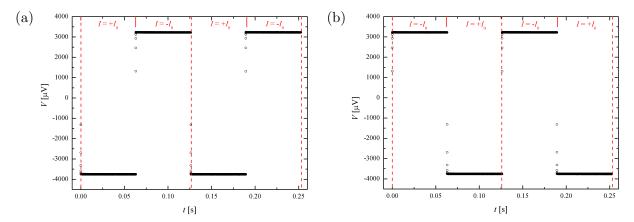
Fig. 3.16: Raw data measured for two periods of $f = 8$ Hz with the phase marker set at (a) $0°$ and (b) $180°$. The vertical dashed lines represent when a phase marker is sent from the power supply.
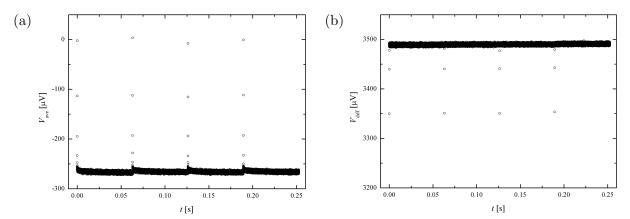
Fig. 3.17: (a) V_{ave} and (b) V_{diff} calculated from the raw data in Fig. 3.16.
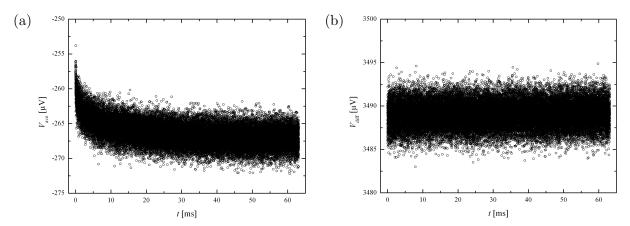
Fig. 3.18: (a) V_{ave} and (b) V_{diff} calculated as the as the average over the four repetitions shown in Fig. 3.17, where the first 10 points have been omitted.

3.5   Magnetic beads and sample preparation

Throughout the project many different magnetic beads were used from two different producers: Micromod and Ocean Nanotech. The different bead sizes and surface coatings used for this project have already been listed in Table 2.1. All beads used are commercially available, except for the 50 nm BNF-starch beads with NH2 surface, which were a special order from Micromod.

In Chapter 5 and Chapter 6 relaxation measurements on bead solutions are presented. Before preparing samples containing any type of beads they were vortexed, to ensure that the beads were homogenously suspended. The beads for these experiments were either diluted with MilliQ water or PBS. The beads from Ocean Nanotech were always diluted with MilliQ water, because diluting them in PBS led to an 50 % increase in the hydrodynamic diameter, which indicates that the beads were not entirely stable when diluted in PBS. The Micromod beads were stable in both solutions. These were in general suspended in PBS, except for the measurement on 250 nm beads in Section 5.1, which were diluted in pure MilliQ water. In Chapter 7 measurements are presented where beads have been mixed with solutions containing bBSA diluted in MilliQ water with PBS and DNA coils formed by RCA diluted in a hybridization buffer (4mM Tris-HCL, 4mM EDTA, 0.02 v/v% Tween-20 and 0.1 M NaCl). The details of the sample preparation for each experiment are described in Chapter 7.

Chapter 4

Temperature dependence of planar Hall effect sensors

The resistivity of almost any material depends on the temperature, and this is also the case for magnetoresistive sensors. Since magnetoresistive sensors rely on measuring changes in resistivity due to magnetic fields, it is important to know how the temperature affects the sensor response. In this study the temperature dependence of planar Hall effect bridge sensors are investigated by measuring the low-field sensitivity at temperatures ranging from 25°C to 90°C. The investigation distinguishes between reversible and irreversible changes. Additionally, the effects of low-temperature annealing are examined. The results presented in this chapter are also published in Paper I.

4.1 Introduction

When the sensors are biased with a current source, the only parameter of the sensor response that depends on temperature is the low-field sensitivity. The low-field sensitivity for a planar Hall effect bridge sensor is given by Eq. (2.35); for convenience repeated here

$$S_0 = \frac{l\Delta\rho}{t_{\text{FM}}w(H_{\text{K}} + H_{\text{ex}})}.$$

The sensitivity is split into three components $\frac{l\Delta\rho}{t_{\text{FM}}w}$, H_{K} and H_{ex} that each may vary with temperature. $\frac{l\Delta\rho}{t_{\text{FM}}w}$ is theoretically proportional to $\frac{V_{\text{pp}}}{I}$, where V_{pp} is the peak to peak voltage of a field sweep. $\frac{V_{\text{pp}}}{I}$, H_{K} and H_{ex} are extracted by minimization of the magnetic energy and least squares fitting to the measured field sweeps. Details of the energy minimization and fitting are found in Paper I.

4.2 Experimental

Prior to performing the temperature study the wafer were characterized as described in Section 3.2. The parameters are repeated in Table 4.1 with the addition of the measured low-field sensitivities.

To investigate the temperature dependencies, field sweeps were measured on planar Hall effect bridge sensors with $l = 280$ µm, $w = 20$ µm from an unannealed wafer and three wafers annealed at 240, 280 and 320°C for 1 hour. Field sweeps were performed at temperatures ranging from 25°C to 90°C. To be able to distinguish between reversible and irreversible temperature changes, reference field sweeps were measured at 25°C in between the field sweep at elevated temperatures.

For each field sweep the low-field sensitivity was found by as the average slope in the range -0.15 mT$< \mu_0 H_y < 0.15$ mT, while $\frac{V_{pp}}{I}$, H_K and H_{ex} were found from least squares curve fitting to the full sweep by minimization of the magnetic energy. The reversible temperature dependence of the four parameters were found as the difference between the value obtained from a field sweep at an elevated temperature and the following reference field sweep at 25°C. The irreversible changes were the differences between the values obtained from the initial field sweeps at 25°C and the reference field sweeps.

4.3   Results and discussion

From the initial characterization of the wafers summarized in Table 4.1 it is seen that annealing the wafers result in an increase of the low-field sensitivity. The low-field sensitivity is increased by 73.5 % when comparing the wafer annealed at 320°C to the wafer not annealed. It is also seen that the primary reason for the increased sensitivity is a reduction of the exchange field.
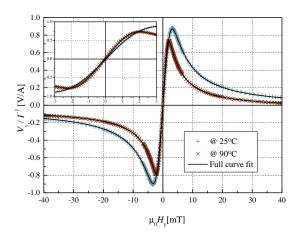
Table 4.1: Wafer parameter obtained from characterization as described in Section 3.2. The values of $\mu_0 H_K$ and $\mu_0 H_{ex}$ were measured by VSM and cannot be compared to values extracted from fitting.

Wafer	Anneal temp. [°C]	S_0/μ_0 [V/(TA)]	$\Delta\rho/t_{FM}$ [Ω]	$\mu_0 H_K$ [mT]	$\mu_0 H_{ex}$ [mT]
224	-	465	0.130	0.39	2.89
225	240	637	0.132	0.41	2.02
226	280	699	0.132	0.50	1.90
227	320	807	0.132	0.46	1.39

In Fig. 4.1 the field sweeps performed at 25°C and 90°C for the unannealed wafer along with the curve fits obtained from minimization of the magnetic energy are shown. It is seen that the model fits well to the measured data. Also some clear effects of changing the temperature are observed: The peak to peak value decreases as temperature is increased, the peak positions are shifted from $\mu_0 H_y \approx \pm 3$ mT to $\mu_0 H_y \approx \pm 2$ mT, and the slope at $\mu_0 H_y = 0$ mT, i.e., the low-field sensitivity increases with increasing temperature.

In Fig. 4.2 the initial field sweeps at 25°C of the unannealed wafer and the wafer annealed at 280°C are shown. It is seen that the wafer annealed at 280°C shows some of the same changes compared to the unannealed as observed when heating the unannealed wafer, i.e., the peak positions are shifted closer toward $\mu_0 H_y = 0$ mT and the slope at $\mu_0 H_y = 0$ mT is increased. The peak-to-peak value is not affected, but a small offset is observed.

The low-field sensitivities normalized with the initial low-field sensitivities are plotted vs. temperature in Fig. 4.3 (a). The open symbols are the low-field sensitivities measured at 25°C

Fig. 4.1: Field sweeps performed at 25°C and 90°C on not annealed wafer. The solid lines are curve fits obtained by minimization of the magnetic energy. The inset shows a zoom-in on the low-field data.

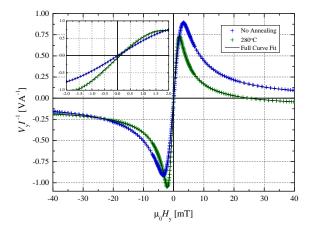**Fig. 4.2:** Field sweeps performed at 25°C for wafer with no annealing and wafer annealed at 280°C. The figure is from Paper I.

after the temperature at which it is plotted. This makes it easy to distinguish the reversible and irreversible parts of the temperature dependence. The figure shows that the sensitivity is increased $\sim$22.5 % when increasing the temperature from 25°C to 90°C for the unannealed wafer. More than 50 % of the change is irreversible. For the unannealed wafer it is also seen that as the temperature increases, a greater fraction of the temperature dependence becomes irreversible, i.e., at 40°C 25 % of the change is irreversible.

It is seen that the temperature dependence decreases as the annealing temperature increases. For the two wafers annealed at 280°C and 320°C the temperature dependence of the low-field sensitivity is less than 3 % when the temperature is increased to 90°C. It is also seen that for the wafer annealed at 280°C the entire temperature dependence is irreversible. For the wafer annealed at 320°C the total temperature change becomes negative.

To determine which terms in the sensitivity are causing the temperature dependence, V_{pp}/I is plotted vs. temperature in Fig. 4.3 (b) and H_{ex} and H_{K} are plotted vs. temperature in Fig. 4.4. From Fig. 4.3 (b) it is seen that the temperature dependence of V_{pp}/I is completely reversible and almost independent of annealing temperature. It is also seen that V_{pp}/I decreases linearly with the temperature for the investigated temperature range. By recalling that $V_{\mathrm{pp}}/I \propto \frac{l\Delta\rho}{t_{\mathrm{FM}}w}$ it is seen that the temperature dependent term is most likely $\Delta\rho$ as the geometrical dimensions are expected to be almost independent of temperature.

From Fig. 4.4 (a) it is seen that the relative temperature dependence of H_{ex} is larger for the unannealed wafer than for the three annealed wafers, which are seen to have the same relative temperature dependence of H_{ex}. Fig. 4.4 (b) shows that the temperature dependence of H_{K} is largest for the unannealed wafer and very irreversible for all four wafers. This means that the irreversible temperature changes of the low-field sensitivity are due to changes in H_{ex} and H_{K}.

This study showed that the low-field sensitivity can be increased by 73.5 % by annealing the wafer at 320°C. It was also found that the low-field sensitivity is temperature dependent. For an unannealed wafer the low-field sensitivity increase by 22.5 % when heating the sensor
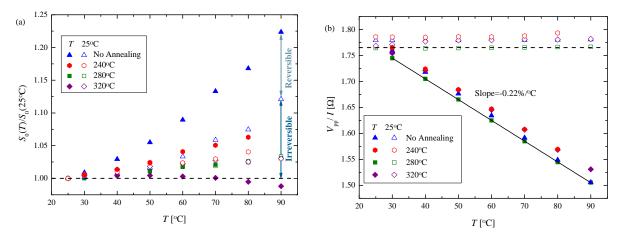
Fig. 4.3: (a) low-field sensitivity normalized with initial value at $25°C$ as function of temperature. (b) peak-to-peak values as function of temperature. The full points are for measurements at the temperature T, the open points are for the following measurement performed at $25°C$. The dashed lines mark the initial value at $25°C$. The solid line in (b) are a linear fit of the points measured at T. The arrows to the right of (a) indicates the reversible and irreversible change of the unannealed wafer. The figure is from Paper I.
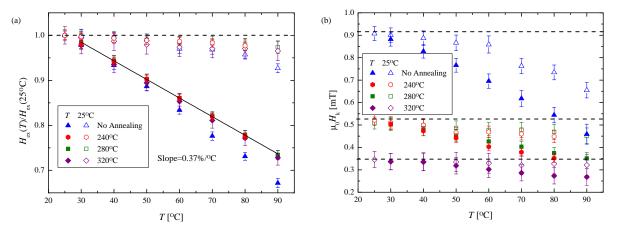
Fig. 4.4: H_{ex} (a) and H_K (b) vs. temperature. The full points are for measurements at the temperature T, the open points are for the following measurement performed at $25°C$. The dashed lines mark the initial value at $25°C$. The solid line in (a) are linear fit of the points measured at T. The figure is from Paper I.

to $90°C$, more than half of this increase is irreversible. By low-temperature annealing the temperature dependence of the low-field sensitivity can be reduced to less than 3 %. However, this temperature dependence is still too large to be able to compare measurements performed at different temperatures, the signal must be corrected for the temperature dependence before a meaningful comparison can be made. It was also shown that heating the sensors leads to irreversible changes, which will make temperature compensation more complicated. At present no temperature compensation exists and measurements that are to be compared should therefore be performed at a constant temperature.

Chapter 5

AC susceptibility measurements of magnetic beads

In this chapter AC susceptibility measurements of magnetic beads using planar Hall effect sensors are presented. Throughout the chapter, parameters, such as temperature, sensor geometry, current amplitude, bead concentration and bead diameter, are changed in order to demonstrate that the measurements follow the theory described in Chapter 2. Thus, it is demonstrated that planar Hall effect sensors can be used as miniaturized AC susceptometers without the need of any external magnets.

This chapter is divided into five sections. In the first section, the temperature dependence of AC susceptibility measurements is investigated. In the second section, AC susceptibility measurements performed using bridge and cross sensors are compared, which also includes a small study on how the measurements depend on the bias current. The third section contains a study of AC susceptibility measurements performed vs. concentration of 40 nm beads. In the fourth section AC susceptibility measurements are performed on six different bead types with different nominal diameters. In the fifth and last section AC susceptibility measurements performed with planar Hall effect sensors are compared to measurements performed with a commercial AC susceptometer (DynoMag from Imego, Sweden).

5.1   Temperature dependence of AC susceptibility measurements

The first parameter that is varied is the temperature of system. This is done to ensure that the relaxation of magnetic beads measured with a planar Hall effect cross sensor follow the expected theory. The results from this study have been published in Paper II.

From Section 2.8.2 it is recalled that the sensor signal for AC susceptibility measurements depends on S_0, I, γ_0, γ_1, χ' and χ''. The temperature dependence of S_0 was investigated in the previous section. I is not temperature dependent. γ_0 and γ_1 depends on the sensor stack, sensor geometry and bead distribution. Thus, it is assumed that neither γ_0 nor γ_1 will show any significant temperature dependence. However, the complex magnetic susceptibility is governed by the Brownian relaxation frequency, which is given by Eq. (2.10) and repeated here

for convenience

$$f_{\mathrm{B}} = \frac{1}{2\pi\tau_{\mathrm{B}}} = \frac{k_{\mathrm{B}}T}{6\pi\eta V_{\mathrm{h}}} = \frac{k_{\mathrm{B}}T}{\pi^2\eta D_{\mathrm{h}}^3}.$$

From this it is seen that f_{B} depends on the temperature due to the thermal energy and the dynamic viscosity. Since the beads are suspended in water, the viscosity is highly temperature dependent. In this study, the temperature is varied in the range from 5°C to 35°C, which corresponds to a change in viscosity from 1.52 mPas to 0.72 mPas [80].

5.1.1   Experimental

The temperature dependence of the Brownian relaxation frequency was found by injecting a bead suspension of 250 nm beads into the fluidic channel and letting the sample sediment for 16 hours to stabilize the signal. Frequency sweeps were then performed at temperatures ranging from 5°C to 35°C in steps of 5°C. Prior to the measurements at 5°C, 15°C and 30°C a control sweep was performed at 25°C, to be able to monitor any irreversible changes.

Table 5.1: Experimental settings for temperature dependence of AC susceptibility study.

Wafer Name	86
Sensor type	Cross $w = 20\mu$m
low-field sensitivity	$S_0/\mu_0 = -36.5$ V/(TA)
Lock-in	SR830 + SR552
Reference points	No
Current amplitude	15 mA
Channel height	1 mm
Bead type	250 nm MM
Bead Concentration	2.5 mg/mL
Temperature	5°C– 35°C

Between each frequency sweep, a waiting time of 15 min was added to ensure a constant temperature of the entire fluidic system. The Cole–Cole model was fitted to all frequency sweeps and the corresponding Brownian relaxation frequencies were extracted. Further detail on the experimental setup are summarized in Table 5.1 and the details can be found in Chapter 3.

5.1.2   Results and discussion

In Fig. 5.1 the in-phase (a) and out-of-phase (b) second harmonic signals are plotted vs. frequency for temperatures ranging from 5°C to 30°C. The solid lines represent the fit of the Cole–Cole model to the measured data. From the figure it is seen that the Brownian relaxation frequency is shifting to a higher frequency as the temperature is increased. It is also seen that the Cole–Cole model does not fit the low-frequency points very well.

From Fig. 5.1 it is also observed that the signal amplitude increases with temperature. This could be due to the temperature dependence of the sensor sensitivity as described in the previous chapter. However, the changes observed for the reference measurements at 25°C (Fig. 5.2) are of similar magnitude, which indicates that all the change is irreversible. In the previous chapter it was shown that only a fraction of the temperature dependence is irreversible. Thus, the increase in signal is not likely to be due to changing the temperature. Another possible explanation for the increase in signal, is that the number of beads near the sensor is increasing. This could either be caused by sedimentation of beads or magnetostatic forces trapping beads on the edges of the sensor stack. In Section 2.9.2 the sedimentation time of the 250 nm beads in a 1 mm channel was estimated to 4.9 hr, which means that all the beads should for sure have sedimented to the sensor surface during the initial waiting time of 16 hr. If the increase is due to magnetostatic
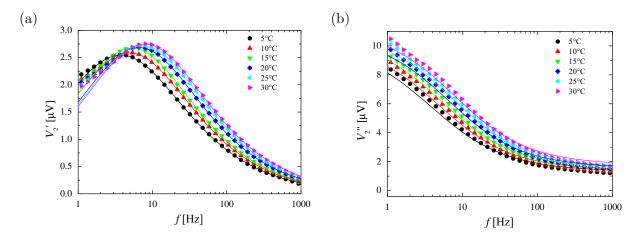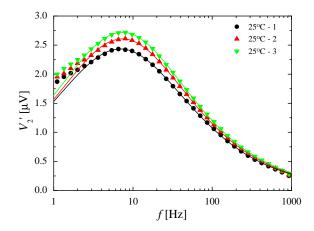
Fig. 5.1: In-phase (a) and Out-of-phase (b) second harmonic signal vs. frequency for 250 nm beads measured at six different temperatures. The figures are from Paper II.

forces capturing the beads at the edges of the sensor stack it would be expected that they would also become less free to rotate, resulting in a shift of the Brownian relaxation peak towards lower frequencies. This is not the case as shown in Fig. 5.2, where the Brownian relaxation frequency is almost constant in time and therefore independent of the increased signal. Thus, the reason for the continued increase of signal cannot easily be explained.

The Brownian relaxation frequencies extracted from the fits of the Cole–Cole model are plotted vs. temperature in Fig. 5.3. The plot shows that the Brownian relaxation frequency is increasing with temperature, and that it is more than doubled from 3.8 Hz at 5°C to 8.8 Hz at 35°C. It is also seen that the repeated measurements at 25°C result in an average Brownian relaxation frequency of 7.1 Hz. In the inset, the hydrodynamic diameters are calculated taking into account the temperature dependence of both the thermal energy and the viscosity of water. The inset shows that after the temperature compensation, the hydrodynamic diameters are independent of temperature. It is also seen that the hydrodynamic diameters are found to be around 400 nm, which is much larger than the nominal size of 250 nm. The difference is believed to be due to a combination of the beads having sedimented to the bottom and being captured by magnetostatic forces. Thus, the beads are lying on the surface and not being as free to rotate as if they had been freely suspended, which is the situation that the theory is valid for. This is discussed in more detail in Section 5.5 where these measurements are compared to measurements from a DynoMag AC susceptometer.

To conclude on this study, it was first of all shown that the planar Hall effect cross sensor could be used for measuring Brownian relaxation of magnetic beads and that the Cole–Cole model could be fitted well to the data to extract the Brownian relaxation frequencies from the fits. Furthermore, the study showed that the Brownian relaxation frequency is greatly dependent on temperature. However, it was also shown that the temperature dependence of the Brownian relaxation frequency followed what was expected by the theory and that reliable values of D_h can be extracted if the temperature is known and the temperature dependence of the dynamic viscosity is corrected for. Thus, to be able to extract the hydrodynamic diameter it is crucial to have information about the exact temperature, to correct for it, and to keep it constant during
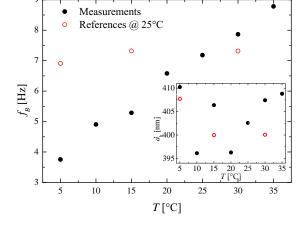
Fig. 5.2: In-phase second harmonic signal vs. frequency for repeated measurements at 25°C.

Fig. 5.3: Extracted Brownian relaxation frequencies vs. temperature. The open symbols are from the reference sweeps at 25°C performed before the temperature at which they are plotted. The inset shows the Brownian relaxation frequencies converted to hydrodynamic diameters. The figure is from Paper II.

the entire frequency sweep to ensure that the dynamic response does not change during the sweep. In the following measurements the temperature are kept constant at 25°C.

5.2   Comparing AC susceptibility measurements using bridge and cross sensors

Above it was shown that AC susceptibility measurements could be performed on a planar Hall effect cross sensor. In this section, AC susceptibility measurements performed with planar Hall effect bridge and cross sensors are compared. This is done to investigate experimentally if it is possible to obtain a larger bead signal from the bridge sensor than from the cross sensor as was predicted by the theoretical expressions in Eq. (2.56) – Eq. (2.59). From the these expressions it is also predicted that the dynamic signal obtained from magnetic beads depends on the bias current amplitude squared. In order to validate this, AC susceptibility measurements are performed with different bias current amplitudes. The results presented in this section have also been published in Paper III.

From Eq. (2.56) – Eq. (2.59) in the theory chapter it is recalled that the ratios between the bead signal for bridge and cross sensors are given by

$$\frac{V_{\mathrm{B}}}{V_{\mathrm{B}}} = \frac{S_{\mathrm{B},0}}{2\sqrt{2}S_{\mathrm{C},0}} \tag{5.1}$$

when γ_1 is assumed to be identical for the bridge and cross sensors. The low-field sensitivities have been found from field sweeps to be $S_{\mathrm{C},0}/\mu_0 = -90$ V/(AT) and $S_{\mathrm{B},0}/\mu_0 = -616$ V/(AT) for the bridge and cross sensor, respectively. Thus, the bead signal from the bridge sensor is expected to be 2.4 times that of the cross sensor.

5.2.1   Experimental

The measurements were performed on a chip where a bridge and a cross sensor were connected in series (see Fig. 5.4), to expose the two sensors to the exact same conditions during measurements. The measurement series were repeated for bias current amplitudes ranging from 6.2 mA to 43.4 mA in steps of 6.2 mA. For each bias current amplitude a series of ten frequency sweeps were performed: first three with only MilliQ water in the channel for reference; at the start of the fourth sweep beads were injected into the channel for 1 min; during the fifth to eighth sweep the bead suspension was in a steady state; at the beginning of the ninth sweep, the beads were washed away; and a tenth sweep was performed to confirm that the signals were back to their initial state. The Cole–Cole model was fitted only to sweeps 5–8. The remaining experimental settings are summarized in Table 5.2 and for further details refer to Chapter 3 or Paper III.

Table 5.2: Experimental settings for bridge vs. cross study.

Wafer Name	208
Sensor types	Cross $w = 20\mu m$
	Bridge $l \times w = 280\mu m \times 20\mu m$
low-field sensitivity	$S_{C,0}/\mu_0 = -90$ V/(TA)
	$S_{B,0}/\mu_0 = -616$ V/(TA)
Lock-in	HF2LI
Reference points	Yes, $f_{ref} = 4667$ Hz
Current amplitude	6.2 mA – 43.4 mA
Channel height	1 mm
Flow rates	In: 30 μL/min, Out: 800 μL/min
Sample volume	30 μL
Bead type	40 nm ON
Bead Concentration	1 mg/mL
Temperature	25°C
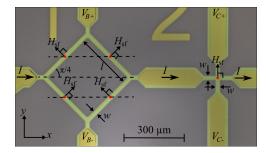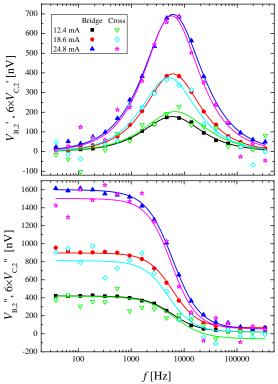
Fig. 5.4: Fig. 2.13 repeated. Bridge and cross sensors connected in series, with directions of self-field acting on the ferromagnetic layer. The figure is from Paper III.

5.2.2   Results and discussion

In Fig. 5.5 the in-phase (top) and out-of-phase (bottom) second harmonic signals are plotted vs. bias current frequency for the eighth frequency sweep. Data is shown for measurements with both bridge and cross sensors using three different bias currents. The signals measured with the cross sensor have been multiplied by six to allow for the data from the two sensors to be on the same scale. Thus, the signals measured with the bridge sensor are six times the signals measured with the cross sensor. From the figure it is seen that the data measured with the cross sensor fluctuate more than the data measured with the bridge sensor, indicating that the signal-to-noise ratio is highest for the bridge sensor. It is also seen that the signal amplitudes increase as the bias current is increased. The shapes of the curves obtained from the bridge and cross sensors appear very similar. The solid lines represent the fits of the Cole–Cole model to the measurements and from these fits the Brownian relaxation frequencies are extracted along with the α value.

In Table 5.3 the average values of f_B and α for sweeps 5–8 are listed for both the bridge and cross sensors. It is seen that the Brownian relaxation frequency extracted from measurements with the bridge sensor is near 6.1 kHz and is not changing significantly with the current. The Brownian relaxation frequencies obtained from the cross are not as stable, but fluctuate around 6 kHz, which is close to the value obtained with the bridge sensor. The α values obtained with

Fig. 5.5: In-phase (top) and out-of-phase (bottom) second harmonic signals plotted vs. bias current frequency for measurements with bridge and cross sensors. The data from the cross sensor have been multiplied by six. Lines are Cole–Cole fits to the data. The figure is from Paper III.

Table 5.3: Average Brownian relaxation frequencies and α-parameters obtained from Cole–Cole fits to the frequency sweep number 5–8 for bridge and cross sensors. The numbers in parentheses indicate the standard deviations obtained from the four measurements. This table is from Paper III.

	f_{B} [kHz]		α	
I_{AC} [mA]	Bridge	Cross	Bridge	Cross
12.4	6.0(1)	6.5(9)	0.068(6)	0.16(6)
18.6	6.05(6)	5.3(3)	0.05(2)	0.04(2)
24.8	6.097(6)	6.1(3)	0.063(6)	0.04(3)

Fig. 5.6: In-phase second harmonic signal measured at $f_{\mathrm{ref}} = 4667$ Hz vs. time. The figure is from Paper III.

the two different sensors are not significantly different when neglecting the values obtained at the lowest current, where the signal-to-noise ratios are lowest.

The Brownian relaxation frequency of 6.1 kHz corresponds to a hydrodynamic diameter of 42.5 nm, which is closer to the nominal diameter of 40 nm than what was achieved in the previous section for the 250 nm beads. From Fig. 5.5 it is also seen that the Cole–Cole is fitted much better to the measurements, which indicate that these 40 nm beads behave more like predicted by theory than the 250 nm beads. From the estimation of forces acting on beads in Section 2.9 it was also found that thermal fluctuation would be the dominating effect for such small beads. Thus they are believed to be more freely suspended than the 250 nm beads that most likely lie at the bottom of the fluid system.
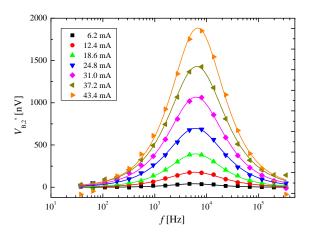
The in-phase signal of the reference points have been plotted vs. time in Fig. 5.6. Here, it is seen that the time evolution of the signals for both the bridge and cross sensors are identical. It is seen that the signals are increasing during the fourth sweep and are stable for the following four sweeps. This also supports the assumption that sedimentation can be neglected for the 40 nm beads and diffusion is the dominating effect. The figure also shows that all the signals

return to zero after washing. This shows that it is possible to wash all the beads away, which allows for reusing the sensors.

Based on these results it is clear that the planar Hall effect bridge sensors are better for measuring Brownian relaxation than the cross sensors. The signals of the bridge sensor turned out to be six times that of the cross sensor, which is more than twice of the 2.4 ratio, which was predicted from the sensitivities. The difference is believed to be due to demagnetization effects, which decrease the low-field sensitivity of the bridge, and the assumption that the current through the cross sensor is evenly distributed across the width w. In reality some of the current extends into the voltage arms. The difference could also be due to γ_1 not being exactly the same for the bridge and cross sensors as assumed.

Varying bias current

In addition to comparing bridge and cross sensors, the effect of changing the bias current is also investigated. In Fig. 5.5 and Fig. 5.6 measurements performed with three different currents are shown. In Fig. 5.7 and Fig. 5.8 measurements with additional four current amplitudes are shown, but only for the bridge sensor.
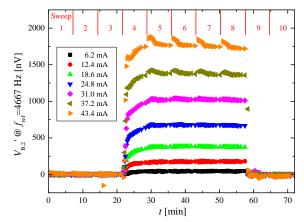
Fig. 5.7: In-phase second harmonic signal vs. frequency for varying bias current amplitudes. Lines are Cole–Cole fits to the data.

Fig. 5.8: In-phase part of the reference points measured at $f = 4667$ Hz vs. time for varying bias current amplitude.

From these figures it is seen that the signal increases with the current squared. From Fig. 5.7 it is seen that the peak shifts slightly towards higher frequencies as the bias current is increased. This is also confirmed by Table 5.4, where the Brownian relaxation frequencies and values of α averaged over sweeps 5–8 are listed. From this table it is seen that the Brownian relaxation frequency increases from 6.1 kHz for $I_{AC} = 24.8$ mA to 6.7 kHz for $I_{AC} = 43.4$ mA. By assuming that this increase is due to a temperature rise caused by the power generated from the current through the sensor, it corresponds to a temperature increase of 3.5°C. It is also seen that the value of α is constant near 0.06 except for the highest and lowest current amplitudes. Thus, the polydispersity of the sample does not depend on the bias current amplitude.

Figure 5.8 shows that the signals are flat after the fourth sweep for the four lowest currents, but become slightly bumpy for the three highest currents. The reason for these bumps are

Table 5.4: Average Brownian relaxation frequencies obtained from Cole–Cole fits to the frequency sweeps number 5–8. The numbers in parentheses indicate the standard deviations obtained from the four measurements.
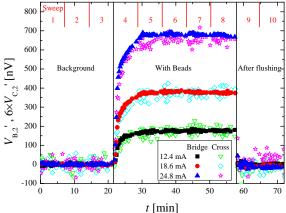
I_{AC} [mA]	f_B [kHz]	α
6.2	5.7(1)	0.03(5)
12.4	6.0(1)	0.07(1)
18.6	6.05(6)	0.06(2)
24.8	6.097(6)	0.06(1)
31.0	6.28(3)	0.06(1)
37.2	6.49(2)	0.06(1)
43.4	6.69(2)	0.03(1)

unknown but they clearly increase with bias current amplitude and are largest for the reference points measured in the beginning of each sweep, which are the points measured after the high frequency points in the frequency sweep. This indicates that the measurements at high bias current frequency and amplitude cause a change of unknown reason to samples.

Based on the above, it is concluded that the bead signal increases with current amplitude squared as expected and increasing the current amplitude results in an increased signal-to-noise ratio. Thus, the current amplitude should be as large as possible. However, increasing the bias current amplitude to above 24.8 mA results in a strange behavior of the signal that cannot be explained. To avoid this effect, the applied bias current amplitude will not exceed 21 mA in all of the following experiments.

5.3   AC susceptibility measurements vs. concentration of 40 nm beads

In this section it is investigated how the AC susceptibility measurements depend on the concentration of beads. The lowest bead concentration necessary for reliably determining the Brownian relaxation frequency is estimated from these measurements. The time evolution of the in-phase signal for varying bead concentration is also investigated as well as the lowest detectable bead concentration. The results presented here have been published in Paper IV.

5.3.1   Experimental

As in the previous section, a series of frequency sweeps were performed for each bead concentration injected into the fluidic channel. Compared to the previous study one of the reference sweeps prior to injection was omitted such that the beads were injected at the beginning of the third sweep, left stagnant during sweeps four to seven and washed out after the seventh sweep. The remaining experimental settings are summarized in Table 5.5, for further details refer to Paper IV.
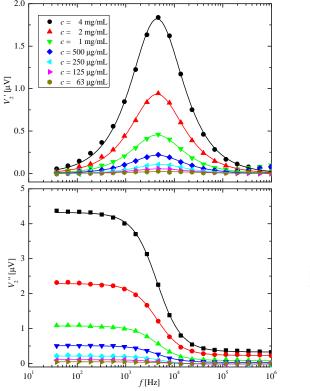
Table 5.5:   Experimental settings for the study of AC susceptibility measurements vs. bead concentration.

Wafer Name	208
Sensor types	Bridge $l \times w = 280\mu m \times 20\mu m$
low-field sensitivity	$S_0 = -531$ V/(TA)
Lock-in	HF2LI
Reference points	Yes, $f_{ref} = 4667$ Hz
Current amplitude	21 mA
Channel height	1 mm
Flow rates	In: 30 μL/min, Out: 800 μL/min
Sample volume	30 μL
Bead type	40 nm ON
Bead Concentration	0.016–4 mg/mL
Temperature	25°C

5.3.2   Results and discussion

In Fig. 5.9 the in-phase (top) and out-of-phase (bottom) second harmonic sensor signals are plotted vs. frequency for seven different bead concentrations ranging from 63 µg/mL to 4 mg/mL. Measurements for lower concentrations cannot be distinguished on this scale and have been omitted. The data shown are all from the seventh sweep, which is immediately before washing the beads away and all the bead suspensions are in a steady state. The solid lines are fits of the Cole–Cole model to the data from which the Brownian relaxation frequencies are obtained. The shapes appear to be independent of the bead concentration, whereas the amplitude of the signals are increasing with the bead concentration.
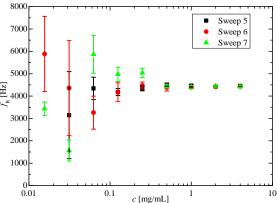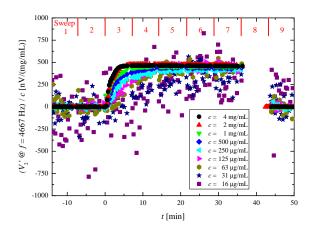
Fig. 5.9: In-phase (top) and out-of-phase (bottom) second harmonic signal vs. frequency for 7 different bead concentration of 40 nm beads. Lines are Cole–Cole fit to the measurements. The figure is from Paper IV.

Fig. 5.10: Brownian relaxation frequencies extracted from sweep 5 to 7 plotted vs. bead concentration. The error bars are standard deviations obtained from least squares curve fits. The figure is from Paper IV.

The Brownian relaxation frequencies obtained from Cole–Cole fitting have been plotted for sweeps 5–7 vs. bead concentration in Fig. 5.10. The error bars correspond to the standard deviations obtained from least squares fitting. It is seen that as the bead concentration increases the extracted Brownian relaxation frequencies narrow in on a value of 4.4 kHz, and the errors decrease. The mean Brownian relaxation frequency is independent of bead concentration except for the two lowest concentrations, where the signal-to-noise is too low for the Cole–Cole model

to be fitted reliably. For $c \geq 0.5$ mg/mL the mean Brownian relaxation frequency is found to 4.4(1) kHz, which corresponds to a hydrodynamic diameter of 47(1) nm.

The reference points normalized with bead concentration are plotted vs. time in Fig. 5.11. The signal scales linearly with the bead concentration. However, it is seen that the signal reaches the steady state level faster for higher bead concentrations. This means that the signal from the samples with low bead concentration will reach a steady state after a longer time, which is also the reason why Brownian relaxation frequencies from sweep four is not plotted in fig. 5.10. The origin of this effect is not known but it could be because of hydrodynamic interactions between beads [81] or electrostatic repulsion of beads due to their surface charge.
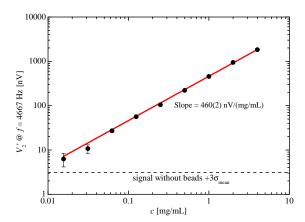
Fig. 5.11: In-phase second harmonic signal measured at $f_{ref} = 4667$ Hz normalized with bead concentration vs. time after injection. The figure is from Paper IV.

Fig. 5.12: Average of the in-phase part of the reference points measured during the seventh sweep. The error bars are three standard deviations of the mean. The dashed line corresponds to three standard deviations of the mean for a measurement without beads. The figure is from Paper IV.

In Fig. 5.12 the averages of the reference points measured during sweep seven are plotted vs. bead concentration. The error bars are three standard deviations of the mean. It is seen that the in-phase signal at $f_{ref} = 4667$ Hz depends linearly on the bead concentration with a slope of 460(2) nV/(mg/mL). It is also seen that bead concentrations down to 16 μg/mL are significantly different from no beads. Thus, the presence of beads at such low concentrations can be detected even though no meaningful Brownian relaxation frequency could be extracted. The particle mass concentration of 16 μg/mL corresponds to a molar concentration of 0.2 nM, which indicates that with the present sensors and bead types, it cannot be expected to reach sensitivities towards analytes much lower than 0.2 nM if each analyte only binds to a single bead. However, increasing the bead diameter will result in a lower molar concentration for the same amount of magnetic material, which is discussed further in Section 5.4, where different bead sizes are investigated.

From the results presented above, it is concluded that the signal from magnetic beads measured with a planar Hall effect bridge sensor scales linearly with the bead concentration. The results also show that the Brownian relaxation frequency does not appear to depend on the bead concentration. However, as the bead concentration is decreased more uncertainty is associated

with the extracted Brownian relaxation frequency. The measurements also show that meaningful Brownian relaxation frequency can be extracted from measurements on samples with a bead concentration as low as 63 μg/mL. And further that the presence of beads can be detected for samples with bead concentrations down to 16 μg/mL. The measurement series also show that the time for reaching a steady signal depends on the bead concentration. Hence, when two measurements are to be compared, it must be ensured that both signals have reached a steady state.

5.4 AC susceptibility measurements of different bead sizes

In this section, AC susceptibility measurements are performed on 6 different bead diameters in the range from 10 nm to 250 nm to investigate if the planar Hall effect bridge sensor is capable of determining the hydrodynamic diameter in this range. The time evolution of the signal is also examined by recording reference points at a frequency near the expected Brownian relaxation frequency. Furthermore, signals per bead concentration are calculated in order to evaluate which of the investigated bead types that is the most promising to use for biosensing. The results presented in this section is a summary of Paper V, which has been submitted to Journal of Applied Physics.

5.4.1 Experimental

To be able to measure as wide a frequency range as possible, both the SR830 and the HF2LI lock-in amplifiers have been used for the measurements. The channel height has been reduced from 1 mm to 0.1 mm in order to reduce the sedimentation time of the larger beads. Other settings are summarized in Table 5.6 and further details are described in Paper V.

Table 5.6: Experimental settings for study of AC susceptibility measurements vs. bead size.

Wafer Name	208
Sensor types	Bridge $l \times w = 280 \mu m \times 20 \mu m$
low-field sensitivity	$S_0 = -581$ V/(TA)
Lock-in	SR830 & HF2LI
Reference points	Yes
Current amplitude	20 mA
Channel height	0.1 mm
Flow rates	In: 13.3 μL/min, Out: 300 μL/min
Sample volume	30 μL
Bead type	10, 25, 40 nm ON
	80, 130, 250 nm MM
Bead Concentration	1 mg/mL
Temperature	25°C

5.4.2 Results and discussion

Measurements performed with both the SR830 and HF2LI lock-in amplifiers for two samples containing 40 nm and 80 nm beads are compared in Fig. 5.13. It is seen that the total frequency span when combining the two lock-in amplifiers is from 0.67 Hz to 5 MHz, which is almost 7 orders of magnitude. It is also possible to measure at even lower frequencies, but the measurement time increases and therefore measurements are generally not performed at frequencies below 1 Hz. At frequencies above 1 MHz it is seen that the out-of-phase signals are not completely constant. This is caused by the instrumental phase shift being almost $\pi/2$ at 5 MHz and therefore very difficult to correct for as a small variation in the temperature may influence the measurement of the raw signals. Figure 5.13 also shows that the fits to the measurements of the 80 nm beads are slightly different for the two lock-in amplifiers. This is because of the in-phase signal at low frequencies that does not decrease to zero, possibly due to the magnetostatic

force from the sensor stack making some of the beads less free to rotate and therefore behaving hydrodynamically larger.
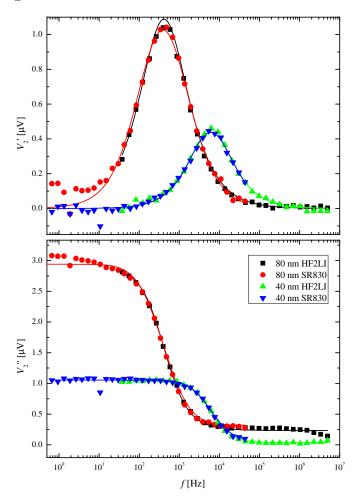
Fig. 5.13: In-phase (top) and out-of-phase (bottom) second harmonic sensor signal vs. current frequency. Measurement performed with both the SR830 lock-in amplifier and the HF2LI lock-in amplifier are compared for samples containing 40 nm and 80 nm beads. The solid lines are fits of the Cole–Cole model to the data.

In Fig. 5.14 the reference points are plotted vs. time for all six bead diameters. The three small bead types (10, 25 and 40 nm) are left in the fluidic channel for about 60 min, whereas the three large bead types (80, 130 and 250 nm) are left for about 240 min. The gaps in the graph for 130 and 250 nm beads are due to the measurement equipment stopping unexpectedly and having to be restarted. It is seen that the obtained signals increase with the bead diameter except for the 130 nm beads, which only gives a signal of the same order as the 40 nm beads.

The time evolution of the signals depends on the bead diameter. The signal of the 10 nm beads increases rapidly immediately after bead-injection followed by a slight increase for 20 min. The signal is then stable until washing. The 25 nm and 40 nm beads also increase rapidly immediately after injection, but a peak appears in the signal followed by a decay of the signal towards a stable level reached after 30 min. The 80 nm, 130 nm and 250 nm beads can all be
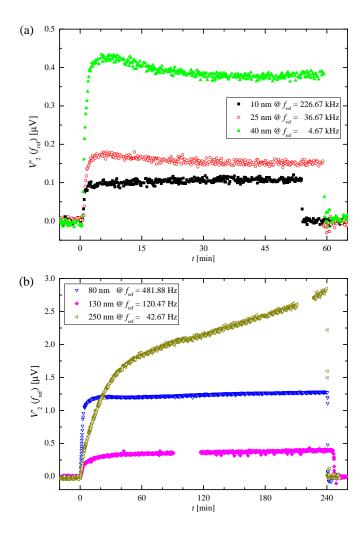
Fig. 5.14: In-phase part of the reference points vs. time for six different bead sizes. Data from 10 nm, 25 nm and 40 nm are plotted in (a), and data for 80 nm, 130 nm, 250 nm plotted in (b). Note that the time scales in (a) and (b) are not identical. The figure is from Paper V.

divided into two regions; first a rapid increase followed by a linear increase. The times at which these transitions occur are after 20 min, 45 min and 60 min for the 80 nm, 130 nm and 250 nm beads, respectively. The slopes of the linear parts are very different for the three bead types. The slope is clearly largest for the 250 nm beads; for the 80 nm and 130 nm the slopes are small. The reason for the linear increase of the signal is most likely due to sedimentation, but can also be due to beads getting trapped near the sensor by magnetostatic forces.

From the reference measurements prior to injection of beads, the standard deviations σ_{NoBeads} are calculated and listed in Table 5.7. These values describe the reproducibility of measurements performed at these frequencies. It is seen that with the HF2LI the standard deviations are around 5.1–5.6 nV, while for the SR830 lock-in amplifier the standard deviation increases from 4.0 nV at $f_{\text{ref}} = 481.88$ Hz to 10.9 nV at $f_{\text{ref}} = 42.67$ Hz. These values will be used below to estimate

Table 5.7: Standard deviation σ_{NoBeads} of baseline in-phase sensor signal at $f = f_{\text{ref}}$ for the six values of f_{ref} used for the different bead types. The table is from Paper V.

Lock-in	f_{ref}	σ_{NoBeads}
HF2LI	226.67 kHz	5.1 nV
HF2LI	36.67 kHz	5.6 nV
HF2LI	4.67 kHz	5.6 nV
SR830	481.88 Hz	4.0 nV
SR830	120.47 Hz	7.6 nV
SR830	42.67 Hz	10.9 nV

how low bead concentrations can be resolved.

Since the signals are not stable over time the data from the frequency sweeps have been normalized with the reference points. This is done by dividing the measurements at each frequency with the reference points measured immediately after. To get the scale back the normalized data is multiplied by the mean of all the reference points for the given sweep. This is shown in Fig. 5.15 for the frequency sweeps measured after 20 min. In Fig. 5.16 the same data is plotted, but where both the in-phase and out-of-phase signals have been normalized with their maximum value, respectively. This has been done to easily compare the shapes of the curves and examine how well the Cole–Cole fits match the measurements.

From the normalized data in Fig. 5.16 it is seen that all the Cole–Cole fits match the data well, except at frequencies above 1 MHz. As mentioned, the phase shifts of the setup are almost $\pi/2$ at these high frequencies, which makes it impossible to correct for. The problem is believed to be due to limitation in the electronic equipment and not the sensor itself. In Table 5.8 the fitting parameters from the Cole–Cole fits are listed. It is seen that the extracted hydrodynamic diameter increases with the nominal diameter, and that the hydrodynamic diameter in general is estimated above the nominal diameter. This makes sense as the nominal diameters are determined from transmission electron microscopy. However, the measurements on the 25 nm beads result in a hydrodynamic diameter lower than the nominal, which is attributed to batch to batch variations in the fabrication of the beads. On the other hand, the hydrodynamic diameter of 349 nm obtained for the nominally 250 nm beads is too large to be explained by batch to batch variation or by differences in measurement techniques alone. This overestimation is hypothesized to be due to beads being trapped by magnetostatic forces and therefore not as free to rotate as if they had been in suspension.

In Table 5.8 the molar concentrations c corresponding to 1 mg/mL for each bead type is listed. The peak signal per concentration has been calculated for each bead type by

$$V'_{2,\text{peak}}/c = -\text{Im}\left[(V_0 - V_\infty)/(1 + \mathrm{i}^{1-\alpha})\right]/c \tag{5.2}$$

and are also listed in Table 5.8. From this it is seen that the signal per bead concentration increases with the nominal bead diameter and ranges from 0.1 nV/nM for 10 nm bead to 17.9 μV/nM for 250 nm beads. Since the 250 nm beads sediment significantly and have a low Brownian relaxation frequency, they are not appropriate for biosensing where a constant background signal from free beads and the possibility to resolve the Brownian relaxation peak
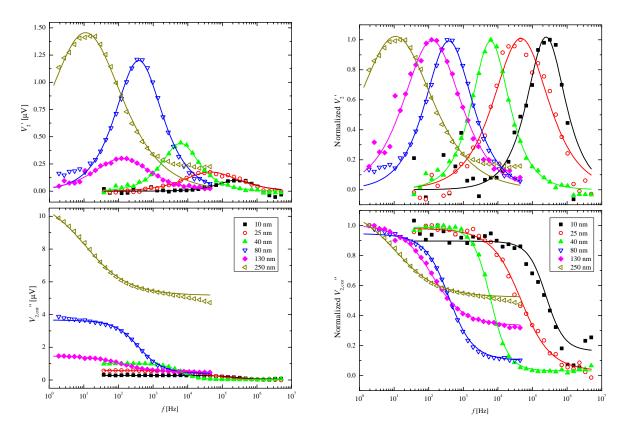
Fig. 5.15: In-phase (top) and out-of-phase (bottom) second harmonic signal vs. frequency for six different bead sizes measure 20 min after injection. Lines are Cole–Cole fits to the data. The figure is from Paper V.

Fig. 5.16: Data from Fig. 5.15 normalized with maximum values. The figure is from Paper V.

of bound beads are preferred. Instead, the 80 nm beads are the preferred choice for detection of low concentrations due to their high signal per bead concentration ratio and the very limited sedimentation. The detection range will be limited upwards by the total bead concentration, which for 80 nm beads is 2 nM, and limited downward by the lowest concentration detectable, which is estimated by σ_{NoBeads} from Table 5.7 divided by $V'_{2,\text{peak}}/c$, which results in 6 pM for the 80 nm beads. If it is necessary to quantify larger concentrations than 2 nM, either a larger initial bead concentration or smaller beads should be used. However, this will also increase the lower limit of detection.

From the measurements shown in this section it is concluded that AC susceptibility measurements can be performed with planar Hall effect bridge sensors in the frequency range from 0.67 Hz to $\sim$ 1 MHz. This wide frequency span of possible frequencies allow for measuring Brownian relaxation of beads with nominal diameters of 10 nm to 250 nm and extraction of the corresponding hydrodynamic diameters. From measurements at frequencies near the Brownian relaxation frequency it was shown that the beads from Ocean Nanotech (10–40 nm) reach a steady state within 30 min. The signal obtained from the 250 nm beads keeps increasing and the signal from the 80 nm and 130 nm beads only increase slightly. Due to the 250 nm beads

Table 5.8: Values of D_h, α, $V_0 - V_\infty$ and V_∞ obtained from Cole–Cole fits to the frequency sweeps initiated 20 min after injection of the bead suspensions. The numbers in parenthesis after the fitting parameter are 95 % uncertainties. The last two columns list the molar concentration c of each bead type in nM and the peak sensor signal normalized with the bead molar concentration $V'_{2,\mathrm{peak}}/c$. This table is from Paper V

D_nom	Producer	D_h	α	$V_0 - V_\infty$	V_∞	c	$V'_{2,\mathrm{peak}}/c$
[nm]		[nm]		[µV]	[µV]	[nM]	[nV/nM]
10	Ocean Nanotech	12.4(3)	0.08(5)	0.23(2)	0.05(18)	860	0.1
25	Ocean Nanotech	21.6(4)	0.28(2)	0.56(2)	0.02(17)	58	3.0
40	Ocean Nanotech	42.4(2)	0.06(1)	0.97(1)	0.03(15)	14	31.4
80	Micromod	107.0(9)	0.20(1)	3.29(4)	0.4(7)	2.0	602
130	Micromod	155(2)	0.31(1)	0.99(2)	0.5(2)	0.48	622
250	Micromod	349(3)	0.43(1)	6.01(7)	5.2(5)	0.08	17.9×10^3

not reaching a steady state, it is concluded that they are inappropriate for biosensing using a planar Hall effect bridge sensor. Rather, it is estimated that the 80 nm beads are best suited for biosensing.

5.5 Comparison of planar Hall effect sensor measurements and DynoMag measurements

In this section, AC susceptibility measurements performed with planar Hall effect sensors and a commercial AC susceptometer called a DynoMag are compared. Only a limited number of samples have been measured in both systems. These samples are: 50 nm BNF-starch beads with NH2 coating, which also are published in Paper III; 80 nm BNF-starch beads with streptavidin coating, which are used in Chapter 7; and 250 nm Nanomag-D beads with plain surface, which are published in Paper II. The DynoMag measurements on the 50 nm and 80 nm beads were performed at Uppsala University, while the measurement on the 250 nm beads were performed at Imego.

The measurements on 50 nm and 80 nm beads were performed with a planar Hall effect bridge sensor and are plotted in Fig. 5.17 along with the corresponding DynoMag measurements. It is seen that the dynamic responses for both measurement techniques are very similar for both bead types. The largest difference is that the out-of-phase signal does not become constant at low frequencies, which is the case for the in-phase magnetic susceptibility of the DynoMag measurements. The reason for this difference is believed to be due to the difference in how the two setups measure. The DynoMag is able to measure on the entire sample volume, whereas, as mentioned in Section 2.7, around 85 % of the signal are obtained within 26 µm of the planar Hall effect sensors [71]. This means that the DynoMag measures on relatively more freely floating beads, whereas the planar Hall effect sensors primarily obtain the signal from beads on and very near the sensor surface. As already discussed in Section 5.1 beads on the surface might not relax as freely as if in suspension. In addition, the magnetostatic force from the sensor stack possibly enhances this effect.

The 250 nm beads have been measured with a cross planar Hall effect sensor and the data is
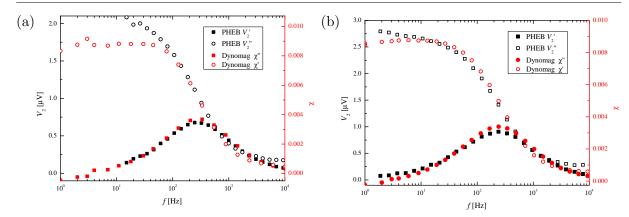
Fig. 5.17: Comparison of AC susceptibility measurement performed with planar Hall effect bridge sensors and DynoMag for beads with nominal diameters of (a) 50 nm and (b) 80 nm.

compared to DynoMag measurements in Fig. 5.18. The differences between the two techniques are much more pronounced. Still the out-of-phase signal shows no sign of becoming stable at low frequencies, but also the peak in the in-phase signal has shifted towards lower frequency and flattens out more. Thus, the measurements indicate that the beads, when measured with the planar Hall effect sensor are hydrodynamically larger and more polydisperse. Again this is believed to due to the beads lying on the sensors surface and likely being trapped by magnetostatic forces. However, the planar Hall effect measurement shown here was performed after 16 hours of sedimentation and all beads were surely at the sensor surface. In the previous section a measurement on a different batch of 250 nm beads was performed after only 20 min of sedimentation with a planar Hall effect bridge, which resulted in a more similar dynamic signal as obtained with the DynoMag.
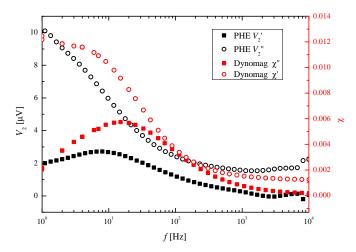

Fig. 5.18: Comparison of AC susceptibility measurement performed with planar Hall effect cross sensor and DynoMag for beads with a nominal diameter of 250 nm.

That magnetostatic forces affect the beads is shown in Fig. 5.19, where a suspension of

250 nm beads are injected into a fluidic channel containing a planar Hall effect bridge sensor. The images are taken at 0, 5, 15 and 60 min after injection of the beads. It is seen that the beads tend to pile up at the edges of the magnetic stack. For all beads smaller than 250 nm, the piling up of beads on the stack edges is not observed. However, it is not to be ruled out that the magnetostatic force might also influence the smaller beads slightly. This corresponds well with the estimates of the magnetostatic force in Section 2.9.4.2 predicting that magnetostatic forces would only dominate the Brownian motion for 130 nm and 250 nm beads. Thus, the magnetostatic force changes the dynamics when measuring on 250 nm beads with the planar Hall effect sensors. Dalslet, Donolato, and Hansen [82] have shown that it is possible to minimize the magnetostatic force by placing an identical magnetic stack exchange biased in the opposite direction below the sensor stack. However, obtaining good insulation between the two stacks was not easy and the resulting sensors were not as sensitive as sensors with only one stack. Therefore, sensors of this type of stack were not pursued in this thesis work.
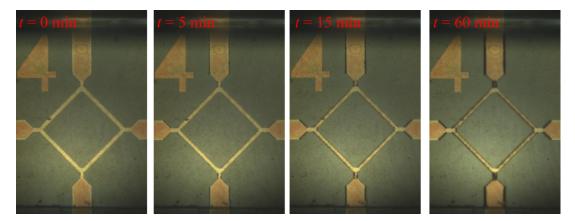
Fig. 5.19: Bead distribution for 250 nm beads near a planar Hall effect sensor as a function of time after injection.

By comparing AC susceptibility measurements performed with planar Hall effect sensors to measurements performed with a DynoMag, it is concluded that the planar Hall effect sensors and DynoMag give similar results for frequencies above 10 Hz. At frequencies below 10 Hz the signals from the planar Hall effect sensors become too large, which implies that some beads behave like they are hydrodynamically larger than they really are. This is believed to be because the beads on the planar Hall effect sensors are not as freely suspended as those measured in the DynoMag. The measurements also show that the planar Hall effect sensor is not well suited for measurements on the 250 nm beads, but works for the 50 nm and 80 nm beads.

Chapter 6

Brownian relaxation measurements in the time domain

In this chapter results of Brownian relaxation measurements in the time domain will be presented. Brownian relaxation measurements performed in the time domain are potentially interesting because they can be performed considerably faster than the frequency sweeps measured in the previous chapter. First, some of initial measurements are presented, where the current amplitude is varied to investigate if the measurements behave as predicted from theory. Then, the effect of activating a low-pass filter at the voltage inputs is evaluated. Followed by Brownian relaxation measurements of samples containing different bead sizes measured in both the time domain and frequency domain for comparison. The measurements on samples with different bead are part of the draft appended as Paper VI.

6.1 Varying current amplitude

In this section the bias current will be varied in order to determine how V_{ave} and V_{diff} depend on the bias current. The theoretical signals were given by Eq. (2.47) and Eq. (2.48), which are repeated here

$$V_{\text{ave}} = S_0 I_0^2 (\gamma_0 + \gamma_{1t} M(t))$$
$$V_{\text{diff}} = S_0 I_0 H_{y,\text{ext}} + R_{\text{offset}} I_0.$$

From these equations it is seen that V_{ave} is expected to scale with the bias current amplitude squared, while V_{diff} , in theory, scales with the bias current amplitude. It is also seen that the signal from magnetic beads should only appear in V_{ave} and not in V_{diff}, which on the other hand is sensitive to external fields.

6.1.1 Experimental

In order to compare effects of γ_0 and γ_{1t} measurements both with and without beads were performed. The 80 nm beads coated with streptavidin were used. As in the frequency domain, measurements were first performed without beads, then the beads were injected and the sample was left stagnant for 60 min for the signal to stabilize before measurements were performed on beads. After waiting additionally 60 min, the measurements were repeated and the beads were then washed away and the measurements without beads were repeated. Other settings are summarized in Table 6.1 and further details can be found in Paper VI.

Table 6.1: Experimental settings for study of time domain measurements vs. current amplitude.

Wafer Name	208
Sensor types	Bridge $l \times w = 280\mu m \times 20\mu m$
low-field sensitivity	$S_0 = -591$ V/(TA)
Current amplitude	3–20 mA
Channel height	0.1 mm
Flow rates	In: 13.3 µL/min, Out: 300 µL/min
Sample volume	30 µL
Bead type	80 nm streptavidin MM
Bead Concentration	1 mg/mL
Temperature	25°C

6.1.2 Results and discussion

In Fig. 6.1, V_{ave} and V_{diff} with and without beads are plotted vs. time, respectively. Data are shown for current amplitudes of $I_0 = 5, 10, 15$ and 20 mA. From this it is seen that V_{ave} increases nonlinearly with the current and that the decay due to the beads becomes more clear with increasing current amplitude. V_{diff} increases linearly with the current amplitude and no clear change is seen due to the beads.
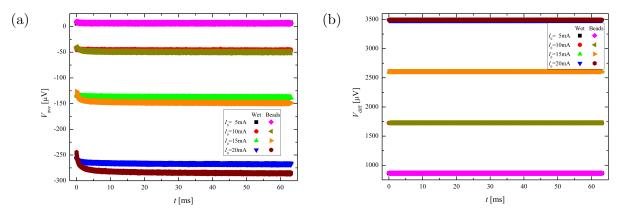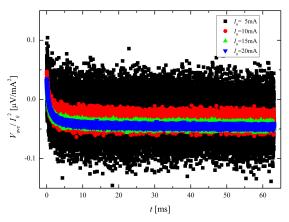
Fig. 6.1: (a) V_{ave} and (b) V_{diff} with and without 80 nm beads vs. time for four different bias current amplitudes measured with a bridge sensor.

In Fig. 6.2 V_{ave} without beads have been subtracted from V_{ave} with beads from Fig. 6.1 (a) and normalized with the current amplitude squared. It is seen that the signals coincide and that the signal-to-noise ratio increases with the current amplitude. It is also seen that the decay from the beads appears independent of current amplitude. The similar plot for V_{diff} is shown in Fig. 6.3, where the data are normalized with the current amplitude. Here is it also seen that the data for the different current amplitudes coincide and is close to 0, and that no time dependence is observed in the signal as expected.

That V_{ave} scales with the current squared can be seen Fig. 6.4. In Fig. 6.4 (a) the average of
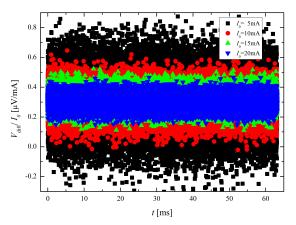
Fig. 6.2: V_{ave} measured with 80 nm beads corrected for offset from measurement without beads and normalized with current squared.

Fig. 6.3: V_{diff} measured with 80 nm beads corrected for offset from measurement without beads and normalized with current.

the last 30 ms of the raw V_{ave} is plotted vs. current squared, and in Fig. 6.4 (b) the mean of the two measurements without beads (wet) have been subtracted from all four measurement series. Fig. 6.4 (a) shows that the offset of V_{ave} due to γ_0 also increases with the current amplitude squared and that this offset is 10 times larger than the signal due to the beads. From Fig. 6.4 (b) it is seen that the measurements before and after beads coincide within the noise. Thus, V_{ave} returns to its initial value after the beads are washed away.
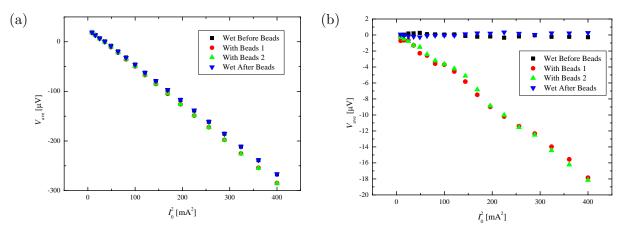
Fig. 6.4: (a) Average of last 30 ms of V_{ave} from Fig. 6.2 vs. current amplitude squared. (b) Plot (a) corrected for offset due to γ_0 measured without beads.

Similar plots for V_{diff} are shown in Fig. 6.5. The plot shows that V_{diff} depends linearly on the current amplitude as predicted from Eq. (2.48). The reason for V_{diff} not to return to the initial values and that the shapes of the wet measurements before and after exposure to beads are different is most likely due to small changes in a external magnetic field. It is seen that the change is around 10 μV for 20 mA, and since the sensitivity of the sensor is $S_0/\mu_0 = -591$ V/(T A) it corresponds to a change in the external field of 0.8 μT or a change in R_{offset} of 0.5 mΩ or perhaps a combination of the two.

(a)

(b)
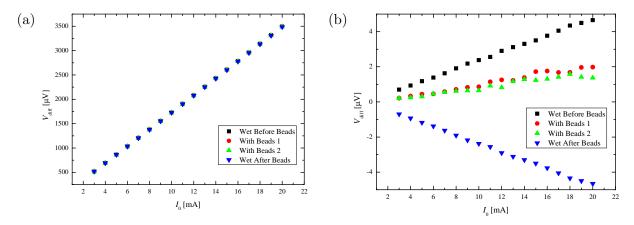
Fig. 6.5: (a) Average of last 30 ms of V_{diff} from Fig. 6.2 vs. current amplitude. (b) Plot (a) corrected for average offset measured without beads.

Curve fitting

As for the Brownian relaxation measurements in the frequency domain the median hydrodynamic diameter can be extracted from the measurements by least squares curve fitting. For the measurements in the time domain Eq. (2.50) is fitted to the data. However, each data set of V_{ave} contains 37500 points, which is too many to perform fast fitting. Instead the data was divided into 500 logarithmically distributed bins and averaged before fitting. The change from time on a linear scale to logarithmic scale also results in the first point being weighted more than the points at equilibrium, which is especially important for fast relaxation times. In Fig. 6.6 the unnormalized data from Fig. 6.2 have been converted to a logarithmic time scale and fitted with Eq. (2.50). It is seen that the first points are more noisy than the last, which is because only few data points are placed in each of the first bins, while many points placed in each of the last.
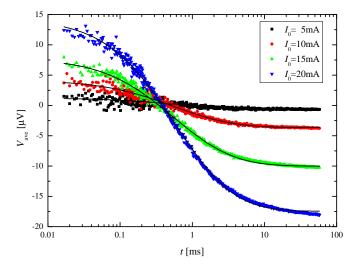
Fig. 6.6: Curve fits to V_{ave} measured on a sample containing 1 mg/mL 80 nm beads with streptavidin. Measurements are shown for current amplitudes of 5, 10, 15 and 20 mA.

The four free fitting parameters of Eq. (2.50) are plotted vs. current amplitude in Fig. 6.7 and Fig. 6.8. The error bars are standard deviations on the parameters found from the least squares curve fits.
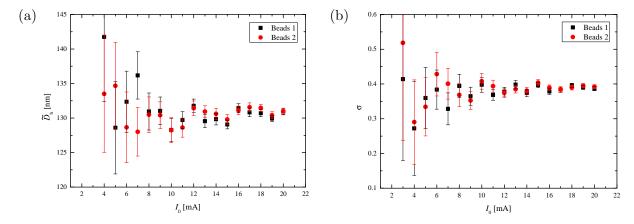
Fig. 6.7: (a) The median hydrodynamic diameter and (b) the standard deviation of the log-normal distribution extracted from curve fits for varying bias current amplitudes.
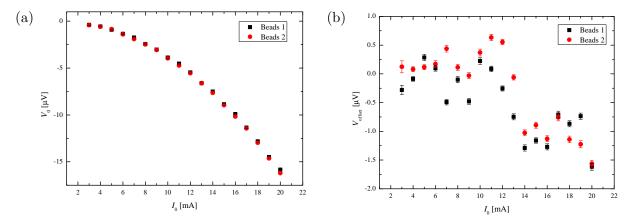
Fig. 6.8: (a) The signal amplitude and (b) the signal offset extracted from curve fits for varying bias current amplitudes.

For the median hydrodynamic diameter and standard deviation it is seen that for low currents the fits produce very uncertain values that scatter around the value obtained at larger currents. It is also seen that the length of the error bar decreases with the current amplitudes, which is because the fitting becomes more robust as the signal-to-noise increases. The average of the median hydrodynamic diameter for $I_0 > 10$ mA is 130 nm, which is much more than the nominal value of 80 nm. Part of this is due to the beads being coated with streptavidin, which makes them hydrodynamically larger. The corresponding average of the log-normal standard deviation is $\sigma = 0.39$. From Fig. 6.7 it is also seen that neither the median hydrodynamic diameter nor the standard deviation change significantly with the current.

In fig. 6.8 (a) the amplitudes of the decays are seen to decrease with the current squared

as expected. The voltage offset plotted in Fig. 6.8 (b) is around 0 for $I_0 < 13$ mA and around -1 μV for $I_0 > 13$ mA. This sudden step is seen for both series of measurements with beads, but cannot be explained. However, it does not seem to influence the determination of the median hydrodynamic diameter or the standard deviation, which are the two most important parameters, as they contain the information of the hydrodynamic bead diameter distribution.

Based on the above measurements in the time domain vs. current amplitude, it is concluded that both V_{ave} and V_{diff} depend on the bias current amplitude as predicted by the theory. The measurements also show that only V_{ave} is influenced by the presence of beads as expected and that V_{ave} returned to its initial value after washing beads away. On the other hand, V_{diff} varies over time, but since the presence of beads is not detected in V_{diff}, this time dependence is not important for bead measurements. Curve fits to the measurements show that the theoretical model describes the Brownian relaxation of beads in the time domain. From the curve fits it is additionally concluded that higher current amplitudes result in a more accurate estimations of the hydrodynamic diameter.

6.2   Low-pass filter

In this short section, the effect of the low-pass filter option of the NI-6281 DAQ is tested. This was done by performing two measurements in the time domain; one with the low-pass filter off and another one with the low-pass filter on at 3 kHz. These measurements were performed with the same experimental settings as in the previous section summarized in Table 6.1.

The measurements without and with the low-pass filter are plotted in 6.9 (a) and (b), respectively. By comparing these two figures it clear that the noise has been reduced by applying the low-pass filter. From least squares curve fit, the median hydrodynamic diameters were found to 122.0(5) nm and 121.8(2) nm without and with the low-pass filter, respectively and the corresponding values of σ were found to 0.31(1) and 0.30(1). From the fits it is seen that the hydrodynamic diameters are not statistically different, while a lower uncertainty obtained from the measurement with the low-pass filter on. For this reason the low-pass filter will be applied at 3 kHz for the remaining time domain measurements.
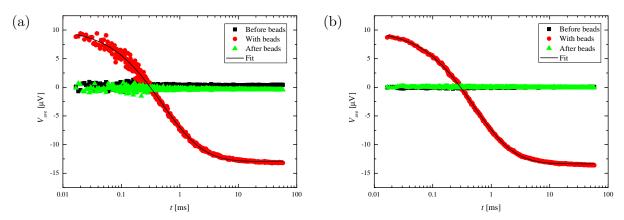

Fig. 6.9: Comparison of bead relaxation recorded in the time domain (a) without and (b) with a low-pass filter at 3 kHz applied.

6.3   Bead sizes

To illustrate the capabilities of the time domain measurement technique, Brownian relaxation measurements were performed for four different bead sizes. For comparison, measurements in the frequency domain were also performed on the same four samples. The results are written into the draft appended as Paper VI.

6.3.1   Experimental

For these measurement the NI-6281 DAQ unit was connected in parallel with the SR830 lock-in amplifier such measurement in the time and frequency domain could be performed on the same samples. For the measurements in the time domain the Keithley 6221 power supply was giving a square wave with an current amplitude of 14.1 mA, while for the frequency domain measurements a sine wave with current amplitude of 20 mA was used. The amplitudes were chosen like this such they have the same root mean square values to eliminate possible changes in temperature due to self-heating.

As mentioned in section 3.4.2 the period of the current square wave was 125 ms and the signal averaged over 192 periods. Since half a period of waiting time was added for every two periods of measurements, the total measurement time was 30 s. The frequency sweeps without reference points, measured for comparison, took 2 min and 21 s. The remaining details are summarized in Table 6.2 and further details can be found in Paper VI.

Table 6.2: Experimental settings for study of time domain measurements vs. bead size.

Wafer Name	208
Sensor types	Bridge $l \times w = 280\mu m \times 20\mu m$
low-field sensitivity	$S_0 = -591$ V/(TA)
Current amplitude DC	14.1 mA
Current amplitude AC	20 mA
Channel height	0.1 mm
Flow rates	In: 13.3 µL/min, Out: 300 µL/min
Sample volume	30 µL
Bead type	40 nm ON, 80, 130 and 250 nm MM
Bead Concentration	1 mg/mL
Temperature	25°C

6.3.2   Results and discussion

In Fig. 6.10 the Brownian relaxation measurements in the time domain are shown for beads with nominal diameters of 40, 80, 130 and 250 nm. The measurements are normalized such that the signal right after flipping of the current is $+1$ and just before flipping is -1. The solid lines represent fits of Eq. (2.50) to the data. It is seen that the relaxation time increases with the nominal diameter as expected. Observing the slopes at $t = 65$ ms it is seen that for the 250 nm bead the slope is nonzero, indicating that measurements should have continued for longer time in order to reach the steady state, that is, where all magnetic moments of the beads are parallel to the self-field. The noise is larger for the 40 nm and 130 nm beads, which is because these beads yield less signal than the 80 nm and 250 nm beads. The 40 nm beads are just on the limit of what can be measured, both in terms of time and signal resolution. The 40 nm beads are fully relaxed after 0.1 ms and since the time resolution of the NI-6281 is only 1.6 µs, the entire relaxation occurs in 62 measurement points. From the noise level after 0.1 ms it can be seen that the change in signal is not considerably greater than the noise level. To be able to measure Brownian relaxation in the time domain of smaller beads would therefore require a faster and more accurate DAQ.

The Brownian relaxation measurements in the frequency domain corresponding to the ones in the time domain are shown in Fig. 6.11 where the in-phase (top) and out-of-phase (bottom) second harmonic signals are plotted vs. frequency. The solid lines represent fits of Eq. (2.63) to the data. The fitting parameters obtained from fits to both the time and frequency domain measurements are listed in Table 6.3.
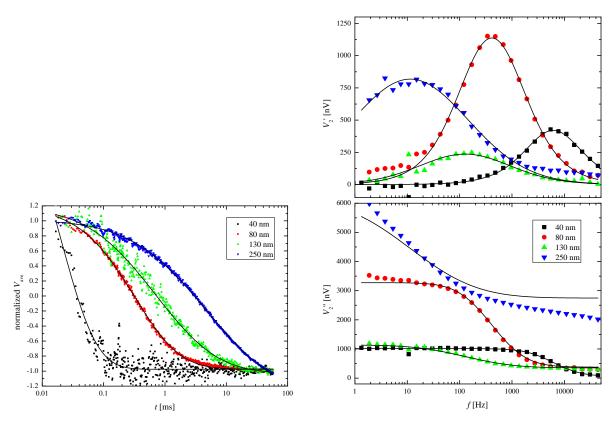
Fig. 6.10: Normalized V_{ave} vs. time after flipping of magnetic field for beads with diameters of 40, 80, 130 and 250 nm. The solid lines are least squares curve fits to Eq. (2.50).

Fig. 6.11: In-phase (top) and out-of-phase (bottom) second harmonic signal vs. frequency for beads with diameters of 40, 80, 130 and 250 nm. The solid lines are least squares curve fits to Eq. (2.63).

Table 6.3: Parameters obtained from least squares fitting of Eq. (2.50) to the time domain measurements and Eq. (2.63) to the frequency domain measurements for the four different bead sizes. The numbers in parentheses are standard deviations obtained from the least squares curve fits.

D_{nom} [nm]	Time domain				Frequency domain			
	$\tilde{D}_h$ [nm]	σ	V_0 [μV]	V_{offset} [μV]	$\tilde{D}_h$ [nm]	σ	$V_0 - V_\infty$ [μV]	V_∞ [μV]
40	41(2)	0.22(5)	1.8(3)	−0.4(3)	42.5(3)	0.18(2)	0.95(2)	0.1(2)
80	108(1)	0.35(1)	4.81(2)	0.48(2)	107(2)	0.32(2)	3.16(5)	0.4(8)
130	152(2)	0.45(2)	1.36(2)	1.85(1)	159(4)	0.50(2)	0.97(2)	0.5(3)
250	299(4)	0.60(1)	7.68(6)	8.15(5)	350(7)	0.64(2)	5.66(7)	5.5(5)

From Table 6.3 it is seen that the median hydrodynamic diameters and standard deviations obtained from Brownian relaxation measurements performed in the time and frequency domains

are not significantly different, except for the 250 nm beads. The reason for the difference in the hydrodynamic diameter of the 250 nm beads is believed to be because the sampling time in the time domain is too short. Thus, the larger beads of the ensemble will not have enough time to align their magnetic moments with the field, hence contribute less to the signal than the smaller beads. Therefor the hydrodynamic diameter is underestimated in the time domain.

Based on the presented measurements it is concluded that the time domain measurements can be utilized to determine the hydrodynamic diameter of beads ranging in nominal diameters from 40 nm to 250 nm and the obtained values roughly correspond to what is measured in the frequency domain. The measurement time in the frequency domain was 2 min and 21 s, while it was only 30 s for the time domain measurements. Thus, the time domain measurements are much faster than the frequency domain measurements and could be even faster by reducing the number of periods used for averaging. However, as will be discussed in more details in the next chapter the time domain might not be as accurate as the frequency measurements.

Chapter 7

Volume-based biosensing using planar Hall effect bridge sensors

In the previous two chapters it was demonstrated that planar Hall effect sensors can be used to extract hydrodynamic diameters of beads in both the frequency and time domain. In this chapter, it is investigated how the measurements in both domains change when the magnetic beads are binding to analytes. In the first part of this chapter, the effects of mixing streptavidin coated beads with bBSA are examined in the two domains. In the second part, the binding of beads to DNA coils formed by rolling circle amplification is investigated. The investigation with DNA coils first includes a study of how the size of the DNA coils affects measurements. Then, a brief test of two different hybridization methods is performed. Finally, measurements are performed vs. concentration of DNA coils, for which a study of possible analysis methods are made to determine the best procedure for acquiring the lowest limit of detection and the largest dynamic range for volume-based biosensing using planar Hall effect sensors.

7.1 Small analytes – bBSA

In the following it is demonstrated how the Brownian relaxation of streptavidin coated 80 nm beads changes when bBSA is added. Brownian relaxation measurements are performed in both the time and frequency domains. The main results from this section are included in the draft appended as Paper VI.

A bBSA molecule has a diameter of only 10 nm and therefore the binding of bBSA to the 80 nm beads will not increase the hydrodynamic size considerably. However, each bBSA molecule is able to bind to more than one streptavidin, which allows for the formation of dimers, trimers or even polymers of beads.

7.1.1 Sample preparation

The samples are prepared by mixing 15 μL of bead solution with a concentration of 2 mg/mL with 15 μL of bBSA solution. The bBSA solution before mixing had twice the concentration values as reported below. Both the beads and the bBSA are suspended in MilliQ water with

PBS to keep the pH stable at 7.5. After mixing, the solution was placed in a magnetic field of 45 mT for 10 min to enhance the formation of bead clusters. The solution was then injected onto the planar Hall effect bridge sensor at 13.3 μL/min for 2 min and 15 s. Then, each solution was left for 20 min in the fluidic channel while measuring, before being washed away. The setup and experimental settings were identical to those in described in Section 6.3.1.

7.1.2   Results and discussion

The measurements performed just before washing away the beads are shown in Fig. 7.1 and Fig. 7.2 for measurements in the time and frequency domain, respectively. The solid lines represent the least squares curve fits of Eq. (2.50) and Eq. (2.63), respectively. Measurements are shown for 2.5 nM, 5 nM and 10 nM of bBSA. Furthermore, data from two measurements without bBSA are shown as well as data from measurements without beads.

Fig. 7.1: V_{ave} as function of time for samples contained streptavidin coated beads and varying concentrations of bBSA. This figure is from Paper VI

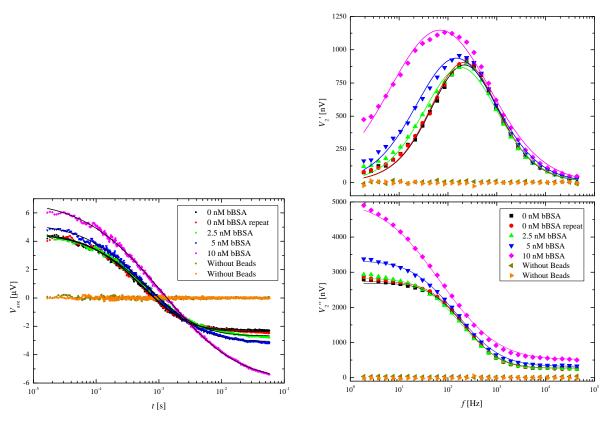**Fig. 7.2:** In-phase (top) and out-of-phase (bottom) second harmonic signal vs. frequency for samples contained streptavidin coated beads and varying concentrations of bBSA. This figure is from Paper VI

From the measurements in the time domain (Fig. 7.1) it is clear that the amplitude of the signal increases with the bBSA concentration. The slope at the end of the measurements (t=62.5 ms) is also increasing with bBSA concentration indicating that not all magnetic moments

had enough time to align themselves with the self-field. Thus, beads with longer relaxation times are present. Similar trends are seen for the measurements in the frequency domain (Fig. 7.2). Here, also the amplitudes of the signals increase with increasing bBSA concentration. The peak in the in-phase data is observed to shift towards lower frequencies, which is also due to longer relaxation times. It is also seen that the fit does not match the measurements of the 10 nM sample very well. This is due to the assumption that the size distribution of the beads is log-normally distributed. This is no longer the case as the sample contains a combination of single beads, and clusters of beads due to the presence of bBSA.

The median hydrodynamic diameters and corresponding logarithmic standard deviations found from both the time and frequency domains are shown in Table 7.1. Here it is seen that the hydrodynamic diameter and logarithmic standard deviation generally increase with the concentration of bBSA for measurements in both time and frequency domain. However, in the time domain the extracted hydrodynamic diameters are not statistically different for bBSA concentrations of 2.5 nM and 5 nM. This indicates that the time domain measurements are not accurate enough at the moment to quantify bBSA concentrations very well. It is also seen that for the sample with 10 nM bBSA, the frequency domain measurement results in a larger hydrodynamic diameter than the time domain measurement. The reason for this could be that the measurement time for the time domain is too short for the largest clusters to align with the field, i.e., the large clusters do not rotate 180° between each flipping of the current direction. Thus, the signal from the large clusters is relatively lower than the signal from the smaller clusters and free beads, as discussed for the 250 nm beads in Section 6.3.1.
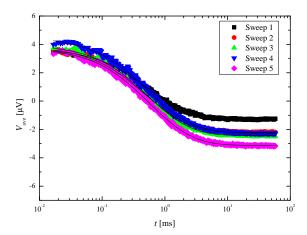
Table 7.1: Parameters obtained from least squares fitting to the measurement in the time and frequency domain for five different bBSA concentrations. The numbers in parentheses are the standard deviations obtained from the least squares curve fits in both the time and frequency domain. This table is from Paper VI

c_{bBSA} [nM]	Time domain		Frequency domain	
	$\tilde{D}_{\text{h}}$ [nm]	σ	$\tilde{D}_{\text{h}}$ [nm]	σ
0	127.1(3)	0.31(1)	129(1)	0.34(1)
0	128.9(4)	0.33(1)	129(1)	0.34(1)
2.5	139.0(4)	0.40(1)	137(2)	0.40(2)
5	138.8(4)	0.43(1)	147(3)	0.47(2)
10	172.7(5)	0.62(1)	190(3)	0.65(2)

Time evolution of signals

Each of the solutions was left in the fluidic system for 20 min before being washed out. In this section, it is shown how the signals evolve over this time period for the samples without bBSA and with 10 nM of bBSA. Time evolution of the signals are shown for both the time and frequency domains.

Measurements on the sample without bBSA are shown in Fig. 7.3 and Fig. 7.4 for time and frequency domain measurements, respectively. From these figures it is seen that the signal amplitudes increase slightly with time. Sweep 1 in Fig. 7.4 differs significantly from the remaining four because the beads were injected during this sweep and therefore not comparable to the other sweeps.
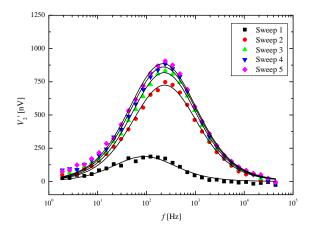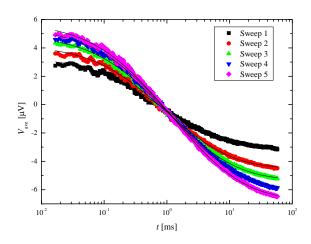
Fig. 7.3: Time evolution of V_{ave} in the time domain for sample without bBSA.

Fig. 7.4: Time evolution of the in-phase signal in the frequency domain for sample without bBSA.

In Fig. 7.5 and Fig. 7.6 the measurements for the sample with 10 nM bBSA are shown. Here, the change in the signals over time is much more pronounced than for the sample without bBSA. It is seen that the amplitudes increase with time for measurements in both domains and the Brownian relaxation peak in the frequency shifts towards lower frequencies. Whether the relaxation time of the time domain measurements also increases cannot be concluded from observing the graphs, but from the fitting parameters it is seen that this is in fact also the case.
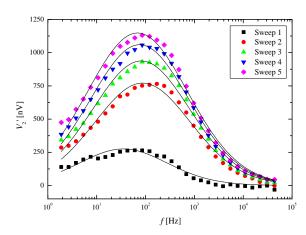
Fig. 7.5: Time evolution of V_{ave} in the time domain for sample containing 10nM of bBSA.

Fig. 7.6: Time evolution of the in-phase signal in the frequency domain for sample containing 10nM of bBSA.

The hydrodynamic diameters obtained from the fits are plotted vs. time for both samples in Fig. 7.7. Here, it is seen that even for the sample without bBSA the hydrodynamic diameter is slightly increasing over time. This is again believed to be due to magnetostatic forces capturing beads at edges of the magnetic stack. The hydrodynamic diameters obtained from the sample with 10 nM of bBSA increase much faster than the sample without bBSA. This is due to the

free beads being at steady state, while the bound beads are sedimenting, which results in the ratio between bound and free beads near the surface increases with time. Thus, the longer time a sample containing bBSA is left in the channel, the more pronounced the effect of the bBSA becomes.
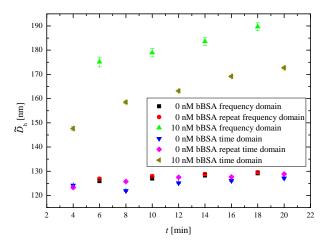
Fig. 7.7: Median hydrodynamic diameter extracted from both time and frequency domain measurement for samples without bBSA and 10 nM of bBSA. This figure is from Paper VI

From these measurements it is seen that the planar Hall effect sensors can detect the presence of bBSA in a sample, but resolving the different concentrations is difficult. Whether this is due to the planar Hall effect sensor or that the bBSA binds poorly to the streptavidin coated beads with the present sample preparation will have to be investigated further. From these measurements, it also appears that the time domain measurements are not as accurate for extracting the hydrodynamic diameter as the frequency domain measurements, but as described in the previous chapter the measurement time in the time domain is one fifth of the measurement time in the frequency domain.

7.2   Large analytes – DNA coils

The experiments of volume-based detection of DNA coils formed by RCA with planar Hall effect sensors presented in this section have been performed in collaboration with the groups of M. Strømme and P. Svedlindh from Uppsala University. Three sets of measurement series on samples with DNA coils are presented below. First the effect of different DNA coil sizes is investigated. Then, two different incubation methods are tested. Finally, measurements on samples containing different DNA coil concentrations have been performed and for these measurements different analysis techniques are applied to determine how the lowest limit of detection is achieved.

7.2.1   Sample preparation

The samples used for all experiments were prepared by members of the collaborating groups at Uppsala University. This included both the functionalization of the magnetic beads and

fabrication of the DNA coils. The technical details on how the samples have been prepared can be found in Paper III and in the work by Zardán Gómez de la Torre *et al.* [55, 83]. Below, only a short description of the magnetic beads and DNA coils is given.

The functionalized magnetic beads prepared at Uppsala University were 50 nm BNF-starch beads with NH_2 surface groups and 80 nm BNF-starch beads with streptavidin functional groups, both types are produced by Micromod. Around ten single stranded detection oligonucleotides were conjugated to each bead and suspended in PBS pH 7.5. The bead concentrations used varied slightly from experiment to experiment and will be stated for each of the three measurements series presented below.

The DNA coils were formed by RCA, resulting in single stranded DNA coil consisting of multiple repetitions of oligonucleotides complementary to the detection oligonucleotides. The number of repetitions was proportional to the RCA-time and an RCA-time of 60 min results in DNA coils with roughly 1000 repetitions; such DNA coils have diameters of roughly 1 µm. As the DNA coils are not linear but entangled into a coil, many of the possible binding sites are not available for attaching beads. The DNA coils received from Uppsala University were suspended in a hybridization buffer (4mM Tris-HCL, 4mM EDTA, 0.02 v/v% Tween-20 and 0.1 M NaCl) with a coil concentration of 4 nM.

Prior to measurements with planar Hall effect sensors, solutions of both beads and DNA coils were prepared with twice the desired final concentration. 15 µL of the bead solution was then mixed gently with 15 µL of the DNA coil solution and incubated. The standard incubation method was to place the sample in an incubator for 30 min at 55°C. The alternative method was to first place the sample in a homogenous magnetic field at 45 mT for 2 min, then 13 min in an incubator at 55°C, followed by another 2 min in the applied field and finally 13 min more in the incubator at 55°C. The sample was then left a few minutes at room temperature to cool down, before the 30 µL sample was injected into the fluidic channel and measurements in the frequency domain recorded. To be able to monitor the time evolution of the signal for the two first measurements series, reference points were also measured; the exact frequencies will be stated for each experiment below.

7.2.2 DNA coil sizes

Initially it was investigated how the size of the coils affects the Brownian relaxation measurements. For this, DNA coils produced with three different RCA-times were used (20 min, 40 min and 60 min), which corresponds roughly to 333, 667 and 1000 repetitions of oligonucleotides complementary to the detection oligonucleotides attached to the beads. The samples were mixed such that the final bead and DNA coil concentrations were 0.5 mg/mL and 200 pM, respectively. The
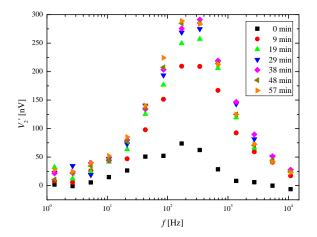
Table 7.2: Experimental settings for the study of different DNA coil sizes.

Wafer Name	208
Sensor types	Bridge $l \times w = 280$µm $\times$ 20µm
low-field sensitivity	$S_0 = -570$ V/(TA)
Lock-in	SR830
Reference points	Yes, $f_{ref} = 267$ Hz and $f_{ref} = 6$ Hz
Current amplitude	20 mA
Channel height	1 mm
Flow rates	In: 30 µL/min, Out: 800 µL/min
Sample volume	30 µL
Bead type	50 nm MM
Bead concentration	0.5 mg/mL
Coil concentration	200 pM
RCA time	20, 40 and 60 min
Temperature	25°C

samples were incubated with the standard method prior to injection into the fluidic system, where they were left for 66 min each. Measurements on a reference sample containing no coils

were also performed.

The in-phase second harmonic signals of seven frequency sweeps for the reference sample without DNA coils are plotted vs. frequency in Fig. 7.8. From this plot it is seen that the signal amplitude increases for the first four sweeps and is more or less constant for the remaining three sweeps. In Fig. 7.9 the in-phase second harmonic signal is plotted for the sample containing coils produced with a RCA-time of 40 min. From this figure it is seen that the signals for all sweeps continuously increase and that the increase after the second sweep is largest at low frequencies. As for the measurements with bBSA above, the reason for this is that the free beads reach a steady state after ~ 30 min, whereas the beads bound to DNA coils continue to sediment. It is also seen that it is not a well-defined peak that occurs at lower frequencies, but a very broad peak.
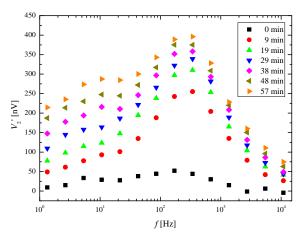
Fig. 7.8: Time evolution of in-phase signal as function of frequency for a sample not containing DNA coils.

Fig. 7.9: Time evolution of in-phase signal as function of frequency for a sample containing 200 pM DNA coils with an RCA time of 40 min.

In Fig. 7.10 the in-phase signals of the seventh sweeps are plotted vs. frequency for the reference samples and the three samples prepared with different RCA-times. It is seen that there is a peak in the signal near $f = 300$ Hz for all samples, which is due to the beads not being bound to DNA coils. The graph also shows that the signal generally increases when the RCA-time increases and that the increase is largest at low frequencies. The dashed vertical lines correspond to the frequencies at which reference points are measured.

To study the time evolution of the signals more thoroughly, reference measurements at $f_{\text{ref}} = 6$ Hz and $f_{\text{ref}} = 267$ Hz were measured in between each frequency of the sweeps. The reference points measured for all four samples are plotted in Fig. 7.11 and Fig. 7.12 for $f_{\text{ref}} = 6$ Hz and $f_{\text{ref}} = 267$ Hz, respectively. From Fig. 7.11 it is seen that the reference signals at $f_{\text{ref}} = 6$ Hz increase linearly with time and that the slope increases with RCA-time and is almost zero for the sample without DNA coils. For the reference points at $f_{\text{ref}} = 267$ Hz it is seen that the signal increase can be split into three regions: a steep signal increase immediately after injection, the signal levels off and the signal becomes linear. The reason for this shape is that due to the parabolic flow profile, few beads are near the surface immediately after injection. Then the diffusion of the free beads makes the signal increase rapidly, which levels off as a steady state
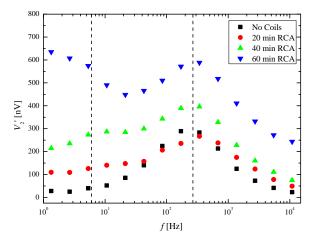
Fig. 7.10: Comparison of DNA coils with different RCA times. In-phase signal vs. frequency measured after roughly an hour of sedimentation.

is reached. The linear part is due to sedimentation of the beads bound to DNA coils. The reason for the sample with the longest RCA-time to increase the fastest is because the larger coils can bind more beads and due to their larger size have a lower diffusivity. Thus, due to the extra beads attached, the agglomerates are heavier and have a lower diffusivity and therefore sedimentation become more pronounced.
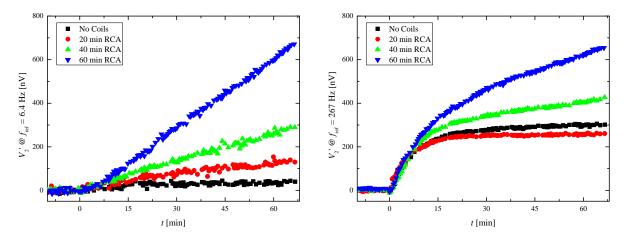
Fig. 7.11: Time evolution of in-phase signal at $f =$ 6.4 Hz for DNA coils with different RCA times

Fig. 7.12: Time evolution of in-phase signal at $f =$ 267 Hz for DNA coils with different RCA times

From these measurements on DNA coils with different RCA-times it is seen that a longer RCA-time results in a larger change of signal in less time. It is also seen that the extra time spent on the RCA can be saved on the time spent on measurements. For example, if the combined RCA and measurement time is limited to 80 min it can be seen from Fig. 7.11 that the signal from coils with 60 min RCA-time is larger after 20 min than both the signal from coils with 40 min RCA-time after 40 min, and the signal from coils with 20 min RCA-time after 60 min. For this reason, only DNA coils produced with a RCA-time of 60 min will be used in

the following experiments.

7.2.3   Incubation method

The incubation of magnetic beads to DNA coils is an important part of the detection of DNA coils. For this reason it was tested if applying a magnetic field during hybridization would increase the binding of beads to DNA coils. Due to a limited amount of functionalized beads received from Uppsala University, these measurements were performed with a final bead concentration of only 0.2 mg/mL of 80 nm beads and only one alternative hybridization method was tested as described

Table 7.3:   Experimental settings for the study of Incubation method.

Wafer Name	208
Sensor types	Bridge $l \times w = 280 \mu m \times 20 \mu m$
low-field sensitivity	$S_0 = -570$ V/(TA)
Lock-in	SR830
Reference points	Yes, $f_{ref} = 267$ Hz and $f_{ref} = 6$ Hz
Current amplitude	20 mA
Channel height	1 mm
Flow rates	In: 30 µL/min, Out: 800 µL/min
Sample volume	30 µL
Bead type	80 nm streptavidin MM
Bead concentration	0.2 mg/mL
Coil concentration	100 pM
RCA time	60 min
Temperature	25°C

above. For each hybridization method, measurements were performed on two samples with a final coil concentration of 100 pM. Also a fifth sample without any coils was measured.

Fig. 7.13: In-phase (top) and out-of-phase (bottom) second harmonic signal vs. frequency for samples prepared with different hybridization methods.

The frequency sweeps measured after 30 min for all five samples are plotted in Fig. 7.13. It is seen that the standard incubation results in a small increase in signal at high frequencies and

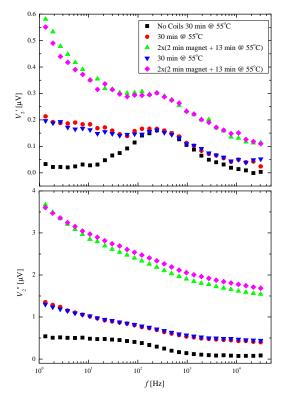a larger increase at lower frequencies compared to the sample without any DNA coils. However, using the alternative incubation method results in an even larger difference for all frequencies. The two measurements with the standard incubation are more alike than the measurements with the alternative method. However, the change in signal obtained from the samples incubated with the alternative method is considerably larger, which more than compensates for the slightly lower reproducibility.

The incubation method could surely be improved more than achieved here. In literature it has been shown that both homogeneously applied fields [84, 85] as used here as well as rotated magnetic fields [7] can enhance the agglutination of magnetic beads to analytes. The focus of this thesis is on the magnetic read-out and not on sample preparation and for this reason the alternative hybridization method will be used for the measurements in next section where the concentration of the DNA coils is varied.

7.2.4   DNA coil concentration

The measurements presented in this section are considered one of the main accomplishments of this project as the main goal was to perform measurement on samples with varying concentrations of DNA coils in order to compare the dose-response measured with planar Hall effect sensors to SQUID measurements performed by Strömberg *et al.* [44] and DynoMag measurement performed by Zardán Gómez de la Torre *et al.* [55] on similar samples.

7.2.4.1   Experimental

In this study, measurements with a planar Hall effect bridge sensor on samples with the DNA coil concentration varying between 1–256 pM were performed. In addition, measurements were also performed on reference samples containing no DNA coils. Measurements on samples with all DNA coil concentrations were replicated over three days. Each sample was left for 30 min in the fluidic channel and 12 consecutive frequency sweeps were performed without any reference points. The remaining experimental settings are summarized in Table 7.4.

Table 7.4: Experimental settings for the study of different DNA coil sizes.

Wafer Name	208
Sensor types	Bridge $l \times w = 280\mu m \times 20\mu m$
low-field sensitivity	$S_0 = -570$ V/(TA)
Lock-in	SR830
Reference points	No
Current amplitude	20 mA
Channel height	0.1 mm
Flow rates	In: 30 μL/min, Out: 800 μL/min
Sample volume	30 μL
Bead type	80 nm streptavidin MM
Bead concentration	0.5 mg/mL
Coil concentration	1–256 pM
RCA time	60 min
Temperature	25°C

7.2.4.2   Results and discussion of analysis method

The analysis method used by Strömberg *et al.* [44] and Zardán Gómez de la Torre *et al.* [55] was to normalize the out-of-phase magnetization signals with the total magnetization of the sample and then measure the decrease at the peak frequency of the free beads due to DNA coils. This analysis method cannot be applied directly to the measurements with planar Hall effect sensors since they only measure on a fraction of the sample volume, whereas both the SQUID and DynoMag measure on the entire sample volume. Thus, a different analysis method

is necessary in order to quantify the DNA coil concentration from measurements with planar Hall effect sensor and two different approaches were tested:

- Fitting a superposition two of two Cole–Cole models to the measurements, one for the free beads and one for the beads bound to DNA coils.

- Normalized to measurements with the average signal of a frequency sweep and looking at where the normalized signal increase and decrease when coils are added.

Previous analysis has shown that the in-phase signals are more reliable than the out-of-signals. This is because the raw out-of-phase signals have significant offsets, which are sensitive to changes of the physical conditions of the sensor, such as temperature or external magnetic fields. For this reason the following investigations will only take into account the in-phase sensor signals.

Fits to the Cole–Cole model In Fig. 7.14 the in-phase (top) and out-of-phase (bottom) second harmonic signals of the 12th sweep for all samples from day 1 are shown. It is seen that the DNA coils change the dynamic response and that a higher coil concentration results in a larger signal, which is because beads bound to coils will sediment more than free beads, i.e., the total number of beads near the sensor surface is increased.

From Fig. 7.14 it is also seen that measurements on all samples have a peak near $f = 300$ Hz, which is due to the beads not bound to DNA coils. It is also seen that as the DNA coil concentration increases so does the signal at low frequencies and it appears from the three largest coil concentrations that a peak occurs below 1 Hz. Therefore it will be tested if a superposition of two Cole–Cole contributions (Eq. (2.60)) can be fitted to the measurements

$$V_{2,\mathrm{Cole}} = V_2' + iV_2'' = i\frac{V_{0,\mathrm{free}} - V_\infty}{1 + (if/f_{\mathrm{B,free}})^{1-\alpha_{\mathrm{free}}}} + i\frac{V_{0,\mathrm{bound}} - V_\infty}{1 + (if/f_{\mathrm{B,bound}})^{1-\alpha_{\mathrm{bound}}}} + iV_\infty, \qquad (7.1)$$

where $f_{\mathrm{B,free}}$ and $f_{\mathrm{B,bound}}$ are the Brownian relaxation frequencies for free and bound beads, respectively. α_{free} and α_{bound} are the α values for the free and bound beads, respectively and $V_{0,\mathrm{free}}$ and $V_{0,\mathrm{bound}}$ are the values proportional to the DC susceptibilities for free and bound beads, respectively. V_∞ is proportional to the susceptibility at infinite frequency. As only the in-phase signal is used it is not possible to uniquely identify V_∞, which therefore is fixed to 0. Hence, six free parameters are left for the fitting routine, which results in too many degrees of freedom for the fitting routine to obtain robust results. Instead, the values of f_{B} and α for free beads are estimated from the measurements without coils and for bound beads from the measurements with coil concentrations ranging from 16 pM to 256 pM. The details of how the values of f_{B} and α are determined are described in Appendix C. Since the values vary with the sweep number and because most signal due to DNA coils were obtained during the last sweep, the values found in Appendix C are averages of the values extracted from sweeps 8–12. The obtained values of f_{B} and α for free and bound beads are listed in Table 7.5.

The values from Table 7.5 are now inserted into Eq. (7.1) and the model is fitted to each frequency sweep with only the scaling parameters (values of V_0) as free. The obtained values for $V_{0,\mathrm{bound}}$ are plotted in Fig. 7.15 and the values for $V_{0,\mathrm{free}}$ in Fig. 7.16. In general it is seen that $V_{0,\mathrm{bound}}$ increases with the sweep number, whereas $V_{0,\mathrm{free}}$ increases to sweep number 5 or 6 and
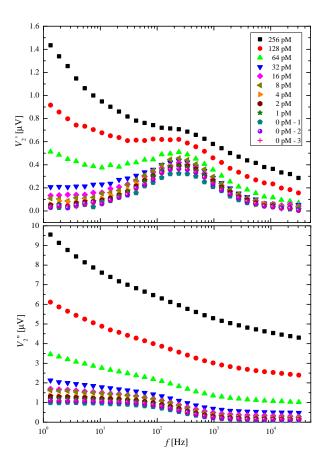
Fig. 7.14: In-phase (top) and out-of-phase (bottom) second harmonic signal vs. frequency for DNA coil concentrations between 0–256 pM measured on day 1.

Table 7.5: Values of f_B and α obtained in Appendix C for free beads and beads bound to DNA coils. The numbers in parentheses are standard deviations.

Parameter	Value
$f_{B,free}$	241(4)
α_{free}	0.17(1)
$f_{B,bound}$	0.1(2)
α_{bound}	0.76(6)

then becomes stable. This is again due to sedimentation of the beads bound to coils due to their lower diffusivity, whereas the free beads reach a steady state. However, it is also noted that for the samples without coils, the value of $V_{0,bound}$ also increases slightly with sweep number. This is most likely due to free beads being trapped by magnetostatic forces giving rise to a small increase in the signal at low frequencies. This effect will add a background level to the analysis method.

In Fig. 7.17 fits of the double peak Cole–Cole model to the in-phase signals of sweep 12 are
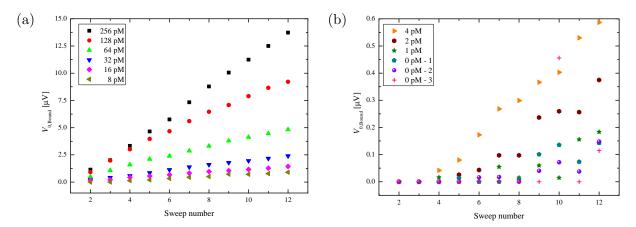
Fig. 7.15: $V_{0,\text{bound}}$ vs. sweep number for coil concentrations (a) 8–256 pM and (b) 0–4 pM.
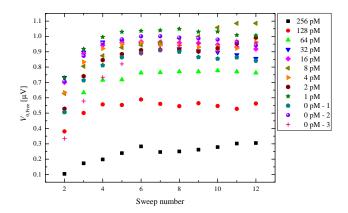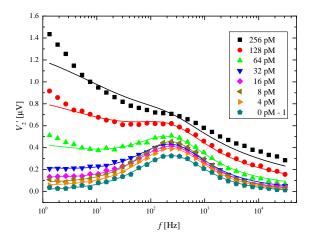
Fig. 7.16: $V_{0,\text{free}}$ vs. sweep number for all coil concentrations.

shown. It is seen that the model does not fit the measurements for the high coil concentrations well, whereas the fits to measurements of coil concentrations less than 32 pM appear better. It looks like the low-frequency peak determined in Appendix C does not match well for the high coil concentrations, which could suggest that larger agglomerates of several coils are formed for high coil concentrations.

The simplest way to obtain a value for the coil concentration is by using the value of $V_{0,\text{bound}}$ from last sweeps where the signal from the coils is largest. However, this would be very sensitive to outliers and rather, the model is fitted to sweeps 8–12 simultaneously, such that the effect of outliers is reduced. That an outlier can result in wrong values of $V_{0,\text{bound}}$ can be seen from Fig. 7.15, where the value obtained for sweep 10 on sample 0 pM-3 is over 0.4 μV, whereas all the other reference measurements result in values of less than 0.1 μV.

In Fig. 7.18 the values of $V_{0,\text{bound}}$ obtained from fitting the model to sweeps 8–12 simultaneously are plotted vs. coil concentration for the measurements performed on all 3 days. The six values in the bottom left corner are obtained from the reference measurements without DNA coils and have been used to calculate the dashed line, which is the mean values plus three standard deviations for the samples without DNA coils. It is seen that the samples containing
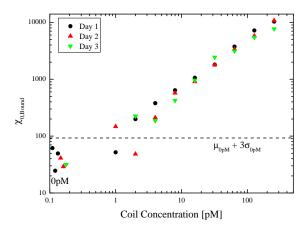
Fig. 7.17: In-phase signal of sweep 12 vs. frequency. The solid lines are fit of the double peak Cole–Cole model with fixed values of f_B and α.

Fig. 7.18: $V_{0,\mathrm{bound}}$ vs. coil concentrations extracted from fits to measurements of sweeps 8–12. The 6 values in the bottom left corner are the reference measurements without DNA coils.

coil concentrations of 4 pM or higher are all well above the dashed line and can therefore be concluded to be significantly different from zero. The samples with only 1 pM and 2 pM are not significantly different from the reference samples. It is also seen that the dose-response curve is linear over the investigated concentration range up to 256 pM.

Normalization of measurements   A different approach to analyze the data is to normalize it with the average signal of each frequency sweep. The normalized signals for the 12th sweep are plotted in Fig. 7.19 for the measurements from day 1. From this plot it is seen that frequency sweeps can be split into three regions marked by vertical lines: at high frequencies ($f_{\mathrm{high}} > 3850$ Hz) the normalized signal increases slightly with increasing coil concentration, at frequencies near the Brownian relaxation frequency for free beads (30 Hz $< f_{\mathrm{med}} <3850$ Hz) the normalized signal decreases with increasing coil concentration and at low frequencies ($f_{\mathrm{low}} < 30$ Hz) the normalized signal again increases with increasing coil concentration.

The changes in the f_{high} region are so small that they will not be used. Instead, three test-values are calculated as a measure for the coil concentration. The two first test-values are calculated as the mean of the normalized signals in the f_{low} and f_{med} regions. The mean value of the normalized signal in the f_{low} region $\mu(f_{\mathrm{low}})$ is a measure of the signal increase at low frequencies due to the DNA coils. The mean value of the normalized signal in the f_{med} region $\mu(f_{\mathrm{med}})$ is a measure of the signal due to the free bead. The third test-value is the ratio between the two $\mu(f_{\mathrm{low}})/\mu(f_{\mathrm{med}})$, which is a measure of the fraction of beads bound to DNA coils compared to free beads.

The values of $\mu(f_{\mathrm{low}})$, $\mu(f_{\mathrm{med}})$ and $\mu(f_{\mathrm{low}})/\mu(f_{\mathrm{med}})$ have been calculated for every frequency sweep made on day 1 and are plotted vs. sweep number in Fig. 7.20 – Fig. 7.22, respectively.

From Fig. 7.20 – Fig. 7.22 it is seen that the $\mu(f_{\mathrm{low}})$ and $\mu(f_{\mathrm{low}})/\mu(f_{\mathrm{med}})$ increase and that $\mu(f_{\mathrm{med}})$ decreases as the coil concentration is increased. It is also seen that, the effect of the DNA coils becomes more pronounced with increasing sweep number. For this reason, the continued analysis will only rely on the last five sweeps, thus the average values for sweeps 8–12
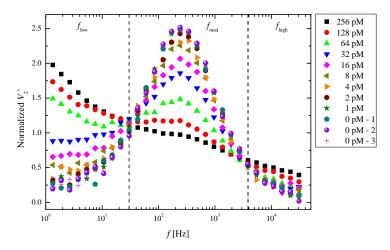
Fig. 7.19: In-phase signal of sweep 12 normalized to the mean signal of each frequency sweep. Data shown are for all concentrations measured on day 1.
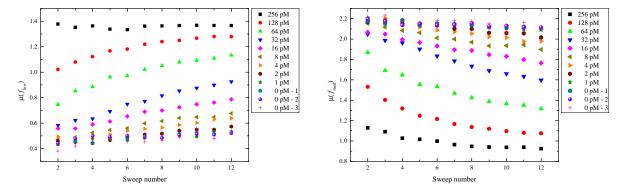
Fig. 7.20: Average value of the normalized in-phase signals in the f_{low} region vs. sweep number for the measurements from day 1.

Fig. 7.21: Average value of the normalized in-phase signals in the f_{med} region vs. sweep number for the measurements from day 1.

are calculated. To be able to compare how each of the three test-values depends on DNA coil concentration, they have all been corrected for the mean value of the reference measurements without DNA-coils $\mu_{0\text{pM}}$ and the sign for $\mu(f_{\text{med}})$ is changed such all three test-values increase with DNA coil concentration:

$$\Delta\mu(f_{\text{low}}) = \mu(f_{\text{low}}) - \mu_{0\text{pM}}(f_{\text{low}}) \tag{7.2}$$

$$\Delta\mu(f_{\text{med}}) = \mu_{0\text{pM}}(f_{\text{med}}) - \mu(f_{\text{med}}) \tag{7.3}$$

$$\Delta(\mu(f_{\text{low}})/\mu(f_{\text{med}})) = \mu(f_{\text{low}})/\mu(f_{\text{med}}) - \mu_{0\text{pM}}(f_{\text{low}})/\mu_{0\text{pM}}(f_{\text{med}}) \tag{7.4}$$

The three test-values averaged over sweeps 8–12 obtained for each of the three days are plotted vs. DNA coil concentration in Fig. 7.23 – Fig. 7.25, respectively. The horizontal lines correspond to 3 times the standard deviation $\sigma_{0\text{pM}}$ of the values obtained from the samples without DNA coils. From all three figures it is seen that the values obtained from the samples containing 4 pM of DNA coils are well above the $3\sigma_{0\text{pM}}$ level and are therefore concluded to
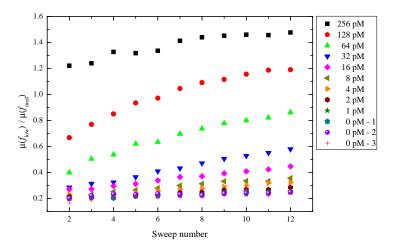
Fig. 7.22: The ratio between the values plotted in Fig. 7.20 and Fig. 7.21 vs. sweep number for the measurements from day 1.

be significantly different from the samples without DNA coils. All three dose-response curves are also linear up to 128 pM, but it appears that the sample at 256 pM is almost saturated i.e., the dose-response curve would level off if higher coil concentrations were measured. Based on this analysis it is not possible to determine if one of the three normalization methods are better than the others. However, the method of determining the ratio between the signals at low and medium frequencies utilizes the most data points and is therefore expected to be the least influenced by potential outliers.
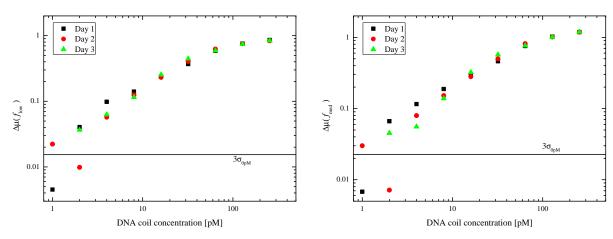
Fig. 7.23: $\Delta\mu(f_{\text{low}})$ averaged over sweeps 8–12 vs. DNA coil concentration for measurements repeated over three days.

Fig. 7.24: $\Delta\mu(f_{\text{med}})$ averaged over sweeps 8–12 vs. DNA coil concentration for measurements repeated over three days.

By comparing the normalization analysis methods presented here to the superpositioned Cole–Cole model above, it is not possible to conclude which of the two approaches is best. However, the normalization method is simpler and fewer assumptions have been made. Thus, the normalization analysis method of calculating the ratio between the signals at low and medium
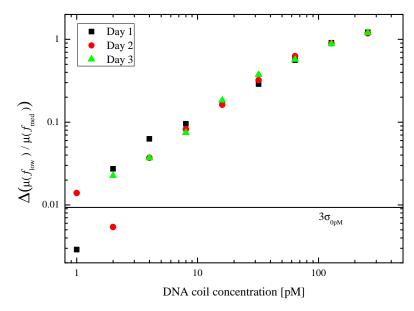
Fig. 7.25: $\Delta(\mu(f_{\mathrm{low}})/\mu(f_{\mathrm{med}}))$ averaged over sweeps 8–12 vs. DNA coil concentration for measurements repeated over three days.

frequencies should be applied to future DNA coil experiments.

From the measurements it is concluded that planar Hall effect bridge sensors can detect DNA coils formed by RCA in concentrations as low as 4 pM. These results are comparable to the detection limits of 3 pM achieved by Strömberg *et al.* [44] using a SQUID magnetometer and the 4 pM achieved by Zardán Gómez de la Torre *et al.* [55] using a DynoMag on similar samples. By use of the planar Hall effect bridge sensor it appears that saturation is reached around 256 pM, which is also comparable to what has been shown by Strömberg *et al.* [44] and Strömberg *et al.* [44]. It is believed that the coil concentration at which all the beads are bound to DNA coils can be increased by increasing the used bead concentration. However, this will also yield additional background signal from free beads for the lower coil concentrations and it is therefore not certain that increasing the bead concentration will allow for the same lower limit of detection.

By comparing the results using volume-based biosensing obtained here and by Strömberg *et al.* [44] and Strömberg *et al.* [44] to the detection limit of 5 fM with a linear dynamic range over 6 orders of magnitude using surface-based biosensing as reported by Gaster *et al.* [34], volume-based sensing still has a long way to go before being a competitive biosensor. In addition, multiplexing is also a lot easier for surface-based biosensing, as each sensor only needs to be functionalized differently. Contrary, multiplexing with volume-based sensing requires a separate fluidic channel for each different functionalization of the beads.

Chapter 8

Outlook

Throughout the thesis-work, several ideas and suggestions on how to improve the relaxation measurements with planar Hall effect sensors have evolved. Due to prioritization to other aspects of the experimental work and subsequent time constraints, these optimization experiments have yet to be carried out. Therefore, this chapter serves the purpose of an outlook, where these suggestions for improving the measurements are described. The suggestions given are within the areas of the sensor design, the fabrication process and the sensing methodology.

8.1   New sensor designs

It is hypothesized that relaxation measurements can be improved by the use of bridge sensors that are constructed slightly differently than those used throughout this thesis. The reasons why sensors of another construct are believed to be better than the standard bridge used throughout the thesis are described below.

The bridge sensors are still to be composed of conductor slaps with widths w and lengths l as shown in Fig. 2.5 and the resistance $R(\alpha_J, \theta)$ is given by Eq. (2.17). To get a better understanding of how the signal from external fields and self-fields are generated, the resistance dependence is investigated for a single segment. For small values of θ, $R(\alpha_J, \theta)$ can be Taylor expanded to first order around 0 to give

$$R(\alpha_J, \theta) = \frac{l}{t_{\mathrm{FM}} w} \left(\rho_\parallel - \tfrac{1}{2} \Delta\rho + \tfrac{1}{2} \Delta\rho (\cos(2\alpha_J) - 2\sin(2\alpha_J)\theta) \right). \tag{8.1}$$

We recall that θ is the angle of the magnetization to the positive x-direction, which is also the easy direction of magnetization. By inserting the expression for the magnetization angle $\theta = \frac{H_{y,\mathrm{ext}} + H_{\mathrm{sf}} \cos(\alpha_J)}{H_{\mathrm{K}} + H_{\mathrm{ex}}}$ $R(\alpha_J, \theta)$ becomes

$$R(\alpha_J, H_{y,\mathrm{ext}}, H_{\mathrm{sf}}) = \frac{l}{t_{\mathrm{FM}} w} \left(\rho_\parallel - \tfrac{1}{2} \Delta\rho + \tfrac{1}{2} \Delta\rho (\cos(2\alpha_J) - 2\sin(2\alpha_J) \frac{H_{y,\mathrm{ext}} + H_{\mathrm{sf}} \cos(\alpha_J)}{H_{\mathrm{K}} + H_{\mathrm{ex}}}) \right) \tag{8.2}$$

This shows that the resistance will be most sensitive to $H_{y,\mathrm{ext}}$ and H_{sf} by maximizing or minimizing $\sin(2\alpha_J)$ and $\sin(2\alpha_J)\cos(\alpha_J)$, respectively. $\sin(2\alpha_J)$ and $\sin(2\alpha_J)\cos(\alpha_J)$ are plotted as function of α_J in Fig. 8.1. This figure shows that $\sin(2\alpha_J)$ is at maximum value for $\alpha_J = \pi/4$

and $\alpha_J = 5\pi/4$ and at minimum value for $\alpha_J = 3\pi/4$ and $\alpha_J = 7\pi/4$. For $\sin(2\alpha_J)\cos(\alpha_J)$ the maximum value is for $\alpha_J \approx 0.615$ and $\alpha_J \approx 2.526$, while the minimum value is at $\alpha_J \approx 3.757$ and $\alpha_J \approx 5.668$. It is also seen that $\sin(2\alpha_J)\cos(\alpha_J)$ is at 91 % of its peak value for $\alpha_J = \pi/4$, $\alpha_J = 3\pi/4$, $\alpha_J = 5\pi/4$ and $\alpha_J = 7\pi/4$. For simplicity only these four angles are considered in the following, but it should be kept in mind that these angles are not optimal for detecting self-fields. In Table 8.1 the sign at these four angles are listed for $\sin(2\alpha_J)$ and $\sin(2\alpha_J)\cos(\alpha_J)$ and it is seen that values of α_J can be chosen such that the contribution from the external field and the self-field has the same or opposite signs.
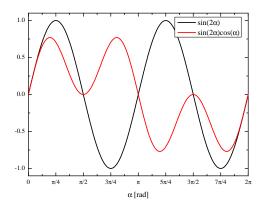
Fig. 8.1: Plot of $\sin(2\alpha_J)$ and $\sin(2\alpha_J)\cos(\alpha_J)$ as function of α_J.

Table 8.1: Sign of $\sin(2\alpha_J)$ and $\sin(2\alpha_J)\cos(\alpha_J)$ as function of α_J

	$\alpha_J = \pi/4$	$\alpha_J = 3\pi/4$	$\alpha_J = 5\pi/4$	$\alpha_J = 7\pi/4$
$\sin(2\alpha_J)$	$+$	$-$	$+$	$-$
$\sin(2\alpha_J)\cos(\alpha_J)$	$+$	$+$	$-$	$-$

By selection of different angles of α_J for R_1 and R_2, the bridge will be sensitive to either both the external field and the self-field or only one of the two at a time. If α_J values are selected such that the signs for $\sin(2\alpha_J)$ in Table 8.1 are opposite, the design, when incorporated in a Wheatstone bridge, will be sensitive to external fields and likewise for $\sin(2\alpha_J)\cos(\alpha_J)$ the design will be sensitive to self-fields. On the other hand, if the signs are identical the design will not be sensitive.

To make a sensor that is sensitive to both external and self-field, the resistances can be chosen to $R_1 = R(\alpha_J = \pi/4, H_{y,\text{ext}}, H_{\text{sf}})$ and $R_2 = R(\alpha_J = 7\pi/4, H_{y,\text{ext}}, H_{\text{sf}})$, which is the standard bridge sensor used through the entire thesis. To make the sensor only sensitive to self-fields, the two resistances are chosen as $R_1 = R(\alpha_J = \pi/4, H_{y,\text{ext}}, H_{\text{sf}})$ and $R_2 = R(\alpha_J = 5\pi/4, H_{y,\text{ext}}, H_{\text{sf}})$, as shown in Fig. 8.2 (a). Thus, results in the bridge voltage

$$V = \frac{l\Delta\rho}{t_{\text{FM}}w}\left(\frac{\frac{1}{\sqrt{2}}H_{\text{sf}}}{H_{\text{K}} + H_{\text{ex}}}\right)I. \tag{8.3}$$

Likewise, a sensor only sensitive to external fields can be designed by letting $R_1 = R(\alpha_J = \pi/4, H_{y,\text{ext}}, H_{\text{sf}})$ and $R_2 = R(\alpha_J = 3\pi/4, H_{y,\text{ext}}, H_{\text{sf}})$, which is sketched in Fig. 8.2 (b). Note

that the current is passed through the sensor in the y-direction. This gives a bridge voltage of

$$V = \frac{l\Delta\rho}{t_{\text{FM}}w}\left(\frac{H_{y,\text{ext}}}{H_{\text{K}} + H_{\text{ex}}}\right)I. \tag{8.4}$$

It is also possible to design a meandering sensor, where the effect of the self-fields do not cancel out. This requires that the part of the sensor stack where the current is running anti parallel is replaced by a material not exhibiting the AMR effect, e.g. gold, as shown in Fig. 8.2 (c). The signal for such a sensor is given by

$$V = \frac{nl\Delta\rho}{t_{\text{FM}}w}\left(\frac{\frac{1}{\sqrt{2}}H_{\text{sf}}}{H_{\text{K}} + H_{\text{ex}}}\right)I, \tag{8.5}$$

where n is the number of magnetoresistive segments in each branch.
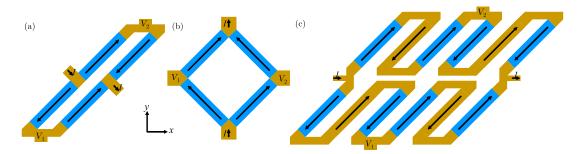
Fig. 8.2: Newly proposed planar Hall effect bridge sensors. (a) is only sensitive to self-fields. (b) is only sensitive to external fields. (c) is a meandering bridge sensor sensitive to only self-fields with $n = 2$.

Sensors only sensitive to self-field as those shown in Fig. 8.2 (a) and (c) have in fact already been fabricated, but measurements with beads have not yet been performed due to lack of time.

8.2   Fabrication

Another place for possible optimization of the sensor signal is in fabrication process. Here, few possible solutions to increase the signal from the bead or to remove signal offsets are proposed.

Low-temperature annealing   As it was briefly mentioned in Chapter 4 annealing the magnetic stack at temperatures between 240°C and 320°C decreased the temperature dependence of the sensors and also increased the sensitivity. However, these wafers were never tested for relaxation measurements because they did not have any protective coating on. It could be interesting to test if low-temperature annealing can also result in more signal from magnetic beads.

Stack composition   With the stack composition used throughout this thesis, the antiferromagnetic layer on top of the sensitive ferromagnetic layer gave rise to an offset in the second harmonic signal that was between 30–100 times larger than the bead signal. It is believed that optimizing the stack composition could reduce this offset. The sensor stack used throughout

this thesis was Ta (3 nm) / $Ni_{80}Fe_{20}$(30 nm)/ $Mn_{80}Ir_{20}$(20 nm) / Ta (3 nm). By increasing the bottom layer of Tantalum and decreasing the $Mn_{80}Ir_{20}$layer it should be possible to reduce the offset in the second harmonic signal. This would allow for using a lower sensitivity setting on the lock-in amplifier and thereby better utilize the bit resolution of the analog to digital converter.

Thickness of protective coating   Another possible approach to increase the signal from magnetic beads is to decrease the protective coating. This would bring the beads closer to the sensor, which would first of all increase the self-field acting on the beads, thereby increase the magnetization of the beads, but also increase the field from the beads acting on the sensor. However, one possible drawback of this could be that the magnetostatic force acting on the beads increases and becomes a bigger problem.

8.3   Setup and measurements

Here, a few additional ideas for measurements that could be interesting to perform and improvements of the setup are described.

Freezing a sample on-chip   It could be interesting to see how the dynamic signal changes if a sample containing magnetic beads are frozen and thereby not free to physically rotate. It is believed that this would allow for measuring the Néel relaxation if the Néel relaxation time is not much above seconds.

Pulling beads to sensor surface by magnetic force   For this thesis the beads samples were injected and left stagnant for diffusion and sedimentation to move the beads closer to the sensor surface. Being able to pull all the beads to the sensor surface by magnetic forces immediately after injection could decrease the waiting time. For measurements with DNA coils it could also result in that the beads bound to coils stay on the surface due to their low diffusivity while unbound beads diffuse away from the surface. Thus, the concentration of bound beads near the sensor surface is the locally increased.

DNA hybridization on-chip   If the irreversible temperature effect of heating the sensor can be eliminated it would be possible to do the hybridization of magnetic beads to DNA coils in the fluidic system. This will allow for a decrease in the total analysis time as the sample will reach a steady state while the hybridization takes place.

Amplification of signal   The measurements performed during this thesis were generally without preamplification of the signal, with the exception of the data presented in Section 5.1 and Paper II. This preamplifier was AC coupled but a later study showed it was not appropriate to use since it attenuated of the signal for frequencies below 10 Hz. However, it was also simultaneously shown that the reproducibility improved when the preamplifier was used. Thus, finding a DC coupled pre amplifier could increase the signal-to-noise ratio, resulting in lower detections limits.

Chapter 9

Conclusion

Based on the results presented in this thesis, it is first of all concluded that it is possible to measure Brownian relaxation of magnetic beads with planar Hall effect sensors without the need for any external magnets. It has been shown that information about the properties of magnetic beads, i.e., the hydrodynamic diameter can be extracted from the measurements and that the degree of polydispersity can be estimated.

To demonstrate that magnetorelaxometry measured with planar Hall effect sensors behave as predicted by theory, measurement series have been performed in the frequency domain where the following parameters were varied: temperature, sensor geometry, current amplitude, bead concentration and bead diameter.

From the measurement series with varied temperature it was shown that the hydrodynamic diameter of the magnetic beads can be extracted reliably as long as the temperature is known and the temperature dependence of the dynamic viscosity is accounted for. It was also shown that the sensor signal itself depends on temperature and signals measured at different temperatures can therefore not directly be compared. By low-temperature annealing the sensors in a magnetic field the temperature dependence can be reduced almost 90 % and at the same time the low-field sensitivity can be increased by 73.5 %.

By performing AC susceptibility measurements with both planar Hall effect cross sensors and planar Hall effect bridge sensors, it is concluded that changing the sensor geometry results in an amplification of the signal from magnetic beads by a factor of six without changing the obtained dynamic responses. As proposed in the outlook (Chapter 8) it is considered possible to design sensors with slightly modified geometries that result in even higher signal from magnetic beads and are insensitive to external fields. Furthermore, it was demonstrated that the dynamic response from magnetic beads scales with the current amplitude squared, but increasing the current above 24 mA is not feasible in the current setup since it yields incorrect measurements at high frequencies.

By performing relaxation measurements on samples of 40 nm beads in varying concentrations, it is concluded that the extracted hydrodynamic diameter is independent of the bead concentration, but larger signal-to-noise ratios were obtained from samples with larger bead concentrations. It was not possible to obtain meaningful hydrodynamic diameters for bead concentrations below 64 µg/mL, but the presence of beads could be detected down to 16 µg/mL of

40 nm beads.

It has been demonstrated that planar Hall effect bridge sensors can be used as AC susceptometers in the frequency range from 0.67 Hz to 1 MHz. This wide span of frequencies allows for measurement of Brownian relaxation of magnetic beads with nominal diameters ranging from 10 nm to 250 nm. The planar Hall effect sensors are best suited for detection of beads smaller than 100 nm as Brownian motion almost eliminates sedimentation and because beads of these sizes are not captured by magnetostatic forces on edges of the magnetic sensor stack.

Relaxation measurements with planar Hall effect bridge sensors can also be performed in the time domain resulting in considerably shorter measurement times. However, presently the frequency domain measurements are more accurate due to a poor voltage resolution of the time domain measurements.

Finally, it has been shown that planar Hall effect bridge sensors can be used for volume-based biosensing. The planar Hall effect bridge sensors can detect the presence of biotin-conjugated bovine serum albumin by measuring changes in the hydrodynamic diameter of streptavidin coated beads. Also, DNA coils formed by rolling circle amplification can be detected with the planar Hall effect bridge sensors. It has been shown that DNA coil concentration ranging from 4 pM to 256 pM can be resolved, which is comparable to measurements on similar samples performed by Strömberg *et al.* [44] using a SQUID and Strömberg *et al.* [44] using a DynoMag. Though, the advantage of the planar Hall effect bridge sensors is that they are simpler devices without the need for external magnets and can easily be integrated as a read-out principle in a future lab-on-a-chip device.

Bibliography

[1] J. D. Newman and A. P. F. Turner, "Home blood glucose biosensors: a commercial perspective," Biosens. Bioelectron. **20**, 2435 (2005).

[2] J. Wang, "Electrochemical glucose biosensors," Chem. Rev. **108**, 814 (2008).

[3] A. P. F. Turner, B. Chen, and S. A. Piletsky, "In vitro diagnostics in diabetes: meeting the challenge," Clin. Chem. **45**, 1596 (1999).

[4] G. Posthuma-Trumpie, J. Korf, and A. van Amerongen, "Lateral flow (immuno) assay: its strengths, weaknesses, opportunities and threats. a literature survey," Anal. Bioanal. Chem. **393**, 569 (2009).

[5] A. Ranzoni, X. J. A. Janssen, M. Ovsyanko, L. J. van IJzendoorn, and M. W. J. Prins, "Magnetically controlled rotation and torque of uniaxial microactuators for lab-on-a-chip applications," Lab Chip **10**, 179 (2009).

[6] P. Kinnunen, I. Sinn, B. H. McNaughton, and R. Kopelman, "High frequency asynchronous magnetic bead rotation for improved biosensors," Appl. Phys. Lett. **97**, 223701 (2010).

[7] A. Ranzoni, J. J. H. B. Schleipen, L. J. van IJzendoorn, and M. W. J. Prins, "Frequency-selective rotation of two-particle nanoactuators for rapid and sensitive detection of biomolecules," Nano Lett. **11**, 2017 (2011).

[8] Ocean NanoTech - http://www.http://oceannanotech.com/, (2013).

[9] Spherotech Inc. - http://www.spherotech.com/, (2013).

[10] Q. A. Pankhurst, J. Connolly, S. K. Jones, and J. Dobson, "Applications of magnetic nanoparticles in biomedicine," J. Phys. D: Appl. Phys. **36**, R167 (2003).

[11] K. M. Krishnan, "Biomedical nanomagnetics: a spin through possibilities in imaging, diagnostics, and therapy," IEEE Trans. Magn. **46**, 2523 (2010).

[12] A. H. Lu, E. L. Salabas, and F. Schüth, "Magnetic nanoparticles: synthesis, protection, functionalization, and application," Angew. Chem. Int. **46**, 1222 (2007).

[13] A. K. Gupta and M. Gupta, "Synthesis and surface engineering of iron oxide nanoparticles for biomedical applications," Biomaterials **26**, 3995 (2005).

[14] M. A. M. Gijs, "Magnetic bead handling on-chip: new opportunities for analytical applications," Microfluid. Nanofluid. **1**, 22 (2004).

[15] N. Pamme, "Continuous flow separations in microfluidic devices," Lab Chip **7**, 1644 (2007).

[16] M. Arruebo, R. Fernández-Pacheco, M. R. Ibarra, and J. Santamaría, "Magnetic nanoparticles for drug delivery," Nano Today **2**, 22 (2007).

[17] R. Kotitz, H. Matz, L. Trahms, H. Koch, W. Weitschies, T. Rheinlander, W. Semmler, and T. Bunte, "Squid based remanence measurements for immunoassays," IEEE Trans. Appl. Supercond. **7**, 3678 (1997).

[18] K. Enpuku, T. Minotani, T. Gima, Y. Kuroki, Y. Itoh, M. Yamashita, Y. Katakura, and S. Kuhara, "Detection of magnetic nanoparticles with superconducting quantum interference device (squid) magnetometer and application to immunoassays," Jpn. J. Appl. Phys. **38**, L1102 (1999).

[19] A. P. Astalan, F. Ahrentorp, C. Johansson, K. Larsson, and A. Krozer, "Biomolecular reactions studied using changes in brownian rotation dynamics of magnetic particles," Biosens. Bioelectron. **19**, 945 (2004).

[20] F. Ludwig, E. Heim, S. Mäuselein, D. Eberbeck, and M. Schilling, "Magnetorelaxometry of magnetic nanoparticles with fluxgate magnetometers for the analysis of biological targets," J. Magn. Magn. Mater. **293**, 690 (2005).

[21] D. R. Baselt, G. U. Lee, M. Natesan, S. W. Metzger, P. E. Sheehan, and R. J. Colton, "A biosensor based on magnetoresistance technology," Biosens. Bioelectron. **13**, 731 (1998).

[22] M. M. Miller, P. E. Sheehan, R. L. Edelstein, C. R. Tamanaha, L. Zhong, S. Bounnak, L. J. Whitman, and R. J. Colton, "A DNA array sensor utilizing magnetic microbeads and magnetoelectronic detection," J. Magn. Magn. Mater. **225**, 138 (2001).

[23] J. C. Rife, M. M. Miller, P. E. Sheehan, C. R. Tamanaha, M. Tondra, and L. J. Whitman, "Design and performance of GMR sensors for the detection of magnetic microbeads in biosensors," Sens. Actuators, A **107**, 209 (2003).

[24] W. Thomson, "On the electro-dynamic qualities of metals: -effects of magnetization on the electric conductivity of nickel and of iron." Proc. R. Soc. Lond. **8**, 546 (1857).

[25] M. N. Baibich, J. M. Broto, A. Fert, F. N. Van Dau, F. Petroff, P. Etienne, G. Creuzet, A. Friederich, and J. Chazelas, "Giant magnetoresistance of (001)Fe/(001)Cr magnetic superlattices," Phys. Rev. Lett. **61**, 2472 (1988).

[26] G. Binasch, P. Grünberg, F. Saurenbach, and W. Zinn, "Enhanced magnetoresistance in layered magnetic structures with antiferromagnetic interlayer exchange," Phys. Rev. B **39**, 4828 (1989).

[27] G. Prinz, "Magnetoelectronics," Science **282**, 1660 (1998).

[28] D. L. Graham, H. Ferreira, J. Bernardo, P. P. Freitas, and J. M. S. Cabral, "Single magnetic microsphere placement and detection on-chip using current line designs with integrated spin valve sensors: Biotechnological applications," J. Appl. Phys. **91**, 7786 (2002).

[29] G. Li, V. Joshi, R. L. White, S. X. Wang, J. T. Kemp, C. Webb, R. W. Davis, and S. Sun, "Detection of single micron-sized magnetic bead and magnetic nanoparticles using spin valve sensors for biological applications," J. Appl. Phys. **93**, 7557 (2003).

[30] W. Shen, X. Liu, D. Mazumdar, and G. Xiao, "In situ detection of single micron-sized magnetic beads using magnetic tunnel junction sensors," Appl. Phys. Lett. **86**, 253901 (2005).

[31] L. Ejsing, M. F. Hansen, A. K. Menon, H. A. Ferreira, D. L. Graham, and P. P. Freitas, "Planar Hall effect sensor for magnetic micro- and nanobead detection," Appl. Phys. Lett. **84**, 4729 (2004).

[32] J. Schotter, P. B. Kamp, A. Becker, A. Pühler, G. Reiss, and H. Brückl, "Comparison of a prototype magnetoresistive biosensor to standard fluorescent DNA detection," Biosens. Bioelectron. **19**, 1149 (2004).

[33] V. C. Martins, F. A. Cardoso, J. Germano, S. Cardoso, L. Sousa, M. Piedade, P. P. Freitas, and L. P. Fonseca, "Femtomolar limit of detection with a magnetoresistive biochip," Biosens. Bioelectron. **24**, 2690 (2009).

[34] R. S. Gaster, D. A. Hall, C. H. Nielsen, S. J. Osterfeld, H. Yu, K. E. Mach, R. J. Wilson, B. Murmann, J. C. Liao, S. S. Gambhir, and S. X. Wang, "Matrix-insensitive protein assays push the limits of biosensors in medicine," Nat. Med. **15**, 1327 (2009).

[35] D. A. Hall, R. S. Gaster, S. J. Osterfeld, B. Murmann, and S. X. Wang, "GMR biosensor arrays: Correction techniques for reproducibility and enhanced sensitivity," Biosens. Bioelectron. **25**, 2177 (2010).

[36] S. J. Osterfeld, H. Yu, R. S. Gaster, S. Caramuta, L. Xu, S. J. Han, D. A. Hall, R. J. Wilson, S. Sun, and R. L. White, "Multiplex protein assays based on real-time magnetic nanotag sensing," P. Natl. Acad. Sci. USA **105**, 20637 (2008).

[37] D. A. Hall, R. S. Gaster, T. Lin, S. J. Osterfeld, S. Han, B. Murmann, and S. X. Wang, "GMR biosensor arrays: A system perspective," Biosens. Bioelectron. **25**, 2051 (2010).

[38] R. S. Gaster, L. Xu, S. J. Han, R. J. Wilson, D. A. Hall, S. J. Osterfeld, H. Yu, and S. X. Wang, "Quantification of protein interactions and solution transport using high-density GMR sensor arrays," Nat. Nanotechnol. **6**, 314 (2011).

[39] R. S. Gaster, D. A. Hall, and S. X. Wang, "nanolab: An ultraportable, handheld diagnostic laboratory for global health," Lab Chip **11**, 950 (2011).

[40] S. X. Wang and G. Li, "Advances in giant magnetoresistance biosensors with magnetic nanoparticle tags: review and outlook," IEEE Trans. Magn. **44**, 1687 (2008).

[41] J. Connolly and T. G. St Pierre, "Proposed biosensors based on time-dependent properties of magnetic fluids," J. Magn. Magn. Mater. **225**, 156 (2001).

[42] S. H. Chung, A. Hoffmann, S. D. Bader, C. Liu, B. Kay, L. Makowski, and L. Chen, "Biological sensors based on Brownian relaxation of magnetic nanoparticles," Appl. Phys. Lett. **85**, 2971 (2004).

[43] C. Y. Hong, C. C. Wu, Y. C. Chiu, S. Y. Yang, H. E. Horng, and H. C. Yang, "Magnetic susceptibility reduction method for magnetically labeled immunoassay," Appl. Phys. Lett. **88**, 212512 (2006).

[44] M. Strömberg, J. Göransson, K. Gunnarsson, M. Nilsson, P. Svedlindh, and M. Strømme, "Sensitive molecular diagnostics using volume-amplified magnetic nanobeads," Nano Lett. **8**, 816 (2008).

[45] H. L. Grossman, W. R. Myers, V. J. Vreeland, R. Bruehl, M. D. Alper, C. R. Bertozzi, and J. Clarke, "Detection of bacteria in suspension by using a superconducting quantum interference device," P. Natl. Acad. Sci. USA **101**, 129 (2004).

[46] L. Tu, Y. Jing, Y. Li, and J. P. Wang, "Real-time measurement of Brownian relaxation of magnetic nanoparticles by a mixing-frequency method," Appl. Phys. Lett. **98**, 213702 (2011).

[47] F. Ludwig, S. Mäuselein, E. Heim, and M. Schilling, "Magnetorelaxometry of magnetic nanoparticles in magnetically unshielded environment utilizing a differential fluxgate arrangement," Rev. Sci. Instrum. **76**, 106102 (2005).

[48] K. Enpuku, Y. Tamai, T. Mitake, T. Yoshida, and M. Matsuo, "ac susceptibility measurement of magnetic markers in suspension for liquid phase immunoassay," J. Appl. Phys. **108**, 034701 (2010).

[49] B. T. Dalslet, C. D. Damsgaard, M. Donolato, M. Strømme, M. Strömberg, P. Svedlindh, and M. F. Hansen, "Bead magnetorelaxometry with an on-chip magnetoresistive sensor," Lab Chip **11**, 296 (2011).

[50] R. Kötitz, P. C. Fannin, and L. Trahms, "Time domain study of Brownian and Néel relaxation in ferrofluids," J. Magn. Magn. Mater. **149**, 42 (1995).

[51] D. Eberbeck, F. Wiekhorst, U. Steinhoff, and L. Trahms, "Aggregation behaviour of magnetic nanoparticle suspensions investigated by magnetorelaxometry," J. Phys. Condens. Matter **18**, S2829 (2006).

[52] A. P. Astalan, C. Jonasson, K. Petersson, J. Blomgren, D. Ilver, A. Krozer, and C. Johansson, "Magnetic response of thermally blocked magnetic nanoparticles in a pulsed magnetic field," J. Magn. Magn. Mater. **311**, 166 (2007).

[53] D. Eberbeck, C. Bergemann, F. Wiekhorst, U. Steinhoff, and L. Trahms, "Quantification of specific bindings of biomolecules by magnetorelaxometry," Journal of nanobiotechnology **6**, 4 (2008).

[54] F. Öisjöen, J. F. Schneiderman, A. P. Astalan, A. Kalabukhov, C. Johansson, and D. Winkler, "A new approach for bioassays based on frequency- and time-domain measurements of magnetic nanoparticles." Biosens. Bioelectron. **25**, 1008 (2010).

[55] T. Zardán Gómez de la Torre, A. Mezger, D. Herthnek, C. Johansson, P. Svedlindh, M. Nilsson, and M. Strømme, "Detection of rolling circle amplified DNA molecules using probe-tagged magnetic nanobeads in a portable AC susceptometer," Biosens. Bioelectron. **29**, 195 (2011).

[56] M. Nilsson, H. Malmgren, M. Samiotaki, M. Kwiatkowski, B. P. Chowdhary, and U. Landegren, "Padlock probes: circularizing oligonucleotides for localized DNA detection," Science **265**, 2085 (1994).

[57] A. Fire and X. Si-Qun, "Rolling replication of short DNA circles," P. Natl. Acad. Sci. USA **92**, 4641 (1995).

[58] D. Liu, S. L. Daubendiek, M. A. Zillman, K. Ryan, and E. T. Kool, "Rolling circle DNA synthesis: Small circular oligonucleotides as efficient templates for DNA polymerases." J. Am. Chem. Soc. **118**, 1587 (1996).

[59] K. Enpuku, H. Watanabe, Y. Higuchi, T. Yoshida, H. Kuma, N. Hamasaki, M. Mitsunaga, H. Kanzaki, and A. Kandori, "Characterization of magnetic markers for liquid-phase immunoassays using brownian relaxation," Jpn. J. Appl. Phys. **51**, 023002 (2012).

[60] R. Haraszczuk, S. Yamada, M. Kakikawa, and T. Ueno, "Monitoring minute changes of magnetic markers' susceptibility by SV-GMR needle-type probe," IEEE Trans. Magn. **47**, 2584 (2011).

[61] F. Oisjoen, J. Schneiderman, M. Zaborowska, K. Shunmugavel, P. Magnelind, A. Kalaboukhov, K. Petersson, A. Astalan, C. Johansson, and D. Winkler, "Fast and sensitive measurement of specific antigen-antibody binding reactions with magnetic nanoparticles and HTS SQUID," IEEE Trans. Appl. Supercond. **19**, 848 (2009).

[62] A. D. Henriksen, B. T. Dalslet, D. H. Skieller, K. H. Lee, F. Okkels, and M. F. Hansen, "Planar Hall effect bridge magnetic field sensors," Appl. Phys. Lett. **97**, 013507 (2010).

[63] S. Sun, "Recent advances in chemical synthesis, self-assembly, and applications of FePt nanoparticles," Adv. Mater. **18**, 393 (2006).

[64] X. J. A. Janssen, A. J. Schellekens, K. Van Ommering, L. J. Van Ijzendoorn, and M. W. J. Prins, "Controlled torque on superparamagnetic beads for functional biosensors," Biosens. Bioelectron. **24**, 1937 (2009).

[65] L. Neél, "Théorie du traînage magnétique des ferromagnétiques en grains fins avec applications aux terres cuites," Ann. Géophys **5**, 99 (1949).

[66] W. Brown, "Thermal fluctuations of a single-domain particle," Phys. Rev. **130**, 1677 (1963).

[67] P. Debye, "Polar molecules," Chemical Catalogue Co. (1929).

[68] K. S. Cole and R. H. Cole, "Dispersion and absorption in dielectrics I. alternating current characteristics," J. Chem. Phys. **9**, 341 (1941).

[69] V. Gehanno, P. P. Freitas, A. Veloso, J. Ferrira, B. Almeida, J. B. Soasa, A. Kling, J. C. Soares, and M. F. Da Silva, "Ion beam deposition of Mn-Ir spin valves," IEEE Trans. Magn. **35**, 4361 (1999).

[70] J. Nogués and I. K. Schuller, "Exchange bias," J. Magn. Magn. Mater. **192**, 203 (1999).

[71] T. B. G. Hansen, C. D. Damsgaard, B. T. Dalslet, and M. F. Hansen, "Theoretical study of in-plane response of magnetic field sensor to magnetic beads magnetized by the sensor self-field," J. Appl. Phys. **107**, 124511 (2010).

[72] H. Bruus, *Theoretical microfluidics*, Vol. 18 (Oxford University Press, USA, 2007).

[73] G. Friedman and B. Yellen, "Magnetic separation, manipulation and assembly of solid phase in fluids," Curr. Opin. Colloid Interface Sci. **10**, 158 (2005).

[74] A. Engel and R. Friedrichs, "On the electromagnetic force on a polarizable body," Am. J. Phys. **70**, 428 (2001).

[75] F. W. Østerberg, B. T. Dalslet, C. D. Damsgaard, S. C. Freitas, P. P. Freitas, and M. F. Hansen, "Bead capture on magnetic sensors in a microfluidic system," IEEE Sens. J. **9**, 682 (2009).

[76] D. J. Griffiths and R. College, *Introduction to electrodynamics*, Vol. 3 (Prentice Hall New Jersey, 1999).

[77] R. Bozorth, *Ferromagnetism*, Vol. 1 (Wiley-VCH, 1993).

[78] D. Sabourin, D. Snakenborg, and M. Dufva, "Interconnection blocks: a method for providing reusable, rapid, multiple, aligned and planar microfluidic interconnections," J. Micromech. Microeng. **19**, 035021 (2009).

[79] D. Sabourin, P. Skafte-Pedersen, M. J. Søe, M. Hemmingsen, M. Alberti, V. Coman, J. Petersen, J. Emnéus, J. P. Kutter, D. Snakenborg, F. Jørgensen, C. Clausen, K. Holmstrøm, and M. Dufva, "The MainSTREAM component platform: A holistic approach to microfluidic system design," Journal of Laboratory Automation (2012).

[80] R. L. E. David, *CRC Handbook on Chemistry and Physics* (CRC Press, Boca Raton, 2005).

[81] C. Mikkelsen, M. F. Hansen, and H. Bruus, "Theoretical comparison of magnetic and hydrodynamic interactions between magnetically tagged particles in microfluidic systems," J. Magn. Magn. Mater. **293**, 578 (2005).

[82] B. T. Dalslet, M. Donolato, and M. F. Hansen, "Planar Hall effect sensor with magnetostatic compensation layer," Sens. Actuators, A **174**, 1 (2011).

[83] T. Zardán Gómez de la Torre, D. Herthnek, H. Ramachandraiah, P. Svedlindh, M. Nilsson, and M. Strømme, "Evaluation of the Sulfo-Succinimidyl-4-(N-Maleimidomethyl) Cyclohexane-1-Carboxylate coupling chemistry for attachment of oligonucleotides to magnetic nanobeads," J. of Nanosci. Nanotechno. **11**, 8532 (2011).

[84] J. Baudry, C. Rouzeau, C. Goubault, C. Robic, L. Cohen-Tannoudji, A. Koenig, E. Bertrand, and J. Bibette, "Acceleration of the recognition rate between grafted ligands and receptors with magnetic forces," P. Natl. Acad. Sci. USA **103**, 16076 (2006).

[85] I. Koh and L. Josephson, "Magnetic nanoparticle sensors." Sensors **9**, 8130 (2009).

Appendix A

Magnetization curve for 80 nm beads

In this appendix a magnetization curve for 80 nm BNF-stach plain beads from Micromod is shown. The curve has been measured on a sample containing 7 mg og beads with a LakeShore model 7407 vibration sample magnetometer (VSM). From the measurement it is seen that the beads have small hysteresis. By ignoring the hysteresis and fitting, the magnetic susceptibility is found to 1.43.
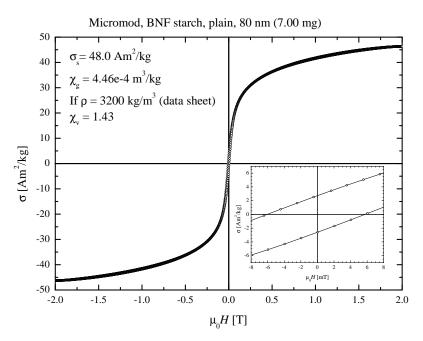

Fig. A.1: VSM measurement of 80 nm BNF-stach plain beads from Micromod.

Appendix B

Optimization of lock-in amplifier settings

This appendix contains supplementary material for Section 3.4.1.

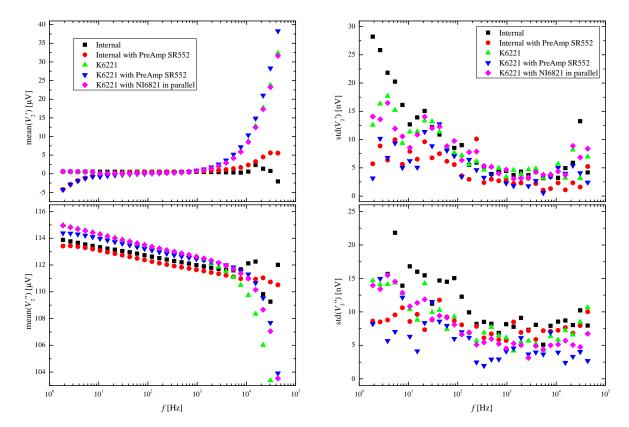## B.1   Stanford Research System SR830 lock-in amplifier

The factors that potentially would influence the measurement results with the SR830 lock-in are listed in Table B.1 along with the possible settings for each factor and which settings were believed to be the best. In the following it will be shown which settings should be used such that the measurements at both correct and as reproducible as possible. It was assumed that the effect of the factors did not interact and the effect of each factor was therefore investigated by changing the setting for one factor at a time. Thus, a series of frequency sweeps were measured changing each setting at a time while keeping the remaining at the initial values. The mean value and standard deviation were calculated for each frequency. The mean values were used to determine if the signal obtained for a setting were correct and the standard deviations were used as a measure of the reproducibility.

The effects of changing power supply, using the SR552 preamplifier and connecting a NI USB-6821 data acquisition box in parallel were investigated first. 41 frequency sweep were performed for each option, from which the mean and the standard deviation were calculated for each frequency. The mean and standard deviation for each configuration are plotted in Fig. B.1 and Fig. B.2, respectively.

From Fig. B.1 it is seen that the phase shifts at high frequencies were much larger when using the Keihtley 6221 than when using the internal power supply of the lock-in. It is also seen that the SR552 preamplifier gave rise to a attenuation of the signal for frequencies below 10 Hz, which was due to the preamplifier being AC coupled. From Fig. B.2 it is seen that the lowest standard deviations were achieved when the SR552 preamplifier was used, and the highest standard deviations were measured when the internal power supply was used. From these results it was concluded that using the Keihtley 6221 was better than using the internal power supply of the SR830 lock-in amplifier. It is also concluded that using the SR552 preamplifier results in the lowest standard deviations. However, the sub 10 Hz decrease in signal could cause problems,

Table B.1: Factors believed to influence measurements with SR830. The second column shows the available settings. The third column shows the settings believed to be the best from experience. The horizontal line separated the physical factors from lock-in setting.

Factor	Possible settings	Initial settings
Power supply	Keihtley 6221 or SR830 Internal	Keihtley 6221
Pre amplifier	Not Connected or SR552	Not Connected
NI USB-6821	Not Connected or Parallel	Not Connected
Coupling	AC or DC	DC
Shield	Ground or Float	Ground
Reserve	High, Normal or Low Noise	Low Noise
Slope	6, 12, 18 or 24 dB/Oct	24 dB/Oct
Synchronous filter	On or Off	Off
Line filters	Out, 50 Hz, 60 Hz or Both In	Out

Fig. B.1: Mean of repeated measurements as function of frequency for SR830 with different power supplies.

Fig. B.2: Standard deviation of repeated measurements as function of frequency for SR830 with different power supplies.

which is addressed below. It is also seen that connecting the NI USB-6821 in parallel with the lock-in amplifier did not affect the results.

To check if measurements performed with the preamplifier were given correct results, mea-

surements on 80 nm beads were performed both with and without the preamplifier. As a reference, measurements were also performed with the HF2LI without any preamplification. The results of this test is shown in Fig. B.3. Here it is seen that the measurements without the preamplifier coincided with the measurements from the HF2LI. The measurements with the preamplifier resulted in an out-of-phase signal that was generally larger, and for the in-phase signal it does not match the two other measurements for frequencies above 10 kHz. The to large out-of-phase signal could be due to the amplification of the preamplifier not being exactly 100. The errors above 10 kHz were most likely due to an additional phase shift (see Fig. B.1) that could not be corrected for appropriately. In order to obtain correct signals a different phase-shift compensation would be necessary. This means that the preamplifiers should only be used if the reproducibility is more important than obtaining correct signals, which could be the case if small changes in the signals were to be detected.
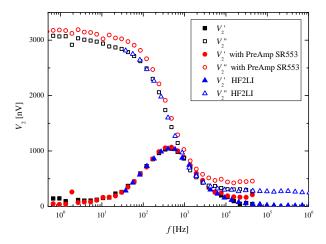
Fig. B.3: Caparison of frequency sweeps performed with SR830 with and without SR552 preamplifier and frequency sweep measured with HF2LI.

The six lock-in settings were investigated using the Keihtley 6221 as power supply and measuring without the preamplifier. The optimal lock-in settings for the SR830 lock-in amplifier were determined by repeating 29 frequency sweeps for each possible setting. The mean and standard deviation for the frequency sweeps were Coupling, Shield, Reserve, Slope and Synchronous filter were changed are plotted in Fig. B.4 and Fig. B.5, respectively. From these figures the following is observed:

- Setting the coupling to AC will resulted in the same decrease in signal for low frequencies as using the preamplifier, but the AC coupling alone did not decrease the noise. Thus, DC coupling was the preferred option.

- Setting the shield to float instead of to ground lowered the noise at high frequencies, but increased it at low. Since the biggest challenge was to decrease the noise at low frequencies the shield was set to ground.

- The synchronous filter did not affect the measurements and were therefore turned off, this was also expected as the sampling method was actually a manual synchronous filter.

- The reserve affected the noise, choosing normal reserve instead of low noise increased the standard deviation for all frequencies. Thus, it was very important to use the low noise reserve.

- The slope did not result in any significant changes to the signal or the noise. Chosen a low slope would allow for decreasing the waiting time. However, lowering it caused the signals to oscillate more, which would then require longer time constants. It was therefore decided to keep it at 24 dB/Oct.
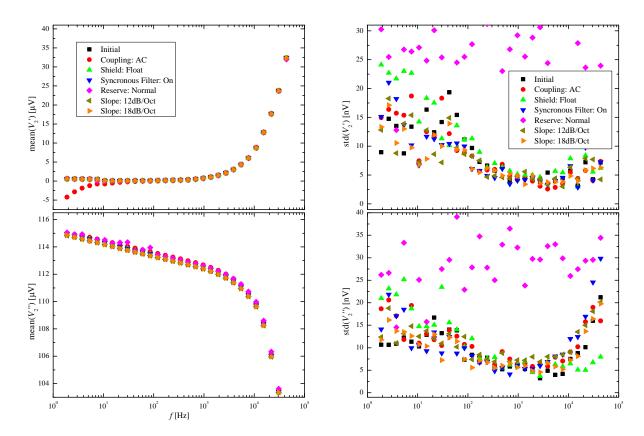
Fig. B.4: Mean from 29 repeated frequency as function of frequency for the following Lock-in settings: Coupling, Shield, Reserve, Slope and Synchronous filter.

Fig. B.5: Standard deviation from 29 repeated frequency as function of frequency for the following Lock-in settings: Coupling, Shield, Reserve, Slope and Synchronous filter.

Similar measurements were also performed for the line filter and plotted in Fig. B.6 and Fig. B.7. From these results it was also be seen that using the line filter are not appropriate as they filter away too broad a spectrum of frequencies. All in all the only setting that is found not to have been chosen optimally from the beginning is the slope, which does not improve the measurement, but could allow for a reduced waiting time.
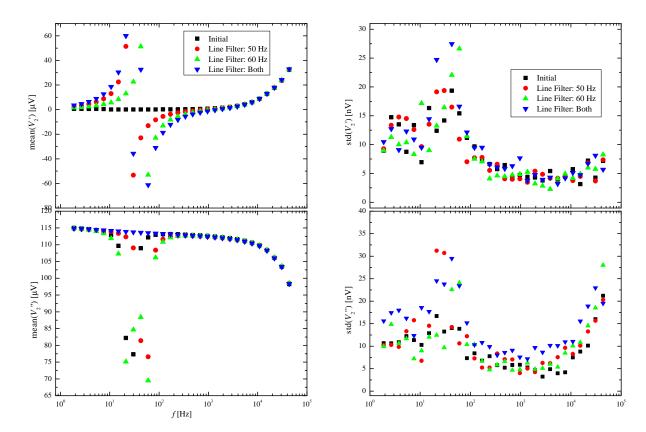
Fig. B.6: Mean from 29 repeated frequency as function of frequency for the line filter setting.

Fig. B.7: Standard deviation from 29 repeated frequency as function of frequency for the line filter setting.

B.2 Zurich Instrument HF2LI lock-in amplifier

To check whether the time constant (TC), sample rate (SR) or slope (S) affected the obtained value or the reproducibility of the value a full factorial design was made for frequencies of 37.7 Hz, 4667 Hz and 577764 Hz. The measurements were repeated 19 times to eliminate random fluctuations. The values used for the ANOVA are the second harmonic out-of-phase signal. First ANOVA is performed for the mean of the 19 repetitions, these results are shown in Tab B.2, form which it is seen that only factor influencing the mean is the frequency. Then ANOVA is performed on the standard deviation of the 19 repetitions, which is shown in Tab B.3. It is seen that only the frequency affects the standard deviation of the 19 repetitions. This was also expected since the low measurement at low frequency will be more affected by noise than the two higher frequencies. The frequency is in fact not a lock-in setting as it is swept when measuring Brownian relaxation.

Table B.2: ANOVA table for the mean of 19 repetitions.

Source	Sum Sq.	d.f.	Mean Sq.	F	Prob>F
f	90642488.52	2	45321244.26	634607.39	0
TC	21.183	1	21.1827	0.3	0.5992
SR	18.652	1	18.6524	0.26	0.6216
S	16.966	1	16.9662	0.24	0.6376
f*TC	92.801	2	46.4004	0.65	0.545
f*SR	65.375	2	32.6877	0.46	0.6467
f*S	106.914	2	53.4568	0.75	0.5004
TC*SR	80.281	1	80.2812	1.12	0.3167
TC*S	50.429	1	50.4295	0.71	0.4225
SR*S	37.106	1	37.1063	0.52	0.4893
Error	642.746	9	71.4162		
Total	90643620.98	23			

Table B.3: ANOVA table for the standard deviation of 19 repetitions.
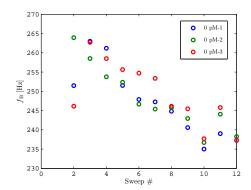
Source	Sum Sq.	d.f.	Mean Sq.	F	Prob>F
f	905.7	2	452.848	11.88	0.003
TC	139.24	1	139.238	3.65	0.0883
SR	61.52	1	61.523	1.61	0.2358
S	130.65	1	130.651	3.43	0.0971
f*TC	228.41	2	114.203	3	0.1006
f*SR	106.18	2	53.089	1.39	0.2971
f*S	264.18	2	132.092	3.47	0.0765
TC*SR	15.35	1	15.35	0.4	0.5415
TC*S	87.83	1	87.827	2.3	0.1633
SR*S	31.41	1	31.415	0.82	0.3876
Error	343.02	9	38.113		
Total	2313.49	23			

Appendix C

Parameters used for double Cole–Cole model

In this Appendix the values of $f_{B,free}$, α_{free}, $f_{B,bound}$ and α_{bound} used in section 7.2.4.2 are determined.

First $f_{B,free}$ and α_{free} are estimated from three negative references (0 pM). The model in Eq. (7.1) is fitted to the data of each frequency sweep for the three repetitions. In the model $V_{0,bound}$ was set to V_∞, such that only one peak will be fitted to the data. The extracted Brownian relaxation frequencies and α values are shown vs. sweep number in Fig. C.1 and Fig. C.2, respectively. In Fig. C.3 the fit and the corresponding in-phase sensor signals of the 12th sweeps are shown for each of the three measurements without beads.
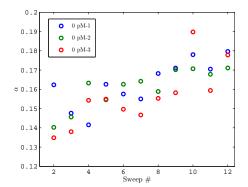
Fig. C.1: Brownian relaxation frequency of free beads extracted from Cole–Cole fits vs. sweep number.

Fig. C.2: α values of free beads extracted from Cole–Cole fits vs. sweep number.

From Fig. C.1 it is seen that the extracted Brownian relaxation frequency decreases from sweeps 5–12. This is not ideal as the aim with these fits was to estimate a general set of f_B and α for free beads. Due to sedimentation of beads bound to DNA coils only the last 5 sweeps will later be used for analyzing the coil concentration, for this reason the values of $f_{B,free}$ and α_{free} are taken as an average over the values extracted from sweeps 8–12. This results in $f_{B,free} = 241(4)$ Hz and $\alpha_{free} = 0.17(1)$.
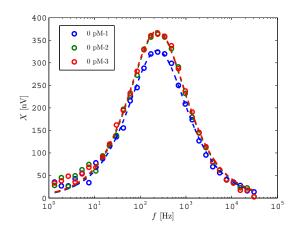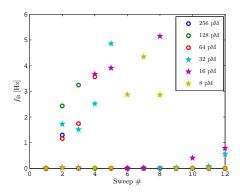
Fig. C.3:   Data of 12th frequency sweeps for three
negative references, with fits to the Cole–Cole model.

Now that estimates of $f_{\mathrm{B,free}}$ and α_{free} have been found, the corresponding values need to be determined for the bound beads. This is done by fixing $f_{\mathrm{B,free}}$ and α_{free} to the values found above and setting $f_{\mathrm{B,bound}}$ and α_{bound}, $V_{\mathrm{0,bound}}$ and $V_{\mathrm{0,free}}$ as free parameters. Fitting of this model is performed to data for coil concentrations of 8 pM and above. The extracted values of $f_{\mathrm{B,bound}}$ and α_{bound} are plotted in Fig. C.4 Fig. C.5, respectively. It is seen that the Brownian relaxation frequency is generally close to 0 Hz and that the α-values are highest for large coil concentrations. Since the higher coil concentrations have the larger signal from beads bound the DNA coils it is decided to average over the coil concentrations ranging from 16 pM – 256pM for sweeps 8–12. This results in $f_{\mathrm{B,bound}} = 0.1(2)$ Hz and $\alpha_{\mathrm{bound}} = 0.76(6)$.
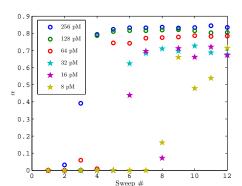
Fig. C.4:   Brownian relaxation frequency of bound
beads extracted from Cole–Cole fits vs. sweep number.

Fig. C.5: α values of bound beads extracted from
Cole–Cole fits vs. sweep number.

Now estimates have been found for $f_{\mathrm{B,free}}$, α_{free}, $f_{\mathrm{B,bound}}$ and α_{bound} and only $V_{\mathrm{0,free}}$ and $V_{\mathrm{0,bound}}$ are left as free parameter for fitting.

Paper   I

G. Rizzi, N. C. Lundtoft, F. W. Østerberg and M. F. Hansen
"Reversible and Irreversible Temperature-induced Changes in Exchange-biased Planar Hall Effect Bridge (PHEB) Magnetic Field Sensors"

Reversible and Irreversible Temperature-induced Changes in Exchange-biased Planar Hall Effect Bridge (PHEB) Magnetic Field Sensors

G. Rizzi, N. C. Lundtoft, F. W. Østerberg, [*] M. F. Hansen

Department of Micro- and Nanotechnology, Technical University of Denmark
DTU Nanotech, Building 345B, DK-2800 Kongens Lyngby, Denmark
[*] E-mail: Mikkel.Hansen@nanotech.dtu.dk

Abstract: We investigate the changes of planar Hall effect bridge magnetic field sensors prepared without field annealing and with field annealing at 240 °C, 280 °C and 320 °C when these are exposed to temperatures between 25 °C and 90 °C. From analyses of the sensor response vs. magnetic field we extract the exchange bias field H_{ex}, the uniaxial anisotropy field H_K and the anisotropic magnetoresistance (AMR) of the exchange biased thin films at a given temperature. By comparing measurements carried out at elevated temperatures T with measurements carried out at 25 °C after exposure to T, we separate the reversible from the irreversible changes of the sensors. The un-annealed sample shows a significant irreversible change of H_{ex} and H_K upon exposure to temperatures above room temperature. The irreversible changes are significantly reduced but not eliminated by the low-temperature field annealing. The reversible changes with temperature are essentially the same for all samples. The results are not only relevant for sensor applications but also demonstrate the method as a useful tool for characterizing exchange-biased thin films. *Copyright © 2012 IFSA.*

Keywords: Magnetic biosensors, Planar Hall effect, Exchange bias, Anisotropic magnetoresistance.

1. Introduction

For applications of any sensor, it is important to know and correct for the effect of varying temperatures of the sensor environment. Moreover, it is important to be aware of irreversible changes of the sensor parameters induced by varying temperatures of the environment. Planar Hall effect magnetic field sensors have proven attractive for magnetic field sensing due to their low intrinsic noise

and potentially high signal-to-noise ratio [1]. We are investigating exchange-biased planar Hall effect sensors for magnetic biodetection [2, 3].

Here, we systematically study the changes of the response of planar Hall effect bridge sensors [4] upon exposure of these to temperatures between 25 °C and 90 °C. These temperatures correspond to the range typically employed in DNA based assays with amplification by polymerase chain reaction (PCR). From analyses of magnetic field sweeps of the sensor response we extract the parameters of thin film sensor stacks at all investigated temperatures and by performing measurements at 25 °C performed after all measurements at elevated temperatures we quantify and distinguish reversible and irreversible changes of each of the sensor parameters. These studies are carried out for a stack which is not exposed to any magnetic field annealing and for stacks that are field annealed at 240 °C, 280 °C and 320 °C. The results are generally relevant for applications of exchange-biased thin film sensors and demonstrate the method as a general tool for studying thin film magnetic properties vs. temperature.

2. Sensor Model

Below, we consider a material showing anisotropic magnetoresistance (AMR) with resistivities $\rho_\parallel$ and $\rho_\perp$ parallel and perpendicular to the magnetization vector **M**, respectively. The AMR ratio, defined as $\Delta\rho/\rho_{av}$, where $\Delta\rho \equiv \rho_\parallel - \rho_\perp$ and $\rho_{av} \equiv \rho_\parallel/3 + 2\rho_\perp/3$, assumes a value of 2-3 % for permalloy ($Ni_{80}Fe_{20}$). Fig. 1 shows a Wheatstone bridge consisting of four pairwise identical elements of the material of width w and length l. The resistance of a single element forming an angle α to the x-axis and with a homogeneous magnetization forming an angle θ to the x-axis is [4]

$$R(\alpha,\theta) = \tfrac{l}{wt}\left[\tfrac{1}{2}\left(\rho_\parallel + \rho_\perp\right) - \tfrac{1}{2}\Delta\rho\,\cos\left[2(\theta-\alpha)\right]\right],\qquad(1)$$

where t is the thickness of the element. A current I injected in the x-direction results in the bridge output

$$V_y = \tfrac{1}{2}I\left[R(\alpha_+,\theta_+) - R(\alpha_-,\theta_-)\right],\qquad(2)$$

where the orientation of magnetization of the elements forming angles α_+ and α_- to the x-axis are denoted θ_+ and θ_-. The maximum bridge output, obtained when $\alpha_+ = -\alpha_- = \pi/4$, is given by

$$V_y = \tfrac{1}{4}I\,\Delta\rho\,\tfrac{l}{wt}\left[\sin(2\theta_+) + \sin(2\theta_-)\right] \equiv \tfrac{1}{4}V_{pp}\left[\sin(2\theta_+) + \sin(2\theta_-)\right],\qquad(3)$$

where we have introduced the nominal peak-to-peak sensor output voltage $V_{pp} = I\Delta\rho l/(wt)$ [4]. Equation (3) is identical to the output voltage from a cross-geometry planar Hall effect sensor multiplied by the geometrical amplification factor l/w. Therefore, we have termed the above sensors planar Hall effect bridge (PHEB) sensors [4].

Theoretically, the angles θ_+ and θ_- can be found by minimizing the single domain energy density for α_+ and α_-, respectively. We divide the volume energy density by the saturation flux density to form the normalized energy density u

$$u = -H_y\,\sin\theta - H_{ex}\,\cos\theta - \tfrac{1}{2}H_K\,\cos^2\theta - \tfrac{1}{2}H_s\,\cos^2(\alpha-\theta),\qquad(4)$$

which expresses the energy density in units of the H-field. In Eq. (4), H_y is the external magnetic field applied in the y-direction, H_{ex} is the exchange field due to a unidirectional anisotropy along $\theta = 0$,

H_K is the anisotropy field due to a uniaxial anisotropy along $\theta = 0$ and H_s is the shape anisotropy field of the element (preferring a magnetization orientation with $\theta = \alpha$). Defining the demagnetization factors along and perpendicular to an element as $N_{\parallel}$ and $N_{\perp}$, respectively, the shape anisotropy field is $H_s = (N_{\perp} - N_{\parallel})M_s$ [5]. Our previous work [4] considered only the case of negligible shape anisotropy where $\theta_+ = \theta_- = \theta$.

We write the low-field sensor output voltage as

$$V_y = S_0 I H_y, \tag{5}$$

where we have defined the low-field sensitivity S_0. For negligible shape anisotropy, minimization of Eq. (4) for $H_s = 0$ and small values of θ yields

$$S_0 = \frac{l}{w} \frac{\Delta\rho}{t} \frac{1}{H_K + H_{ex}}. \tag{6}$$

If the shape anisotropy is significant but still small, the sensor response curve will be modified such that it flattens near zero applied field, resulting in a decrease of S_0 compared to Eq. (6), while still maintaining a peak-to-peak signal V_{pp} given by Eq. (3) (unpublished results).

3. Experimental

A batch of four wafers with top-pinned PHEB sensors was prepared on 4" silicon substrates with a 1 μm thick thermally grown oxide as follows: First, the stack Ta(3 nm)/Ni$_{80}$Fe$_{20}$(30 nm)/Mn$_{80}$Ir$_{20}$ (20 nm)/Ta(3 nm) was grown in a K. J. Lesker company CMS 18 multitarget sputter system in an Argon pressure of 3 mTorr with an RF substrate bias of 3W. The easy magnetization direction and axis of the permalloy layer were defined by applying a uniform magnetic field of $\mu_0 H_x = 20$ mT along the x-axis during the deposition. Subsequently, contacts of Ti(10 nm)/Pt(100 nm)/Au(100 nm)/Ti(10 nm) were deposited by e-beam evaporation and defined by lift-off. The negative lithography process employed a reversal baking step at 120 °C for 120 s on a hot plate in zero magnetic field.

One of the nominally identical four wafers was not given any further treatment and was labeled 'not annealed'/'un-annealed'. The other three wafers were annealed in vacuum in the sputter deposition chamber at temperatures of 240 °C, 280 °C and 320 °C for 1 hour in the presence of a saturating magnetic field $\mu_0 H_x = 20$ mT applied along the x-axis.

The dimensions of the elements of all investigated sensors were w=20 μm and $l = 280$ μm (Fig. 1). All sensors were surrounded by magnetic stack with a 3 μm gap to reduce the shape anisotropy of the elements. The simple theory presented in section 2 accounts for the elements but not the corners connecting the elements. The effect of corners was therefore investigated by finite element analysis of the sensor output for a single domain sensor structure. The calculations showed a sensor response that can be described by an effective sensor aspect ratio $l/w = 14.87$, which is 6% higher than the nominal one of l/w=14.

The magnetic properties of continuous thin films with dimensions 3×3 mm^2 were characterized for all four wafers using a LakeShore model 7407 vibrating sample magnetometer (VSM) and values of H_{ex} and H_K were extracted from easy axis hysteresis loop measurements.
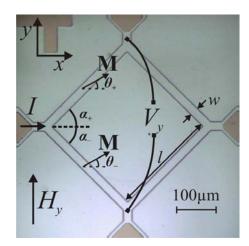
Fig. 1. Image of planar Hall effect magnetic bridge sensor with
definition of geometric variables and symbols.

Values of the stack sheet resistances $\rho_\parallel/t$ and $\rho_\perp/t$ for the four wafers were obtained from electrical measurements of the resistance on transmission line test structures placed near the investigated sensor chips on the wafers in saturating magnetic fields applied parallel and perpendicular to the current, respectively.

Measurements of the sensor response vs. applied field were carried out as follows: the sensors were biased with an alternating current of root-mean-square (RMS) amplitude $I_{RMS} = 1/\sqrt{2}$ mA and frequency $f = 65$ Hz provided by a Keithley 6221 precision current source. A Stanford Research Systems model SR830 lock-in amplifier was used to record the first harmonic in-phase root-mean-square (RMS) signal $V_{y,RMS}$. Note, that Eq. (3) also holds for the RMS values I_{RMS} and $V_{y,RMS}$. To simplify the notation below, we will therefore refer to the RMS values as V_y and I. The applied magnetic field $\mu_0 H_y$ was generated by a custom built electromagnet and monitored using commercially available Hall probes. Field sweeps were carried out by sweeping the field in both directions between $\mu_0 H_y = \pm 40$ mT. The sensor temperature was regulated to stability better than 0.1°C by use of a Peltier element, platinum RTD and a precision temperature controller. Sensor characteristics of all sensors were measured at temperatures from 25°C to 90°C in steps of 10°C. Each measurement performed at an elevated temperature was followed by a reference measurement performed at 25°C.

In addition, we also studied the effect of repeated exposure to 90 °C for an un-annealed sensor and a sensor from the wafer that was field annealed at 280 °C. These temperature cycling experiments were carried out as follows: first, the temperature was set to 25 °C and left for 10 min before a field sweep was carried out. The field sweep took about 8 min to complete. Then, the temperature was set to 90 °C and the measurement procedure was repeated. Finally, this cycle between 25 °C and 90 °C was repeated for about 7 hours.

4. Results

4.1. As Deposited Samples

In this section, we present results obtained for the samples at 25 ºC in their as-deposited state (i.e. prior to sensor characterization at elevated temperatures). We establish the model used for analyzing the field sweeps and compare to electrical and magnetic reference measurements.

The sensor signal V_y normalized with the bias current I, was measured vs. the sweeping field H_y for all four wafers. Fig. 2 shows the initial field sweeps measured for the samples with no annealing and with annealing at 280 °C. The annealing is observed to shift the peak of the sensor response towards lower field values and to increase the low-field sensitivity. The peak-to-peak value of the sensor response is found to be essentially unchanged by the annealing.
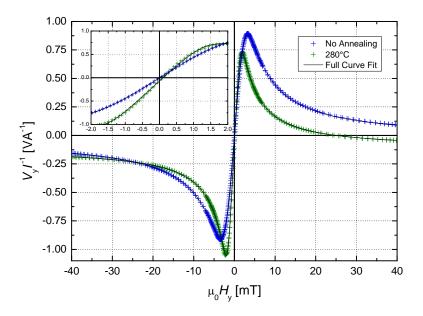

Fig. 2. Normalized sensor output (V_y/I) vs. external field (H_y) for sensors from the wafers with no annealing and with field annealing at 280°C in their initial condition. The inset shows the low-field region of the sensor response. The lines are fits to the single domain model for the sensor response described in the text.

The solid lines in Fig. 2 are least-squares fits to Eq. (3) with values of θ_+ and θ_- obtained by minimizing Eq. (4). The investigated free parameters in the fitting were V_{pp}/I, H_{ex} and H_K. The value of H_s was found to vary only marginally between the different temperature and annealing conditions and was fixed to the average value $\mu_0 H_s = 0.789$ mT obtained from fitting data for all sensors and temperatures with this parameter set free. In the fitting we also allowed for offsets in the sensor output and the applied field. The quality of all fits was comparable to those shown in Fig. 2. Table 1 shows the values of $\mu_0 H_{ex}$ and $\mu_0 H_K$ obtained from the VSM measurements, the values of $\Delta\rho/t$ and the AMR ratio obtained from reference electrical measurements on the transmission line structure as well as the values of $\mu_0 H_{ex}$, $\mu_0 H_K$, S_0 and V_{pp}/I obtained from fits to field sweeps of the sensor response. Values reported for the low-field sensitivities S_0 were taken as the slope of the fits between ± 0.15 mT.

Table 1. Parameters of the magnetic stack obtained from VSM measurements, electrical measurements on a transmission line structure and from fits to sensor field sweeps. All measurements were carried out at 25ºC on as-deposited samples (i.e. prior to any experiments at elevated temperatures). Numbers in parentheses indicate the uncertainties reported by the least squares fitting routine.

Annealing conditions	VSM		Electrical ref.		Sensor field sweeps			
	$\mu_0 H_{ex}$ [mT]	$\mu_0 H_K$ [mT]	$\Delta\rho/t$ [Ω]	AMR [%]	$\mu_0 H_{ex}$ [mT]	$\mu_0 H_K$ [mT]	S_0 [V/(AT)]	V_{pp}/I [V/A]
No annealing	2.89(5)	0.39(5)	0.1296(1)	1.88	2.66(1)	0.90(3)	465	1.779(2)
240 °C	2.02(5)	0.41(5)	0.1318(1)	2.03	1.91(1)	0.52(2)	637	1.785(3)
280 °C	1.90(5)	0.50(5)	0.1319(3)	1.95	1.60(1)	0.50(2)	699	1.764(4)
320 °C	1.39(5)	0.46(5)	0.1317(1)	2.03	1.32(1)	0.34(3)	807	1.768(7)

The values of H_{ex} obtained from VSM measurements and fits to the sensor field sweeps correspond well to each other although the values from the field sweeps are slightly lower than those obtained from the VSM measurements. The values of H_K obtained by VSM and from the sensor field sweeps are comparable for the annealed samples, but they differ about a factor of two for the un-annealed sample. The main effect of the low-temperature annealing is that H_{ex} is found to decrease monotonously with increasing annealing temperature. A decrease of about a factor of two is observed for annealing at 320 °C. The values of H_K extracted from the sensor field sweeps are found to decrease with increased annealing temperature, whereas no systematic change is found from the VSM studies. The value of $\Delta\rho/t$ remains essentially unchanged by the annealing. The low-field sensitivity is found to increase with annealing and increases almost by a factor of two for the highest annealing temperature.

4.2. Temperature Dependence of Parameters

In this section, we first present results of the experiments carried out at elevated temperatures for the un-annealed sample and show that our measurement procedure enables us to clearly distinguish reversible and irreversible changes of the sensor parameters upon exposure to a given elevated temperature. Then, we report the results of the corresponding experiments carried out on sensors from the low-temperature field annealed wafers. All parameters shown below have been obtained from fits to sensor field sweeps as described in section 4.1.

Fig. 3 shows the values of S_0, H_{ex} and H_K obtained from analysis of sensor field sweeps in a series of experiments carried out on a sensor from the wafer with no annealing at sequentially increasing temperatures T. First, the sensor response was measured at 25 °C. Then, the temperature was increased to 30 °C and the sensor response was measured after a waiting time of 2 min and finally, the temperature was reduced to 25 °C to carry out a reference measurement after a waiting time of 2 min. This procedure was repeated for temperatures increasing up to 90 °C in steps of 10 °C. The sensor parameters measured at the elevated temperature T result from the sum of reversible and irreversible changes, whereas the series of reference measurements carried out at 25 °C show only the irreversible changes. This enables us to clearly distinguish the reversible and irreversible changes of the sensor parameters as indicated by the colored areas in Fig. 3.

In Fig. 3, the value of S_0 is found to increase about 20% when the temperature is increased from 25 °C to 90 °C. Slightly more than half of this increase is irreversible. The values of H_{ex} and H_K are found to decrease approximately linearly with increasing temperature with temperature coefficients of −0.42%/°C (27% total decrease) and −0.68%/°C (44% total decrease), respectively, in good agreement with a previous study [6]. For H_{ex} about 20% of the change is irreversible and for H_K about 50 % of the change is irreversible. Thus, the irreversible changes are significant for this sample.

Corresponding series of experiments were carried out for the wafers exposed to the low-temperature field annealing.

Fig. 4(a) shows the values of V_{pp}/I for the measurements carried out on all samples. These values are proportional to $\Delta\rho/t$. The values obtained at 25 °C are close to identical and show no systematic variation with annealing conditions. Upon exposure to elevated temperatures, the values are found to decrease linearly with temperature with a temperature coefficient of −0.22 %/°C. The change is found to be fully reversible, i.e. no irreversible changes result from the increased temperature. This shows that the low-temperature field annealing and the experiments performed at elevated temperatures do not result in any detectable changes of the AMR properties of the sensor stack.

Fig. 4(b) shows the values of the low-field sensitivities S_0 normalized to the initial values obtained at 25 °C (given in Table 1) for the four investigated wafers as function of the measuring temperature T.

The data for the sample with no field annealing from Fig. 3 are shown for comparison. The field annealed samples show a much smaller temperature variation than the sample with no annealing. For the sample annealed at 240 °C the relative change of S_0 is about 7 % when the temperature is increased to 80 °C, but more than half of this change is irreversible. For the sample annealed at 280 °C, the points measured at T coincide with the reference points measured at 25 °C, indicating that the entire change of S_0 of about 3 % is irreversible. For the sample annealed at 320 °C, there is a net decrease of S_0 with T of about 2 % resulting from an irreversible increase of S_0 of about 3 % and a reversible decrease of S_0 of about 5 %.
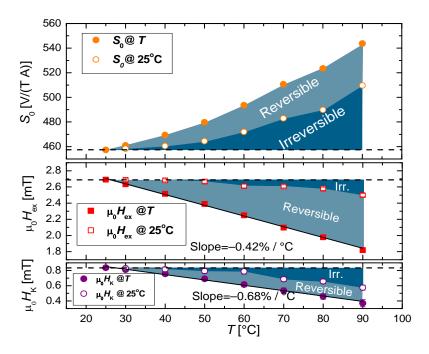
Fig. 3. Values of S_0 (top), H_{ex} (middle) and H_K (bottom) extracted from fits of the field sweeps on the un-annealed sample. Filled points are measured at temperature T, empty points are measured at the reference temperature 25°C after exposure to T. The full lines are linear fits corresponding to the indicated temperature coefficients.
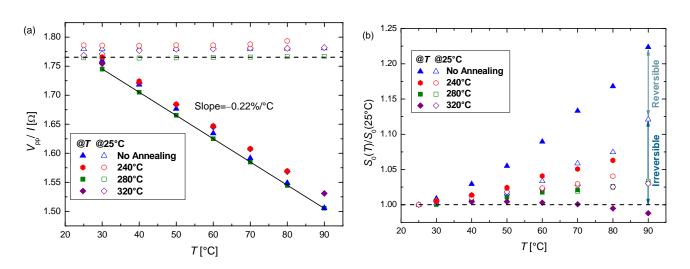
Fig. 4. Values of (a) the peak-to-peak sensor response V_{pp}/I and (b) the low-field sensitivity S_0 normalized to its initial value at 25°C obtained from field sweep fits. Different data sets are for sensors from wafers with the indicated annealing conditions. Filled points are measured at T, open points are measured at 25 °C after exposure to temperature T. The arrows to the right indicate the reversible and irreversible change for the un-annealed sample at T=90 °C.

Figs. 5(a) and (b) show the values of H_{ex} (normalized to their initial values given in Table 1) and H_K obtained for the four investigated wafers as function of the measuring temperature T, respectively. For all annealing conditions, the reversible change of H_{ex} with temperature is linear and can be described by the temperature coefficient –0.37%/°C. For the un-annealed sample the irreversible change of H_{ex} is about 8 % when the temperature is increased from 25 °C to 90 °C. The field annealed samples show a smaller, but not negligible irreversible change of H_{ex}, which appears to be independent of the annealing temperature.

Fig. 5. Values of (a) the normalized exchange bias field $H_{ex}(T)/H_{ex}(25°C)$ and (b) the anisotropy field H_K. Different data sets are for sensors from wafers with the indicated annealing conditions. Filled points are measured at T, open points are measured at 25 °C after exposure to temperature T. The dashed lines indicate the initial values of the parameters.

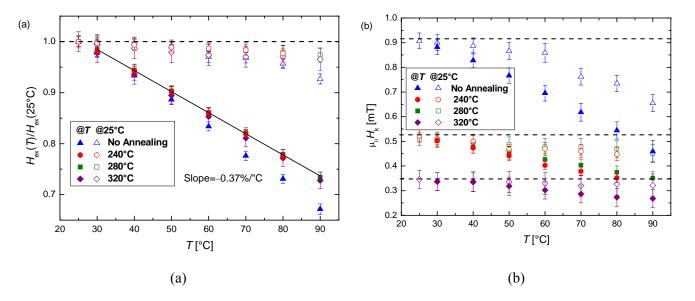The initial values of H_K are found to decrease monotonically with annealing conditions. For the sample with no field annealing, the value of H_K changes almost 50 % when the temperature is increased from 25 °C to 90 °C and approximately half of this change is irreversible. The field annealed samples show a much smaller change and the irreversible change is smaller than the error on the individual points (and smallest for the sample annealed at 320 °C). The reversible decrease of H_K with temperature for these samples is about 20 %.

4.3. Temperature Cycling

Fig. 6 shows the effect of prolonged exposure at 90 °C on S_0, H_{ex} and H_K vs. the time of the temperature cycling experiment. Note, that only half of this time was spent at 90°C. Field sweeps were measured on the sensor annealed at 280 °C and on the un-annealed sensor while cycling the temperature between 25 °C and 90 °C with each temperature step taking 18 min. The lines in Fig. 6 connect points measured at the same temperature. The extracted values for the different parameters are normalized by the value reached at 90 °C after about 7 h of temperature cycling.

Fig. 6(a) shows the normalized value of S_0 vs. the time of the temperature cycling experiment. As for the results discussed above, the sensitivity of the sensor annealed at 280 °C changes little upon heating compared to the un-annealed sensor. The parameters obtained at 25 °C for the un-annealed wafer show a big change (>7 %) after first exposure at 90 °C and then slowly approach their asymptotic values.

For this sample, the sensitivity at 25 °C still changes after 7h of cycling with a total irreversible change of about 20 %. The values measured during the cycle steps at 90 °C show a similar settling over a period of hours. The chip from the wafer annealed at 280 °C shows a significant initial change in the first cycle after which the parameters slowly settle near their asymptotic values. Thus, for this sample, the irreversible change of S_0 is less than 5 % during the whole cycling experiment, and the value at 25 °C reaches 98.4 % of its final value after the first exposure to 90 °C.
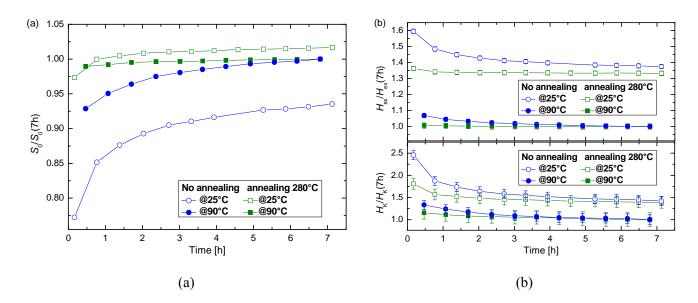

Fig. 6. Values of (a) low-field sensitivity S_0 and (b) H_{ex} and H_K normalized by their value measured at 90 °C after 7 h temperature cycling between 25 °C and 90 °C. Different data sets are for sensors from wafers with the indicated annealing conditions. Filled points are measured at 90 °C open points are measured at 25 °C. The temperature was cycled between 25 °C and 90 °C, each temperature was held constant for 18 min.

Fig. 6(b) shows the corresponding normalized values of H_{ex} and H_K. The value of H_{ex} measured at 25 °C decreases for both sensors but the relative change for the annealed sensor is seven times smaller than for the un-annealed sensor. Again, the values measured at 90 °C show a similar behavior. The relative change in H_K is bigger than for H_{ex} for both sensors, although the change for the un-annealed sensor is twice as big as that for the sample annealed at 280 °C. We also notice for both H_{ex} and H_K and independent of low-temperature field annealing that the ratio between the values obtained at 90 °C and 25 °C approach the same value.

5. Discussion

5.1. Analysis Method

The presented single domain model for the sensor response provides excellent fits of all measured field sweeps. The parameters obtained from the fits are generally found to agree well with corresponding parameters obtained by VSM and on electrical reference samples although some differences appear. In section 4.1 in Table 1 that the value of H_K from the fits of the sensor measurements was about twice that obtained from the VSM measurements. This difference is in agreement with previous studies [6] and is attributed to effects of the sensor structuring.

Assuming negligible shape anisotropy, the low-field sensitivity is given by $S_0 = (l/w)(\Delta\rho/t)(H_{ex}+H_K)^{-1}$ (cf. Eq. (6)) and the peak-to-peak sensor output is given by $V_{pp}/I = (\Delta\rho/t)(l/w) = 14.87(\Delta\rho/t)$

(cf. Eq. (3)). Inserting the values for the reference samples, we find that the measured low-field sensitivities are generally about 20 % lower than the calculated values and the measured values of V_{pp}/I are about 9 % smaller than the calculated values. This is attributed to demagnetization effects due to the sensor geometry, which cause the magnetization of the sensor elements to deviate from the nominal single domain state near their edges [7]. From fits we found the shape anisotropy field $\mu_0 H_s =$ 0.789 mT, which is comparable to the values of $\mu_0 H_{ex}$ and $\mu_0 H_K$ reported in Table 1 and hence is significant.

These results indicate that the even though the results are influenced to some degree by demagnetization effects, the analysis method is robust and the parameters obtained from the fits to the single domain model reflect the variation of the physical parameters of the thin film stack. This means that field sweeps of the sensor response can be used to quantify the exchange and anisotropy fields as well as the magnetoresistive properties of the thin film stack.

5.2. Temperature Dependence of Parameters and Effect of Low-temperature Field Annealing

The studies on the as-deposited samples show that the effect of the low-temperature annealing is to decrease H_{ex} and H_K while $\Delta\rho/t$ remains essentially unchanged. The latter indicates that the microstructure of the stack is not significantly changed by the field annealing. The changes of H_{ex} and H_K indicate that the interaction between the ferromagnetic and antiferromagnetic layers is sensitive to the low-temperature field annealing. Considering the exchange bias as an interface phenomenon, the exchange bias field and the coupling energy per area J are related by $J = \mu_0 M_s t_{FM} H_{ex}$, where $\mu_0 M_s \approx 1.0$ T is the saturation flux density of permalloy and $t_{FM} = 30$ nm is the thickness of the permalloy layer. Inserting the values of H_{ex} from the VSM measurements in Table 1, we obtain $J_{eb} = 0.07$ mJ/m^2, which is comparable to values reported in the literature for similar stacks [8, 9].

The low-temperature annealing at 280 °C and 320 °C resulted in reductions of H_{ex} of 34 % and 52 %, respectively. Similar observations have been made in studies of similar structures with a top-pinned ferromagnet [8-11]. Previous studies have generally used measurements of the magnetic hysteresis by magnetometry [9-11], magnetooptical measurements [9] or Lorentz microscopy [8] to characterize the variation of H_{ex} and H_K with temperature, but they have not systematically studied the reversible and irreversible changes induced by exposure to elevated temperatures.

In this work we were able to separate reversible and irreversible changes of the parameters for the magnetic stack vs. temperature for samples exposed to different low-temperature field annealing conditions. We find that the temperature variation of $\Delta\rho/t$ is fully reversible. For the exchange bias field H_{ex} we find that the relative *reversible* change with temperature is the same for all samples (Fig. 5(a)). The *irreversible* change of H_{ex}, however, is sensitive to the field annealing and is significantly reduced compared to a sample without field annealing. For all field annealed samples, H_{ex} still shows irreversible change upon heating above 25 °C with a relative change that seems to be insensitive to the annealing conditions (Fig. 5(a)). For the anisotropy field H_K we find from Fig. 5(b) that both the reversible and irreversible changes upon exposure to elevated measuring temperatures are significant for the sample that was not field annealed, whereas the samples that were field annealed show significantly smaller changes with temperature. Only the sample annealed at 320 °C shows a negligible irreversible change of H_K upon exposure to 90 °C. The observed increase of the low-field sensitivity S_0 with field annealing and with exposure to elevated temperatures results from the combined effect of the reversible decrease of $\Delta\rho/t$ and the decrease of H_K+H_{ex} (cf. Eq. (6)), where the latter term dominates the temperature dependence.

To further investigate the effect of repeated exposure to elevated temperatures, we studied in Section 4.3 the samples with no annealing and with field annealing at 280 °C for repeated cycles between

90 °C and 25 °C. In Fig. 6(a), we found that for both the annealed and the un-annealed sample that the irreversible changes in the sensitivity as measured at 25 °C take place upon repeated exposure to 90 °C on a time scale of hours. Moreover, the relative change in sensitivity for the un-annealed sample is several times bigger than for the annealed sample. This change in sensitivity has to be attributed to the change in H_K and H_{ex}. Indeed, these two parameters show decay upon long exposure to 90 °C. Also, they show reduced irreversible changes in the annealed sensor compared to the un-annealed one.

For all samples, we find that even after field annealing at temperatures up to 320 °C, the values of H_{ex} and H_K still show irreversible changes upon exposure to temperatures above room temperature. These changes have to be taken into account when these stacks and sensors are used for sensing purposes in environments at elevated temperatures. The largest changes are found for the sample that was not field annealed and we have found that the field annealing significantly reduces the irreversible changes.

5.3. Possible Mechanisms

Several reports in the literature have studied the effect of annealing at low temperatures on the microstructure. King *et al.* [8] studied the magnetization reversal of NiFe/IrMn exchange bias couples by Lorentz transmission electron microscopy. For an un-annealed sample, they found that the magnetic domain structure in the ferromagnetic layer was highly complex on a microscopic scale near room temperature with no clear overall orientation. After field annealing of the sample at 300 °C, they found significantly larger magnetic domains that were essentially oriented along the cooling field. They could not detect any changes of the microstructure and therefore attributed the change of behavior to a reduction of the local pinning strength of the IrMn grains upon annealing. Thus, the IrMn grains strongly pinned the ferromagnetic layer before annealing resulting in the highly complex domain structure, but after annealing the pinning strength decreased due to relaxation in the spin structure of the IrMn grains such that the local pinning was insufficient to force the ferromagnet to orient along the local pinning field.

Geshev *et al.* [10] carefully studied the interface between Co and IrMn by high resolution cross-sectional TEM and X-ray reflectivity measurements and found no effect of annealing at 215 °C on the microstructure at the interface. Upon annealing in a magnetic field applied along the initial exchange bias direction they observed a clear reduction of H_{ex} that they attributed to relaxation of frustrated spins in the top IrMn layer. They hypothesized that the first few atomic layers of the IrMn layer show paramagnetic behavior and align themselves with the moments from the ferromagnet. When enough atomic layers of the IrMn film to sustain antiferromagnetic order are deposited, the competition between the alignment of the interface spins with those of the ferromagnetic layer and the antiferromagnetic ordering will result in high frustration of the spin structure of the IrMn layer near the interface and a high number of uncompensated spins at the interface, where the latter gives rise to the high initial exchange bias. The annealing enables relaxation of the spin structure resulting in a reduction of the pinning strength and hence of H_{ex}.

Our findings that irreversible changes of H_{ex} appear slightly above room temperature even for a sample annealed at 320 °C for one hour and that repeated exposure to elevated temperatures result in gradually decreasing values of H_{ex} indicate that a slow, thermally activated process is involved in the change of H_{ex} vs. time and temperature and that the number of uncompensated interfacial spins of the IrMn layer decreases as a result of the relaxation process. Thus, our observations are consistent with the above interpretation in terms of thermal relaxation of frustrated spins in the IrMn layer near the interface to the ferromagnet. We hope that our studies will provide further inspiration to further theoretical work on this interesting topic.

5. Conclusion

We have shown that measurements of the response vs. magnetic field of planar Hall effect Wheatstone bridges can be used to extract the exchange field H_{ex}, the anisotropy field H_K and the magnetoresistive properties of the exchange-biased stack of the sensors. We have studied the temperature variation of these parameters for a top-pinned NiFe/IrMn stack in the interval between 25 °C and 90 °C for samples that were not annealed and samples that were low-temperature field annealed at 240 °C, 280 °C and 320 °C for one hour. In our experiments we separated reversible and irreversible parameter changes. We found that the magnetoresistive effect is not significantly affected by the low-temperature field annealing and only shows reversible changes upon exposure to elevated temperatures. Both H_{ex} and H_K are sensitive to annealing as well as the exposure to elevated temperatures and the relative reversible decrease of H_{ex} with temperature can be described by a single temperature coefficient. Field annealing significantly reduces but does not eliminate the irreversible changes of both H_{ex} and H_K upon exposure to temperatures even slightly above room temperature. In experiments where both field annealed and un-annealed sensors were repeatedly exposed to 90 °C, we found a large initial change and a gradual reduction of the change upon further exposure. We take these observations as indicative of a slow thermally activated process that reduces the local pinning strength of the IrMn at the interface. The observations are consistent with previous interpretations in the literature in terms of thermal relaxation of frustrated spins in the antiferromagnet near the interface to the ferromagnet, but further work is required to firmly establish this hypothesis.

The present results have important consequences for the use of permalloy-IrMn exchange-bias couples in magnetic field sensors operating at variable temperatures. Stacks with no annealing are strongly influenced by exposure to temperatures above room temperature and these should thus be used with care in applications where the sensor is exposed to elevated temperatures and high accuracy is required. Examples of such applications could be magnetic biosensors operating at variable temperatures (e.g. for studies of biological interactions vs. temperature) and magnetic field sensors operating in variable temperature conditions. The presented method provides an attractive approach to quantitative characterization of the temperature-induced changes by exposure to given temperature conditions. We have shown that low-temperature field annealing and prolonged exposure to the highest operating temperature substantially reduces subsequent irreversible changes with increasing temperatures but also that it is difficult to completely eliminate irreversible changes of the sensor parameters. These therefore have to be considered for the use of the structures in sensing applications.

Acknowledgements
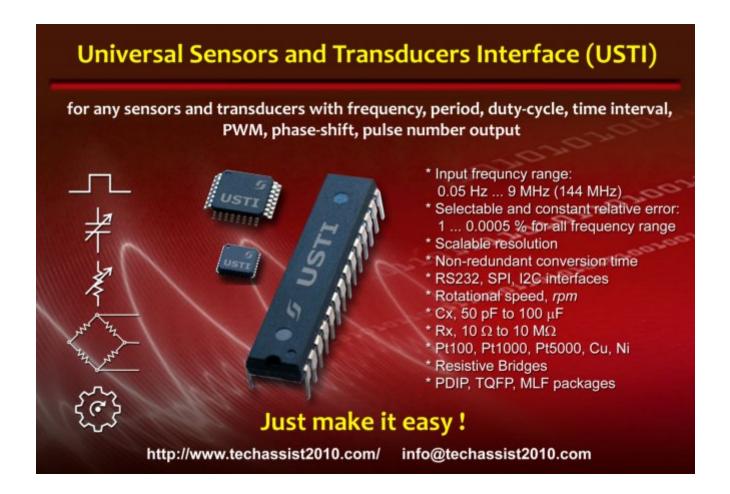
References

[1]. A. Persson *et al.*, Low-frequency noise in planar Hall effect bridge sensors, *Sensors and Actuators A: Physical,* 171, 2011, pp. 212-218.
[2]. C. Damsgaard *et al.*, Temperature effects in exchange-biased planar hall sensors for bioapplications, *Sensors and Actuators A: Physical*, 156, 2009, pp. 103-108.
[3]. B. Dalslet *et al.*, Bead magnetorelaxometry with an on-chip magnetoresistive sensor, *Lab Chip,* 11, 2011, pp. 296-302.
[4]. A. Henriksen *et al.,* Planar Hall effect bridge magnetic field sensors, *Appl. Phys. Lett.,* 97, 2010, 013507.
[5]. S. Blundell, Magnetism in condensed matter, Oxford master, *Oxford University Press*, 2001.
[6]. C. Damsgaard *et al.*, Exchange-biased planar Hall effect sensor optimized for biosensor applications,

J. Appl. Phys., 103, 2008, 07A302.

[7]. M. Donolato *et al*., Size-dependent effects in exchange-biased planar Hall effect sensor crosses, *J. Appl. Phys.,* 109, 2011, 064511.

[8]. J. King *et al*., Magnetization reversal of NiFe films exchange-biased by IrMn and FeMn, *J. Phys. D: Applied Physics*., 34, 2001, pp. 528-538.

[9]. J. Van Driel *et al*., Exchange biasing by $Ir_{19}Mn_{81}$: Dependence on temperature, microstructure and antiferromagnetic layer thickness, *J. Appl. Phys*., 88, 2000, pp. 975.

[10].J. Geshev *et al*. Role of the uncompensated interface spins in polycrystalline exchange-biased systems, *J. Phys. D: Applied Physics,* 44, 2011, 095002.

[11].A. Devasahayam *et al*., Magnetic, temperature, and corrosion properties of the NiFe/IrMn exchange couple, *J. Appl. Phys.,* 83, 1998, pp. 7216.

_____

Paper II

Chip-Based Measurements of Brownian Relaxation of Magnetic Beads Using a Planar Hall Effect Magnetic Field Sensor

Frederik W. Østerberg[a], Bjarke T. Dalslet[a], Detlef Snakenborg[a],
Christer Johansson[b] and Mikkel F. Hansen[a,*]

[a]*Department of Micro- and Nanotechnology, Technical University of Denmark, DTU Nanotech,
Building 345 East, DK-2800 Kongens Lyngby, Denmark,*
[b]*Imego AB, Arvid Hedvalls backe 4, SE-400 14 Göteborg, Sweden*
*E-mail:Mikkel.Hansen@nanotech.dtu.dk

Abstract. We present a simple 'click-on' fluidic system with integrated electrical contacts, which is suited for electrical measurements on chips in microfluidic systems. We show that microscopic magnetic field sensors based on the planar Hall effect can be used for detecting the complex magnetic response using only the self-field arising from the bias current applied to the sensors as excitation field. We present measurements on a suspension of magnetic beads with a nominal diameter of 250 nm vs. temperature and find that the observations are consistent with the Cole-Cole model for Brownian relaxation with a constant hydrodynamic bead diameter when the temperature dependence of the viscosity of water is taken into account. These measurements demonstrate the feasibility of performing measurements of the Brownian relaxation response in a lab-on-a-chip system and constitute the first step towards an integrated biosensor based on the detection of the dynamic response of magnetic beads.

Keywords: magnetorelaxometry, Brownian relaxation, lab-on-a-chip, planar Hall effect
PACS: 75.75.Jn, 85.70.-w, 85.70.Ay, 85.70.Kh

INTRODUCTION

Brownian relaxation, i.e., the detection of change in the rotation dynamics of magnetic beads, has been proposed for biodetection as the hydrodynamic size of the beads changes when biomolecules attach to the surface of the beads [1, 2]. Due to the inevitable size variation of the beads and the typical small size of the biomolecules, the direct detection of the binding of biomolecules to the surfaces of beads has proven difficult. Thus, other approaches that lead to significant changes of the hydrodynamic size of the beads have been pursued, such as bead agglutination assays [3] and binding of beads to a solid support [4]. Recently, a very sensitive assay based on Brownian relaxation measurements has been proposed for the detection of DNA, where the target oligonucleotide is first recognized by a padlock probe and then amplified by rolling circle amplification [5]. When magnetic beads attach to the resulting DNA coils, their rotation dynamics change significantly, thus facilitating their detection. Hence, volume-based or 'lab-on-a-bead' assays based on the detection of Brownian relaxation response of magnetic beads hold great promise for sensitive biodetection.

At present, the Brownian relaxation measurements are usually either carried out in commercial SQUID magnetometers [5] or in inductive set-ups [2]. These have in common that only a single sample of a comparatively large volume can be studied. These techniques hold little promise for integration and parallelization in a lab-on-a-chip platform due to their size and cost. Some efforts have been made to miniaturize SQUID sensors and integrate these into a lab-on-a-chip system [6], but these are complex devices that also require cryogenic coolants. Here, we demonstrate the measurement of the Brownian relaxation response using a planar Hall effect (PHE) sensor chip suitable for lab-on-a-chip systems. The ability to carry out measurements of the dynamic magnetic response at room temperature in a lab-on-a-chip system will facilitate the parallel in-line detection of Brownian relaxation response of beads, which can be used for biodetection or continuous monitoring purposes.

Below, we first briefly summarize the theories for Brownian relaxation and PHE sensors. Then, we present the theory for the lock-in detection of magnetic beads that are magnetized by the sensor self-field. This is followed by a description of our experimental set-up and our 'click-on' fluidic system with integrated contacts and finally we present and discuss our measured data on bead suspensions.

THEORY

Brownian relaxation

We consider a magnetic bead with a magnetic moment m dispersed in a liquid. The magnetic moment of the bead can respond to an applied magnetic field by either a rotation of the moment without a physical rotation of the particle (Néel relaxation) or by a physical rotation of the particle (Brownian relaxation). The characteristic relaxation time for Néel relaxation is $\tau_N = \tau_0 \exp(K V_p / k_B T)$, where $\tau_0 \sim 10^{-10} - 10^{-9}$ s and K and V_p are the anisotropy constant and the volume of the relaxing unit, respectively. k_B is Boltzmann's constant and T is the absolute temperature. For Brownian relaxation, the relaxation time is $\tau_B = 3\eta V_h / k_B T$ [1], where η is the dynamic viscosity of the liquid and V_h is the hydrodynamic volume of the bead. The effective relaxation time is given by $\tau^{-1} = \tau_B^{-1} + \tau_N^{-1}$. Below, we assume that the Brownian relaxation dominates, such that $\tau = \tau_B$. We can then write the characteristic frequency $f = (2\pi\tau)^{-1}$ as

$$f_B = \frac{k_B T}{6\pi\eta V_h}. \tag{1}$$

When low-frequency alternating magnetic fields with $f \ll f_B$ are applied, the bead will rotate so its magnetic moment easily follows the applied field. At high frequencies, $f \gg f_B$, the bead rotation cannot follow the applied field. At intermediate frequencies, the dynamics of the moment will lag behind the applied field. The dynamic magnetic response is described by the complex magnetic susceptibility $\chi = \chi' - i\chi'' = |\chi|(\cos\phi - i\sin\phi)$, where ϕ is the phase lag of the magnetic response with respect to the applied magnetic field. Thus, if a magnetic field $H(t) = H_{ac}\sin(\omega t)$ is applied, the measured magnetic moment of a bead is $m(t) = H_{ac}|\chi|V_{bead}\sin(\omega t - \phi)$. In the frequency domain, this is written as $m = m' - im'' = H_{ac}|\chi|V_{bead}(\cos\phi - i\sin\phi)$. Debye derived an expression for the relaxation behavior of an entity with a single relaxation time [7], which was later modified by Cole-Cole [8] to account empirically for a distribution of relaxation times to give

$$\chi = \chi' - i\chi'' = \frac{\chi_0 - \chi_\infty}{1 + (if/f_B)^{1-\alpha}} + \chi_\infty, \tag{2}$$

where α is the Cole-Cole parameter ($0 < \alpha < 1$), which equals zero for a single relaxation time (monodisperse sample). χ_0 is the equilibrium susceptibility ($f = 0$) and χ_∞ is the susceptibility at $f = \infty$. For fitting purposes, the most reliable results are obtained from the analysis of χ'' data, because χ' data are more sensitive to impurity signals. The χ'' data show a peak at $f = f_B$.
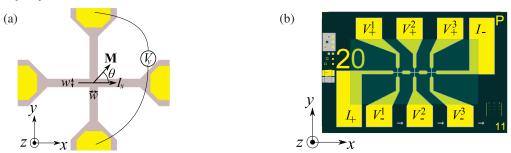
FIGURE 1. (a) Sensor layout and definition of coordinates and variables. The grey areas indicate the magnetic stack and the yellow areas indicate the gold contacts. The sensor cross has the dimensions $w \times w = (20 \text{ μm})^2$. (b) Chip layout. Each chip has the dimensions 5.5 mm $\times$ 3.6 mm and contains three sensors. The sensor stack (grey) is deposited first, then the gold contact layer (yellow). The area with the protective coating is indicated by a semitransparent rectangle. The symbols I_+ and I_- indicate the pads for the current supply. The six remaining pads are used for measuring the voltage across each sensor.

Planar Hall effect cross sensors

We will use magnetic field sensors based on the planar Hall effect in exchange-biased ferromagnetic films [9, 10]. Figure 1(a) shows a schematic of a sensor cross with definitions of variables and coordinates. The planar Hall effect arises when a current I_x is injected in the x-direction in a ferromagnetic film of thickness t_{FM} exhibiting anisotropic

magnetoresistance (AMR). The AMR gives rise to $\rho_\parallel > \rho_\perp$, where $\rho_\parallel$ and $\rho_\perp$ are the resistivities parallel and perpendicular to the magnetization direction $\hat{\mathbf{M}} = (\cos\theta, \sin\theta)$, and results in a voltage increase in the y-direction of [9]

$$V_y = -I_x(\rho_\parallel - \rho_\perp)(2t_{\text{FM}})^{-1}\sin(2\theta). \tag{3}$$

Our sensors are exchange-biased in the x-direction, such that $\theta = 0$ in the absence of an applied magnetic field. The response of the sensing layer to a magnetic field H_y applied in the y-direction can be found by minimizing the energy volume density u, which for a single domain with saturation magnetization M_s is given by [10]

$$u/(\mu_0 M_s) = -H_{\text{ex}}\cos\theta - \tfrac{1}{2}H_{\text{K}}\cos^2\theta - H_y\sin\theta, \tag{4}$$

where H_{ex} and H_{K} are the exchange and anisotropy fields, respectively and μ_0 is the permeability of free space. For low applied fields, the result is $\theta \approx H_y/(H_{\text{ex}} + H_{\text{K}})$. Defining the sensor sensitivity

$$S = V_y(I_x\mu_0 H_y)^{-1}, \tag{5}$$

we obtain the low-field sensor response

$$V_y = I_x S_0 \langle H_y \rangle, \tag{6}$$

where $\langle H_y \rangle$ is the average magnetic field acting on the active sensor area in the y-direction and $S_0 = -(\rho_\parallel - \rho_\perp)[t_{\text{FM}}\mu_0(H_{\text{ex}} + H_{\text{K}})]^{-1}$.

Lock-in detection of sensor response

In this section, we calculate the response of the sensor when beads are being magnetized by the sensor self-field due to the bias current passed trough the sensor. This field has recently been subject to a theoretical investigation [11]. There it was shown that the average field $\langle H_{\text{by}} \rangle$ acting on the sensor area from beads being magnetized by the sensor self-field can be written as

$$\langle H_{\text{by}} \rangle = I_x \gamma_1 \chi, \tag{7}$$

where γ_1 is a positive constant that depends on the sensor geometry, the bead dimensions and the bead distribution. When no beads are present, $\gamma_1 = 0$. In ref. [11], only the response of beads that was in-phase with the applied magnetic field was considered. Here, we will allow a phase lag ϕ of the bead response, such that we write the bead response to a current $I_x(t) = I_{\text{ac}}\sin(\omega t)$ as $\langle H_{\text{by}}(t) \rangle = I_{\text{ac}}\gamma_1|\chi|\sin(\omega t - \phi)$. Moreover, in our present sensors, part of the bias current is shunted through the antiferromagnetic layer used for exchange-biasing the ferromagnetic layer. This gives rise to a magnetic field $H_{\text{sf},y} = I_x\gamma_0$ acting on the active sensing layer, where γ_0 is a constant that depends on the sensor stack and the sensor geometry. Combining these fields with Eq. (6), we obtain

$$V_y(t) = I_{\text{ac}}^2 S_0 \sin(\omega t)\left[\gamma_0\sin(\omega t) + \gamma_1|\chi|\sin(\omega t - \phi)\right]. \tag{8}$$

As $V_y(t)$ is proportional to $\sin^2(\omega t)$ no signal can be detected using lock-in technique tuned to the 1st harmonic of the excitation signal [11]. The 2nd harmonic lock-in signal, however, is non-zero and can be written as $V_2 = V_2' + iV_2''$ where the in-phase and out-of-phase signals are given by $V_2' = (\pi\sqrt{2})^{-1}\int_0^{2\pi}\sin(2\omega t)V_y(t)\mathrm{d}(\omega t)$ and $V_2'' = (\pi\sqrt{2})^{-1}\int_0^{2\pi}\sin(2\omega t + \frac{\pi}{2})V_y(t)\mathrm{d}(\omega t)$ [11], respectively, with the result

$$V_2' = -(2\sqrt{2})^{-1}I_{\text{ac}}^2 S_0 \gamma_1 \chi'' \tag{9}$$
$$V_2'' = -(2\sqrt{2})^{-1}I_{\text{ac}}^2 S_0 (\gamma_0 + \gamma_1 \chi'). \tag{10}$$

Thus, for a constant bead distribution (constant γ_1), the frequency dependence of χ' and χ'' can be extracted from V_2'' and V_2', respectively.

EXPERIMENTAL

Chip fabrication

The sensor stack, Ta (3 nm) / Ni$_{20}$Fe$_{80}$ (30 nm) / Mn$_{76}$Ir$_{24}$ (20 nm) / Ta (3 nm), was sputter-deposited in a Kurt J. Lesker CMS-18 magnetron sputter system on a 4" Silicon substrate with an 800 nm thick thermal oxide. The sensor stack was defined by a negative lithography step combined with lift-off. During deposition a magnetic flux density of 20 mT was applied to define an easy direction of the ferromagnetic layer in the positive x-direction. The electrical contacts of Ti (10 nm)/Au (200 nm) were deposited by e-beam evaporation and defined by lift-off using a positive lithography process. Finally, a 580 nm thick protective coating of Ta$_2$O$_5$ was reactively sputter-deposited from a Ta target through a shadow mask.

Figure 1(b) shows the sensor layout on a chip. The gold is deposited on the entire sensor stack except near the three sensor crosses, where the central sensitive area has the dimensions $w \times w = (20 \ \mu m)^2$. The rectangle in the middle that extends to the contacts indicates the protective Ta$_2$O$_5$ coating. Figure 1 (b) also shows the electrical connections to the chip during measurements; the current inlet/outlet are denoted I_+ and I_-, and the voltage connectors for the ith sensor are denoted V_+^i and V_-^i.
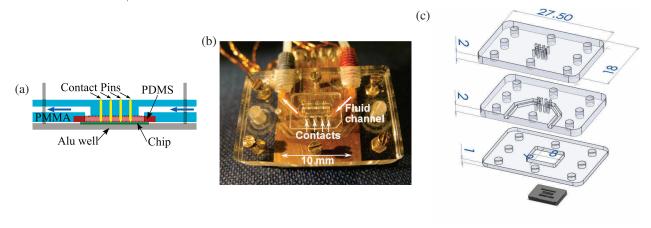

FIGURE 2. (a) Schematic of the cross-section of the 'click-on' fluidic system. (b) Assembled fluidic system with indications of the spring-loaded electrical contact pins and the fluid path. (c) Schematic drawing of the three PMMA layers used for the fluidic system and the PDMS gasket that defines the fluidic channel. Dimensions are indicated in mm.

Measurement setup

In order to perform Brownian relaxation measurements on the PHE sensors, a bead suspension must be positioned on top of the sensor and the electrical equipment must be connected to the contact pads. In order to fulfill both requirements a click-on fluidic system was designed. The fluidic system has built-in spring-loaded contact pins, which ensures a quick and easy way to connect the chip to measurement equipment without wire bonding.

To perform measurements the chip was placed in an aluminium well as indicated in Fig. 2(a). Good thermal contact to the bottom of the well was ensured by applying a small amount of thermally conducting paste to the bottom of the chip. The temperature of the aluminium well was controlled by a Peltier element with PID temperature control.

Figure 2(b) shows a bottom view of the fluidic system with integrated electrical contacts. When used, the fluidic system is mounted on top of the sensor chip. Spring-loaded electrical contact pins (POGO-PIN-5.94-1, Emulation Technology, Inc., Camarillo, CA, USA) sandwiched between the chip and a printed circuit-board as illustrated in Figs. 2(a) and 2(b) provide the electrical contact to the chip. The fluidic system has an inlet and an outlet channel to the sample chamber, which is defined by a polydimethylsiloxane (PDMS) gasket. The chip and the fluidic system defines the bottom and top of the sample chamber (cross-section: 1 mm × 1 mm), respectively, as illustrated in Fig. 2(a).

The fluidic system was fabricated from three layers of polymethylmethacrylate (PMMA) structured as schematically shown in Fig. 2(c). The structures in the three PMMA parts were defined by use of a micro milling machine. To bond the three parts together, the surfaces were first cleaned with isopropanol and then exposed to UV light for 60-90 s.

179

Subsequently, the parts were aligned and placed in a bonding press at a temperature of 88°C with an applied force of 3 kN for 1 hour.

The PDMS gasket was cast in a mould fabricated in PMMA by micro milling. The PDMS used is Sylgard 184 silicone elastomer kit, which was mixed in a 1:10 mass ratio between the curing agent and the base. To remove air bubbles in the solution it was placed in a vacuum chamber for 30 min, before the PDMS solution was poured into the mould. A flat piece of PMMA was used as top and the two pieces were pressed tightly together before being placed in an oven at 80°C for 1 hour.

For all measurements, an alternating bias current of amplitude $I_{ac} = 15$ mA was supplied by a Keithley 6221 current source connected to the I_+ and I_- pads sketched in Fig. 1 (b). Each of the sensor voltage responses was amplified 100 times in a Stanford Research Systems (SRS) SR552 bipolar preamplifier and detected by a dual-phase SRS SR830 lock-in amplifier. All data presented were corrected for this pre-amplification factor. All measurements were performed without electric and magnetic shielding.

Experimental procedure

Both the sensitivity and frequency response of the sensors were characterized prior to exposure of the sensors to beads. By measuring V_y as a function of an externally applied field in the y-direction, the sensor sensitivity was found to $S_0 = -36.5$ V T^{-1} A^{-1}. Measurements of the 2nd harmonic sensor response vs. the frequency f of the applied current revealed that the signal was subject to instrumental phase shift. This phase shift was subsequently corrected for by a phase rotation of the measured data based on the phase shifts determined from the measurements on the dry sensor without magnetic beads. These phase corrections were chosen such that $V_2' = 0$. Subsequently, milli-Q water was injected into the fluidic system and it was verified that a constant signal was obtained after application of the phase shift correction determined on the dry sensor.

For measurements on bead suspensions, we used plain Nanomag-D beads with a nominal diameter of 250 nm (09-00-252, Micromod Partikeltechnologie GmbH, Rostock-Warnemünde, Germany). The stock solution was diluted with milli-Q water to a bead concentration of 2.5 mg/mL.

After injection of the bead suspension into the fluidic system, the signal from the stagnant bead suspension was observed to depend on time due to the sedimentation of the beads on the sensor surface. Measurements of $V_2(f)$ vs. time showed a signal of growing intensity but with essentially unchanged shape of the frequency response. To obtain constant measuring conditions, the setup required 16 hours for the bead suspension to stabilize. The reason for this sensitivity to bead sedimentation is that the sensor response is mainly sensitive to beads in the vicinity of the sensor surface. A theoretical investigation has shown that about 85% of the signal from homogeneously dispersed beads arises from beads within a distance of $1.3w = 26$ μm from the x-axis through the sensor center [11]. By multiplying the area of this half circle with radius 26 μm with the length w of the active area, it is estimated that the volume being sampled by a sensor is on the order of 20 pL. After the stabilization, series of measurements of V_2 vs. f were performed at temperatures in the range 5°C - 35°C in steps of 5°C. In each measurement, which took about XX min, the frequency was swept from 1000 Hz to 1 Hz in XX points. Prior to the measurements performed at 5°C, 15°C and 30°C, reference measurements were carried out at 25°C to verify that the signal or the beads were not affected by the temperature changes.

For benchmarking, a 200 μL suspension of beads from the same batch and with the same concentration was characterized at 26°C in a commercial AC susceptometer (DynoMag, Imego AB, Gothenburg, Sweden) after a brief vortex mixing. The amplitude of the applied magnetic field was 0.5 mT.

Data treatment and analysis

Figure 3 shows data measured with milli-Q water in the fluidic system and representative data measured on a bead suspension before and after the correction for the instrumental phase shift. After correction, the data measured on the sensor without beads show values of V_2' close to zero and constant values of V_2'' as predicted by Eqs. (9) and (10). The data on the sensor with beads show a different behavior with a peak in V_2' and values of V_2'' that monotonically decrease towards the level measured for the sensor without beads for increasing f. This significant change in the measured values originates from the presence of the magnetic beads and is consistent with the expectations from Eqs.
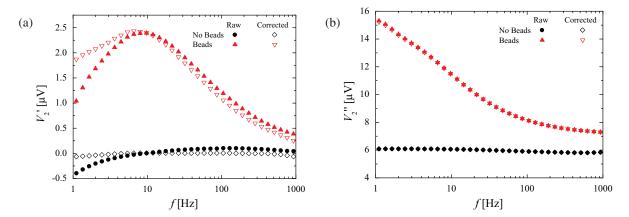
180

FIGURE 3. Examples of $V_2 = V_2' - iV_2''$ data measured on a wet sensor without beads and with a bead suspension before and after correction for the instrumental phase shift described in the text. Panel (a) shows V_2' data and panel (b) shows V_2'' data.
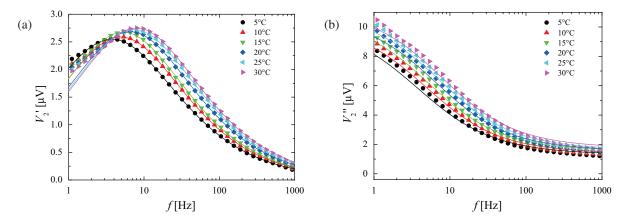

FIGURE 4. Values of $V_2 = V_2' - iV_2''$ measured on a bead suspension at the indicated temperatures. The data were corrected for the instrumental phase shift and the described offset in V_2'' was subtracted. Panel (a) shows V_2' data and panel (b) shows V_2'' data.

(9) and (10). All data on the bead suspension presented below have been corrected for the instrumental phase shift and the constant offset in V_2'', determined from the data measured without beads, has been subtracted.

The resulting data were analysed using the Cole-Cole model, Eq. (2). Only the in-phase electrical signal, V_2', was fitted, corresponding to analyzing only the out-of-phase susceptibility, χ''. The parameters obtained from fitting of the frequency dependence of V_2' were used to compute and plot corresponding values for V_2'' (except for an offset). Due to the significant instrumental phase shifts observed at lower frequencies, these values were not trusted as much as the values obtained at higher frequencies, and therefore only data in the frequency range 2 Hz - 1000 Hz were used for the fitting.

RESULTS AND DISCUSSION

Figure 4 shows measured and corrected values of V_2' and V_2'' vs. f obtained for selected temperatures. The data have the shapes expected for χ'' and χ' data, respectively, for a bead suspension that exhibits Brownian relaxation. The peak in the V_2' data (corresponding to a peak in χ'' data) is observed to shift to higher frequencies upon an increase of the temperature. The amplitudes of both V_2' and V_2'' are found to increase with increasing temperature. As the measurements were carried out with increasing temperatures, this is likely an effect of further bead sedimentation rather than of the temperature. This is also supported from the reference measurements carried out at 25°C, which also show an intensity
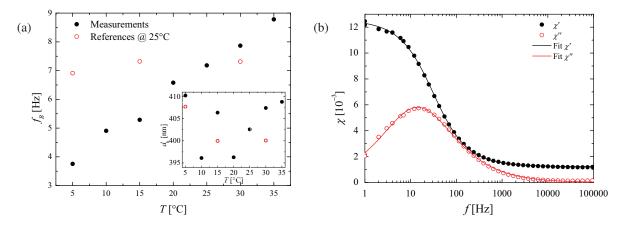
FIGURE 5. (a) Brownian relaxation frequencies vs. temperature. Inset: Hydrodynamic diameter vs. temperature The reference measurement at 25°C were performed prior to the measurement at 5°C, 15°C and 30°C, which is why they are plotted at these temperatures. (b) AC susceptometer measurements corresponding to those on the PHE sensor shown in Fig. 4. The measurements were performed at 26°C. The lines shown are fits to the Cole-Cole model obtained separately for χ' and χ''.

increase (data not shown).

The fits to the Cole-Cole model obtained as described in Sec. are shown as the solid lines in Fig. 4. The fits are observed to match the V_2' data well except at frequencies below 2 Hz that were not used for the analysis as previously described. The values of V_2'' calculated from the parameters obtained from the fits of the V_2' data essentially reproduce the experimental data, although it is observed that a slightly different scale factor (and another free parameter) would improve the fit. Thus, the experimental data are well approximated by the described Cole-Cole model and it is meaningful to extract and discuss the Brownian relaxation frequency f_B.

Figure 5(a) shows the values of f_B extracted from the Cole-Cole fits of the V_2' data obtained at the indicated temperatures and the described reference measurements carried out at 25°C at selected steps in the measurement series. The values of f_B obtained for the reference measurements at 25°C are found to be nearly constant at about 7 Hz showing that the measurement procedure and the properties of the sensor and the beads are reproducible over time. The values of f_B measured vs. temperature show a nearly linear increase with the temperature. In all fits, the value of the Cole-Cole parameter was $\alpha = 0.34(1)$ with no systematic variation with the temperature.

The inset in Fig. 5(a) shows the corresponding hydrodynamic diameters calculated from $d_h = [k_B T / (\pi^2 \eta (T) f_B)]^{1/3}$ using tabulated values of the temperature-dependent dynamic viscosity of water [12]. The calculated values of d_h show no systematic variation in the studied temperature range and all fall within 2% of their mean value of $d_h = 403$ nm. Hence, the results are consistent with the Cole-Cole model for beads with a constant value of d_h and the temperature dependent dynamic viscosity of water. This shows the feasibility and consistency of this approach.

Figure 5(b) shows the corresponding measurements obtained in the commercial DynoMag AC susceptometer at 26°C. An analysis of the out-of-phase magnetic response χ'' to the Cole-Cole model results in $f_B = 14.3$ Hz, $\alpha = 0.31$ and $d_h = 323$ nm. A similar analysis of the in-phase magnetic response χ' to the Cole-Cole model results in $f_B = 31.2$ Hz, $\alpha = 0.22$ and $d_h = 249$ nm. A more detailed analysis to the Debye model with a log-normal distribution of hydrodynamic volumes as described in [3] yields a median hydrodynamic diameter of 283 nm with a geometric standard deviation of 1.54 nm.

The hydrodynamic diameters obtained in the commercial AC susceptometer are significantly smaller than that obtained by the on-chip PHE sensor measurements, but still larger than the nominal bead dimension specified by the manufacturer. Several factors can contribute to this. Both measurements were carried out on the same batch of beads and with the same concentration after vortex mixing of the bead suspension. Bead agglomeration can significantly increase the average hydrodynamic diameter and this is usually also accompanied by an increase of the Cole-Cole parameter α. As the beads in the on-chip measurements had more time to agglomerate and also sedimented near the bottom of the fluid channel, agglomeration is likely contributing to the larger observed values of d_h and α by this technique. Moreover, the two techniques also measure fundamentally different properties. The AC susceptometer measures the average properties of a large volume where the beads are essentially homogeneously dispersed and only a very small fraction of the signal originates from sedimented beads. The on-chip method measures mainly beads that are

sedimented on or near the sensor surface. These beads may therefore be of larger sizes (as these will sediment first) and will be subject to interactions both between the beads and between the beads and the sensor surface. These interactions are expected to increase the rotational friction compared to beads that are homogeneously distributed in suspension thus resulting in increased values of d_h. The beads are also subject to a magnetic force due to the inhomogeneity of the self-field and the magnetostatic field from the sensor that attracts them towards the sensor surface. In addition to instrumental uncertainties, the slightly elevated measured values of V_2' at low frequencies can also be due to beads that are more strongly coupled to the sensor surface and thus show a much slower dynamic response.

However, it is noteworthy that the results obtained from the on-chip measurements are consistent and reproducible over time and can be adequately described by the Cole-Cole model with the temperature dependent dynamic viscosity of water. Therefore, although the details of the determining factors for the magnetic dynamics are more complex than for homogeneously dispersed magnetic beads, the method is applicable for measurements of the dynamic magnetic response in a lab-on-a-chip setting.

CONCLUSION

We have presented a click-on microfluidic system with integrated electrical contacts and demonstrated that the complex dynamic magnetic response of magnetic beads can be measured using solely the self-field from the bias current passed through a planar Hall effect sensor. Futhermore, it has been shown that the measured response is consistent and reproducible and due to Brownian relaxation of beads on or near the sensor surface. We have measured the dynamic magnetic response for the same bead suspension at temperatures between 5°C and 35°C. The observed magnetic relaxation can be described in terms of the usual Cole-Cole expression for the complex dynamic magnetization due to Brownian relaxation with a constant hydrodynamic diameter and the temperature-dependent viscosity of water. This demonstrates for the first time the feasibility of measurements of the complex magnetic susceptibility by use of the self-field of a sensor integrated in a microfluidic system.

The hydrodynamic diameter obtained from the on-chip measurements is about 25% higher than that obtained from a measurement on the same batch of beads in a commercial AC susceptometer. This is likely due to stronger interactions between beads and between the beads and the sensor surface that increase the rotational friction in the on-chip measurements, which are mainly sensitive to beads in the close vicinity of the sensor surface.

A deeper understanding of these interactions and the demonstration of biological sensing in our system are the subjects of our future work.

ACKNOWLEDGMENTS

REFERENCES

1. J. Connolly, and T. G. St.Pierre, *J. Magn. Magn. Mater.* **225**, 156–160 (2001).
2. A. P. Astalan, F. Ahrentorp, C. Johansson, K. Larsson, and A. Krozer, *Biosens. Bioelectron.* **19**, 945–951 (2004).
3. A. P. Astalan, C. Johansson, K. Petersson, J. Blomgren, D. Ilver, A. Krozer, and C. Johansson, *J. Magn. Magn. Mater.* **311**, 166–170 (2007).
4. D. Eberbeck, C. Bergemann, F. Wiekhorst, U. Steinhoff, and L. Trahms *J. Nanobiotechnol.* **6**, 4 (2008).
5. M. Strömberg, J. Göransson, K. Gunnarsson, M. Nilsson, P. Svedlindh, and M. Strømme, *Nano Lett.* **8**, 816–821 (2008).
6. F. Oisjoen, J. F. Schneiderman, A. P. Astalan, A. Kalabukhova, C. Johansson, and D. Winkler, *Biosens. Bioelectron.* **25**, 1008–1013 (2010).
7. P. Debye, *Polar molecules*, Chemical catalogue, New York, 1929.
8. K. S. Cole, and R. H. Cole, *J. Chem. Phys.* **9**, 341 (1941).
9. L. Ejsing, M. F. Hansen, A. K. Menon, H. A. Ferreira, D. L. Graham, and P. P. Freitas, *Appl. Phys. Lett.* **84**, 4729–4731 (2004).
10. C. D. Damsgaard, S. C. Freitas, P. P. Freitas, and M. F. Hansen, *J. Appl. Phys.* **103**, 07A302 (2008).
11. T. B. G. Hansen, C. D. Damsgaard, B. T. Dalslet, and M. F. Hansen, *J. Appl. Phys.* **107**, 124511 (2010).
12. D. R. L. (Ed.), *CRC Handbook on Chemistry and Physics*, CRC Press, Boca Raton, 2005.

Paper III

F. W. Østerberg, G. Rizzi, T. Zardán Gómez de la Torre, M. Strömberg, M. Strømme, P. Svedlindh and M. F. Hansen
"Measurements of Brownian relaxation of magnetic nanobeads using planar Hall effect bridge sensors"
Biosens.Bioelectron. **40**, 147 (2013)

Measurements of Brownian relaxation of magnetic nanobeads using planar Hall effect bridge sensors

F.W. Østerberg [a], G. Rizzi [a], T. Zardán Gómez de la Torre [b], M. Strömberg [b], M. Strømme [b], P. Svedlindh [b], M.F. Hansen [a,*]

[a] Department of Micro- and Nanotechnology, Technical University of Denmark, DTU Nanotech, Building 345B, DK-2800 Kongens Lyngby, Denmark
[b] Department of Engineering Sciences, Uppsala University, The Ångström Laboratory, Box 534, SE-751 21 Uppsala, Sweden

ARTICLE INFO

ABSTRACT

We compare measurements of the Brownian relaxation response of magnetic nanobeads in suspension using planar Hall effect sensors of cross geometry and a newly proposed bridge geometry. We find that the bridge sensor yields six times as large signals as the cross sensor, which results in a more accurate determination of the hydrodynamic size of the magnetic nanobeads. Finally, the bridge sensor has successfully been used to measure the change in dynamic magnetic response when rolling circle amplified DNA molecules are bound to the magnetic nanobeads. The change is validated by measurements performed in a commercial AC susceptometer. The presented bridge sensor is, thus, a promising component in future lab-on-a-chip biosensors for detection of clinically relevant analytes, including bacterial genomic DNA and proteins.

© 2012 Elsevier B.V. All rights reserved.

1. Introduction

In recent years, the interest in using magnetic particle-based biosensors has increased (Göransson et al., 2010; Jaffrezic-Renault et al., 2007; Koh and Josephson, 2009; Wang and Li, 2008). One of the main reasons for this is the lack of magnetic background in most biological samples. Furthermore, magnetic particles of dimension in the sub-micrometer range, so called nanobeads, have high physical and chemical stability, are inexpensive to produce, and can easily be made biocompatible.

Brownian relaxation was first proposed for biosensing by Connolly and St Pierre (2001). The principle behind using Brownian relaxation for biodetection is that a naked magnetic particle will have a smaller hydrodynamic diameter than the same particle bound to a biomolecule. This means that the naked particle will relax faster than a particle bound to a biomolecule. Brownian relaxation has been demonstrated to work for both detection of DNA (Strömberg et al., 2008) and proteins (Astalan et al., 2004; Öisjöen et al., 2010; Zardán Gómez de la Torre et al., 2012). Traditionally, Brownian relaxation is measured in a SQUID magnetometer, which is expensive and requires cryogenic liquids for cooling; other methods include inductive setups and fluxgates (Ludwig et al., 2005). None of these methods are easily integrated into a lab-on-a-chip system, thus there is a need for a sensor suited for integration onto a lab-on-chip platform. We have previously demonstrated that Brownian relaxation can be measured using a cross-shaped planar Hall effect (PHE) sensor without the need for any externally applied field since the beads are magnetized by the field generated by the alternating sensor bias current (Dalslet et al., 2011; Østerberg et al., 2010).

In the present work, we compare results obtained from measurements of Brownian relaxation of 40 nm magnetic beads using two different PHE sensor geometries; the traditional cross geometry and the newly proposed bridge (PHEB) geometry (Henriksen et al., 2010; Persson et al., 2011). We first show that the two sensor types yield the same frequency dependence of the measured signal from magnetic nanobeads and that the signals measured by the bridge sensor are six times as large as those measured by the cross-shaped sensor. We then present results of the first on-chip experiments, where functionalized magnetic nanobeads are mixed and hybridized to DNA coils formed in a rolling circle amplification (RCA) process. These results are found to compare well with those obtained in experiments carried out using a commercial AC susceptometer. The presented findings open up for the development of inexpensive on-chip magnetic read-out devices for detection of clinically relevant analytes including bacterial genomic DNA and proteins.

2. Theory

Below, the theoretically expected signals from magnetic beads when they are magnetized by the sensor self-field for both the

---

* Corresponding author. Tel.: +45 45256338.
E-mail addresses: frederik.osterberg@nanotech.dtu.dk (F.W. Østerberg), Mikkel.Hansen@nanotech.dtu.dk (M.F. Hansen).

cross and bridge geometries of planar Hall effect sensors are derived. It is also described how the dynamic magnetic bead response can be extracted using lock-in technique.

2.1. Low-field sensor response

The sensors rely on the anisotropic magnetoresistance (AMR) effect measured in the cross and bridge geometries shown in Fig. 1. The cross consists of two orthogonal arms each of width w. The bridge consists of four arms of width w and length l that form angles $\pm \pi/4$ to the x-axis as illustrated in Fig. 1. The sensors consist of a ferromagnetic layer exhibiting the AMR effect, which is exchange pinned along the positive x-direction in zero external magnetic field by an antiferromagnet. The sensors are connected in series and are biased by a current I applied in the positive x-direction. The resulting sensor output voltages V_C and V_B of the cross and the bridge, respectively, are measured along the y-direction. In zero magnetic field both sensors will ideally give zero output voltage. Upon application of a small magnetic field H_y in the y-direction, the magnetization of the ferromagnetic layer will rotate resulting in non-zero values of V_C and V_B due to the AMR effect. The cross sensor is usually termed planar Hall effect sensor because it shares the geometry with ordinary Hall sensors. The bridge sensor presented here has recently been shown to have exactly the same response as the cross sensor except for a geometrical amplification factor and hence this particular class of AMR sensors was termed planar Hall effect bridge sensors (Henriksen et al., 2010). For both sensors, the output for low applied magnetic fields can be written as

$$V_C = IS_{C,0}H_y,\tag{1}$$

$$V_B = IS_{B,0}H_y,\tag{2}$$

where $S_{C,0}$ and $S_{B,0}$ are the low-field sensitivities of the cross and bridge sensors, respectively. When the two sensors have the same value of w, the two sensitivities are ideally related as $S_{B,0} = (l/w)S_{C,0}$ (Henriksen et al., 2010).

2.2. Response to sensor self-field and magnetic beads

We consider the self-field H_{sf} acting on the sensor in the directions indicated in Fig. 1 due to the applied sensor bias current. For the present sensors, part of the sensor bias current is shunted in the antiferromagnetic layer. This gives rise to an effective in-plane magnetic field acting on the ferromagnetic layer aligned perpendicular to the direction of the current I_c through the conductor. We write this effective field as $I_c\gamma_0$, where γ_0 is a constant that depends on the sensor stack and sensor geometry. Likewise, magnetic beads that are present on and near the conductor will be magnetized by the field from the sensor bias
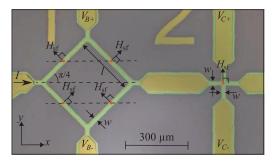
current and give rise to a net positive field acting on the conductor. This we write as $I_c\gamma_1\chi$, where γ_1 depends on the sensor geometry and bead distribution and χ is the magnetic bead susceptibility (Hansen et al., 2010). Hence, we write the total self-field acting on the sensor due to the applied bias current as

$$H_{sf} = I_c\gamma_0 + I_c\gamma_1\chi.\tag{3}$$

For the cross sensor, the entire current passes through the sensor and the self-field acts in the positive y-direction. Inserting $I_c = I$ and $H_y = H_{sf}$ in Eq. (1) yields the expected self-field signal:

$$V_C = I^2 S_{C,0}(\gamma_0 + \gamma_1\chi).\tag{4}$$

For the bridge sensor, only half of the bias current passes through each branch and the sensor is sensitive only to the y-component of the self-field. Inserting $I_c = I/2$ and $H_y = H_{sf}/\sqrt{2}$ in Eq. (2) yields the expected self-field signal:

$$V_B = 2^{-3/2}I^2 S_{B,0}(\gamma_0 + \gamma_1\chi),\tag{5}$$

where we have implicitly assumed that γ_0 and γ_1 are the same for the two sensor types. Combining Eqs. (4) and (5), we find that the ratio of the self-field signals for the two sensors is

$$V_B/V_C = 2^{-3/2}(S_{B,0}/S_{C,0})\tag{6}$$

and that, ideally, $V_B/V_C = 2^{-3/2}(l/w)$.

2.3. Dynamic magnetic susceptibility measurements

To probe the dynamic magnetic properties of magnetic nanobeads, we apply an alternating sensor bias current $I(t) = I_{AC}\sin(2\pi ft)$, where I_{AC} is the current amplitude, f is the frequency and t is the time. The response of a bead ensemble to the alternating magnetic field is described by the complex magnetic susceptibility:

$$\chi = \chi' - i\chi'' \equiv |\chi|\cos\phi - i|\chi|\sin\phi,\tag{7}$$

where χ' and χ'' are the components of χ in-phase and out-of-phase with the magnetic field, respectively, and ϕ is the phase lag of the magnetic response with respect to the magnetic field. As the self-field signals are proportional to I^2, the signals must be detected at twice the frequency $(2f)$ of the bias current. This can be achieved by measuring the 2nd harmonic signal $V_2 = V_2' + iV_2''$ using lock-in technique, where V_2' and V_2'' are the in-phase and out-of-phase signals, respectively. We have previously shown (Dalslet et al., 2011; Østerberg et al., 2010) that the 2nd harmonic signals for the cross sensor are

$$V_{C,2}' = -2^{-3/2}I^2 S_{C,0}\gamma_1\chi'',\tag{8}$$

$$V_{C,2}'' = -2^{-3/2}I^2 S_{C,0}(\gamma_0 + \gamma_1\chi').\tag{9}$$

Hence, $V_{C,2}'$ is directly proportional to the out-of-phase susceptibility χ'' and $V_{C,2}''$ depends linearly on the in-phase susceptibility χ'. The corresponding expressions for the bridge sensor can be found using Eq. (6).

2.4. Brownian relaxation of magnetic beads

We consider a magnetic bead, where the superparamagnetic relaxation time due to internal flipping of the magnetic moment of the bead is much longer than the Brownian relaxation time due to a physical rotation of the bead (Brown, 1963). Hence, we assume that Brownian relaxation is the dominating relaxation mechanism in the investigated frequency window. Brownian relaxation is characterized by the Brownian relaxation frequency

Fig. 1. Picture of a bridge and a cross sensor connected in series with definition of geometric variables and the orientation of self-fields acting on the sensor. The current is applied in the x-direction, while sensor signals are measured across the sensors in the y-direction.

f_B given by

$$f_B = \frac{k_B T}{6\pi\eta V_h}, \tag{10}$$

where T is the absolute temperature, k_B is Boltzmann's constant, η is the dynamic viscosity of the liquid and V_h is the hydrodynamic volume of the relaxing entity.

For an ensemble of monodisperse non-interacting particles the complex susceptibility χ is described by the Debye (1929) theory. To account for a possible polydispersity, Cole and Cole (1941) have later provided the empirical expression:

$$\chi = \frac{\chi_0 - \chi_\infty}{1 + (if/f_B)^{1-\alpha}} + \chi_\infty, \tag{11}$$

where α ($0 \le \alpha < 1$) is the Cole–Cole parameter, which equals zero for a monodisperse sample, and χ_0 and χ_∞ are the DC and high-frequency susceptibilities. It should be noted that the DC susceptibility χ_0 in a Brownian relaxation sense is strongly sensitive to whether the beads are dynamically active or not whereas the high-frequency susceptibility χ_∞ depends only on the amount of beads.

3. Material and methods

3.1. Sensor fabrication

The sensors were fabricated on a silicon wafer with a 1 μm thick thermal oxide. The sensor stack Ta(3 nm)/Ni$_{80}$Fe$_{20}$(30 nm)/Mn$_{80}$Ir$_{20}$(20 nm)/Ta(3nm) was deposited in a Kurt J. Lesker CMS-18 magnetron sputter system and defined by liftoff. During deposition, a magnetic field of 20 mT was applied to define an easy magnetization direction along the positive *x*-direction (Henriksen et al., 2010). The contact stack Ti(10 nm)/Pt(100 nm)/Au(100 nm)/Ti(10 nm) was deposited in a Wordentech QLC 800 metal evaporator and also defined by liftoff. Finally, a 900 nm thick layer of Ormocomp (Micro resist technology GmbH, Germany) was spun on to the wafer and patterned by photo lithography, to leave the sensors covered and the contact pads uncovered. The Ormocomp layer prevents electrical contact between the sensors and the liquids during measurements, such that the sensors can be operated at voltages up to at least 10 V during measurements without formation of bubbles or sensor corrosion. For this study the bridge sensor has the dimensions $l = 280$ μm and $w = 20$ μm and the cross sensor has the dimension $w \times w = 20$ μm $\times$ 20 μm, for definitions see Fig. 1.

3.2. Measurement setup

Electrical contact to the chip was made using a click-on fluidic system with integrated spring-loaded electrical contacts. The click-on fluidic system has a polydimethylsiloxane (PDMS) gasket, which defines the sidewalls and the top of the fluidic channel of which the chip forms the bottom. The channel height, width and length are 1 mm, 1 mm and 5 mm, respectively. For further details on the click-on system, see Østerberg et al. (2010). During measurements, the chip was placed in a measurement set-up where the temperature was held constant at 25 °C using a PID Peltier temperature control system.

Measurements of the 2nd harmonic sensor signal vs. frequency were carried out using an HF2LI lock-in amplifier (Zurich Instruments, Switzerland). The bias current was provided by the built-in function generator of the lock-in amplifier. The two sensors tested in this study were connected in series, which means that the same current was passed through the two sensors. The resistance of the two sensors in series was 222.9 Ω. Three

different voltage amplitudes were applied corresponding to the bias current amplitudes $I_{AC} = 12.4$ mA, 18.6 mA and 24.8 mA.

The low-field sensor sensitivities were found measuring the 1st harmonic sensor response vs. magnetic field applied in the *y*-direction as described by Henriksen et al. (2010). For the cross and bridge sensors, we obtained $S_{C,0} = -90$ V/(AT) and $S_{B,0} = -616$ V/(AT), respectively.

3.2.1. Brownian relaxation measurements using cross and bridge sensors

The relaxation measurements were performed by measuring the 2nd harmonic signals as a function of bias current frequency. All frequency sweeps comparing the bridge and cross were performed with 18 equally spaced points on a log scale from 338.2 kHz down to 37.7 Hz. After each of the 18 points in the frequency sweep, a reference point was recorded at 4667 Hz, which is near the expected Brownian relaxation frequency of the studied beads. The total time for such a sweep with 18 different frequencies and 18 reference points was 7 min and 15 s. The sweeps were set to run continuously, such that when a sweep ended, a new sweep started automatically.

Prior to introduction of magnetic nanobeads in the fluidic system, three background sweeps were performed with MilliQ water in the fluidic channel. These sweeps were used to correct for an instrumental phase shift at high frequencies and to subtract the offset due to the self-field from the current shunted through the antiferromagnetic layer. Hence, all data shown below have been corrected for γ_0 (cf. Eq. (9)).

At the beginning of the fourth frequency sweep, a suspension of 1 mg/mL 40 nm SHP beads with COOH surface (Ocean Nano-tech, AR, USA) was injected into the fluidic channel at a flow rate of 30 μL/min and the nanobead suspension was left stagnant in the fluid channel for the subsequent four frequency sweeps (sweeps number 5–8). When the 9th frequency sweep started, the fluid channel was flushed with MilliQ water for 3 min at a flow rate of 800 μL/min. Finally, a tenth sweep was measured to verify that the sensors were back to their initial state.

3.2.2. Brownian relaxation measurements on samples containing DNA coils and oligonucleotide-tagged magnetic nanobeads

The samples for the DNA coil detection experiments were prepared as described in Zardán Gómez de la Torre et al. (2011a) using amine-functionalized magnetic nanobeads with a nominal diameter of 50 nm (Micromod Partikeltechnologie GmbH, Germany). Briefly, single-stranded detection oligonucleotides (5′-SH-TTT TTT TTT TTT TTT TTT TTG TTG ATG TCA TGT GTC GCAC-3′-FAM) complementary to the repeating sequence of the DNA coils were conjugated to the beads (10 oligonucleotides per nanobead) using the sulfo-succinimidyl-4-(*N*-maleimidomethyl) cyclohexane-1-carboxylate (sulfo-SMCC) chemistry as described in Zardán Gómez de la Torre et al. (2011b) and suspended in 1 × PBS pH 7.5 to a concentration of 1 mg/mL. A 4 nM suspension of DNA coils was produced through the padlock probe target recognition (Nilsson et al., 1994) and the RCA technology (Fire and Si-Qun, 1995; Liu et al., 1996) using an RCA-time of 60 min. This resulted in long single-stranded DNA coils containing about 1000 repetitions of the complement of the padlock probe sequence. The DNA coils were suspended in hybridization buffer (4 mM Tris–HCl, 4 mM EDTA, 0.02 v/v% Tween-20 and 0.1 M NaCl). The sequences of the target and padlock probes were 5′-CCC TGG GCT CAA CCTAGG AAT CGC ATT TG-3′ and 5′-TAG GTT GAG CCC AGG GAC TTC TAG AGT GTA CCG ACC TCA GTA GCC GTG ACT ATC GAC TTG TTG ATG TCA TGT GTC GCA CCA AAT GCG ATT CC-3′, respectively.

Detection experiments were carried out by first diluting the DNA coil suspension with hybridization buffer to a DNA coil

concentration of 400 pM. Then, a 30 μL solution of oligonucleotide-tagged beads was added to a 30 μL solution of hybridization buffer (reference sample) or 400 pM of DNA coils (200 pM after addition of oligonucleotide-tagged beads). The mixture was gently homogenized and thereafter incubated for 30 min at 70 °C. Immediately after, 30 μL of the incubated sample was injected into the chip system and characterized using the planar Hall effect bridge sensor. Another 30 μL sample was diluted to 200 μL with 1 × PBS and characterized in a DynoMag commercial AC susceptometer (Imego, Sweden).

4. Results

4.1. Brownian relaxation measurements using cross and bridge sensors

Fig. 2 shows the in-phase (top) and out-of-phase (bottom) 2nd harmonic sensor signals vs. frequency obtained from measurements of the Ocean Nanotech beads with a nominal diameter of 40 nm for the three indicated amplitudes of the bias current. The data for the cross sensor have been scaled by a factor of 6. All data have been corrected for an instrumental phase shift and the data measured on MilliQ water have been subtracted. Hence, the corrected in-phase sensor response is proportional to the out-of-phase magnetic susceptibility and the corrected out-of-phase sensor response is proportional to the in-phase magnetic susceptibility. The figure shows that the signals, as expected from Eqs. (4)
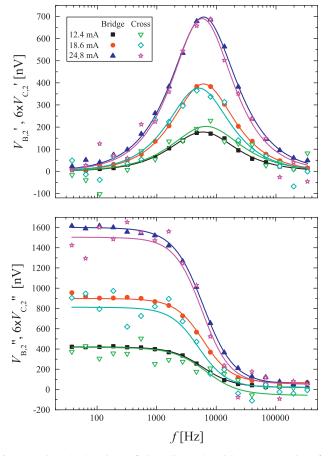
and (5), are quadrupled when the current amplitude is doubled and that the signal from the bridge sensor is close to six times that from the cross sensor.

The solid lines in Fig. 2 are curve fits to the Cole–Cole model, Eq. (11). The nanobead suspension was injected during the fourth frequency sweep and the signal was stable during sweeps number 5–8. These frequency sweeps were analyzed in terms of the Cole–Cole model and the resulting Brownian relaxation frequencies are shown in Table 1. The errors on the values of f_B in Table 1 are the standard deviations found from the four repeated measurements. The results show that f_B increases slightly with the bias current for measurements on the bridge sensor, whereas no clear trend is observed for measurements on the cross sensor. Furthermore, Table 1 shows that the uncertainties in f_B decrease significantly when the bias current is increased and also that the uncertainties are substantially smaller for the bridge than for the cross. For example, for the highest bias current, the relative error on the determination of f_B is 0.1% for the bridge and 5% for the cross. The obtained Brownian relaxation frequencies correspond to hydrodynamic diameters in the range 42–45 nm.

The reference points measured at $f = 4667$ Hz after each point in the frequency sweep are plotted in Fig. 3 vs. the time t after initiation of the experiment for the indicated amplitudes of the current. The figure also indicates the frequency sweeps in chronological order. Again the data for the cross sensor have been scaled by a factor of 6.

For all measurements, a constant signal is observed until the nanobead suspension is injected at $t = 22$ min. Then, the signal increases to an approximately constant level, which is reached at

Table 1
Average Brownian relaxation frequencies and α-parameters obtained from Cole–Cole fits to the frequency sweeps number 5–8 for cross and bridge sensors. The numbers in parentheses indicate the standard deviations (σ) of the four measurements.

I (mA)	f_B (kHz)		α	
	Bridge	Cross	Bridge	Cross
12.4	6.0(0.1)	6.5(0.9)	0.068(0.006)	0.16(0.06)
18.6	6.05(0.06)	5.3(0.3)	0.054(0.015)	0.04(0.02)
24.8	6.097(0.006)	6.1(0.3)	0.063(0.006)	0.04(0.03)

Fig. 2. In-phase (top) and out-of-phase (bottom) 2nd harmonic signal vs. frequency for the indicated bias currents measured for cross and bridge shaped sensors. The signals measured for the cross are multiplied by 6. The data shown are from the last frequency sweep with nanobeads (sweep number 8). The solid lines are curve fits to the Cole–Cole model.

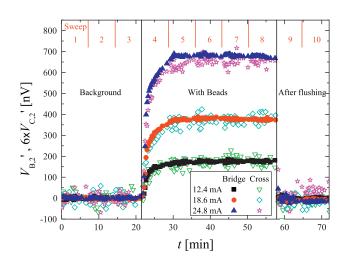**Fig. 3.** In-phase signal of reference measurements ($f = 4667$ Hz) plotted vs. time for the indicated bias currents. Signals from the cross sensor are multiplied by a factor of six. The graph is separated into three regions by two vertical lines: background (prior to nanobead injection), with nanobeads and after flushing. The numbers from 1 to 10 at the top show the number of the frequency sweep where the points were obtained.

$t \approx 29$ min corresponding to the initiation of frequency sweep number 5. After frequency sweep number 8 is completed at $t \approx 58$ min, the fluidic system is rinsed with water and the signal returns to the background level. The scaled signal levels for both sensor types show the same behavior with nearly identical signal levels. However, the data noise for the cross sensor is significantly higher than for the bridge sensor. Table 2 shows the average value and standard deviation for the measurements in Fig. 3 obtained during sweeps number 5–8. The average values for the bridge sensor are close to six times as large as those for the cross, whereas the standard deviations for the bridge sensor are less than two times those for the cross sensor. The standard deviation varies only little with the bias current and hence the relative standard deviation decreases approximately as the inverse signal, i.e., as the inverse square of the bias current. The lowest relative standard deviation of 0.9% is obtained for the bridge sensor with a bias current amplitude of $I_{AC} = 24.8$ mA.

4.2. Brownian relaxation measurements on samples containing DNA coils and oligonucleotide-tagged magnetic nanobeads

Fig. 4 shows the dynamic magnetic measurements on oligo-nucleotide-tagged nanobeads incubated with a suspension of DNA coils with a concentration of 200 pM as well as correspond-ing reference measurements on a sample containing no DNA coils. The measurements have been carried out simultaneously in both the DynoMag AC susceptometer (top panel) and in the chip system using the bridge sensor (bottom panel). The Brownian relaxation frequency of the individual nanobeads was measured to $f_B \approx 297$ Hz. To obtain data values that are independent of the nanobead concentration, all data have been normalized with the in-phase susceptibility measured well above f_B that approximates χ_∞. This normalization procedure was recently validated by Zardán Gómez de la Torre et al. (2011a) by comparing results obtained in the DynoMag AC susceptometer normalized with the high-frequency value of χ' with those obtained in a SQUID AC susceptometer normalized with the saturation magnetic moment. Nanobeads that are bound to DNA coils relax at a frequency of the order of 1 Hz (Strömberg et al., 2008), which is outside the investigated frequency window. Therefore, nanobeads that are bound to DNA coils will be dynamically inactive for the investi-gated frequencies and will not contribute to the peak in χ'' but still contribute to the high-frequency value of χ'. The binding of nanobeads to DNA coils is therefore detected as a reduction of the height of the peak in χ'' as well as in the low-frequency value of χ'.

The results displayed in Fig. 4 show that the same Brownian relaxation frequencies are obtained in the DynoMag system and by the bridge sensor in the chip system. In both cases the intensity of the peak in the normalized out-of-phase magnetic susceptibility (χ'' for the DynoMag system and V_2' for the bridge sensor) is reduced when the nanobeads are immobilized to the

Table 2
Average in-phase signal for cross and bridge sensors at three different bias currents for the 4×18 reference points from sweeps number 5 to 8. The numbers in parentheses indicate the standard deviations. The relative standard deviations are also calculated.

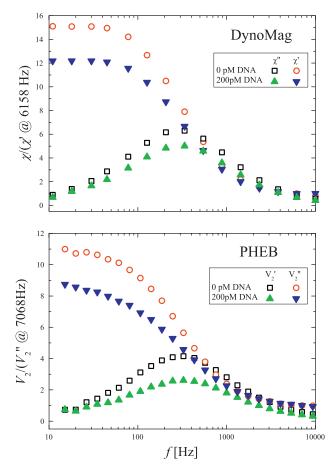| I (mA)	V_2' (nV)		$\sigma_{V_2'}/V_2' \times 100\%$ (%)	
	Bridge	Cross	Bridge	Cross
12.4	174(5)	29(3)	2.9	10.3
18.6	377(5)	62(4)	1.3	6.5
24.8	679(6)	108(4)	0.9	3.7

Fig. 4. Top: complex susceptibility vs. frequency measured with the DynoMag AC susceptometer. Measurements are normalized to the in-phase susceptibility at 6158 Hz. Bottom: in-phase and out-of-phase 2nd harmonic signal vs. frequency measured with a planar Hall effect bridge sensor. Measurements are normalized to the out-of-phase signal at 7068 Hz.

DNA coils. The observations in the DynoMag system are consis-tent with previously reported results (Zardán Gómez de la Torre et al., 2011a). The relative reduction of the peak height for the bridge sensor is larger than that observed in the DynoMag system.

5. Discussion

5.1. Brownian relaxation measurements using cross and bridge sensors

First, we note that the ratio between the measured low-field sensitivities for the bridge and cross sensor is $S_{B,0}/S_{C,0} = 6.8$, which is considerably lower than the ratio of 14 expected solely from the sensor geometry. We attribute this to demagnetization effects of the sensor, which reduce the sensitivity of the bridge sensor and increase the sensitivity of the cross sensor (Donolato et al., 2011). Using the ratio between the low-field sensitivities, we estimate from Eq. (6) that the nanobead signals should have a ratio of $V_B/V_C = 2.4$, which is significantly lower than the experi-mentally observed ratio of about six. This deviation is likely caused by a combination of demagnetization effects and the simplifying assumption that the current through the cross sensor is uniformly distributed over the sensor width w, also in the central part of the cross. The detailed origin of the differences will be topic of our continued studies.

In all measurements, we have found that the highest signal is obtained for the bridge sensor with the highest applied bias

current. Part of the observed noise in the measurements originates from electrical noise in the measurement set-up as the signals are small. However, we have chosen not to use a pre-amplifier as they typically induce significant instrumental phase shifts at high frequencies. Higher values of the sensor bias current than those employed here can be used, but they will result in non-negligible self-heating of the sensor, which is undesirable.

The extracted Brownian relaxation frequencies shown in Table 1 increase slightly with bias current. This increase could be due to self-heating of the sensor, which would correspond to a temperature increase of 0.6 °C when taking the temperature dependence of the viscosity of water into consideration. However, the increase is within the uncertainty limits of the measurements and thus, it cannot be concluded to be due to temperature changes. In general the extracted values are more stable for measurements performed on the bridge sensor than on the cross sensor. This shows that the higher signal-to-noise ratio results in smaller variations of the parameters extracted from the fits and hence that the measurements are robust and reproducible.

The results from measurements at the reference frequency in Fig. 3 show the time dependence of the dynamic bead signal. It is observed that the signal for 40 nm beads stabilizes 7 min after injection of the nanobead suspension. This time dependence originates from the time needed to equilibrate the bead concentration after the bead suspension is injected into the water-filled channel where the initial bead concentration near the sensor is lower due to the parabolic flow profile. Fig. 3 also shows that after flushing nanobeads away with 800 μL/min for 3 min, the signal returns to the background level, which allows for reusing the sensor.

5.2. Brownian relaxation measurements on samples containing DNA coils and oligonucleotide-tagged magnetic nanobeads

The results from relaxation measurements on nanobeads with and without DNA coils shown in Fig. 4 in general indicate the same trends whether measured with the bridge sensor or the DynoMag. In both cases the normalized peak levels become smaller in the presence of DNA coils. This was also the effect of DNA coils demonstrated by Zardán Gómez de la Torre et al. (2011a), where the DynoMag results were compared to SQUID results. A reason why the responses are not completely identical could be that the DynoMag AC susceptometer measures on the entire sample volume, whereas the bridge sensor is more sensitive to beads near to the sensor surface. The latter can in fact prove useful for detecting DNA coils since nanobeads bound to DNA coils will sediment faster than free nanobeads. Therefore, the ratio between bound and free nanobeads near the sensor surface will become larger and this will make it easier to detect smaller DNA coil concentrations.

6. Conclusion

We have compared on-chip Brownian relaxation measurements carried out using planar Hall effect sensors with cross and bridge geometries with the same sensor width. For the investigated geometries we found that the bead signal from the bridge sensor is six times that from the cross. Moreover, the Brownian relaxation frequencies were determined with significantly less variation for the bridge sensor than for the cross.

The bridge sensor was also used to measure the difference between two samples of nanobeads with 0 pM and 200 pM of DNA coils produced by RCA. For comparison, equivalent samples were measured in a commercial AC susceptometer, and the differences between 0 pM and 200 pM samples were found to be very similar in the two systems. The presented bridge sensor may, thus, open up for new possibilities to build inexpensive biosensors for detecting pathogens and other clinically relevant analytes that can be amplified using RCA, including DNA sequences and proteins.

References

Astalan, A.P., Ahrentorp, F., Johansson, C., Larsson, K., Krozer, A., 2004. Biosensors and Bioelectronics 19, 945–951.
Brown, W., 1963. Physical Review 130, 1677–1686.
Cole, K.S., Cole, R.H., 1941. The Journal of Chemical Physics 9, 341.
Connolly, J., St Pierre, T.G., 2001. Journal of Magnetism and Magnetic Materials 225, 156–160.
Dalslet, B.T., Damsgaard, C.D., Donolato, M., Strømme, M., Strömberg, M., Svedlindh, P., Hansen, M.F., 2011. Lab on a Chip 11, 296–302.
Debye, P., 1929. The Chemical Catalogue Co. New York.
Donolato, M., Dalslet, B.T., Damsgaard, C.D., Gunnarsson, K., Jacobsen, C.S., Svedlindh, P., Hansen, M.F., 2011. Journal of Applied Physics 109, 064511.
Fire, A., Xu, S.-Q, 1995. Proceedings of the National Academy of Sciences of the USA 92, 4641–4645.
Göransson, J., Zardán Gómez De La Torre, T., Strömberg, M., Russell, C., Svedlindh, P., Strømme, M., Nilsson, M., 2010. Analytical Chemistry 82, 9138–9140.
Hansen, T.B.G., Damsgaard, C.D., Dalslet, B.T., Hansen, M.F., 2010. Journal of Applied Physics 107, 124511.
Henriksen, A.D., Dalslet, B.T., Skieller, D.H., Lee, K.H., Okkels, F., Hansen, M.F., 2010. Applied Physics Letters 97, 013507.
Jaffrezic-Renault, N., Martelet, C., Chevolot, Y., Cloarec, J.P., 2007. Sensors 7, 589–614.
Koh, I., Josephson, L., 2009. Sensors 9, 8130–8145.
Liu, D., Daubendiek, S.L., Zillman, M.A., Ryan, K., Kool, E.T., 1996. Journal of the American Chemical Society 118, 1587–1594.
Ludwig, F., Mäuselein, S., Heim, E., Schilling, M., 2005. Review of Scientific Instruments 76, 106102.
Nilsson, M., Malmgren, H., Samiotaki, M., Kwiatkowski, M., Chowdhary, B.P., Landegren, U., 1994. Science 265, 2085–2088.
Öisjöen, F., Schneiderman, J.F., Astalan, A.P., Kalabukhov, A., Johansson, C., Winkler, D., 2010. Biosensors and Bioelectronics 25, 1008–1013.
Østerberg, F.W., Dalslet, B.T., Snakenborg, D., Johansson, C., Hansen, M.F., 2010. AIP Conference Proceedings, 176–183.
Persson, A., Bejhed, R.S., Nguyen, H., Gunnarsson, K., Dalslet, B.T., Østerberg, F.W., Hansen, M.F., Svedlindh, P., 2011. Sensors and Actuators A: Physical 171, 212–218.
Strömberg, M., Göransson, J., Gunnarsson, K., Nilsson, M., Svedlindh, P., Strømme, M., 2008. Nano Letters 8, 816–821.
Wang, S.X., Li, G., 2008. IEEE Transactions on Magnetics 44, 1687–1702.
Zardán Gómez de la Torre, T., Mezger, A., Herthnek, D., Johansson, C., Svedlindh, P., Nilsson, M., Strømme, M., 2011a. Biosensors and Bioelectronics 29, 195–199.
Zardán Gómez de la Torre, T., Herthnek, D., Ramachandraiah, H., Svedlindh, P., Nilsson, M., Strømme, M., 2011b. Journal of Nanoscience and Nanotechnology 11, 8532–8537.
Zardán Gómez de la Torre, T., Ke, R., Mezger, A., Svedlindh, P., Strømme, M., Nilsson, M., 2012. Small, 2174–2177.

Paper IV

F. W. Østerberg, G. Rizzi and M. F. Hansen

On-chip measurements of Brownian relaxation vs. concentration of 40 nm magnetic beads

Frederik Westergaard Østerberg,[a] Giovanni Rizzi, and Mikkel Fougt Hansen[b]
*Department of Micro- and Nanotechnology, Technical University of Denmark, DTU Nanotech, Building 345B,
DK-2800 Kongens Lyngby, Denmark*

We present on-chip Brownian relaxation measurements on a logarithmic dilution series of 40 nm beads dispersed in water with bead concentrations between 16 μg/ml and 4000 μg/ml. The measurements are performed using a planar Hall effect bridge sensor at frequencies up to 1 MHz. No external fields are needed as the beads are magnetized by the field generated by the applied sensor bias current. We show that the Brownian relaxation frequency can be extracted from fitting the Cole-Cole model to measurements for bead concentrations of 64 μg/ml or higher and that the measured dynamic magnetic response is proportional to the bead concentration. For bead concentrations higher than or equal to 500 μg/ml, we extract a hydrodynamic diameter of 47(1) nm for the beads, which is close to the nominal bead size of 40 nm. Furthermore, we study the signal vs. bead concentration at a fixed frequency close to the Brownian relaxation peak and find that the signal from bead suspensions with concentrations down to 16 μg/ml can be resolved. © 2012 American Institute of Physics. [http://dx.doi.org/10.1063/1.4769796]

I. INTRODUCTION

Magnetic beads have proven useful for biosensing as most biological samples are non-magnetic such that magnetic beads can be manipulated and detected independently of the sample chemistry. Furthermore, magnetic biosensors rely on magnetic methods for detecting the magnetic beads, which provide an electrical signal that can be directly read out. Among the typical methods for detecting magnetic beads are inductive methods,[1] fluxgates,[2] superconducting quantum interference device (SQUID) magnetometers,[3,4] and magnetoresistive sensors.[5–7] There are pros and cons for each method; for instance, SQUID magnetometers are very sensitive but are costly, require cryogenics and are not easily integrated with a sample preparation system. Magnetoresistive sensors are not as sensitive as SQUID magnetometers but they can be operated at room temperature, they are small in dimensions, they are potentially inexpensive and they can be integrated in lab-on-a-chip systems. Thus, magnetoresistive sensors are attractive for use in lab-on-a-chip magnetic biosensing platforms.

Magnetic beads have been used for biosensing in surface-based[8] and volume-based[1,9,10] assays. In a surface-based assay, the surfaces of both the sensor and the beads are functionalized such that the presence of the analyte results in specific binding of the beads to the sensor surface. In a volume-based assay, only the beads are functionalized prior to detection and the analyte modifies the hydrodynamic size of the beads, either due to its size[11] or by inducing bead agglutination.[1] The dispersion of hydrodynamic sizes for a magnetic bead ensemble can be characterized via Brownian relaxation measurements, which were first proposed for biosensing by Connolly and St Pierre.[12]

For volume-based bioassays, the limit of detection is sensitive to the bead concentration: for a high bead concentration, only a small fraction of the beads are affected by a given amount of analyte, whereas the opposite is the case for a low bead concentration. On the other hand, a low bead concentration results in a smaller dynamic range of analyte concentrations that can be detected. Thus, the bead concentration is an important parameter for the sensitivity and dynamic range for volume-based biosensing. For any read-out principle for volume-based bioassays, it is therefore important to know its dependence on the bead concentration and the range of bead concentrations for which the magnetic dynamics can be reliably characterized.

In this study, we investigate the dependence of the on-chip measurements of the dynamic magnetic bead signal on the concentration of beads with a nominal diameter of 40 nm. The study is carried out using so-called planar Hall effect bridge (PHEB) sensors[13] currently being investigating for volume-based magnetic biodetection.[10] The sensors are integrated in a microfluidic system and do not rely on any external magnetic fields. We determine the lower limit of bead concentrations required for obtaining reliable measurements of the dynamic magnetic Brownian relaxation response and we also investigate the lowest bead concentration that can be detected by the present sensors.

II. THEORY

The magnetic field sensors used in the study are based on the anisotropic magnetoresistance (AMR) effect, which causes the resistivity to be largest when the current and applied magnetic field are parallel and lowest when they are orthogonal. The sensor geometry is composed of four segments to form a Wheatstone bridge as shown in Fig. 1. Here, the potential difference V_y in the y-direction is measured upon injection of a current I in the x-direction. The sensor

[a]Electronic address: Frederik.Osterberg@nanotech.dtu.dk.
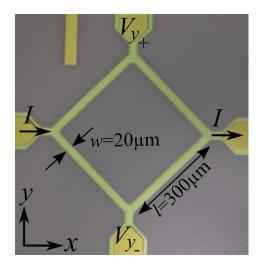[b]Electronic address: Mikkel.Hansen@nanotech.dtu.dk.

FIG. 1. Picture of sensor with definitions of dimensions. The bias current I is applied through the arms in the x-direction, while the potential difference V_y is measured across the y-direction. The length l and width w of a bridge segment are also shown.

consists of a ferromagnetic layer exhibiting the AMR effect, which is pinned along the positive x-direction by an antiferromagnetic layer. This ensures that the magnetization of the sensor is single domain and has a fixed orientation in the absence of external magnetic fields. It has recently been shown that the signal from the bridge structure shown in Fig. 1 is identical to that from a regular planar Hall effect sensor cross, except for a geometrical amplification.[13] To distinguish this particular geometry from other AMR sensor geometries, we have named sensors with this geometry planar Hall effect bridge sensors.

For low magnetic fields, the sensor signal is linear and given by[13]

$$V_y = I S_0 H_y, \qquad (1)$$

where S_0 is the low-field sensitivity and H_y is the magnetic field in the y-direction.

Measurements on magnetic bead suspensions are carried out without application of external magnetic fields. Instead, the magnetic beads are magnetized by the sensor self-field arising from the bias current passed through the sensor. For an alternating bias current $I(t) = I_{AC} \sin(2\pi f t)$, both the bias current and the field from the beads will oscillate at the frequency f of the bias current. As the sensor response due to the presence of magnetic beads is proportional to I^2, these will give rise to a signal oscillating at $2f$. The dynamic magnetic response of the magnetic beads is described by their complex susceptibility $\chi = \chi' - i\chi''$, where χ' and χ'' are the in-phase and out-of-phase magnetic susceptibilities of the beads, respectively. We have previously shown that the dynamic magnetic bead response for beads magnetized by the self-field can be detected using lock-in technique[10,14,15] and that the second harmonic in-phase and out-of-phase sensor signals V_2' and V_2'' for a PHEB sensor are given by[10]

$$V_2' = -2^{-3} I_{AC}^2 S_0 \gamma_1 \chi'', \qquad (2)$$

$$V_2'' = -2^{-3} I_{AC}^2 S_0 (\gamma_0 + \gamma_1 \chi'), \qquad (3)$$

where γ_0 is a constant that depends on the sensor stack and sensor geometry and γ_1 is a constant that depends on the sensor geometry and distribution of beads. Thus, the in-phase second harmonic sensor signal is proportional to the out-of-phase magnetic bead susceptibility and the out-of-phase second harmonic sensor signal depends linearly on the in-phase magnetic bead susceptibility.

A. Brownian relaxation of magnetic of beads

When a magnetic bead is placed in a magnetic field, the magnetization of the bead will align with the field either by internal flipping of the magnetic moment (Néel relaxation[16]) or by a physical rotation of the bead (Brownian relaxation[17]). For the beads used in this study, the Néel relaxation time is much longer than the Brownian relaxation time, which therefore dominates the relaxation dynamics of the beads. Brownian relaxation is characterized by the Brownian relaxation frequency,

$$f_B = \frac{k_B T}{6\pi \eta V_h}, \qquad (4)$$

where $k_B T$ is the thermal energy, η is the viscosity of the liquid in which the bead is suspended, and V_h is the hydrodynamic volume of the bead. The Brownian relaxation frequency is the frequency at which the phase-lag between the magnetic moment of the bead and the applied field is largest, meaning that a peak will appear in the out-of-phase magnetic susceptibility at $f = f_B$.

The complex susceptibility of a monodisperse ensemble of beads is described by the Debye theory.[18] The complex susceptibility of an ensemble of polydisperse beads is usually described by the empirical Cole-Cole model,[19]

$$\chi = \frac{\chi_0 - \chi_\infty}{1 + (if/f_B)^{1-\alpha}} + \chi_\infty, \qquad (5)$$

where χ_0 and χ_∞ are the DC and high-frequency susceptibilities, respectively, and $0 \leq \alpha \leq 1$ is a measure of the polydispersity ($\alpha = 0$ for a monodisperse sample). The Cole-Cole model has been used for analyzing the data in the present work to extract f_B, α, and the DC and high-frequency susceptibilities.

III. EXPERIMENTAL

The geometric variables of the sensor are defined in Fig. 1. Each of the four branches in the sensor bridge used in the present study has a length of $l = 300$ μm and a width of $w = 20$ μm and was fabricated as follows: First, an 800 nm thick oxide was grown on a silicon wafer by wet oxidation. Then, the sensor stack Ta(3 nm)/Ni$_{80}$Fe$_{20}$(30 nm)/Mn$_{80}$Ir$_{20}$(20 nm)/Ta(3 nm) was deposited in a Kurt J. Lesker Co. CMS-18 sputter system and defined by lift-off. During deposition, a magnetic field of 20 mT was applied to define the easy direction of the magnetization along the positive x-direction in Fig. 1. Electrical contacts to the sensors of Ti(5 nm)/Au(100 nm)/Pt(100 nm)/Ti(5 nm) were deposited by e-beam evaporation and defined by lift-off. Subsequently,

a protective coating of Ormocomp (Micro Resist Technology GmbH, Germany) with a thickness of 800 nm was spin-coated and patterned by UV lithography. This coating ensured that the sensors could be operated at voltages up to 10 V without failure or bubble formation when the sensor was exposed to ionic solutions.

During measurements, the chip was mounted in a click-on fluidic system[14] providing electrical contacts to the chip and defining a fluidic channel of dimensions length-× width × height = 5 mm × 1 mm × 1 mm (Fig. 2(a)). To align the chip with the channel and electrical contact, the chip was placed in an aluminum well (Fig. 2(b)). The temperature of the aluminum well was kept constant at (25.00 ± 0.01) °C during all measurements using a Peltier element. The set-up was neither magnetically nor electrically shielded.

Electrical measurements on the sensor were carried out using an HF2LI lock-in amplifier (Zurich Instruments, Switzerland) operating at a fixed voltage amplitude of 3.2 V corresponding to a current amplitude of $I_{AC} = 21$ mA. The 1st harmonic sensor response was measured vs. applied field resulting in a low-field sensor sensitivity of $S_0 = -531$ V/(T A).

Measurements were performed on nominally 40 nm magnetic beads with a COOH functional surface group (Ocean Nanotech, AR, USA). In this study, the bead concentration was varied from $c = 16$ μg/ml to $c = 4$ mg/ml in a 2-fold logarithmic dilution series. In the experiments, the bead concentration was varied in the following order: c [mg/ml] = 1, 0.25, 0.063, 0.5, 0.125, 0.031, 0.016, 4, 2.

Measurements on bead suspensions were carried out in ambient magnetic field where the 2nd harmonic sensor response was measured as a function of the frequency of the applied bias voltage. Each frequency sweep consisted of 20 points equally distributed on a log scale between $f = 986.9$ kHz and 37.7 Hz. After each measurement at f, a reference measurement was carried out at $f_{ref} = 4667$ Hz, which is near the expected Brownian relaxation frequency for the beads used in the experiments. Each of the above sweeps took a total time of 7 min and 20 s to complete. For each bead concentration, a cycle of 9 frequency sweeps, numbered 1–9, was performed. First, two sweeps (1 and 2) were performed without beads and were used as reference. At the start of sweep 3, beads were injected into the fluidic channel for 1 min at a flow rate of 30 μl/min. Then, the flow was stopped for the remaining part of sweep 3 and left stagnant in the following four sweeps (sweeps 4–7). At the start
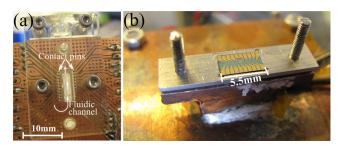
of sweep 8, the beads were washed out at a flow rate of 800 μl/min and sweep 9 was performed to confirm that the signal returned to its initial level from sweeps 1 and 2.

IV. RESULTS

A. Frequency sweeps

Figure 3 shows the in-phase (top) and out-of-phase (bottom) second harmonic sensor signals as a function of the bias current frequency for sweep 7, which is started 29 min after injection of the beads. Only measurements for the seven highest bead concentrations (63 μg/ml-4 mg/ml) are shown, as the lower concentrations are indistinguishable from $c = 63$ μg/ml on this scale. The solid lines in the figures are curve fits of the Cole-Cole model to the measured data. From Fig. 3, it is seen that the curve shape is independent of the concentration and that it scales with the bead concentration.

Figure 4 shows the Brownian relaxation frequencies f_B extracted from curve fits of the Cole-Cole model vs. bead concentration. The fits of the in-phase and out-of-phase data were carried out simultaneously with a single set of parameters. For each concentration, the values of f_B were found separately for sweeps 5–7. The error bars on each of the f_B-values in Fig. 4 correspond to the standard deviation reported by the least-squares fitting routine. It is also seen

FIG. 2. (a) Fluidic system with 20 spring-loaded electrical contact pins. (b) Picture of chip in set-up prior to mounting of the fluidic system.
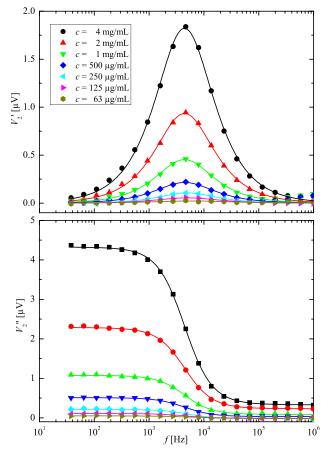

FIG. 3. In-phase (top) and out-of-phase (bottom) signals vs. bias frequency for the indicated bead suspension concentrations. The solid lines are fits of the Cole-Cole model to the measurements.
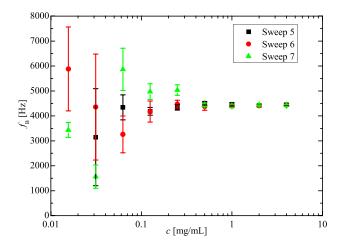
FIG. 4. Brownian relaxation frequencies extracted from sweeps 5–7 plotted against bead concentration. The length of the error bars corresponds to the standard deviations obtained from the fitting.

that for the four highest concentrations, the extracted frequencies coincide with a mean Brownian relaxation frequency of 4.4(0.1) kHz corresponding to a hydrodynamic diameter of 47(1) nm. Down to $c = 63 \, \mu g/ml$ the mean Brownian relaxation frequency is still 4.4 kHz, but the standard deviation increases to 0.8 kHz. The average value of the Cole-Cole parameter α was found to 0.05(0.01) for the fits shown in Fig. 4. This supports the conclusion that the curve shape is independent of the bead concentration for the investigated samples.

B. Signal at $f \simeq f_B$ vs. bead concentration

Figure 5 shows the in-phase second harmonic sensor signal of the reference points measured at $f_{ref} = 4667$ Hz normalized with c plotted vs. time t after injection of the bead suspension. The figure also shows the sweep numbers for each of the bead concentrations. Sweeps 1 and 2 are carried out without beads; the bead suspension is injected at the start of sweep 3 resulting in a signal increase and during sweeps 4–7, the signal is almost constant. During sweep 8
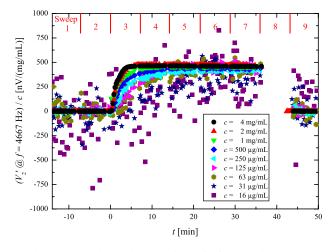
(not shown), the beads are washed away and the data obtained during sweep 9 shows that the signal returns to its baseline level from sweeps 1 and 2. From Fig. 5 it is observed that the signal-to-noise ratio increases with increasing bead concentration. It is also seen that a level near 460 nV/(mg/ml) is reached for all bead concentrations, except for the two lowest concentrations that are clearly at a lower level. From Fig. 5, it is also noticed that the signal rise after injection depends on the bead concentration. When the bead concentration is high, the signal reaches its steady-state value faster.

Figure 6 shows the mean values of the twenty reference points obtained during sweep 7 (last sweep before washing) as a function of the bead concentration. The error bars indicate three times the standard deviation of the mean (σ_{mean}). The line is a linear fit to the data with the intercept fixed to zero and a slope of 460(2) nV/(mg/ml). Analysis of the reference measurements obtained during sweeps 2, where the mean value defined the zero signal level in the subsequent measurements, resulted in a noise level (taken as 3 σ_{mean}) of 3.1 nV, which is shown as the horizontal dashed line in Fig. 6. It is seen that the signals from all the measured bead concentrations are significantly above the sensor noise level.

V. DISCUSSION

A. Frequency sweeps

From the frequency sweeps plotted in Fig. 3, it is seen that the shape is independent of the bead concentration, and hence that the signal scales with the concentration. This was also confirmed by the similar values of f_B and α obtained from the Cole-Cole fits for $c \geq 63 \, \mu g/ml$. For the two lowest concentrations, the signal-to-noise ratio was too low to extract reliable values of f_B and α. The obtained α-value of 0.05 indicates that the bead suspension is nearly monodisperse. It is important for volume-based biodetection that the bead suspension is close to monodisperse as this results in a well defined peak in the in-phase sensor signal, which

FIG. 5. In-phase 2nd harmonic sensor signal of reference points measured at $f_{ref} = 4667$ Hz normalized with bead concentration plotted as a function of the time t after injection of the bead suspension.
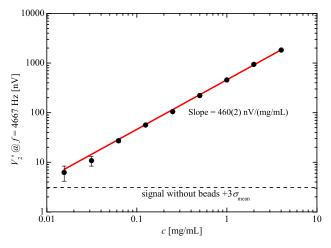

FIG. 6. Mean value of the 20 reference points measured during sweep 7 vs. bead concentration. The error bars are given as 3 σ_{mean}. The solid line is a linear fit to the data points with the intercept fixed at 0. The horizontal dashed line indicates the noise level plus 3 σ_{mean} for a measurement without any beads.

potentially allows for distinguishing the peak from isolated beads from a peak at lower frequencies due to beads bound to the target analyte.

The extracted Brownian frequencies are found to 4.4(0.8) kHz for $c \geq 63 \,\mu\mathrm{g/ml}$ and 4.4(0.1) kHz for $c \geq 500 \,\mu\mathrm{g/ml}$. The mean values are identical within the uncertainties, but the standard deviation increases as the bead concentration decreases due to the lower signal-to-noise ratio. This means that if the hydrodynamic diameter needs to be extracted accurately for the present beads, a bead concentration of at least $500 \,\mu\mathrm{g/ml}$ should be used.

B. Signal at $f \simeq f_B$ vs. bead concentration

Figure 5 shows the reference points measured at $f \simeq f_B$ vs. time for several bead concentrations. The values are normalized with the bead concentration and adjusted such that the injection of beads is initiated at $t = 0 \,\mathrm{min}$. From this plot it is observed that the signals stabilize near 460 nV/(mg/ml) for all concentrations except for the two lowest, which do not reach this level. Figure 5 also shows that the signal returns to its baseline level after the beads are washed away, which allows for reusing the sensor.

From Fig. 5 it is seen that the rate by which the signal changes after the beads have been injected depends on the bead concentration such that a faster equilibration is found for higher bead concentrations. The equilibration arises from the fact that the bead suspension is injected into the channel containing water and that the liquid exchange near the channel wall is slower due to the parabolic velocity profile. The detailed origin of the faster equilibration for higher bead concentrations is still unknown, but we hypothesize that it could be due to cooperative phenomena, e.g., hydrodynamic interactions between the beads[20] or electrostatic repulsion between the beads due to their surface charges, which accelerate the equilibration when the bead density is high.

Figure 6 shows the average of the in-phase signal for the 20 reference points measured during sweep seven plotted vs. bead concentration. From the plot it is seen that the signal is proportional to the bead concentration with a slope of 460(2) nV/(mg/ml). It is also seen that all the measured concentrations are significantly different from reference measurement without beads on a $3 \,\sigma_{\mathrm{mean}}$ level. The lowest bead mass concentration measured was $16 \,\mu\mathrm{g/ml}$, which corresponds to a particle concentration of 0.2 nM. When used in a volume-based bioassay, a lower bead concentration will increase the sensitivity and lower the dynamic range. Hence, one approach to increase the sensitivity could be to use larger magnetic beads such that the same magnetic signal can be obtained from fewer beads. However, in our system, beads that are larger than about 100 nm tend to sediment to the bottom of the fluidic channel and as the sensors are more sensitive to beads near the sensor surface, such sedimented beads will contribute significantly to the signal. The investigation of the choice of beads and optimization of the bioassay sensitivity is one focus of our future research.

VI. CONCLUSION

Based on the presented data, it is concluded that Brownian relaxation frequencies can be extracted using planar Hall effect

bridge sensors for bead concentration as low as $64 \,\mu\mathrm{g/ml}$. However, a higher bead concentration results in more reliable determination of the Brownian relaxation frequency. The mean Brownian relaxation frequency for $c \geq 500 \,\mu\mathrm{g/ml}$ was 4.4(0.1) kHz, which corresponds to a hydrodynamic diameter of 47(1) nm, which agrees well with the nominal size of 40 nm. The study also demonstrated that the shape of the dynamic signal is independent of the bead concentration and the amplitudes of the signals are proportional to the bead concentration once steady-state is reached. Monitoring the time dependence of the signal during bead injection showed that the signal reaches a steady state faster for higher bead concentrations. Finally, it can be concluded that the presence of beads can be detected for bead concentrations as low as $16 \,\mu\mathrm{g/ml}$.

[1]A. P. Astalan, F. Ahrentorp, C. Johansson, K. Larsson, and A. Krozer, "Biomolecular reactions studied using changes in Brownian rotation dynamics of magnetic particles," Biosens. Bioelectron. **19**, 945 (2004).

[2]F. Ludwig, S. Mäuselein, E. Heim, and M. Schilling, "Magneto-relaxometry of magnetic nanoparticles in magnetically unshielded environment utilizing a differential fluxgate arrangement," Rev. Sci. Instrum. **76**, 106102 (2005).

[3]K. Enpuku, T. Minotani, T. Gima, Y. Kuroki, Y. Itoh, M. Yamashita, Y. Katakura, and S. Kuhara, "Detection of magnetic nanoparticles with superconducting quantum interference device (SQUID) magnetometer and application to immunoassays," Jpn. J. Appl. Phys., Part 2 **38**, L1102 (1999).

[4]H. Grossman, W. Myers, V. Vreeland, R. Bruehl, M. Alper, C. Bertozzi, and J. Clarke, "Detection of bacteria in suspension by using a superconducting quantum interference device," Proc. Natl. Acad. Sci. USA **101**, 129 (2004).

[5]D. R. Baselt, G. U. Lee, M. Natesan, S. W. Metzger, P. E. Sheehan, and R. J. Colton, "A biosensor based on magnetoresistance technology," Biosens. Bioelectron. **13**, 731 (1998).

[6]L. Ejsing, M. F. Hansen, A. K. Menon, H. A. Ferreira, D. L. Graham, and P. P. Freitas, "Planar Hall effect sensor for magnetic micro- and nanobead detection," Appl. Phys. Lett. **84**, 4729 (2004).

[7]S. X. Wang and G. Li, "Advances in giant magnetoresistance biosensors with magnetic nanoparticle tags: Review and outlook," IEEE T. Magn. **44**, 1687 (2008).

[8]R. S. Gaster, D. A. Hall, C. H. Nielsen, S. J. Osterfeld, H. Yu, K. E. Mach, R. J. Wilson, B. Murmann, J. C. Liao, S. S. Gambhir, and S. X. Wang, "Matrix-insensitive protein assays push the limits of biosensors in medicine," Nat. Med. **15**, 1327 (2009).

[9]A. Prieto Astalan, C. Jonasson, K. Petersson, J. Blomgren, D. Ilver, A. Krozer, and C. Johansson, "Magnetic response of thermally blocked magnetic nanoparticles in a pulsed magnetic field," J. Magn. Magn. Mater. **311**, 166 (2007).

[10]F. W. Østerberg, G. Rizzi, T. Zardán Gómez de la Torre, M. Strömberg, M. Strømme, P. Svedlindh, and M. F. Hansen, "Measurements of Brownian relaxation of magnetic nanobeads using planar Hall effect bridge sensors," Biosens. Bioelectron. **40**, 147 (2013).

[11]M. Strömberg, J. Göransson, K. Gunnarsson, M. Nilsson, P. Svedlindh, and M. Strømme, "Sensitive molecular diagnostics using volume-amplified magnetic nanobeads," Nano Lett. **8**, 816 (2008).

[12]J. Connolly and T. G. St Pierre, "Proposed biosensors based on time-dependent properties of magnetic fluids," J. Magn. Magn. Mater. **225**, 156 (2001).

[13]A. D. Henriksen, B. T. Dalslet, D. H. Skieller, K. H. Lee, F. Okkels, and M. F. Hansen, "Planar Hall effect bridge magnetic field sensors," Appl. Phys. Lett. **97**, 013507 (2010).

[14]F. W. Østerberg, B. T. Dalslet, D. Snakenborg, C. Johansson, and M. F. Hansen, "Chip-based measurements of Brownian relaxation of magnetic beads using a planar Hall effect magnetic field sensor," AIP Conf. Proc. **1311**, 176–183 (2010).

[15]B. T. Dalslet, C. D. Damsgaard, M. Donolato, M. Strømme, M. Strömberg, P. Svedlindh, and M. F. Hansen, "Bead magnetorelaxometry with an on-chip magnetoresistive sensor," Lab Chip **11**, 296 (2011).

[16]L. Neél, "Théorie du traînage magnétique des ferromagnétiques en grains fins avec applications aux terres cuites," Ann. Géophys. **5**, 99 (1949).

[17]W. Brown, "Thermal fluctuations of a single-domain particle," Phys. Rev. **130**, 1677 (1963).

[18]P. Debye, *Polar Molecules* (Chemical Catalogue Co. 1929).

[19]K. S. Cole and R. H. Cole, "Dispersion and absorption in dielectrics I. Alternating current characteristics," J. Chem. Phys. **9**, 341 (1941).

[20]C. Mikkelsen, M. F. Hansen, and H. Bruus, "Theoretical comparison of magnetic and hydrodynamic interactions between magnetically tagged particles in microfluidic systems," J. Magn. Magn. Mater. **293**, 578 (2005).

Paper V

F. W. Østerberg, G. Rizzi and M. F. Hansen

On-chip measurements of Brownian relaxation of magnetic beads with diameters from 10 nm to 250 nm

Frederik Westergaard Østerberg,[1, a)] Giovanni Rizzi,[1] and Mikkel Fougt Hansen[1, b)]

Department of Micro- and Nanotechnology, Technical University of Denmark,
DTU Nanotech, Building 345B, DK-2800 Kongens Lyngby, Denmark

We demonstrate the use of planar Hall effect magnetoresistive sensors for AC susceptibility measurements of magnetic beads with frequencies ranging from DC to 1 MHz. This wide frequency range allows for measuring Brownian relaxation of magnetic beads with diameters ranging from 10 nm to 250 nm. Brownian relaxation is measured for six different magnetic bead types and their hydrodynamic diameters are determined. The hydrodynamic diameters are found to be within 40% of the nominal bead diameters. We discuss the applicability of the different bead types for volume-based biosensing with respect to sedimentation, magnetic trapping and signal per bead. Among the investigated beads, we conclude that the beads with a nominal diameter of 80 nm are best suited for future on-chip volume-based biosensing experiments using planar Hall effect sensors.

I. INTRODUCTION

Magnetic beads have proven to be a promising ingredient in future biosensors[1–4]. Since most biological samples are non-magnetic, the read out will not be disturbed by chemical or biological components of the sample. Magnetic beads also have the advantage that they can be manipulated magnetically and are generally well dispersed in a liquid sample such that diffusion times can be significantly reduced. Finally, the presence and properties of magnetic beads can be detected by magnetic field sensors to directly provide an electrical signal.

Connolly and St Pierre[5] first proposed to use Brownian relaxation measurements of magnetic beads for biosensing. Brownian relaxation is the physical rotation of a bead in response to an oscillating magnetic field and it is characterized by the Brownian relaxation frequency, which is inversely proportional to the hydrodynamic volume of the bead. Using functionalized magnetic beads it is possible to bind a target analyte to the beads to obtain a detectable increase of their hydrodynamic size.

The simplest assay is to directly detect a hydrodynamic size change of the free beads in suspension due to bound analytes. However, as most analytes are typically much smaller than the beads, this will only give rise to a limited change of hydrodynamic size[6]. Moreover, the change may be difficult to resolve due to the inevitable bead size distribution. A more effective assay strategy is to use the target analyte to form clusters of beads and hence induce bead agglutination[7]. Yet another strategy is to use amplification of the target analyte to form substantially larger entities, e.g., by forming large

DNA coils by a rolling circle amplification[8,9]. Such coils have the advantage of both changing the hydrodynamic size of single beads significantly and that each coil can bind multiple beads[10]. The drawback is that the rolling circle amplification requires additional sample preparation.

Brownian relaxation of magnetic beads can be measured with various techniques including: Inductive methods[6], fluxgates[11], SQUID magnetometers[12] and magnetoresistive sensors[13,14]. Particularly magnetoresistive sensors are promising in future lab-on-chip devices as they are small, potentially inexpensive, require small sample volumes and can be integrated with sample preparation in a microfluidic device.

The frequency range in which a given technique operates determines the bead sizes for which Brownian relaxation can be measured. Thus, it is advantageous to have a detection system that can operate at frequencies spanning many orders of magnitude.

Here, we demonstrate on-chip measurements of Brownian relaxation of magnetic beads with diameters ranging from 10 nm to 250 nm using so-called planar Hall effect bridge sensors[15,16] and that these sensors are feasible for dynamic magnetic measurements up to MHz frequencies. Finally, we discuss the best choice of bead type and size for future on-chip volume-based bioassays employing these sensors.

II. THEORY

A. Brownian relaxation of magnetic of beads

When a magnetic bead is placed in an external magnetic field, the magnetic moment will align with the direction of the applied field. The moment of the bead may relax by an internal flipping of the moment (Néel

---

a)Electronic mail: Frederik.Osterberg@nanotech.dtu.dk
b)Electronic mail: Mikkel.Hansen@nanotech.dtu.dk

relaxation[17]) and by a physical rotation (Brownian relaxation[18]). For the beads used in this study, Brownian relaxation dominates and we will neglect Néel relaxation. When the bead is placed in a magnetic field oscillating at frequency f, the dynamic behavior is characterized by the Brownian relaxation frequency

$$f_{\mathrm{B}} = \frac{k_{\mathrm{B}}T}{6\pi\eta V_{\mathrm{h}}}, \qquad (1)$$

where $k_{\mathrm{B}}T$ is the thermal energy, η is the dynamic viscosity of the liquid in which the bead is suspended and V_{h} is the hydrodynamic volume of the bead. The dynamic magnetic behavior of a magnetic bead ensemble in response to an applied magnetic field is described by the complex magnetic susceptibility $\chi = \chi' - \mathrm{i}\chi''$, where χ' and χ'' denote the in-phase and out-of-phase magnetic susceptibilities, respectively. For $f \ll f_{\mathrm{B}}$, the beads rotate in phase with the applied field and for $f \gg f_B$ the field is oscillating too fast for the beads to respond. When $f = f_B$, the component of the bead moment lagging behind the applied field assumes its maximum, resulting in a peak in the out-of-phase magnetic susceptibility. Cole and Cole[19] have shown empirically that the complex magnetic susceptibility due to Brownian relaxation for a polydisperse ensemble of beads is often well described by

$$\chi = \frac{\chi_0 - \chi_\infty}{1 + (\mathrm{i}f/f_{\mathrm{B}})^{1-\alpha}} + \chi_\infty, \qquad (2)$$

where χ_0 and χ_∞ are the DC and high frequency susceptibilities, respectively. The parameter α is a measure of the polydispersity of the bead ensemble and can assume values between 0 and 1. For a monodisperse sample, $\alpha = 0$ and the Cole-Cole model reduces to the Debye model[20].

B. Sensor signal

The sensors used in this study are based on the anisotropic magnetoresistance (AMR) effect[21]. The sensors are structured in a bridge geometry as shown in Fig. 1. A bias current I is applied in the x-direction and the potential difference V_y is measured across the y-direction. The signal from the sensor bridge is the same as for cross-shaped planar Hall effect sensors except for a geometrical amplification[15]. To distinguish them from other AMR bridge geometries we have therefore named them planar Hall effect bridge (PHEB) sensors[15].

For low magnetic fields, the sensor signal is linear and given by[15]

$$V_y = IS_0 H_y, \qquad (3)$$

where S_0 is the low-field sensitivity and H_y is the average magnetic field acting on the sensor area in the y-direction.

Our measurements of the magnetic bead susceptibility are performed in nominally zero externally applied
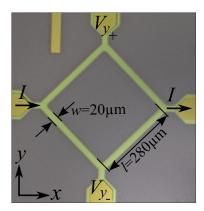

FIG. 1. Picture of a sensor with definition of dimensions. The bias current I is applied through the arms in the x-direction, while the potential difference V_y is measured across the y-direction.

magnetic field and the beads are magnetized by the magnetic field arising from the alternating bias current $I(t) = I_{\mathrm{AC}}\sin(2\pi f t)$ passed through the sensors. We have previously shown[16] that the in-phase and out-of-phase components of the complex second harmonic sensor signal $V_2 = V_2' + \mathrm{i}V_2''$ measured using lock-in technique can be written

$$V_2' = -2^{-3}I_{\mathrm{AC}}^2 S_0 \gamma_1 \chi'' \qquad (4)$$
$$V_2'' = -2^{-3}I_{\mathrm{AC}}^2 S_0 (\gamma_0 + \gamma_1 \chi'). \qquad (5)$$

Here, γ_0 is a constant depending on the sensor stack and geometry that describes the sensor self-biasing and γ_1 is a parameter depending on the sensor geometry and distribution of beads that describes the magnetic field acting on the sensor from magnetic beads magnetized by the sensor self-field. The value of γ_1 is positive in the presence of beads and zero in the absence of beads[22]. Thus, the in-phase second harmonic sensor signal is proportional to the out-of-phase magnetic bead susceptibility and the out-of-phase second harmonic sensor signal depends linearly on the in-phase magnetic bead susceptibility. The term γ_0 can be found from a measurement without beads and subtracted from the out-of-phase sensor signal. The resulting corrected value $V_{2,\mathrm{cor}}''$ is proportional to the in-phase magnetic bead susceptibility. In the data presentation and analysis it is convenient to use this to relate the corrected second harmonic sensor signal $V_{2,\mathrm{cor}} = V_2' + \mathrm{i}V_{2,\mathrm{cor}}''$ to the Cole-Cole expression, Eq. (2), as

$$-\mathrm{i}V_{2,\mathrm{cor}} = V_{2,\mathrm{cor}}'' - \mathrm{i}V_2' = \frac{V_0 - V_\infty}{1 + (\mathrm{i}f/f_{\mathrm{B}})^{1-\alpha}} + V_\infty, \quad (6)$$

where V_0 and V_∞ are defined as

$$V_0 = -2^{-3}I_{\mathrm{AC}}^2 S_0 \gamma_1 \chi_0 \qquad (7)$$
$$V_\infty = -2^{-3}I_{\mathrm{AC}}^2 S_0 \gamma_1 \chi_\infty. \qquad (8)$$

We note that the value of γ_1 cannot be determined unless the bead distribution is known and that it is sensitive

to changes of the bead distribution and concentration near the sensor surface over the duration of an experiment. Thus, the method provides relative and not absolute values of the complex magnetic susceptibility and care should be taken if beads tend to sediment.

III.   EXPERIMENTAL

The planar Hall effect bridge sensor used for the following experiment consist of four segments arranged in a Wheatstone bridge configuration as shown in Fig. 1, each bridge segment has a length of $l = 280$ μm and a width of $w = 20$ μm. The exchange-biased sensor stack consisting of Ta(3 nm)/Ni$_{80}$Fe$_{20}$(30 nm)/Mn$_{80}$Ir$_{20}$(20 nm)/Ta(3 nm) has been sputter-deposited in an applied magnetic field of 20 mT to define an easy direction of magnetization along the positive x-direction. For further details on the fabrication please see Ref 16. The low-field sensitivity for this sensor was found to be $S_0 = -581$ V/(T A), and the bridge resistance along the current was found to be 151.5 Ω.

Electrical contact to the sensor was made with a click-on fluidic system[14], which also defined the fluidic channel on top of the sensor. The channel dimensions were length×width×height = 5 mm×1 mm×0.1 mm. During all measurements the temperature of the sensor mount was kept constant at $(25.00\pm0.01)°$C using a PID controlled Peltier element. The sensor was not electrically or magnetically shielded.

A.   Brownian relaxation measurements

The second harmonic sensor signals were measured using two different lock-in amplifiers depending on the investigated interval of frequencies.

Frequency sweeps below 50 kHz were carried out using a Stanford Research Systems model SR830 lock-in amplifier. The alternating sensor bias current of amplitude $I_{AC} = 20$ mA was supplied by a Keithley model 6221 AC current source. The two instruments were synchronized via a trigger link. The frequency of the current was swept from $f = 43$ kHz to $f = 1.88$ Hz in 29 logarithmically equidistant steps. After each measurement at frequency f a reference measurement was performed at a reference frequency f_{ref} near the expected Brownian relaxation frequency of the beads under investigation. A full frequency sweep consisting of the 30 measurements at different frequencies and the 30 reference measurements, which in total took 3 min and 45 s to record.

Frequency sweeps extending up to 5 MHz were carried out using a Zurich Instruments HF2LI lock-in amplifier. The internal voltage output of the lock-in amplifier was used to bias the sensors corresponding to a current of amplitude 20 mA. The frequency was swept from $f = 5$ MHz to $f = 37.7$ Hz in 30 logarithmically equidistant steps. Also for these measurements, reference points were measured between each frequency. A full frequency sweep took 5 min and 20 s.

Brownian relaxation measurements were performed for six different bead types with nominal diameters D_{nom} ranging from 10 nm to 250 nm. The following bead types were studied: (1)-(3) SHP Iron Oxide nanoparticles with nominal diameters of $D_{nom} = 10$ nm, 25 nm and 40 nm and carboxylic acid surface groups from Ocean Nanotech, USA, suspended in MilliQ water; (4) plain BNF-starch beads with a nominal diameter of $D_{nom} = 80$ nm (cat. 10-00-801) from Micromod, Germany, suspended in phosphate buffered saline (PBS); (5)-(6) plain Nanomag-D beads with nominal diameters of $D_{nom} = 130$ nm (cat. 09-00-132) and 250 nm (cat. 09-00-252) from Micromod, Germany, suspended in PBS. Beads with nominal diameters from 10 nm to 40 nm were characterized using the high-frequency set-up, and beads with nominal diameters from 80 nm to 250 nm beads were characterized using the low-frequency set-up. The bead concentration was kept constant at 1 mg/mL for all six bead types.

For measurements with both lock-ins, reference frequency sweeps without beads were measured with liquid in the fluidic channel to correct for γ_0 before injection of the bead suspension. Then, 20 μL of bead suspension was injected into the liquid channel on the chip at a flow rate of 13.3 μL/min for 1.5 min. This volume corresponds to 40 times the channel volume. After injection of the bead suspension, the beads were left for characterization in the fluidic channel for about 60 min (Ocean Nanotech beads) or 240 min (Micromod beads) before being washed out at flow rate of 300 μL/min. Measurements were also performed after washing to verify that the signals returned to their initial values. Measurements on the same bead suspension using both set-ups were found to give identical results in the overlapping intervals although with a slightly lower data noise at low frequencies using the set-up for low frequencies (data not shown).

B.   Data treatment

First, the data were corrected for instrumental phase shifts and offsets due to γ_0 using the reference sweeps measured without beads. Then, the data recorded at different frequencies were corrected for the variation of the signal amplitude due to bead sedimentation over the duration of a frequency sweep. This was done by normalizing the measurement at each frequency f with the in-phase second harmonic sensor data recorded at $f = f_{ref}$. Finally, all data in the frequency sweep were multiplied with the average value of the measurements at $f = f_{ref}$ obtained during the frequency sweep. Bead sedimentation over a single frequency sweep was mainly an issue for the 250 nm beads from Micromod. Subsequently, the modified Cole-Cole model, Eq. (6), was fitted to the corrected data with f_B, α, V_0 and V_∞ as the four free fitting parameters. The model was fitted to the in-phase and

out-of-phase sensor data simultaneously with a single set of parameters. The hydrodynamic diameters were calculated from the obtained Brownian relaxation frequency using Eq. (1) assuming that the beads are spherical and the PBS does not change the dynamic viscosity. The hydrodynamic diameters will be reported instead of the Brownian relaxation frequencies.
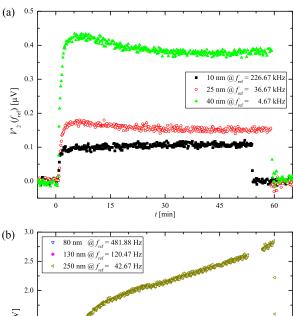
IV. RESULTS

A. Signal vs. time at $f = f_{ref}$

The in-phase signals measured at $f = f_{ref}$ chosen near the Brownian relaxation frequencies are plotted vs. time t after injection of the bead suspension in Fig. 2 for all bead types. The value of f_{ref} is indicated in the figure for each bead type. The signals from the Ocean Nanotech beads (Fig. 2(a)) show a steep increase over the first few minutes and become stable after ~5-15 min. The signals from the Micromod beads (Fig. 2(b)) show a steep initial increase followed by a slow linear increase with time for at least several hours. The initial signal increase takes place at a higher rate for smaller beads than for larger beads. The transition to the region with a linearly increasing signal occurs at t ~10 min, ~15 min and ~45 min for the Micromod beads with D_{nom}=80 nm, 130 nm and 250 nm, respectively, and the linear increase is significantly larger for the 250 nm beads than for the other two bead sizes. From the figure it is also seen that, except for the 130 nm beads, the signal magnitude increases with increasing bead size. It is also noted that all signals return to their baseline level after washing.

From the reference measurements, the standard deviation of the baseline in-phase sensor signal is estimated for each of the six reference frequencies. This is done by finding the standard deviation of the points measured without beads present in the fluidic system ($\sigma_{NoBeads}$). This number represents the combined effect of the sensor and amplifier noise and fluctuations of the ambient conditions (temperature, magnetic and electric fields) during an experiment and defines the smallest signal change that can be resolved under our experimental conditions. The six values are listed in Table I. It is seen that the values of $\sigma_{NoBeads}$ are constant at 5-6 nV for the frequencies between 226.67 kHz and 4.67 kHz measured with the HF2LI lock-in amplifier, whereas they increase from 4 nV to 10.9 nV when decreasing the frequency from 481.88 Hz to 42.67 Hz for the SR830 lock-in amplifier.

B. Brownian relaxation measurements with PHEB

In Fig. 3 the in-phase (top) and out-of-phase (bottom) second harmonic sensor signals are plotted as function of frequency for measurements initiated at $t = 20$ min. The solid lines are least square curve fits of the Cole-Cole model to the data. The model generally provides good
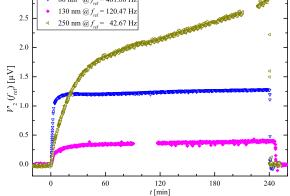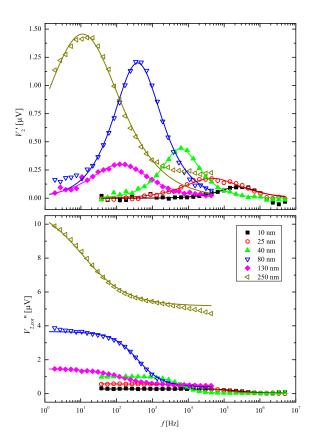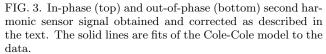
FIG. 2. In-phase second harmonic signal measured at the indicated values of f_{ref} vs. time t after injection of the bead suspension for (a) Ocean Nanotech beads with nominal diameters of 10 nm, 25 nm and 40 nm, and (b) Micromod beads with nominal diameters of 80 nm, 130 nm and 250 nm. In the final part of each experiment, the bead suspension is washed out of the channel.

TABLE I. Standard deviation $\sigma_{NoBeads}$ of baseline in-phase sensor signal at $f = f_{ref}$ for the six values of f_{ref} used for the different bead types.

Lock-in	f_{ref}	$\sigma_{NoBeads}$
HF2LI	226.67 kHz	5.1 nV
HF2LI	36.67 kHz	5.6 nV
HF2LI	4.67 kHz	5.6 nV
SR830	481.88 Hz	4.0 nV
SR830	120.47 Hz	7.6 nV
SR830	42.67 Hz	10.9 nV

fits to the data. In order to better illustrate the shape of the curves and the quality of the fits, the second harmonic signals have been normalized to their maximum values and plotted in Fig. 4. From the normalized plots it is seen that the peaks in the in-phase signals are comparatively narrow for the 10 nm, 40 nm and 80 nm beads and wide for 25 nm, 130 nm and 250 nm beads.

FIG. 3. In-phase (top) and out-of-phase (bottom) second harmonic sensor signal obtained and corrected as described in the text. The solid lines are fits of the Cole-Cole model to the data.

FIG. 4. In-phase (top) and out-of-phase (bottom) second harmonic sensor signal from Fig. 3 normalized to their respective maximum values. The solid lines are fits of the Cole-Cole model to the data.

The values of the fitting parameters are shown in Table II. The height of the peak in the V_2' data depends only on $V_0 - V_\infty$ and α and is given by $V_{2,\text{peak}}' = -\text{Im}\left[(V_0 - V_\infty)/(1 + i^{1-\alpha})\right]$. For $\alpha = 0$, $V_{2,\text{peak}}' = \frac{1}{2}(V_0 - V_\infty)$. From the table, it observed that the hydrodynamic diameters obtained from the fits are all within 40 % of the nominal bead sizes. It is also seen that for the 10 nm - 80 nm beads the value of $V_0 - V_\infty$ increases with the bead diameter. V_∞ is found to be close to zero for the beads from Ocean Nanotech.

1. Sensor signal vs. nominal bead concentration

From the measurements it is possible to estimate the signal normalized with the bead molar concentration for the six different bead types. This number is important when estimating the suitability of each bead type for volume-based biosensing. The signal per bead molar concentration is calculated by dividing the in-phase peak signal $V_{2,\text{peak}}'$ with the molar concentration c of beads. The in-phase peak signal per concentration is listed in Table II. From this table it is seen that although the

bead concentration by mass is the same for all samples, the samples with larger beads provide more signal. Obviously, when the signal is normalized with the molar concentration of the bead suspension, the larger beads provide a substantially higher signal. For example, the signal for the 250 nm beads is found to be 5 orders of magnitude larger than that for the 10 nm beads. If the bead magnetizations were the same, this difference would be anticipated to be $25^3 = 15625$, which is one order of magnitude smaller than the observed ratio. However, it should be noted that the larger beads also sediment such that the actual bead concentration near the sensor surface is higher than the nominal one.

V. DISCUSSION

A. Brownian relaxation measurements

It is seen from the results that the planar Hall effect sensor can be used to measure Brownian relaxation over the frequency range 1 Hz - 1 MHz. With this frequency range it is shown that Brownian relaxation can be measured for beads ranging in diameters from 10 nm

TABLE II. Values of D_h, α, $V_0 - V_\infty$ and V_∞ obtained from Cole-Cole fits to the frequency sweeps initated 20 min after injection of the bead suspensions. The numbers in parenthesis after the fitting parameter are 95 % uncertainties. The last two columns list the molar concentration c of each bead type in nM and the peak sensor signal normalized with the bead molar concentration $V'_{2,\text{peak}}/c$.

D_{nom} [nm]	Producer	D_{h} [nm]	α	$V_0 - V_\infty$ [μV]	V_∞ [μV]	c [nM]	$V'_{2,\text{peak}}/c$ [nV/nM]
10	Ocean Nanotech	12.4(3)	0.08(5)	0.23(2)	0.05(18)	860	0.1
25	Ocean Nanotech	21.6(4)	0.28(2)	0.56(2)	0.02(17)	58	3.0
40	Ocean Nanotech	42.4(2)	0.06(1)	0.97(1)	0.03(15)	14	31.4
80	Micromod	107.0(9)	0.20(1)	3.29(4)	0.4(7)	2.0	602
130	Micromod	155(2)	0.31(1)	0.99(2)	0.5(2)	0.48	622
250	Micromod	349(3)	0.43(1)	6.01(7)	5.2(5)	0.08	17.9×10^3

to 250 nm and meaningful hydrodynamic diameters can be extracted from the measurements. The hydrodynamic diameters for the small beads from Ocean Nanotech are within a few nm of their nominal size. These differences can be due to batch to batch variations. The hydrodynamic diameters found for the beads from Micromod are found to be significantly larger than their nominal values. It is expected that the hydrodynamic diameters are larger than their nominal values, because the nominal diameters are determined from transmission electron microscopy (TEM), which measures the core size. However, the hydrodynamic size obtained for the 250 nm beads is too large to be explained by differences in measuring techniques alone. Effects that could contribute to a higher measured hydrodynamic size are trapping of beads by the magnetostatic field from the sensor stack, interactions between the bead and the sensor surface and bead-bead interactions.

B. Signal vs. time at $f = f_{\text{ref}}$

In the experiments, we found a steep initial increase of the signal followed by either a stable signal for the beads that are smaller than 100 nm or a slowly increasing signal for the beads that are larger than about 100 nm (cf. Fig. 2). The steep initial signal increase is due to the injection of the bead suspension in the already liquid-filled fluidic system; due to the parabolic velocity profile of the liquid during injection, the liquid near the channel walls is replaced more slowly than that in the center of the channel. This results in an equilibration process, where the bead concentration at the sensor surface increases due to continued injection of the bead suspension as well as due to gravitational sedimentation and diffusion of the beads.

The beads are subject to gravitational sedimentation at a velocity $u = D^2(\rho_{\text{b}} - \rho_{\text{f}})g/(18\eta)$,[23] where D is the bead diameter, ρ_{f} and ρ_{b} are the densities of the fluid and beads, respectively, and g is the gravitational acceleration. Taking $D = D_{\text{nom}}$ we can find the characteristic time t_{sed} for sedimentation of the beads in the channel as h/u, where $h = 0.1$ mm is the channel height. For the Mi-

cromod beads, $\rho_b \approx 3$ g/cm^3 and we find $t_{\text{sed}}[\text{min}] \simeq 25$, 90 and 240 for the beads with $D_{\text{nom}}[\text{nm}]=250$, 130 and 80, respectively.

The corresponding characteristic time t_{dif} for diffusion over the height of the liquid channel is estimated from the Stokes-Einstein diffusivity $D_{\text{dif}} = k_{\text{B}}T/(3\pi\eta D_{\text{nom}})$ using that $D_{\text{dif}} \sim h^2/t_{\text{dif}}$. For the Micromod beads with $D_{\text{nom}}[\text{nm}]=250$, 130 and 80, we obtain $t_{\text{dif}}[\text{min}] \simeq 96$, 50 and 31, respectively. These simple arguments show that bead sedimentation dominates over the random thermal motion of the beads for the 250 nm beads, that sedimentation and thermal motion are comparable for the 130 nm beads and that thermal motion dominates for beads with sizes of 80 nm and below.

Experimentally, we have observed an initial steep increase of the signal measured vs. time at $f = f_{\text{ref}}$ in Fig. 2 upon injection of the bead suspension. As previously mentioned, due to the parabolic velocity profile and that liquid without beads is already present in the channel during injection, the bead concentration near the bottom of the channel, where the sensor is located, is therefore initially lower than in the bulk of the bead suspension. This concentration increases due to exchange of liquid in the channel, sedimentation and equilibration of the bead concentration by diffusion. For the 250 nm beads this equilibration is dominated by sedimentation and the estimated sedimentation time of about 25 min is consistent with the observed time of about 45 min in Fig. 2(b). For the beads with sizes below 130 nm, the equilibration time is mainly attributed to diffusion of the beads. The beads from Ocean Nanotech are so small that the equilibration takes place while the bead suspension is injected. After the initial equilibration, the signals from all bead types stabilize and remain essentially constant except for the 250 nm Micromod beads, where the signal shows a significant increase with time. We attribute this increase to accumulation of beads near the sensor edges due to the magnetostatic field from the sensor stack. This accumulation was clearly visible in micrographs of the sensor during the experiments and was also visible in the frequency sweeps as a signal occurring at a lower frequency than that due to freely rotating beads. For the other bead types, no bead accumulation

near the sensor edges could be observed visually and the signal tail at low frequencies in the sensor measurements due to immobilized or partially immobilized beads was significantly smaller or negligible. Thus, the sedimentation and trapping of the 250 nm beads results in a time dependence of the signal due to the bead suspension itself, i.e., prior to introduction of biomolecules, which is clearly undesirable. These beads are therefore not suited for biosensing with the present sensors.

1. Sensor signal vs. nominal bead concentration

From the value of signal per bead concentration listed in Table II, it is clear that the choice of bead type will be very important for the sensitivity of a volume-based biosensor. For the beads investigated here, the peak signal normalized with the nominal bead molar concentration varies over 5 orders of magnitude, which means that the choice of bead has a high impact on the sensitivity and dynamic range of concentrations that can be detected. For instance, the bead concentration of the 10 nm beads is 860 nM, which means that, at least in principle, it will be possible to detect analyte concentrations up to this value. The downside is a low signal per bead which for the 10 nm beads is only 0.1 nV/nM. Comparing to the baseline resolution from Table I of 5.1 nV it implies that the limit of detection is expected to be higher than ~51 nM. On the other hand, for the 250 nm beads the theoretical dynamic range is 0.6-81 pM, the drawback of these beads is that they sediment, which will make them difficult to use for biosensing. The sedimentation of the 80 nm beads is limited and the signal is large. Thus, these beads will be the best compromise for biosensing to achieve a low detection limit. The theoretical dynamic range for the 80 nm beads is 6 pM - 2 nM. The upper sensitivity limit can be moved to higher concentrations by increasing the bead concentration, but this will also increase the background signal and potentially make it more difficult to measure low concentrations. The lower limit of detection can be decreased further by decreasing the bead concentration and/or increasing the signal-to-noise ratio of the measurement system. The latter may be achieved by improving the sensor design, using lower noise amplification electronics, by applying magnetic and electrical shielding and by increasing the measurement time.

VI. CONCLUSION

It has been demonstrated that planar Hall effect bridge sensors can be used to measure AC susceptibility of magnetic beads for frequencies spanning from DC to 1 MHz. This wide frequency span allows for measuring Brownian relaxation of beads with nominal diameters ranging from 10 nm to 250 nm. The hydrodynamic diameters obtained from the measurement are all within 40% of the nominal diameter supplied by the manufacturer. From the measurements it is also concluded that among the investigated beads the 80 nm beads are most promising for volume-based biosensing, because they provide the largest signal per bead among the bead types that do not suffer from sedimentation and magnetic trapping issues on the sensors.

[1] I. Koh and L. Josephson, "Magnetic nanoparticle sensors." Sensors, **9**, 8130 (2009).
[2] S. X. Wang and G. Li, "Advances in Giant Magnetoresistance Biosensors With Magnetic Nanoparticle Tags: Review and Outlook," IEEE T. Magn., **44**, 1687 (2008).
[3] N. Jaffrezic-Renault, C. Martelet, Y. Chevolot, and J.-P. Cloarec, "Biosensors and Bio-Bar Code Assays Based on Biofunctionalized Magnetic Microbeads," Sensors, **7**, 589 (2007).
[4] J. Göransson, T. Zardán Gómez De La Torre, M. Strömberg, C. Russell, P. Svedlindh, M. Strømme, and M. Nilsson, "Sensitive detection of bacterial DNA by magnetic nanoparticles." Anal. Chem., **82**, 9138 (2010).
[5] J. Connolly and T. G. St Pierre, "Proposed biosensors based on time-dependent properties of magnetic fluids," J. Magn. Magn. Mater., **225**, 156 (2001).
[6] A. P. Astalan, F. Ahrentorp, C. Johansson, K. Larsson, and A. Krozer, "Biomolecular reactions studied using changes in brownian rotation dynamics of magnetic particles," Biosens. Bioelectron., **19**, 945 (2004).
[7] C. Hong, C. Wu, Y. Chiu, S. Yang, H. Horng, and H. Yang, "Magnetic susceptibility reduction method for magnetically labeled immunoassay," Appl. Phys. Lett., **88**, 212512 (2006).
[8] A. Fire and X. Si-Qun, "Rolling replication of short dna circles," Proc. Natl. Acad. Sci. USA., **92**, 4641 (1995).
[9] D. Liu, S. L. Daubendiek, M. A. Zillman, K. Ryan, and E. T. Kool, "Rolling Circle DNA Synthesis: Small Circular Oligonucleotides as Efficient Templates for DNA Polymerases." J. Am. Chem. Soc., **118**, 1587 (1996).
[10] M. Strömberg, J. Göransson, K. Gunnarsson, M. Nilsson, P. Svedlindh, and M. Strømme, "Sensitive molecular diagnostics using volume-amplified magnetic nanobeads." Nano lett., **8**, 816 (2008).
[11] F. Ludwig, S. Mäuselein, E. Heim, and M. Schilling, "Magnetorelaxometry of magnetic nanoparticles in magnetically unshielded environment utilizing a differential fluxgate arrangement," Rev. Sci. Instrum., **76**, 106102 (2005).
[12] H. Grossman, W. Myers, V. Vreeland, R. Bruehl, M. Alper, C. Bertozzi, and J. Clarke, "Detection of bacteria in suspension by using a superconducting quantum interference device," Proc. Natl. Acad. Sci. USA., **101**, 129 (2004).
[13] B. T. Dalslet, C. D. Damsgaard, M. Donolato, M. Strømme, M. Strömberg, P. Svedlindh, and M. F. Hansen, "Bead magnetorelaxometry with an on-chip magnetoresistive sensor." Lab Chip, **11**, 296 (2011).
[14] F. W. Østerberg, B. T. Dalslet, D. Snakenborg, C. Johansson, and M. F. Hansen, "Chip-Based Measurements of Brownian Relaxation of Magnetic Beads Using a Planar Hall Effect Magnetic Field Sensor," in *AIP Conf. Proc.*, Vol. 1311 (2010) pp. 176–183.
[15] A. D. Henriksen, B. T. Dalslet, D. H. Skieller, K. H. Lee, F. Okkels, and M. F. Hansen, "Planar Hall effect bridge magnetic field sensors," Appl. Phys. Lett., **97**, 013507 (2010).
[16] F. W. Østerberg, G. Rizzi, T. Zardán Gómez de la Torre, M. Strömberg, M. Strømme, P. Svedlindh, and M. F. Hansen,

"Measurements of brownian relaxation of magnetic nanobeads using planar hall effect bridge sensors," Biosens. Bioelectron., **40**, 147 (2013).

[17] L. Neél, "Théorie du traînage magnétique des ferromagnétiques en grains fins avec applications aux terres cuites," Ann. Géophys, **5**, 99 (1949).

[18] W. Brown, "Thermal Fluctuations of a Single-Domain Particle," Phys. Rev., **130**, 1677 (1963).

[19] K. S. Cole and R. H. Cole, "Dispersion and Absorption in Dielectrics I. Alternating Current Characteristics," J. Chem. Phys., **9**, 341 (1941).

[20] P. Debye, "Polar Molecules," Chemical Catalogue Co. (1929).

[21] W. Thomson, "On the electro-dynamic qualities of metals: - effects of magnetization on the electric conductivity of nickel and of iron." Proc. R. Soc. Lond., **8**, 546 (1857).

[22] T. B. G. Hansen, C. D. Damsgaard, B. T. Dalslet, and M. F. Hansen, "Theoretical study of in-plane response of magnetic field sensor to magnetic beads magnetized by the sensor self-field," J. Appl. Phys., **107**, 124511 (2010).

[23] F. W. Østerberg, B. T. Dalslet, C. D. Damsgaard, S. C. Freitas, P. P. Freitas, and M. F. Hansen, "Bead capture on magnetic sensors in a microfluidic system," IEEE Sensors Journal, **9**, 682 (2009).

Paper   VI

F. W. Østerberg, G. Rizzi and M. F. Hansen
"On-chip measurements of Brownian relaxation in both frequency- and time domain"
Draft (January 2013)

On-chip measurements of Brownian relaxation in both frequency- and time domain

Frederik Westergaard Østerberg,[1, a)] Giovanni Rizzi,[1] and Mikkel Fougt Hansen[1, b)]

Department of Micro- and Nanotechnology, Technical University of Denmark,
DTU Nanotech, Building 345B, DK-2800 Kongens Lyngby, Denmark

Brownian relaxation of magnetic beads are measured in the time domain using a magnetoresistive sensor called planar Hall effect bridge sensor. Brownian relaxation of four different beads sizes (40 nm, 80 nm, 130 nm and 250 nm) are measured with both the new time domain technique and the already established frequency domain technique. For both techniques hydrodynamics sizes are determined based on the relaxation dynamics, and both methods are found to agree well with the nominal size of the beads. Relaxation measurements are also performed in both domains to detect clustering of streptavidin coated beads by addition of different concentrations of biotin-conjugated bovine serum albumin. The measurement time for the time domain measurements is less than one sixth of the measurement time in the frequency domain, which potentially allows for monitoring binding kinetics of magnetic beads with better time resolution.

I. INTRODUCTION

Magnetic beads have been demonstrated as a useful component in future biosensors[1–4]. A major advantage of using magnetic beads for biodetection is that most biological samples are nonmagnetic, thus no background signal from the sample will add noise to the measurements. Magnetic beads are also easy to functionalize such they will bind specifically to antibodies or proteins.

Traditionally two approaches are used for biosensing with magnetic beads, one is surface based and the other volume based. For surface based sensing both the sensor surface and the beads are functionalized such the analyte will act as glue between the beads and surface. Thus the presence of the analyte will result in an increase of bead concentration near the sensor surface[2,5,6]. For volume based sensing only the beads are functionalized and instead of measuring the presence of beads, the hydrodynamic size-increase of the beads due to the attached analytes is measured. Connolly and St Pierre [7] first proposed to use Brownian relaxation for detecting size changes due to binding of analytes to magnetic beads.

Brownian relaxation of magnetic beads are often measured in the frequency domain by AC susceptibility measurements with either inductive methods[8], fluxgates[9], SQUID magnetometers[10] and magnetoresistive sensors[11,12], however it is also possible to measure brownian relaxation in the time domain[13–15]. The advantage of the measurements in the time domain is that measurement can be performed much faster, ideally only one measurement lasting less than a second is required, whereas the AC susceptibility methods require multiple measurements at different frequencies, which results in measurement times on the order of minutes.

Recently we have demonstrated that Brownian relaxation measurements in the frequency domain can be performed on so called planar Hall effect bridge sensors without the need for any external magnets[16]. Here we demonstrate that the same sensors can also be used for Brownian relaxation measurements in the time domain.

II. THEORY

A. Brownian relaxation of magnetic of beads

We consider a magnetic bead with the magnetization (M) placed in an applied magnet field. For convenience the magnetization is defined to be positive when parallel to the applied field, such that the magnetization is $+M_0$ and $-M_0$ when all the magnetic moments are parallel and anitparallel to the applied field, respectively. The magnetization of the bead placed in the magnetic field will align with the field either by internal flipping of the magnetization (Néel relaxation[17]) or by a physical rotation of the bead (Brownian relaxation[18]). For the beads used in this study the Néel relaxation time is much longer than the Brownian relaxation time, which therefore dominates the relaxation dynamics of the beads. The Brownian relaxation of magnetic beads can be measured in both the time domain and the frequency domain. The theory for both domains are described below.

1. Time domain

When Brownian relaxation is measured in the time domain a characteristic time is the Brownian relaxation

---

[a)]Electronic mail: Frederik.Osterberg@nanotech.dtu.dk
[b)]Electronic mail: Mikkel.Hansen@nanotech.dtu.dk

time, which is given by

$$\tau_B = \frac{3\eta V_h}{k_B T}, \tag{1}$$

where η is the viscosity of the liquid in which the bead is suspended, V_h is the hydrodynamic volume of the bead and $k_B T$ is the thermal energy.

For this study the measurements in the time domain will be performed by passing a square wave current (I) with an amplitude of I_0 though the sensor and a period of T. The current through the sensor will generate a magnetic self-field (B) around the sensor proportional to the current, such the direction of the magnetic field changes with the direction of the current. The mmagnetization of the bead rotates to align itself with the magnetic field. This means that just after flipping of the current from $+I_0$ to $-I_0$ the magnetization of the bead will be antiparallel with the self-field, and then relax to being parallel. This is illustrated in Fig. 1.
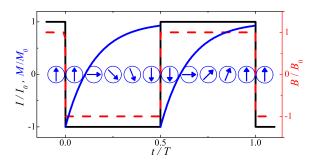

FIG. 1. Schematics of how a magnetic bead relaxes in a flipping magnetic field. The magnetic field changes direction when the current changes direction. Before flipping of the magnetic field the magnetization of the bead will be parallel with the field. Immediately after flipping of the magnetic field the magnetization of the bead will be anti-parallel, meaning the the magnetization along the applied field is $M = -M_0$, the bead will then relax by rotation to become parallel with the field ($M = M_0$).

The relaxation of the bead will be an exponential decay with the Brownian relaxation time as the exponential time constant. Since the magnetization of the bead will relax from being antiparallel to being parallel with the magnetic field, the magnetization will decay from $-M_0$ to $+M_0$, thus the magnetization as function of time is described by

$$M(t) = M_0(1 - 2\exp(-t/\tau_B)), \tag{2}$$

where t is the time after each flipping the magnetic field.

2. Frequency domain

The traditional method of measuring Brownian relaxation with planar Hall effect sensors is by passing an alternating current through the sensor

$$I(t) = \sqrt{2}I_{RMS}\sin(2\pi f), \tag{3}$$

where I_{RMS} is the root mean square value of the current and f is the frequency of the current.

When measurements are performed in the frequency domain the characteristic frequency is the Brownian relaxation frequency

$$f_B = \frac{1}{2\pi\tau_B} = \frac{k_B T}{6\pi\eta V_h}, \tag{4}$$

The Brownian relaxation frequency is the frequency at which the phase-lag between the magnetic moment of the bead and the applied field is largest, meaning that a peak will appear in the out-of-phase magnetic susceptibility at $f = f_B$.

For measurements in the frequency domain the complex magnetic susceptibility is given by the Debye theory[19]

$$\chi(f) = \chi' - i\chi'' = \frac{\chi_0 - \chi_\infty}{1 + (if/f_B)} + \chi_\infty, \tag{5}$$

where i is the imaginary unity defined as $i = \sqrt{-1}$, χ' and χ'' are the in-phase and out-of-phase magnetic susceptibilities, χ_0 and χ_∞ are the DC and high frequency susceptibility, respectively.

3. Size distribution

The equations for the magnetization in the time domain and magnetic susceptibility in the frequency domain are only valid for a monodisperse ensemble of beads. Hence, the equations need to be averaged over a bead distribution. Traditionally the size distribution of magnetic beads are described by the log-normal distribution, which is given by

$$f_{LN}(D_h)dD_h = \frac{1}{D_h\sigma\sqrt{2\pi}}\exp\left(-\frac{(\ln D_h - \mu)^2}{2\sigma^2}\right)dD_h, \tag{6}$$

where μ and σ are the mean and standard deviation on the log-scale. Since the beads signals obtained are proportional to the bead volume the probability density function is also assumed to be volume weighted, i.e. the volume fraction of the particles with hydrodynamic diameters between D_h and $D_h + dD_h$ is $f_{LN}(D_h; \mu, \sigma)dD_h$. The median of the distribution is given by $\tilde{D}_h = \exp(\mu)$.

B. Sensor signals

For low magnetic fields, the sensor signal is linear and given by[20]

$$V = S_0 I H_y + R_{offset} I, \tag{7}$$

where S_0 is the low-field sensitivity, H_y is the magnetic field acting in the y-direction. R_{offset} is due to a possible unbalance in the sensor. H_y is given by

$$H_y = \gamma_0 I + H_{y,beads} + H_{y,ext}. \tag{8}$$

Here γ_0 is a constant that describes the effect of the self-field, γ_0 is dependent on the geometry of the sensor. $H_{y,\text{beads}}$ and $H_{y,\text{ext}}$ are magnetic field acting on the sensor in the y-direction from the beads and external sources, respectively. $H_{y,\text{beads}}$ will be defined slightly differently for measurements in the time and frequency domains. In the time domain

$$H_{y,\text{beads}}^{\text{time}} = \gamma_{1t} M(t) I \qquad (9)$$

and in the frequency domain

$$H_{y,\text{beads}}^{\text{freq}} = \gamma_1 \chi(f) I, \qquad (10)$$

where γ_{1t} and γ_1 are constants that depend on the sensor geometry and bead distribution.

1. Time domain

When measurements are performed in the time domain the current is alternating between $+I_0$ and $-I_0$, which leads to the following two signals

$$V|_{I=+I_0} = S_0 I_0^2 (\gamma_0 + \gamma_{1t} M(t)) + S_0 I_0 H_{y,\text{ext}} + R_{\text{offset}} I_0 \qquad (11)$$

$$V|_{I=-I_0} = S_0 I_0^2 (\gamma_0 + \gamma_{1t} M(t)) - S_0 I_0 H_{y,\text{ext}} - R_{\text{offset}} I_0 \qquad (12)$$

From this it is seen that R_{offset} and $H_{y,\text{ext}}$ can be eliminated by calculating the average of the two and $\gamma_0 + \gamma_{1t} M(t)$ can be eliminated by calculating the difference

$$V_{\text{ave}} = \frac{V|_{I=+I_0} + V|_{I=-I_0}}{2} = S_0 I_0^2 (\gamma_0 + \gamma_{1t} M(t)) \qquad (13)$$

$$V_{\text{diff}} = \frac{V|_{I=+I_0} - V|_{I=-I_0}}{2} = S_0 I_0 H_{y,\text{ext}} + R_{\text{offset}} I_0. \qquad (14)$$

The offset due to γ_0 in V_{ave} can be corrected for by subtracting a measurement performed without beads. After this correction V_{ave} is proportional to the time dependent magnetization. It is seen that V_{diff} is linearly dependent on $H_{y,\text{ext}}$.

The function that is fitted to the measurements is the theoretical signal times the log-normal distribution integrated over the hydrodynamic size

$$V_{\text{fit},t} = V_{0t} \int_0^\infty \left(1 - 2\exp\left(\frac{-t}{\tau_{\text{B}}(D_{\text{h}})}\right)\right) f_{\text{LN}}(D_{\text{h}})\mathrm{d}D_{\text{h}} + V_{\text{offset}}, \qquad (15)$$

where $V_{0t} = S_0 I_0^2 \gamma_{1t} M_0$ is the amplitude of the decay and V_{offset} is correcting for potential offsets. The free fitting parameters are V_0, V_{offset}, $\tilde{D}_{\text{h}}$ and σ, where the two last are defining the log-normal distribution.

2. Frequency domain

For measurement in the frequency domain it has previously been shown[16] that the complex magnetic susceptibility can be measured in the second harmonic in-phase and out-of-phase sensor signals

$$V_2' = -2^{-2} I_{\text{RMS}}^2 S_0 \gamma_1 \chi'' \qquad (16)$$

$$V_2'' = -2^{-2} I_{\text{RMS}}^2 S_0 (\gamma_0 + \gamma_1 \chi'), \qquad (17)$$

Thus, the in-phase second harmonic sensor signal is proportional to the out-of-phase magnetic bead susceptibility and the out-of-phase second harmonic sensor signal depends linearly on the in-phase magnetic bead susceptibility. Again the offset due to γ_0 can be corrected for by subtracting a measurement without beads.

The function used for fitting to the measurements in the frequency is again the sensor signals times the lognormal distribution integrated over the hydrodynamic diameter.

$$V_{\text{fit},f} = V_2'' + \mathrm{i}V_2' = \mathrm{i} \int_0^\infty \frac{V_0 - V_\infty}{1 + (\mathrm{i}f/f_{\text{B}}(D_{\text{h}}))} f_{\text{LN}}(D_{\text{h}})\mathrm{d}D_{\text{h}} + \mathrm{i}V_\infty \qquad (18)$$

where $V_0 = -2^{-2} I_{\text{RMS}}^2 S_0 \gamma_{1f} \chi_0$ and $V_\infty = -2^{-2} I_{\text{RMS}}^2 S_0 \gamma_{1f} \chi_\infty$. Along with V_0 and V_∞ the free fitting parameters are $\tilde{D}_{\text{h}}$ and σ of the log normal distribution.

III. EXPERIMENTAL

A. Fabrication and Set-up

The magnetic field sensor used is a so called planar Hall effect bridge sensor. It is based on the anisotropic magnetoresistance of permalloy. The sensor stack $\text{Ta}(3\text{ nm})/\text{Ni}_{80}\text{Fe}_{20}(30\text{ nm})/\text{Mn}_{80}\text{Ir}_{20}(20\text{ nm})/\text{Ta}(3\text{ nm})$ was deposited in an applied field of 20 mT along the positive x-direction to define an easy magnetization direction. The stack was patterned in wheatstone bridge geometry consisting of four segments each with a length of $l = 280$ μm and a width of $w = 20$ μm. For a more detailed description of the fabrication see Ref 16. The low field sensitivity of the sensor have been measured to $S_0 = -591$ V/(T A) and the resistance along the current was measured to 161.7 Ω.

In order to allow for electrical contact to the sensor a click-on fluidic system[12,16] was used, which also defined the fluidic channel with dimensions length×width×height = 5 mm×1 mm×0.1 mm. The temperature of the sensor was kept constant at $(25.00\pm0.01)^\circ$C by a PID controlled Peltier element. The sensor was not electrically nor magnetically shielded.

B. Measurement equipment

The current through the sensor was supplied by a 6221 AC and DC Current Source (Keithley Instruments,

USA). For time domain measurements it delivered a square wave with a current amplitude of $I_0 = 14.1$ mA at a frequency of 8 Hz, which allowed 62.5 ms between each flipping of the current. For measurements in the frequency domain a sine wave with a current amplitude of 20 mA which corresponds to $I_{\mathrm{RMS}} = 14.1$ mA was used, while the frequency was varied in 29 logarithmically equidistant steps from 43.69 kHz to 1.88 Hz.

For the time domain measurements the sensor signals were recorded using a NI USB-6281 (National Instruments, USA), which is an 18-Bit data acquisition box. The lowest measuring range of 0.1 V was used, which corresponds to a resolution of 0.8 μV. The sample rate was set to 600,000 samples per second, and in addition a low pass filter of 3 kHz was applied to filter away any high frequency noise. To improve the signal to noise ratio the signal was averaged over 192 periods. Thus, the time used for time domain measurements was 24 s. For the analysis of the measurements the recorded measurements were transformed from being on a linear time scale to being on a logarithmic time scale by placing the measurements into "bins" that are logarithmic increasing with time.

Measurements in the frequency domain were recorded using a SR830 Lock-In Amplifier (Stanford Research Systems, USA). The NI USB-6281 and SR830 were connected in parallel such that measurements with both instruments were performed immediately after one another. As mentioned above a frequency sweep consisted of 30 individual frequencies, which resulted in a measurement time of 2 min and 21 s, almost 6 times the measurement time for the time domain measurement.

C. Measurements

1. Bead sizes

Brownian relaxation have been measured in both the time and frequency domains for four different bead types with nominal diameters of 40 nm, 80 nm, 130 nm and 250 nm. The 40 nm beads were SHP Iron oxide nanoparticles with carboxylic acid group (Ocean Nanotech, USA), the 80 nm beads were BNF-starch with a plain surface (Micromod, Germany) and the 130 nm and 250 nm were Nanomag-D also with plain surface (Micromod, Germany).

All bead types were diluted to a concentration of 1 mg/mL with MilliQ water for the 40 nm and a phosphate buffered saline (PBS) solution for the remain three bead types. 20 μL of each sample was subsequently injected into the fluidic channel at a flow rate of 13.3 μL/min for 1.5 min. The beads were left in the channel for 10 min to allow for a steady state, before the shown measurements were recorded. Finally, the beads were washed out at a flow rate of 300 μL/min for 1-2 min. In between measurements on the four samples measurements were performed with PBS in the channel to be able

to correct for γ_0.

2. Bead clustering

In addition to measuring different bead sizes, measurements of bead clustering was also performed. Here, biotin-conjugated bovine serum albumin (bBSA) (A8549, Sigma-Aldrich, USA) was mixed with streptavidin coated 80 nm BNF-starch beads (Micromod, Germany) suspended in PBS. Time and frequency domain relaxation were measured for five different samples: two without any bBSA and three with bBSA in concentrations of 2.5 nM, 5 nM and 10 nM, respectively. The concentration of beads was kept constant at 1 mg/mL. Each sample was left 20 min in the fluidic system, which allowed for acquiring five measurement in both the time and frequency domain for each sample. However, the first measurement in the frequency domain was performed during the injection of beads. Thus, the bead concentration changed a lot during this sweep and was for this reason not analyzed. In between measurements on the five samples, reference measurements were performed with PBS in the channel to be able to correct for γ_0.

IV. RESULTS

3. Bead sizes

In Fig. 2 the Brownian relaxation measurements in the time domain are plotted for the four different bead sizes. The measurements have been normalized such that the decay of each bead size can be easily compared. It is seen that the relaxation time increases with the bead size. The points measured for the 40 nm and 130 nm beads look more scattered on this normalized scale. The lines plotted through each data set are least square curve fits of Eq. (15). The parameters obtained from the fits are shown in Table I, which shows the median hydrodynamic diameter is increasing with the nominal diameter. For the Micromod beads the median hydrodynamic diameters are found to be significantly larger than the nominal diameters. The σ is also seen to increase with the bead size.

Figure 3 shows the Brownian relaxation measurements in the frequency domain, the in-phase (top) and out-of-phase (bottom) second harmonic sensor signals are plotted vs. bias current frequency. From the figure it is seen that the signal amplitudes varies with the bead types. The lines plotted are least square curve fits of Eq. (18) to the measurements. It is seen that the fit match the measured data well except for the 250 nm. The parameter obtained from the fits are listed in Table I. The median hydrodynamic diameter and σ follow the same trends observed for the time domain measurements, however the hydrodynamic diameter for the 250 nm beads are found

TABLE I. Parameters obtained from least square fitting of Eq. (15) to the time domain measurements and Eq. (18) to the frequency domain measurements for the four different bead sizes. The number in parentheses are the error on an $\alpha = 5\%$ level obtained from the least square curve fits.

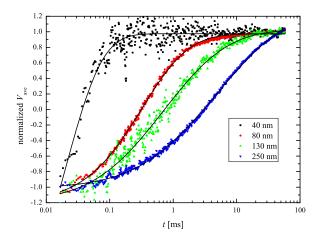| D_{nom} [nm]	Time domain				Frequency domain			
	$\tilde{D}_{\mathrm{h}}$ [nm]	σ	V_0 [μV]	V_{offset} [μV]	$\tilde{D}_{\mathrm{h}}$ [nm]	σ	$V_0 - V_\infty$ [μV]	V_∞ [μV]
40	41(2)	0.22(5)	1.8(3)	-0.4(3)	42.5(3)	0.18(2)	0.95(2)	0.1(2)
80	108(1)	0.35(1)	4.81(2)	0.48(2)	107(2)	0.32(2)	3.16(5)	0.4(8)
130	152(2)	0.45(2)	1.36(2)	1.85(1)	159(4)	0.50(2)	0.97(2)	0.5(3)
250	299(4)	0.60(1)	7.68(6)	8.15(5)	350(7)	0.64(2)	5.66(7)	5.5(5)

FIG. 2. Brownian relaxation measurements in the time domain. Normalized V_{ave} vs. time for four different bead sizes. The signals are normalized such that the signal are -1 at the start and 1 at the end.

to be significantly larger from the frequency domain compared to the time domain.

A. Bead clustering

In Fig. 4 the time domain measurements for bead clustering with bBSA are shown. All the measurements shown are the last performed before washing away the beads and have been corrected for offsets. The lines are least square curve fits of Eq. (15) to the data. Data from seven different measurements are shown: Two measurements with bead but without bBSA; three measurements with beads and with varying bBSA concentrations; and finally two reference measurements without beads nor bBSA. It is seen that the two measurements without bBSA almost coincide. As the bBSA concentration is increased both the signal amplitude as well as the slope after 50 ms increases.

Figure 5 shows the corresponding measurements to Fig. 4 in the frequency domain. Again it is seen that the measurements on the two samples without bBSA are very similar. For the samples with bBSA it is seen that the peak in the in-phase signal increase and shifts towards lower frequency as the concentration of bBSA is
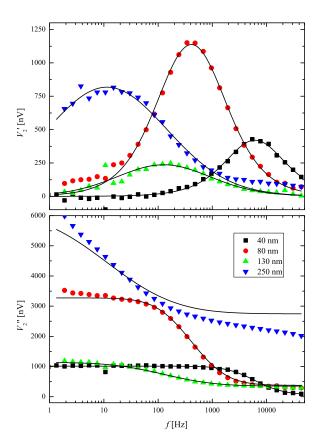

FIG. 3. Brownian relaxation measurements in the frequency domain. Second harmonic in-phase (top) and out-of-phase (bottom) signal vs. frequency for 5 different bead sizes. The data is recorded from high to low frequency. The lines are least square curve fits of Eq. 18 to the data.

increased. Least square curve fits of Eq. (18) are performed for the five measurements with beads and plotted as solid lines

The median hydrodynamic diameter and σ obtained from both fitting in the time and frequency domain are listed in Table II. It is seen that both the median hydrodynamic diameter and σ increase with concentration of bBSA in general. However, the hydrodynamic diameters obtained in the time domain are not significantly different for bBSA concentrations of 2.5 nM and 5 nM.
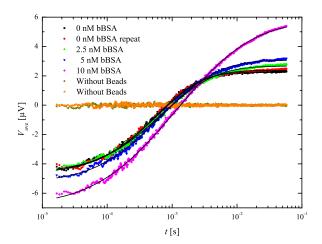
In Fig. 6 the hydrodynamic diameters extracted from

FIG. 4. Time domain measurements of clustering of streptavidin coated bead by binding to bBSA. V_{ave} is plotted vs. time.
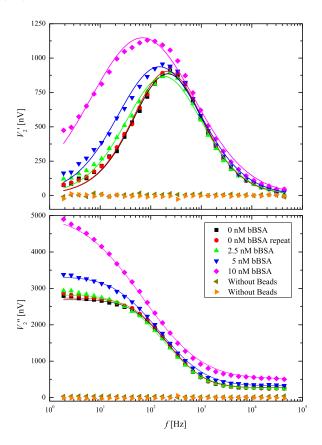

FIG. 5. Frequency domain measurements of clustering of streptavidin coated beads by bBSA. The in-phase (top) and out-of-phase (bottom) second harmonic sensor signals are plotted vs. bias current frequency. The lines are curve fits of Eq. 18 to the data.

fitting are shown for the measurements with 0 nM and 10 nM as function of time after injection of beads. It is seen that for both time and frequency domain the sample

TABLE II. Parameters obtained from least square fitting to the measurement in the time and frequency domain for five different bBSA concentrations. The number in parentheses are the error on an $\alpha = 5$ % level obtained from the least square curve fits.

c_{bBSA} [nM]	Time domain		Frequency domain	
	$\tilde{D}_{\text{h}}$ [nm]	σ	$\tilde{D}_{\text{h}}$ [nm]	σ
0	127.1(6)	0.31(1)	129(2)	0.34(2)
0	128.9(8)	0.33(1)	129(2)	0.34(2)
2.5	139.0(8)	0.40(1)	137(4)	0.40(3)
5	138.8(8)	0.43(1)	147(5)	0.47(3)
10	172.7(9)	0.62(1)	190(6)	0.65(3)

without bBSA result in hydrodynamic diameters slightly increasing with time, when bBSA is present the hydrodynamic diameters increase faster with time. It is also seen that the obtained hydrodynamic diameters are found to be larger from the frequency domain measurements.
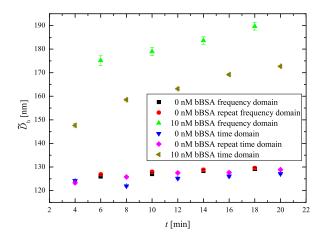

FIG. 6. Hydrodynamic diameters obtained in both time and frequency domain vs. time after injection. Results are plotted for samples with 0 nM and 10 nM of bBSA.

V. DISCUSSION

A. Bead size

The Brownian relaxation measurements recorded in the time and frequency domain generally agree well. The biggest difference is seen for 250 nm beads, where the frequency domain measurement result in a significantly larger hydrodynamic diameter. It is also seen that the fit to the data from 250 nm in the frequency domain is not perfect. These differences are due to the 250 nm beads not being at a steady state during the measurement, instead they are sedimenting. This means that the bead concentration near the sensor surface increase during a sweep, resulting in a higher concentration for the measurements at the lower frequencies. The increased bead

concentration will also increase the sensor signals meaning that the low frequency measurement are too high compared to the high frequency measurements. Thus the Brownian relaxation peak is wrongly shifted towards lower frequencies due to sedimentation. Since the time spent for measurements in the time domain is only one sixth of what is spent in the time domain, sedimentation is a much smaller problem. ?? It could also be because we do not measure for long enough time, and the beads are therefor not all aligned when the field flips ??

Brownian relaxation of 40 nm beads are almost on the limit of what can be resolved with the NI USB-6281 in terms of both signal and time resolution. The signal relax in less than 100 µs and the time resolution of the NI USB-6281 is only 1.6 µs. From the scattering of the points for the measurements on 40 nm beads it is also seen that the signal change due to relaxation is only a few times the noise.

The time domain measurements look more noisy than the frequency domain measurements. Some the noise can be explained by the equipment. As mentioned the lowest range of the NI USB-6281 is 0.1 V, which is not optimal when the signals due to the beads are less than 50 µV. Amplifying the signals by a factor of 1000 would result in a better usage of the input range. Another possible reason for noise in the time domain measurements are that any electrical or magnetic noise near the setup will be picked up, whereas for the frequency domain the lock-in amplifier filters away most of the noise not present at f. A possible solution to this problem could be to shield the setup, amplify the signal or change the electronics.

B. Bead clustering

Both time and frequency domain measurements can be used to detect the presence of bBSA by measuring an increase in the hydrodynamic diameters. However with the present setup it is seen that the frequency domain measurements are more sensitive to bBSA, which again is due to the low signal to noise ratio of the time domain measurements.

It is also seen that for samples contained bBSA the median hydrodynamic diameter increases with time, whereas without bBSA it is almost constant. This is because the beads that have formed clusters are sedimenting and thereby increasing the ratio between bound and free beads near the sensor surface. This effect will make the planar Hall effect bridge sensors more sensitive the longer time before performing the measurement. Potentially, the sedimentation can be enhanced by applying a magnetic force pulling the beads to the sensor surface, when the magnetic force is removed most of the clusters will stay and if small enough beads with high diffusivity are used, the free beads will diffuse away from the sensor.

VI. CONCLUSION

We have shown that hydrodynamic sizes can be measured with planar Hall effect bridge sensors in both the time and frequency domain. It has also been demonstrated that both methods can be used to detect clustering of streptavidin coated beads by adding biotin-conjugated bovine serum albumin. For the measurements presented here time domain measurements takes only one sixth of the time for frequency domain measurements. The time needed for time domain measurements could potentially be reduced to less than a second by optimizing the electronics, this would allow for monitoring real time binding kinetics of magnetic beads and biological samples.

[1] I. Koh and L. Josephson, "Magnetic nanoparticle sensors." Sensors, **9**, 8130 (2009).

[2] S. X. Wang and G. Li, "Advances in Giant Magnetoresistance Biosensors With Magnetic Nanoparticle Tags: Review and Outlook," IEEE T. Magn., **44**, 1687 (2008).

[3] N. Jaffrezic-Renault, C. Martelet, Y. Chevolot, and J.-P. Cloarec, "Biosensors and Bio-Bar Code Assays Based on Bio-functionalized Magnetic Microbeads," Sensors, **7**, 589 (2007).

[4] J. Göransson, T. Zardán Gómez De La Torre, M. Strömberg, C. Russell, P. Svedlindh, M. Strømme, and M. Nilsson, "Sensitive detection of bacterial DNA by magnetic nanoparticles." Anal. Chem., **82**, 9138 (2010).

[5] J. Schotter, P. Kamp, A. Becker, A. Pühler, G. Reiss, and H. Brückl, "Comparison of a prototype magnetoresistive biosensor to standard fluorescent dna detection," Biosensors and Bioelectronics, **19**, 1149 (2004).

[6] R. S. Gaster, D. A. Hall, C. H. Nielsen, S. J. Osterfeld, H. Yu, K. E. Mach, R. J. Wilson, B. Murmann, J. C. Liao, S. S. Gambhir, and S. X. Wang, "Matrix-insensitive protein assays push the limits of biosensors in medicine," Nat. Med., **15**, 1327 (2009).

[7] J. Connolly and T. G. St Pierre, "Proposed biosensors based on time-dependent properties of magnetic fluids," J. Magn. Magn. Mater., **225**, 156 (2001).

[8] A. P. Astalan, F. Ahrentorp, C. Johansson, K. Larsson, and A. Krozer, "Biomolecular reactions studied using changes in brownian rotation dynamics of magnetic particles," Biosens. Bioelectron., **19**, 945 (2004).

[9] F. Ludwig, S. Mäuselein, E. Heim, and M. Schilling, "Magnetorelaxometry of magnetic nanoparticles in magnetically unshielded environment utilizing a differential fluxgate arrangement," Rev. Sci. Instrum., **76**, 106102 (2005).

[10] H. Grossman, W. Myers, V. Vreeland, R. Bruehl, M. Alper, C. Bertozzi, and J. Clarke, "Detection of bacteria in suspension by using a superconducting quantum interference device," Proc. Natl. Acad. Sci. USA., **101**, 129 (2004).

[11] B. T. Dalslet, C. D. Damsgaard, M. Donolato, M. Strømme, M. Strömberg, P. Svedlindh, and M. F. Hansen, "Bead magnetorelaxometry with an on-chip magnetoresistive sensor." Lab Chip, **11**, 296 (2011).

[12] F. W. Østerberg, B. T. Dalslet, D. Snakenborg, C. Johansson, and M. F. Hansen, "Chip-Based Measurements of Brownian Relaxation of Magnetic Beads Using a Planar Hall Effect Magnetic Field Sensor," in *AIP Conf. Proc.*, Vol. 1311 (2010) pp. 176–183.

[13] R. Kötitz, P. Fannin, and L. Trahms, "Time domain study of brownian and néel relaxation in ferrofluids," Journal of magnetism and magnetic materials, **149**, 42 (1995).

[14] D. Eberbeck, C. Bergemann, F. Wiekhorst, U. Steinhoff, L. Trahms, *et al.*, "Quantification of specific bindings of biomolecules by magnetorelaxometry," Journal of nanobiotechnology, **6**, 4 (2008).

[15] F. Öisjöen, J. F. Schneiderman, A. P. Astalan, A. Kalabukhov, C. Johansson, and D. Winkler, "A new approach for bioassays based on frequency- and time-domain measurements of magnetic nanoparticles." Biosens. Bioelectron., **25**, 1008 (2010).

[16] F. W. Østerberg, G. Rizzi, T. Zardán Gómez de la Torre, M. Strömberg, M. Strømme, P. Svedlindh, and M. F. Hansen, "Measurements of brownian relaxation of magnetic nanobeads using planar hall effect bridge sensors," Biosens. Bioelectron., 10.1016/j.bios.2012.07.002 (2012).

[17] L. Neél, "Théorie du traînage magnétique des ferromagnétiques en grains fins avec applications aux terres cuites," Ann. Géophys, **5**, 99 (1949).

[18] W. Brown, "Thermal Fluctuations of a Single-Domain Particle," Phys. Rev., **130**, 1677 (1963).

[19] P. Debye, "Polar Molecules," Chemical Catalogue Co. (1929).

[20] A. D. Henriksen, B. T. Dalslet, D. H. Skieller, K. H. Lee, F. Okkels, and M. F. Hansen, "Planar Hall effect bridge magnetic field sensors," Appl. Phys. Lett., **97**, 013507 (2010).